University of Alberta

Library Release Form

Name of Author: Abdelkareem M. Alzo'ubi

Title of Thesis: The effect of tensile strength on the stability of rock slopes

Degree: Doctor of Philosophy

Year this Degree Granted: 2009

Abdelkareem M. Alzo'ubi
205-10735 81 Ave
Edmonton, Alberta
Canada, T6E 1Y2

Date: ___________________

University of Alberta

THE EFFECT OF TENSILE STRENGTH ON THE STABILITY OF ROCK SLOPES

by

Abdelkareem M. Alzo'ubi

A thesis submitted to the Faculty of Graduate Studies and Research in partial fulfillment of the requirements for the degree of **Doctor of Philosophy**.

in

Geotechnical Engineering

Department of Civil and Environmental Engineering

Edmonton, Alberta
Spring 2009

University of Alberta

Faculty of Graduate Studies and Research

The undersigned certify that they have read, and recommend to the Faculty of Graduate Studies and Research for acceptance, a thesis entitled **The effect of tensile strength on the stability of rock slopes** submitted by Abdelkareem M. Alzo'ubi in partial fulfillment of the requirements for the degree of **Doctor of Philosophy** in *Geotechnical Engineering*.

____

Dr. Derek Martin

____

Dr. Doug Stead

____

Dr. David Cruden

____

Dr. Robert Donahue

____

Dr. Ben Jar

____

Dr. Timothy G. Joseph

Date: ____________________

To my Family,
You are my everything.

Abstract

The stability of a rock slope is generally considered a function of the shear strength of the rupture surface. In natural slopes the rupture surfaces are often discontinuous and may be composed of fractures and joints separated by blocks of massive rock. In those situations the strength of the rupture surface is composed of three strength components: tensile strength, cohesion and friction. While the effect of the shear strength components, cohesion and friction, on slope stability are well understood, little research has been carried out on the role of tensile strength in rock slope stability.

The main goal of this thesis is to examine the effect of tensile strength and tensile fracturing on rock slope toppling. Toppling of rock slopes is defined by thin slabs of rock displacing out of the slope, eventually forming a rupture surface. This toppling process involves slip between the thin slabs and tensile rupture across the slabs. A numerical modeling methodology based on a discrete element framework was developed and used to investigate the effect of each strength component (tensile, cohesion, friction) on toppling stability. The methodology, which includes internal flaws in the intact rock, was first evaluated using the results from direct shear tests of discontinuous fractures. The procedure was then applied to centrifuge model tests of a toppling slope. Two case studies of large-scale slopes were also evaluated using the developed modeling methodology.

The results from this research show that the tensile strength of the intact blocks that separate fractures is a key parameter in the development of the rupture surface. For toppling slopes, friction and cohesion of the intact rock play a minor role, while the tensile strength play a major role in controlling the stability of the slope. A comparison of conventional discrete element modeling with the modeling methodology developed for this research at all scales investigated shows that the measured deformation patterns, and location of the rupture surface were in better agreement with the simulation results from the proposed methodology. The results indicate that the long-term stability of toppling slopes is likely controlled by the degradation of the tensile strength.

Acknowledgements

I would like to thank my supervisor, Professor Derek Martin, for giving me the opportunity to study at the Univeristy of Alberta. His support, insight, and patience are greatly appreciated. I consider myself fortunate to have had the opportunity to study under the guidance of Dr. Martin. I would also like to thank Professor David Cruden for his advice during the course of this thesis. I am also grateful for the support provided by the staff of the Civil and Environmental Engineering Department at the University of Alberta.

I would also like to thank and acknowledge my examiners, Dr. Doug Stead, Dr. Robert Donahue, Dr. Ben Jar, Dr. Timothy G. Joseph. I wish to extend my thanks and appreciation to all my professors and other staff at the Department of Civil Engineering, University of Alberta, for their support and encouragement.

I would like to acknowledge the financial contribution of the Railway Ground Hazard Research Program sponsored by CP Rail, CN and Transport Canada, and the Natural Sciences and Engineering Research Council of Canada. The completion of this thesis would not have been possible without their support.

Eternal thanks for my parents, my brothers and sisters, and my relatives for their love and encouragement during my studies here. The completion of my studies here has been an overwhelmingly great experience. I thank all those who made it possible.

Finally, this work would never have been completed without the support and love provided by my dear wife, Dr. Sana Rawaqa.

Table of Contents

1 Introduction 1

1.1 Statement of the problem . . . 3

1.2 Scope of Thesis . . . 5

1.3 Organization of Thesis . . . 6

2 Modeling of rock slopes 8

2.1 Introduction . . . 8

2.2 Experimental Studies . . . 11

2.2.1 Failure in compression . . . 11

2.2.2 Failure in shear . . . 16

2.3 Stability Analysis . . . 24

2.3.1 Limit equilibrium analysis . . . 25

2.3.2 Continuum modeling . . . 29

2.3.3 Discontiuum modeling . . . 37

2.3.4 Hybrid methods . . . 39

2.4 Summary . . . 45

3 A discrete element damage model for rock slopes 46

3.1 Introduction . . . 46

3.2 Damage Model . . . 49

3.3 Flaw patterns in rock . . . 53

3.4 Failure criterion of the flaws . . . 54

3.5 Damage Model on direct shear tests . . . 58

3.6 The effect of discontinuity persistence . . . 63

3.7 Effect of tensile strength in the direct shear test 68
3.8 Scale effect in UDEC-DM 68
3.9 Summary 70

4 Toppling Failure in Centrifuge Models 72
4.1 Introduction 72
4.2 Adhikarys's centrifuge experimental results 74
    4.2.1 Introduction 74
    4.2.2 Numerical modeling: conventional UDEC 76
    4.2.3 The Damage Model toppling simulation 77
4.3 Longtan Hydropower Project centrifuge model 91
    4.3.1 Introduction 91
    4.3.2 Conventional UDEC 93
    4.3.3 UDEC-DM simulation 94
4.4 Conclusions 98

5 Toppling and Buckling in Rock Slopes 100
5.1 Introduction 100
5.2 Toppling 101
    5.2.1 Underdip toppling 101
    5.2.2 Common toppling 105
5.3 Buckling failure 115
    5.3.1 Introduction 115
    5.3.2 Buckling failure in open-pit coal mines 115
    5.3.3 Buckling in natural rock slopes 117
5.4 Conclusion 128

6 Toppling at Highland Valley Copper Mine 130
6.1 Introduction 130
    6.1.1 Geology of the Site 133
6.2 Movement mode at Lornex Pit 134
6.3 Material testing 136

6.3.1 Hydrology of the Site 137
6.4 Geomechanics assessment and strength properties 138
6.5 Displacement monitoring and movement rate 141
6.6 The Numerical model 143
6.7 Calibration of the model 146
6.8 The UDEC-DM results 149
6.8.1 Movement mode in the numerical model 150
6.8.2 Deformation comparison between the field and the numerical model 153
6.8.3 Deformation comparison between conventional UDEC and the UDEC-DM approaches 156
6.8.4 Effect of tensile strength 157
6.9 Conclusions 159

7 Progressive Failure in Rock Slopes, Checkerboard Rock Slope 161
7.1 Introduction 161
7.2 Geology 164
7.3 Instrumentation and monitoring of the slope 164
7.4 Groundwater and climate 166
7.5 Previous work 167
7.6 The numerical model 169
7.7 Effect of weathering and stability analysis 171
7.7.1 Tensile strength degradation 172
7.7.2 Displacement rate boundary condition 178
7.8 Suggested supporting system 180
7.9 Conclusion 185

8 Summary and Conclusion 186
8.1 Summary 186
8.2 Conclusion 190
8.3 Recommendations 192
Bibliography 194

List of Tables

2.1 Frank Slide rock mass properties used in the Numerical Model determined using Hoek-Brown Failure Criteria, (modified from Cruden and Martin, 2007) 35

3.1 Comparison between Lajtai's plaster of Paris model properties and those used in the UDEC-DM 63

4.1 Properties of the ilmenite-gypsum material, (modified from Adhikary and Dyskin, 2006) 74

4.2 Properties of the artificial rock (modified from Zhang et al., 2006) . 94

4.3 Elastic properties and the flaws properties used in the simulation . . 96

5.1 Material properties used in modeling of the underdip example . . . 104

5.2 Initial strength and deformation properties used in the UDEC-DM . 109

5.3 Strength and deformation properties used to study the layer thickness effect 114

5.4 Material properties used in modeling of the open-pit buckling examples. 117

5.5 Buckling numerical model properties 121

6.1 Strength properties of the geological units used in the model, modified from Tosney (2001) 140

6.2 Rock mass elastic properties, modified from Tosney et al. (2000) . . 140

6.3 The discontinuities properties used in the model, modified from Tosney et al. (2000) 141

6.4 Cumulative mining-induced displacement, after Tosney et al. (2000) 146

6.5 Normal and shear stiffness resulting from the calibration process . . 149

7.1 Elastic properties for the rock formations 169
7.2 Strength properties for the flaws 172
7.3 Joints properties used in the UDEC-DM 172
7.4 Unconfined compressive strength versus the back calculated tensile strength at Failure 175
7.5 Support system properties 182

List of Figures

2.1 Example of discrete blocks that form during a small rock slope failure in competent rock. 9
2.2 Class-one rock instabilities controlled by continuous through-going rupture surface (modified from Martin and Kaiser, 1984) 10
2.3 Class-two rock slopes in which non-continuous joints are present . . 10
2.4 Fracturing of plaster of Paris under uniaxial loading (modified from Lajtai, 1974) 12
2.5 Limestone specimen failure under uniaxial compression (modified from Ingraffea and Heuze, 1980) 13
2.6 Fracturing of sandstone under uniaxial Loading (modified from Petit and Barquins, 1988) 14
2.7 The sample after failure and the fracturing of a sample under uniaxial loading (modified from Mughieda and Alzo'ubi, 2004) 15
2.8 Shear zone formation in direct shear loading 16
2.9 Development of slip surfaces in clay subjected to shear loading (modified from Skempton, 1967) 17
2.10 Detailed shear zone in Clays (modified from Morgenstern and Tchalenko, 1967a) 18
2.11 Lajtai's set-up to examine the mobilization of shear strength along the non-continuous joint in direct shear tests 19
2.12 Stress state at the intact bridge area between two joint segments (modified from Lajtai, 1969a) 20
2.13 Direct shear test results obtained by Lajtai (1969c) 21

2.14 Shear zone development at different stages of stress-displacement curve on overconsolidated Clay (modified from Tchalenko, 1970) . 22

2.15 Development of fracture on discrete element modeling of synthetic rock (modified from Cho et al., 2008) 24

2.16 Slope stability analysis using the general limit equilibrium method using the SLIDE program, (Rocscience, 2006) 27

2.17 Failure in non-persistent joints (modified from Einstein et al., 1983) 28

2.18 Finite difference model using the FLAC program of the Frank slide of Alberta, Canada, (modified from Benko and Stead, 1998) 30

2.19 Finite Element model using the PHASE2 Program of the Frank slide of Alberta, Canada, (modified from Cruden and Martin, 2007) 31

2.20 Tensile stresses generated using the Finite Element Method (modified from Stacey et al., 2003) 32

2.21 The relationship between the Hoek-Brown and Mohr-Coulomb failure criterion (modified from Hoek et al., 2002) 34

2.22 Cohesion weakening and friction strengthening as a function of plastic strain (modified from Hajiabdolmajid et al., 2002c) 37

2.23 Discrete Element model of the Frank slide (Alberta, Canada) by using the UDEC Program (modified from Benko and Stead, 1998) . 38

2.24 Rock slope simulation by using Discrete Element method (modified from Nichol et al., 2002) 40

2.25 Rock slope failure simulation by using the PFC program (modified from Wang et al., 2003) 42

2.26 Randa rock slope failure simulation by using the ELFEN program (modified from Pine et al., 2007) 43

2.27 Rock slope failure simulation by using the ELFEN program (modified from Stead and Coggan, 2006) 44

2.28 Block caving by using the ELFEN program (modified from Vyazmensky et al., 2007) 44

3.1 Calculation step in discrete element method (modified from Itasca, 2004b) 48
3.2 Mohr-Coulomb surface in principal stress space 49
3.3 Block assembly subjected to compression forces and the resulting tensile stresses at the bond (Modified from Potyondy and Cundall, 2004) 50
3.4 Illustration of the polygonal structure used to simulate intact rock using 100 iterations to generate the flaws. 51
3.5 Rock mass block shape, The numbers refer to various flaw sets (modified from Dearman (1991)) 55
3.6 Coulomb-slip model used to simulate the flaws behaviour 57
3.7 Definition of zone dimension used in stiffness calculation, Equation 4.9 59
3.8 The unconfined compressive strength of plaster of Paris 61
3.9 Effect of cohesion on the uniaxial strength 62
3.10 The UDEC-DM model used to simulate Lajtai's direct shear experimental results. 62
3.11 Comparison of UDEC-DM model results with the results from direct shear tests on plaster of Paris and open joints (data from Lajtai, 1969c) 64
3.12 Comparison of UDEC-DM model results with the results from direct shear tests on plaster of Paris and closed joints (data from Lajtai, 1969c) 64
3.13 Non-persistent joints direct shear model 65
3.14 Failure envelope of non-persistence joint direct shear model 66
3.15 Normalized shear strength of jointed rock to the strength of the intact material 67
3.16 Failure envelope and the tensile strength effect on direct shear discrete element damage model simulation 69
3.17 Direct shear results for different edge lengths 70

4.1 Toppling modes observed in the field, (a) Flexural Toppling, (b) Block toppling, (c)Block-flexural toppling (modified from Goodman and Bray, 1976) (d) underdip toppling (modified from Cruden and Hu, 1994) 73
4.2 Centrifugal experimental results, g is gravity, (modified from Adhikary and Dyskin, 2006) 75
4.3 The physical model after testing (modified from Adhikary and Dyskin, 2006) 75
4.4 Conventional UDEC numerical model, 40 beds across base 77
4.5 Comparison between conventional UDEC and the experimental results, c=15kPa 78
4.6 Comparison between conventional UDEC and the experimental results, c=5kPa 78
4.7 The plasticity indicators in conventional UDEC compared to the actual failure surface 79
4.8 The UDEC-DM model used to model Adhikary's experiments and the boundary conditions 80
4.9 The effect of normal and shear stiffness at the deformation pattern, x10 GPa/m 81
4.10 Comparison between the horizontal displacement between Adhikary's results and those from UDEC-DM model 82
4.11 The deformation at the monitoring points at failure 82
4.12 UDEC-DM simulation at failure 83
4.13 Rupture surface as predicted by the UDEC-DM model 84
4.14 Horizontal displacement patterns with variations in the tensile strength 86
4.15 Tensile strength and friction angle of the flaws effects on the failure load 86
4.16 The flaws' friction angle effect on the deformation pattern 88
4.17 Comparison of failure surfaces at different tensile strength values (failure surface drawn based on the open joints) 89

4.18 Deformation patterns from the numerical models at 15.0 kPa and 5.0 kPa of bedding planes' cohesion, along with the actual deformations from the centrifugel experiments 91
4.19 Failure surfaces at cohesions of 15 kPa and 5 kPa, along with the actual rupture surface, Tensile strength= 1.1MPa 92
4.20 The model at failure, bedding planes' cohesion = 5.0 kPa 93
4.21 Failure of the model at 130g (modified from Zhang et al., 2006) . . 94
4.22 Sketch of the centrifugel model at failure (modified from Zhang et al., 2006), scale is shown in Figure 4.23 95
4.23 The conventional UDEC model 95
4.24 Conventional UDEC model at failure 96
4.25 The UDEC-DM model used to simualte the centrifugel experiment . 97
4.26 Rupture surface formation based on the UDEC-DM and the experimental one 98

5.1 Example of an under-dip topple described by Cruden and Hu (1994). The beds are approximately 5 to 20 cm thick 102
5.2 Locations in the Highwood Pass (modified from Cruden and Hu, 1994) 103
5.3 Geometry of the underdip toppling example 104
5.4 Initiation of toppling at the slope's toe (uniform bed thickness) . . . 105
5.5 Underdip slope failure using the UDEC-DM (non-uniform beds) . . 106
5.6 The model used for common toppling failure analysis using the UDEC -DM model 108
5.7 Rupture surfaces formation inside the UDEC-DM 110
5.8 Common toppling failure using the UDEC-DM model 111
5.9 Deformation pattern observed in the block-flexural model for two points 112
5.10 Critical slope height (Hc) for rock masses with different layer thicknesses and tensile strengths 114

5.11 Buckling failure: (a) The Model, (b) failure initiation at the toe of the slope. 116
5.12 Buckling in natural rock slope at the Highwood Pass (modified from Hu and Cruden, 1993, scale shown in Figure 5.13) 119
5.13 Sketch of the Highwood Pass buckling example with different rock units (modified from Hu and Cruden, 1993) 120
5.14 Numerical model for buckling site. The insert shows the details of flaws and joints in the model 122
5.15 Buckling initiation at the toe of the slope 123
5.16 Buckling deformation at the toe and the middle of the slope 124
5.17 The displacement pattern in the buckling example at two points. See the insert for the points' location 125
5.18 General cross-section through the buckling site location, notice the location of the buckle 127
5.19 Horizontal to vertical stress ratio effect on the tensile strength at failure 128
5.20 Buckling failure at the slope. Tensile strength=0.25MPa 129

6.1 The location of the Highland Valley Copper Mine in British Columbia, Canada 131
6.2 Overview of the Lornex Pit and the Valley Pit and the location of the instability location (modified from Newcomen et al., 2003b) . . 132
6.3 Conceptual toppling movement mode observed at HVC (modified from Tosney et al., 2000) 135
6.4 Surface expression of the movement mode at Highland Valley Copper Mine (modified from Tosney, 2001) 136
6.5 Groundwater profile at southeast wall of Lornex Pit (modified from Tosney, 2001) 137
6.6 Lornex southeast wall RMR rating (modified from Tosney et al., 2004) 139

6.7 The location of the slope-monitoring prisms and regions of instablities in the Lornex Pit (modified from Newcomen et al., 2003b) . . 142
6.8 Typical movement rate pattern recorded at Lornex southeast wall (SMP#458), (modified from Newcomen et al., 2003b) 143
6.9 Blocks excavation sequence at Lornex southeast wall 145
6.10 Locations of the slope-monitoring prisms at the UDEC-DM 145
6.11 The Lornex southeast wall UDEC-DM; the insert shows the details of the flaws 147
6.12 The conventional UDEC model used to determine the area susceptible to toppling 148
6.13 The RMR values and locations assigned to the UDEC-DM (modified from Tosney, 2001) 149
6.14 Cumulative displacement comparison for the calibrated model . . . 150
6.15 The movement mode at the Lornex southeast wall simulated by the UDEC-DM; the insert provides a closer look at the crest 151
6.16 Plot of the numerical model, showing the rupturing in the slope . . . 152
6.17 Bulging and crushed rock at the toe of the UDEC-DM model 153
6.18 Comparison between mining-induced deformation at the field and the UDEC-DM at SMP#468 154
6.19 Comparison between mining-induced deformation at the field and the UDEC-DM at SMP#454 155
6.20 Deformation pattern observed in block toppling 155
6.21 Comparison between measured mining-induced displacements and the simulated UDEC-DM displacements at SMP#413 156
6.22 Comparison between measured mining-induced displacements and the simulated UDEC-DM displacements at SMP#560 157
6.23 Rupturing of the Lornex pit at $\sigma_t = 1.0$ MPa, (compare this figure with Figure 6.16) 158
6.24 Deformation comparison at $\sigma_t = 1.0$ MPa, $\sigma_t = 1.0$ MPa at SMP#413 159

7.1 The general location of the dam 162

7.2 The dam and the the outline of the slide (modified from Watson et al., 2006) 163

7.3 Detailed cross-section along the Checkerboard Creek slope (modified from Watson et al., 2006) 165

7.4 Location of the cross-section AA, 1 and 2 are locations of weathered and unweathered rock photographs, Figure 7.11 and Figure 7.12, respectively, (modified from Watson et al., 2006) 166

7.5 Deformation pattern along with the temperature and the variation of water level (modified from Watson et al., 2004) 167

7.6 Weathering at the surface of the slope adjacent to the highway . . . 168

7.7 Rock mass surface exposure showing the blocky nature of the rock mass 170

7.8 The numerical model used in the study 170

7.9 The details of the joints and flaws 171

7.10 Effect of weathering on tensile strength and strain at failure (modified from Aydin and Basu, 2006) 173

7.11 Weathered rock mass along cross-section A-A, the photograph has been taken at location 1, as shown in Figure 7.3 (1) 174

7.12 Unweathered rock mass along cross-section A-A, the photograph has been taken at location 2, as shown in Figure 7.3 (2) 175

7.13 Hoek-Brown strength envelope used to obtain the friction angle and cohesion used in this study 176

7.14 Initiation of failure at the side of the highway 177

7.15 Failure development at the toe of the slope 178

7.16 Progressive movement of the failed material toward the reservoir . . 179

7.17 Fracturing in the weathered rock mass after 1.8 m of displacement under constant velocity 180

7.18 Continuous failure after the removal of the first failed material . . . 182

7.19 Proposed support system contains of 20 cm shotcrete and cables at an average distance of 8.0 m 183

7.20 Effect of a support system at the displacements at point A (see Figure 7.19 for location of A) 184

... ...

Chapter 1

Introduction

In nature, rock slopes are highly heterogeneous and are associated with many unknowns such as the state of the stress, the structures inside the rock mass, and the strength parameters. These three factors control the design of rock slopes and the failure mechanism. Rocks may fail in tension or shear, depending on the mechanism of loading and the stress path in the field or in the laboratory. Rock slopes can be divided into two main categories: structurally controlled slopes, such as the planer and wedge failures, and the non-structurally controlled slopes. The structurally controlled slopes normally fail by shear sliding along one or more continuous discontinuities, whereas, in the non-structurally controlled slopes, failure is a complicated process and involves failure in both the discontinuity and the intact material (Terzaghi, 1962).

The assumption that a single discontinuity controls the slope failure is a simplified approach for analyzing rock slopes and is applicable only for small-scale slopes, while for large slopes, the continuity has limited validity unless a fault or any continuous large rock structure existed prior to failure. Many authors have discussed this issue and argued that rock joints in large-scale slopes are rarely continuous, and that intact rock exists between the joint segments (Terzaghi, 1962, Lajtai, 1969a, Jennings, 1970, Ladanyi and Archambault, 1980, Einstein et al., 1983). These authors argued that a rupture surface in rock slopes passed through the intact rock to form a kinematical admissible release surface. This process may occur progressively, and rupture surface propagates from the pre-existing rock joints through the intact material. Some stepping may be required to form a kinematic admissible rupture surface. This stepping is due to the tensile stress concentrations at the rock bridges and the tips of the joints (Ladanyi and Archambault (1980), Shen et al. (1995)) . Einstein et al. (1983), Shen et al. (1995), Jennings (1970), and Lajtai (1969c) argued that the bridge between the joint segments fails in tension and that the tensile strength plays an important role in the failure mechanism of rock slopes in a low-confinement stress environment.

Lajtai (1969c) obtained interesting direct shear results for rock-like material and argued that the bridges failed by different mechanisms depending on the normal stress level. He also used a non-linear failure envelope to describe the effect of the normal stress on the shear strength of the rock. Lajtai (1969c) found that the friction and the cohesion did not mobilize simultaneously, but that the cohesion mobilized first, and then the friction mobilized to allow progressive failure to occur inside the rock mass. Martin (1997) also discussed such non-simultaneous strength parameters' mobilization. Hajiabdolmajid and Kaiser (2002a) used the concept of cohesion weakening and friction strengthening at different plastic strain levels in a continuum modeling framework to analyze the Frank Slide by using what they called a "brittleness index". These researchers suggested that the frictional strength starts at zero and is mobilized as the plastic strain increases while the cohesion is destroyed progressively with increasing damage in the rock mass. They modeled the direct shear test and compared their results with Lajtai's direct shear results. These results clearly indicated a non-linear failure envelope for the jointed rock mass. The Hoek-Brown failure criterion also suggested a non-linear failure envelope for the rock mass, as opposed to the linear failure envelope suggested by the Mohr-Coulomb criterion (Hoek and Brown, 1980).

Although the rock bridges between discontinuities fail in tension, and the shear failure occurs as a secondary failure, the effect of the tensile strength on the rock slopes is rarely taken into consideration, mainly because of the lack of a suitable failure criterion and the lack of tools for accounting for the tensile strength effect (Einstein et al., 1983, Shen et al., 1995, and Sjoberg, 1999). This thesis introduces a new discrete element modeling methodology to capture the effect of the tensile strength on rock slope instability and to examine if this modeling approach is capable of capturing rock slopes' behaviour and instability.

1.1 Statement of the problem

Rock masses are heterogenous and composed of both intact material and structures: joints, bedding planes, and faults. These structures are rarely continuous. Terzaghi (1962) and Einstein et al. (1983) suggest that the persistence of discontinuities is limited in reality and that a complex interaction between the pre-existing joints and brittle fracture propagation through intact rock is required to provide a rupture surface. The strength components of rock masses are the tensile strength, cohesion and friction. For example, intact granite has a tensile strength of 6-10 MPa, cohesion of 30-40 MPa and friction of 45-50°(Martin, 1993). The friction angle is hardly affected by the time-dependent strength degradation, while the cohesion and tensile strength are vulnerable to it. In natural rock masses, the amount of the tensile strength is less than the cohesion. If both the cohesion and tensile strength degrade with time at the same rate, the tensile strength is destroyed before the cohesion.

Lajtai (1969b) discussed the direct shear testing method and its advantages and disadvantages in detail, and described its compatibility with the natural loading conditions. He argued that in the case of non-continuous joints, the major principal stress at the bridges is tensile even if the all-around stresses are compression, and that these tensile stresses are responsible for forming tension fractures inside the rock bridges.

A rock mass can be described as randomly sized blocks bonded to each other with cohesion, tensile strength and friction. Failure is initiated when the bonds among the blocks are broken. Our new discrete element modeling approach allows failure to be initiated and propagated inside the rock mass whenever the stresses exceed the strength of that rock. Fundamentally, rocks are composed of complex-shaped grains, which create interlocking inside the rock mass. As a rock block is subjected to stresses, localized tensile stresses in the direction of the least principal stresses may cause a failure, especially at a low-confinement stress (Lajtai, 1969b, Kemeny, 1991).

Cundall (1971) proposed the discrete element numerical modeling method. A new degree of freedom is added to the discrete element method by using a Voronoi tessellation generator to generate random blocks inside the rock mass. This methodology is able to produce randomly sized blocks to simulate the heterogeneity of the rock mass and enable the tensile stresses to arise.

In non-persistent jointed rock masses, the strength is attributable to both the bridge and the joint segment. In the traditional design approach, limit equilibrium, it is assumed that the strength is governed by the joints, and the bridge strength is neglected. As a result, designs based on this approach are conservative, for a small bridge may greatly contribute to the strength of the rock mass. In addition, tensile fracturing is rarely considered due to the difficulty in dealing with the complicated failure mechanisms in large-slope problems. As well, if kinematic release does not occur along the dominant features,joints, or bedding planes, internal shear and internal distortion as well as brittle and ductile fracturing are required to form admissible failure. This brittle, ductile behaviour and internal deformation produce a complicated failure mechanism inside the rock mass. Einstein et al. (1983) and Shen et al. (1995) concluded that rock bridges fail in tension and that shear failure occurs as a second phenomenon.

Aydin and Basu (2006) concluded that the tensile strength of intact rock is highly affected by the degree of weathering in weathered rock. This conclusion shows the importance of the tensile strength degradation effect on rock slopes, and this effect should be considered in order to evaluate the stability of rock slopes.

Rock slope failure processes should be explored while considering both the effect of tensile fracturing on rock failure kinematics as well as the strength derived from both bridges and joints. These processes will be studied by exploring the influence of adding an extra degree of freedom inside the rock mass to produce fracture initiation, propagation and coalescence between the pre-existing discontinuous joints, or along the discontinuous basal slip surface. Field observations and numerical modeling have shown that in brittle rocks, fracture initiation and propagation are important factors in progressive failure and that they usually lead to catastrophic failure. For this reason, one key element in modeling the failure process is the simulation of the fracture propagation and rock mass disintegration.

1.2 Scope of Thesis

This thesis focus is to explore rock slope failure processes and mechanisms by developing a distinct element approach capable of modeling the damage process inside rock masses and able to capture the tensile strength degradation effect on rock slope instability. The main objectives are to answer the following questions:

1. What is the effect of the tensile strength on slope instability?
2. Is there a class of problems where failure can occur only if the slope kinematics have an extra degree of freedom?
3. Does the tensile strength or the friction control the rock slopes instability?
4. What are the effects of support on the slope behaviour process?

1.3 Organization of Thesis

The thesis is structured into seven chapters. This chapter (**Chapter 1**) introduces the problem of the thesis, the research objectives, and the organization of the thesis adapted to support the thesis hypothesis.

Chapter 2 discusses the current state of knowledge in rock slope engineering. The discussion covers tensile fracturing in experimental studies and the methods of analysis and design that handle tensile strength in rock masses.

The proposed method of rock slope analysis is introduced in **Chapter 3**. The discrete element damage model is used to simulate the direct shear test, and the results are compared to the experimental direct shear results from Lajtai (1969c). The effect of tensile strength on the direct shear and degree of persistence of the joints are discussed.

Two centrifugel experiments on rock slopes are modeled in **Chapter 4** to examine the ability of the discrete element damage model to simulate toppling failure in the laboratory. The ability of the discrete element damage model to capture the rupture surface is examined. In this chapter, the deformation pattern observed in the laboratory is compared to the one predicted by the UDEC-DM.

Chapter 5 presents three movement modes that might occur in rock slopes. Underdip toppling, common toppling, and buckling in both natural and man-made slopes are simulated by using the discrete element damage model. The tensile strength effect on the stability of these rock slope movements is tracked.

In **Chapter 6**, to increase our confidence in the proposed method, the discrete element damage model is used to explore large-scale rock slopes. An open-pit mine slope from British Columbia, Canada, is examined and modeled using the damage model approach. This example explores the toppling mechanism in a man-made slope. The slope displacement and movement mode in the field is compared to that predicted by the discrete element damage model.

Chapter 7 examines a case study from the Revelstoke Dam Project, British Columbia, Canada. The Checkerboard Creek rock slope is susceptible to extensive weathering. The weathering process was modeled by degrading of the tensile strength of the rock mass. The support's effect on limiting the displacement amount is also presented.

Finally, **Chapter 8** presents the conclusion and recommendations derived from the current research. This chapters includes a summary of the thesis and an outline of the conclusions drawn from this research.

Chapter 2

Modeling of rock slopes

2.1 Introduction

Discontinuities in rock slopes are rarely continuous at the scale of the slope; even when a small highway cut fails, the result can be characterized as a ”pile of rock blocks” (Figure 2.1). The failure does not take place as a single block sliding on a single discrete plane, but the process requires the development of fractures through intact material such that many discrete blocks form. This result implies that the rock mass is composed of discontinuous pre-existing joints or flaws that propagate as the rock slope moves. For non-persistent rock joints to form a continuous rupture surface, failure must occur throughout the intact rock and along the existing joints. In such a case, the strength of a rock mass must be derived from both the solid rock and the discontinuities.

Rock slopes susceptible to instability can be divided into two general classes: discontinuity controlled slopes and complex rock slopes. In the first category, rock slopes are controlled by a well-defined through-going rupture surface; examples include wedge failure and planar failure. Figure 2.2 shows rock slopes of this category. These rock slopes instability can be handled easily by using the limit equilibrium methods.

In the second class, complex rock slope instability can be formed through a “discontinuous rupture surface” where slope movements may lead to the formation

Figure 2.1: Example of discrete blocks that form during a small rock slope failure in competent rock.

of new fractures that may link to form a continuous rupture surface. Figure 2.3 demonstrates the complexity of the problem; notice that rock slopes usually consist of a network of discontinuities with different degrees of persistency and orientations and not only continuous discontinuities. Terzaghi (1962) pointed out that most rock joints are limited in their continuity and that the rock bridge's cohesion contributes to the rock mass's shear strength. In such rock slopes, progressive failure may cause the non-continuous joints to propagate and coalesce to form the failure surface. A slope's overall stability can be determined by the amount of strength derived from both the discontinuities and the intact rock. To handle the stability of the second class of problems, many approaches have been adapted, ranging from experimental studies to advanced numerical approaches.

Many methods for rock slope analysis and design are available and can be used by engineers, ranging from empirical methods to complex numerical modeling approaches. The method of analysis has to be chosen based on the problem to be

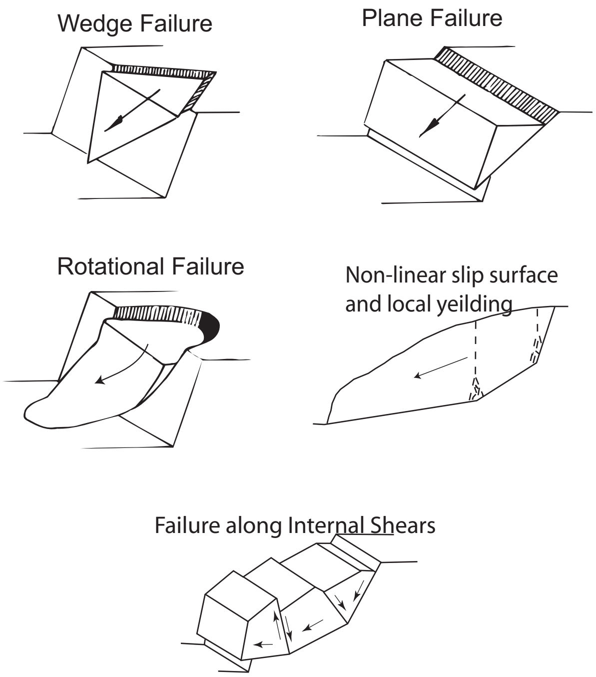

Figure 2.2: Class-one rock instabilities controlled by continuous through-going rupture surface (modified from Martin and Kaiser, 1984)
.

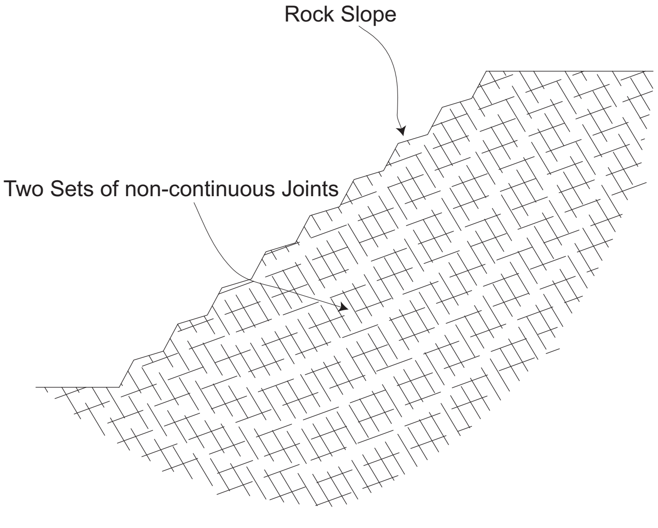

Figure 2.3: Class-two rock slopes in which non-continuous joints are present
.

analyzed. For example, a simple sliding analysis can be performed on a sliding block along a persistent surface, while complex calculations are required to analyze a heavily jointed rock mass. More than one method might be needed for slope stability analysis in order to account for the shortcomings of any individual method. Stead et al. (2001) discussed the different approaches for rock slope stability analysis and presented the advantages and disadvantages of each method. In general, the methods of analysis can be used for three purposes: back calculating of an already failed slope, designing a slope for a roadway cut or open-pit mine, and predicting the behaviour of a slope. The following approaches for rock slope analysis and modeling will be discussed briefly: limit equilibrium, continuum modeling, discrete element modeling, and hybrid methods. In the following, failure in compression of rocks, failure in shear of rocks, and the current approaches to solving class-two problems are reviewed.

2.2 Experimental Studies

2.2.1 Failure in compression

To investigate the failure of non-continuous jointed rocks in compression, many researchers have performed uniaxial and biaxial compression tests. In general, cracking was found to be initiated at the joint tips by tensile stresses, and the rock bridges were found to fail in tension, shear or combination of both. Many of the experiments included in this review conducted on artificial rocks due to the difficulty of using natural rocks. The following discussion provides a brief description of such studies.

Lajtai (1974) performed a uniaxial compression on Plaster of Paris specimens. He found that “tensile” fractures were initiated first and then were followed by “normal” and “inclined shear” fractures. The tensile stresses around the tip of the pre-existing joint initiated the wing cracks first and were followed by shear fracturing. Figure 2.4 illustrates the fracturing pattern observed in Lajtai’s (1974) experiments under uniaxial loading. The direct shear and the uniaxial tests showed the strong role of the tensile strength and tensile fracturing in rock mass strength.

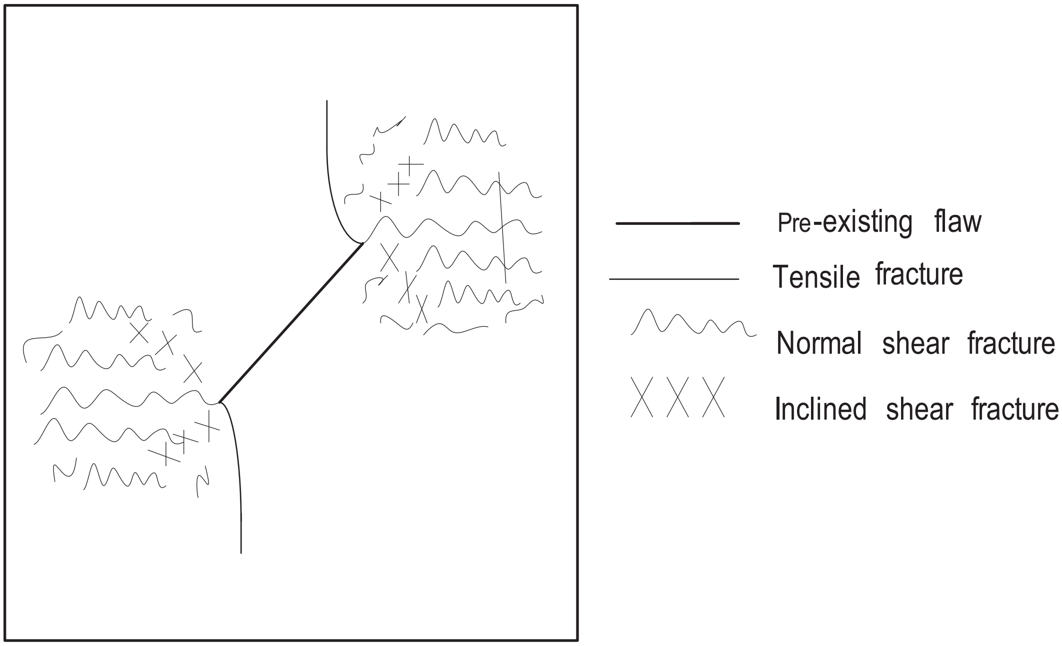

Figure 2.4: Fracturing of plaster of Paris under uniaxial loading (modified from Lajtai, 1974)

Ingraffea and Heuze (1980) tested two rock types, Granodiorite and Limestone specimens, under a uniaxial loading. The crack initiation and propagation throughout the samples were similar to those observed by Lajtai (1974). Ingraffea and Heuze (1980) referred to cracks that initiated due to tensile stresses at the tip of the joint, and propagated in a curvilinear path as the load increased, as primary cracks. After considerable primary crack propagation, secondary cracks, originating from the compressive stresses appeared. A through-going rupture surface formed as a result of the secondary cracks. Figure 2.5 illustrates the fracturing observed in Ingraffea and Heuze's (1980) experiments.

Petit and Barquins (1988) tested low- and high-porosity Sandstone specimens under uniaxial loading and concluded that, as in all the previous crack growth processes, the first cracks to be initiated were branch fractures "bf," followed by the shear zones "sz." Figure 2.6 shows the fracturing observed in Petit and Barquins's (1988) tests. The Branch cracks "bf" are the same as wing cracks, and the shear

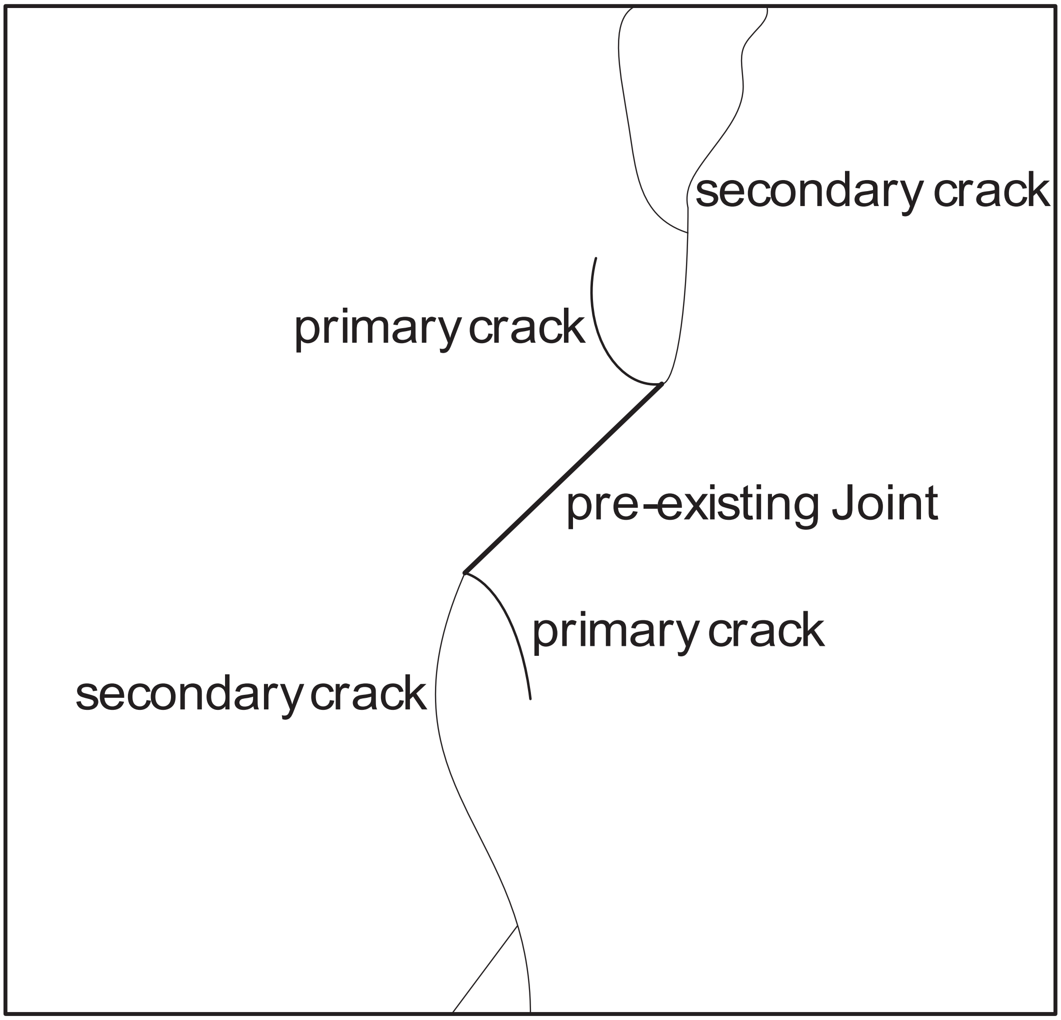

Figure 2.5: Limestone specimen failure under uniaxial compression (modified from Ingraffea and Heuze, 1980)

zones are the same as the secondary fractures.

Shen et al. (1995) performed a series of uniaxial compression tests on small Synthetic Rock specimens with dimensions of 152.4 x 76.2 x 30 mm. These researchers tested both closed and opened joints. The fracture mechanism was monitored with a camera. The results showed that the coalescence of the inclined fracture was due to shear failure and/or tensile failure. The final shape of the fracturing was highly dependent on the position of the joints; i.e., when the fractures were overlapping in the direction of the load. The coalescence was generated by tensile

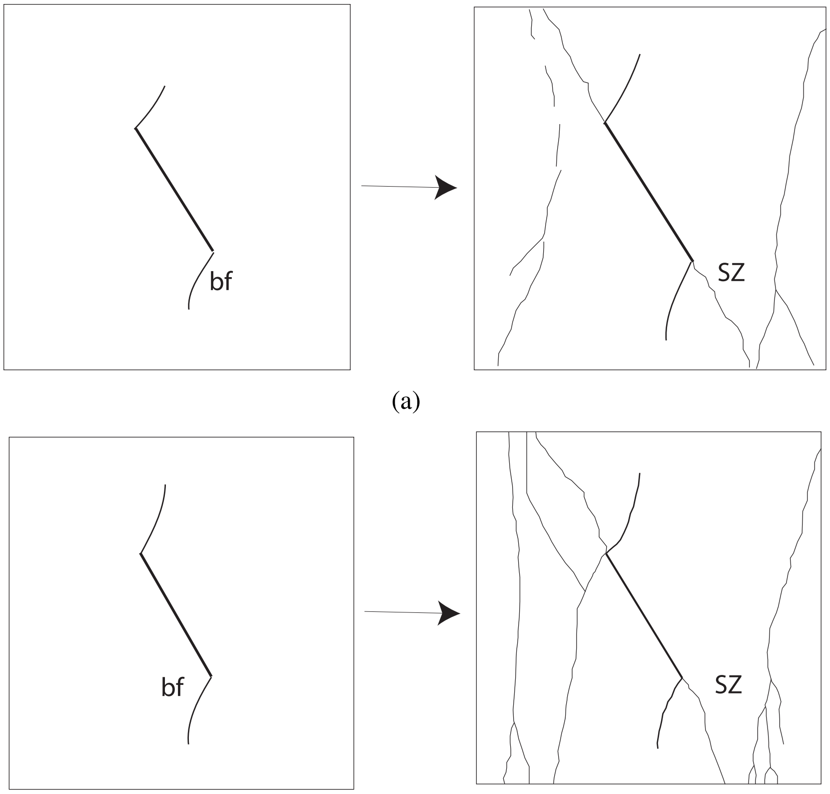

(a)

(b)

Figure 2.6: Fracturing of sandstone under uniaxial Loading (modified from Petit and Barquins, 1988)

and shear fracturing, whereas when the joints were coplanar or slightly offset, they claimed that the coalescence was generated by Shear Fracturing.

Mughieda and Alzo'ubi (2004) conducted uniaxial loading tests on a material made of Silica Sand, Cement and Water. To study the failure mechanisms of joints and rock bridges in jointed rock masses, a series of uniaxial compression tests was performed on specimens made of rock-like material. The open-joint inclination angle was maintained at 45°, while the offset angle, i.e., angle between the plane of the joint and the line that connected the two inner tips of the joints, was changed from 0° to 120° in increments of 15°. In all of the tested samples, curvilinear cracks "wing cracks" were initiated at the joint tips due to the high tensile stress concentrations. These wing cracks propagated toward the direction of the loading.

The coalescence mechanism of two cracks was investigated. The results showed that open cracks could coalesce by shear failure or tensile failure. The coalescence path was found to be dependent mainly on the inclination of the rock bridge between the cracks. Figure 2.7 shows the fracturing of a sample with a bridge angle of 75°. The results showed that wing cracks initiated by the tensile stresses and the tensile and shear fracturing caused coalescence between the pre-existing joints.

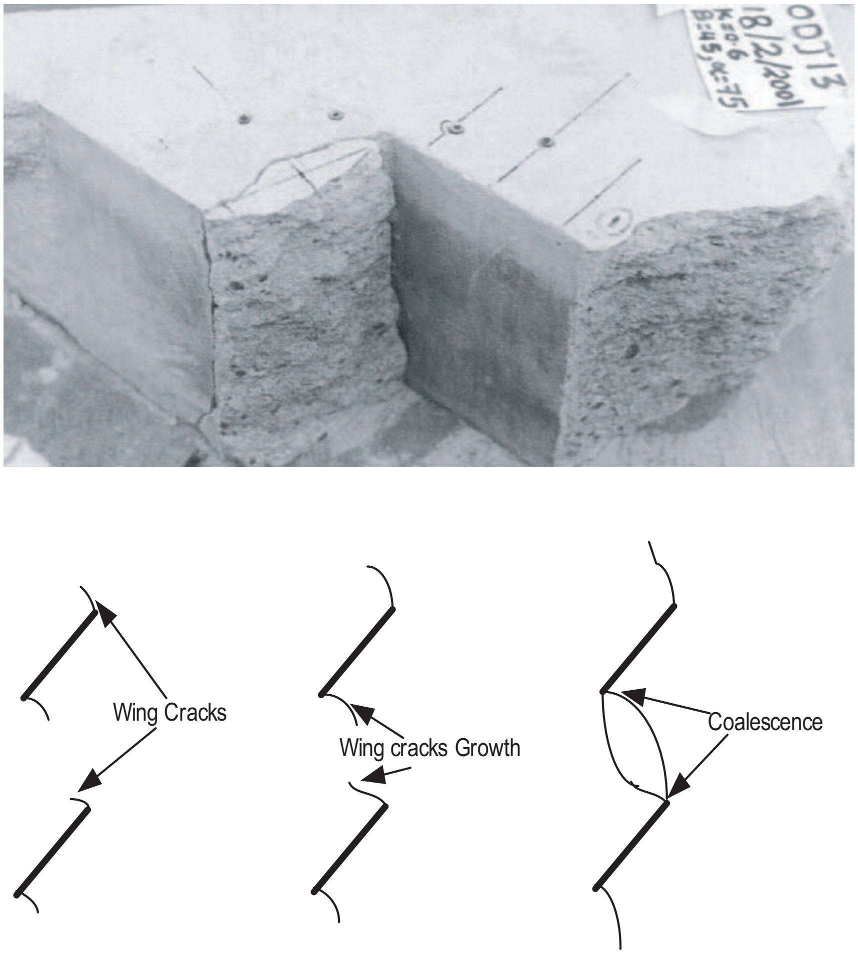

Figure 2.7: The sample after failure and the fracturing of a sample under uniaxial loading (modified from Mughieda and Alzo'ubi, 2004)

2.2.2 Failure in shear

Under shear loading, rocks and soils develop a shear zone within which most of the sliding occurs. The scale of this shear zone may range in size from microscopic scale to regional faults. As the shear loading increases, the fracturing nucleates and propagates to form a slip surface inside the material to allow sliding along that surface. In the shear zone, many fractures referred to as “Reidel shears” (R) and “conjugate Riedel shears” (R) are formed prior to the formation of a principal displacement shear (Skempton, 1967). These fractures are *en echelon* fractures formed at an angle to the direction of shearing and are, arguably, shear or tension fractures(Figure 2.8).

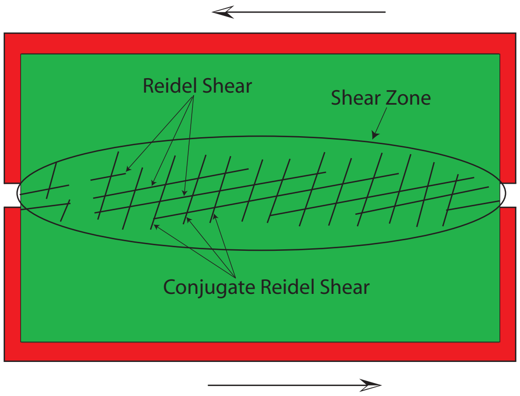

Figure 2.8: Shear zone formation in direct shear loading

Cloos (1955) performed simple-shear tests on Clay-Cake placed on a movable square of wire cloth to examine the fracture patterns as the shear loading increased. He showed that the shear zone is made up of a series of *en echelon* discrete fractures forming at various angles to the direction of shearing. Cloos (1955) found many examples of this type of movement in the field.

Skempton (1967) conducted a detailed field mapping of shear zones in Clays, Sandstones, and Siltstones and concluded that in large deformations, the R shears are linked by the principal displacement shear (Figure 2.9). The R shears were formed at the early stages of shearing while the principal displacement shears were formed late, and most of the movement was concentrated along this main slip surface.

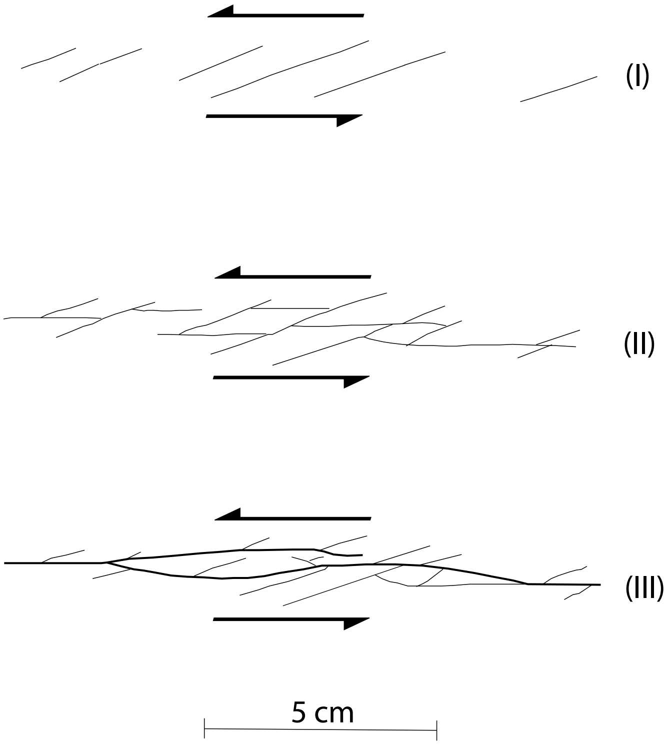

Figure 2.9: Development of slip surfaces in clay subjected to shear loading (modified from Skempton, 1967)

Morgenstern and Tchalenko (1967b) examined the microstructure of shear zones in different natural Landslides and found a well-developed Riedel shears pattern, conjugate set, and principal displacement shears. Morgenstern and Tchalenko (1967b) found that the shear zone thickness ranged from several millimetres to several centimetres (Figure 2.10).

Lajtai (1969c) conducted a series of tests by using Plaster of Paris to simulate the mobilization of shear strength along a discontinuous rupture surface in direct shear tests. Figure 2.11 illustrates the test set-up.

The blocks, containing rectangular voids to represent the discontinuous na-

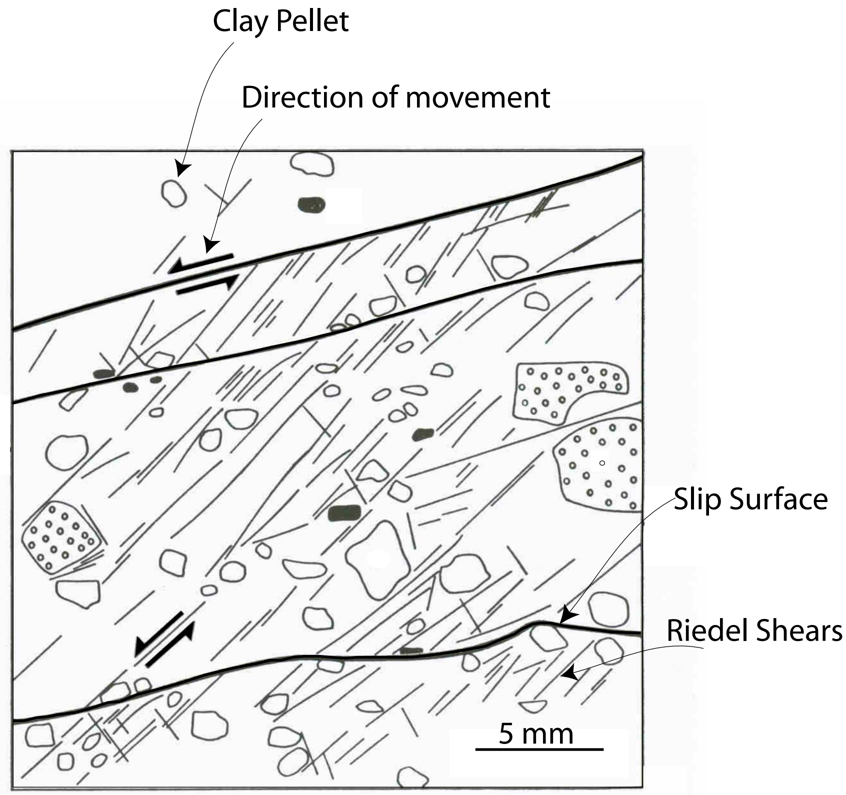

Figure 2.10: Detailed shear zone in Clays (modified from Morgenstern and Tchalenko, 1967a)

ture of the joints, were subjected to direct shear at various normal stresses. Lajtai (1969c) argued that for non-continuous joints, the minor principal stress in the rock bridge is tensile even if the all-around stresses are compressive, and that these tensile stresses are responsible for forming the fractures in the rock bridges (Figure 2.12). In his study, Lajtai (1969c) concluded that at low normal stress, tensile fracturing in the rock bridge was the dominant mode of failure, but that as the normal stress increased, the failure mode progressively became dominated by shear mechanisms. Based on his finding, Lajtai (1969c) suggested that the failure of rock containing intact rock bridges between joints could be represented by a nonlinear envelope. The first part of the nonlinear failure envelope is controlled by the tensile

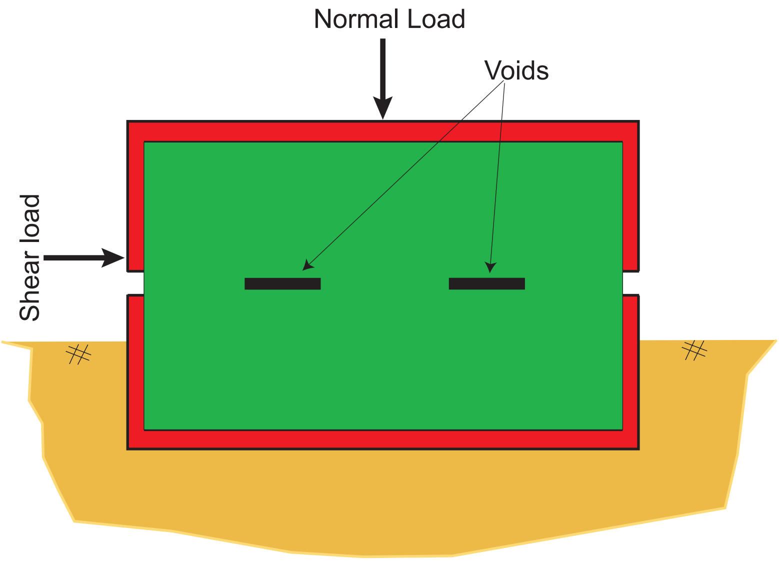

Figure 2.11: Lajtai's set-up to examine the mobilization of shear strength along the non-continuous joint in direct shear tests
.

strength, the second part is controlled by the cohesion, and the third part is governed by the friction angle of the material. Lajtai (1969a) used the Mohr-Coulomb criteria to support his argument and to show that tensile stresses inside the bridges might initiate the failure.

Lajtai's (1969c) results show non-linearity in the failure envelope. He argued that this non-linearity is associated with the tensile fracturing as the sample is subjected to shear loading (Figure 2.13).

Tchalenko (1970) examined the formation and development of shear zones on microscopic (direct shear test), intermediate (Riedel experiment) and regional scales (earthquake faults) . He suggested that shear zones have the same characteristics regardless of their scale (see Figure 2.14). At peak (Stage A), en echelon Riedel shears appear at $\phi/2$ counter-clockwise from the horizontal, where ϕ is the internal friction angle of the Clay. At Stage B, a few Riedel shears are generated at about 8° counter-clockwise from the horizontal, and some of the Riedel shears are extended. At stage C, new shears named “P shears” or Thrust shears are formed

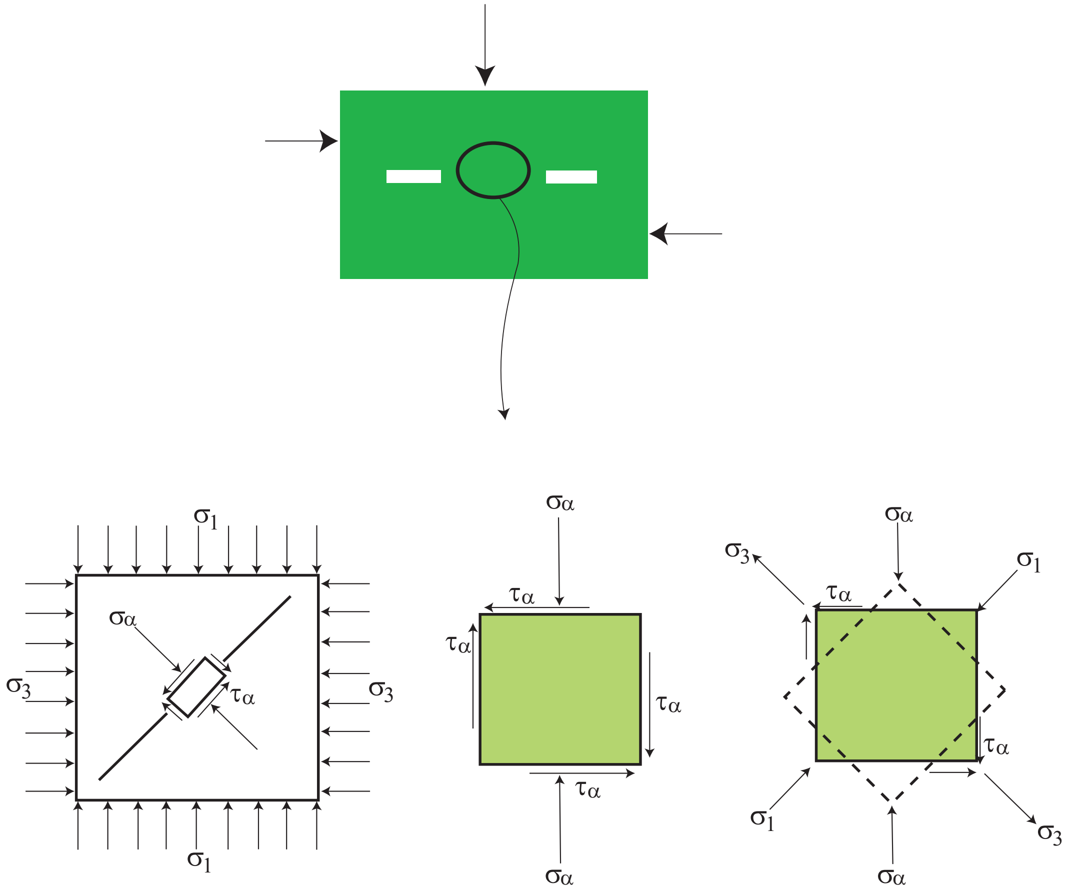

Figure 2.12: Stress state at the intact bridge area between two joint segments (modified from Lajtai, 1969a)

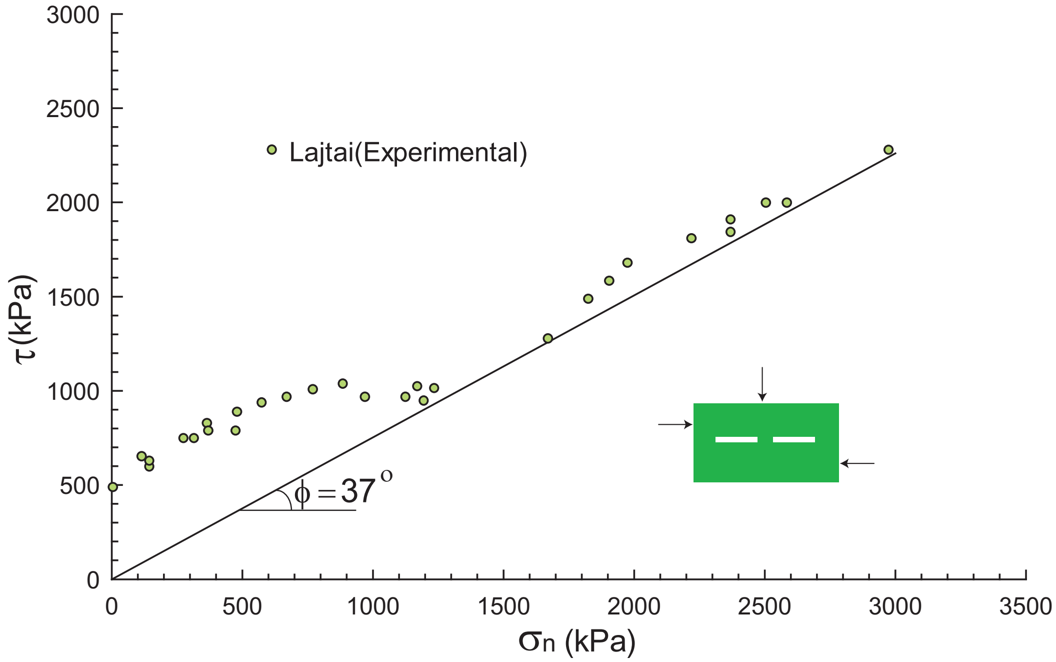

Figure 2.13: Direct shear test results obtained by Lajtai (1969c)

at -10° to the horizontal. Finally, at stage D the shear stress approach the residual, the P shears and the Reidel shears coalesce, and further displacement forms the principal displacement shears.

Vallejo (1982) suggested that the fracture morphology in these Stiff Clay experiments did not result from shear stresses, but rather from tensile stresses. He proposed that during direct shear testing of brittle materials, the pre-existing cracks propagate across specimens at angles controlled by the tensile strength properties in response to the principal stresses at the tips of the cracks.

Ortlepp (2000) observed similar shear zone features in a mining-induced faults in an intact rock mass in deep south African Gold Mines. Ahlgren (2001) used field mapping and three-dimensional digital modeling to explore the Riedel fractures in porous Sandstones. Cresswell and Barton (2003) conducted direct shear tests on Locked Sand and Sandstones. The results showed that Reidel shears and tension fractures developed in the samples as the shearing load was applied to the sample.

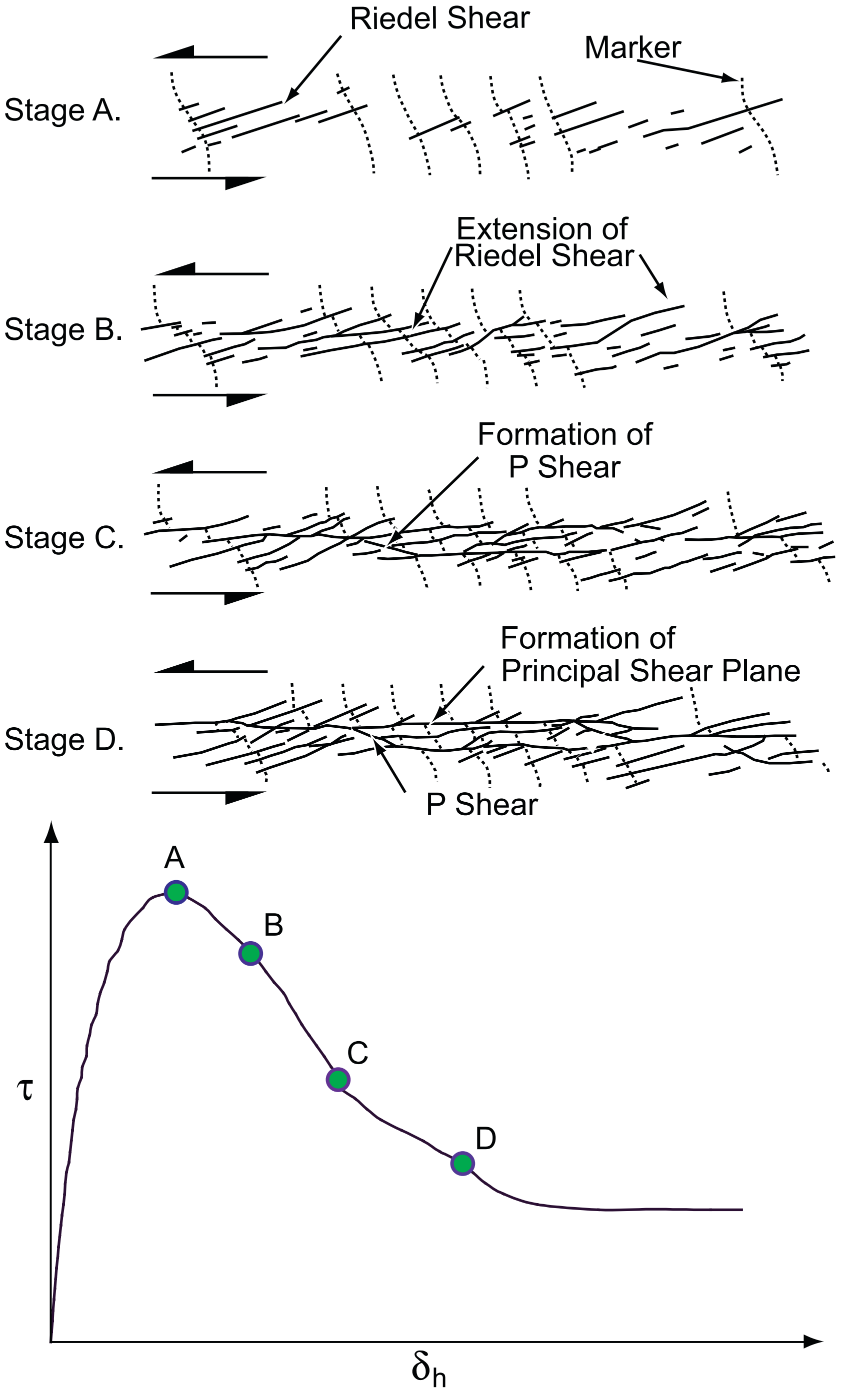

Figure 2.14: Shear zone development at different stages of stress-displacement curve on overconsolidated Clay (modified from Tchalenko, 1970)

Cho et al. (2008) conducted laboratory and numerical laboratory tests on a brittle Synthetic Rock to examine the fractures' initiation, development and coalescence at various normal loads. As the normal load increased, the observed fracture patterns changed. Cho et al. (2008) used the discrete element model to track the stress path at the centre of the sample and concluded that at low normal stress, the minor principal stress at the center of the numerical model was tension.

Cho et al. (2008) used discrete element numerical simulations to investigate the fracture pattern that occurred in at various stages of loading. The simulation results showed that the cracks that developed during the test were predominantly tension cracks. The fracture development observed in the discrete element simulation models showed that *En echelon* inclined tensile fractures developed parallel to the maximum principal stress direction. These tension-induced micro-cracks eventually coalesced to form the macro-scale shear band in the direct shear tests. Figure 2.15 shows the shear zone development at low normal stress (1 kPa).

At all stages of the test, the tension cracks dominated the failure process, and this result agreed with cracks morphology observed in the laboratory test. Figure 2.15 also shows a rose diagram for the orientation of the micro-cracks. The main orientation of the R cracks is in the same direction as that of the major principal stress. Cho et al. (2008) were able to identify the major fracture patterns (R,R‘,P) and the principal displacement shears that had been reported in the literature and concluded that most of theses cracks were initiated by tension.

The previous discussion reveals that the failure in direct shear is caused by progressive linkage of the tensile fractures to form a shear zone. At low normal stress, which is the case in many rock slopes, the tensile strength and tensile fracturing may control the slope behaviour.

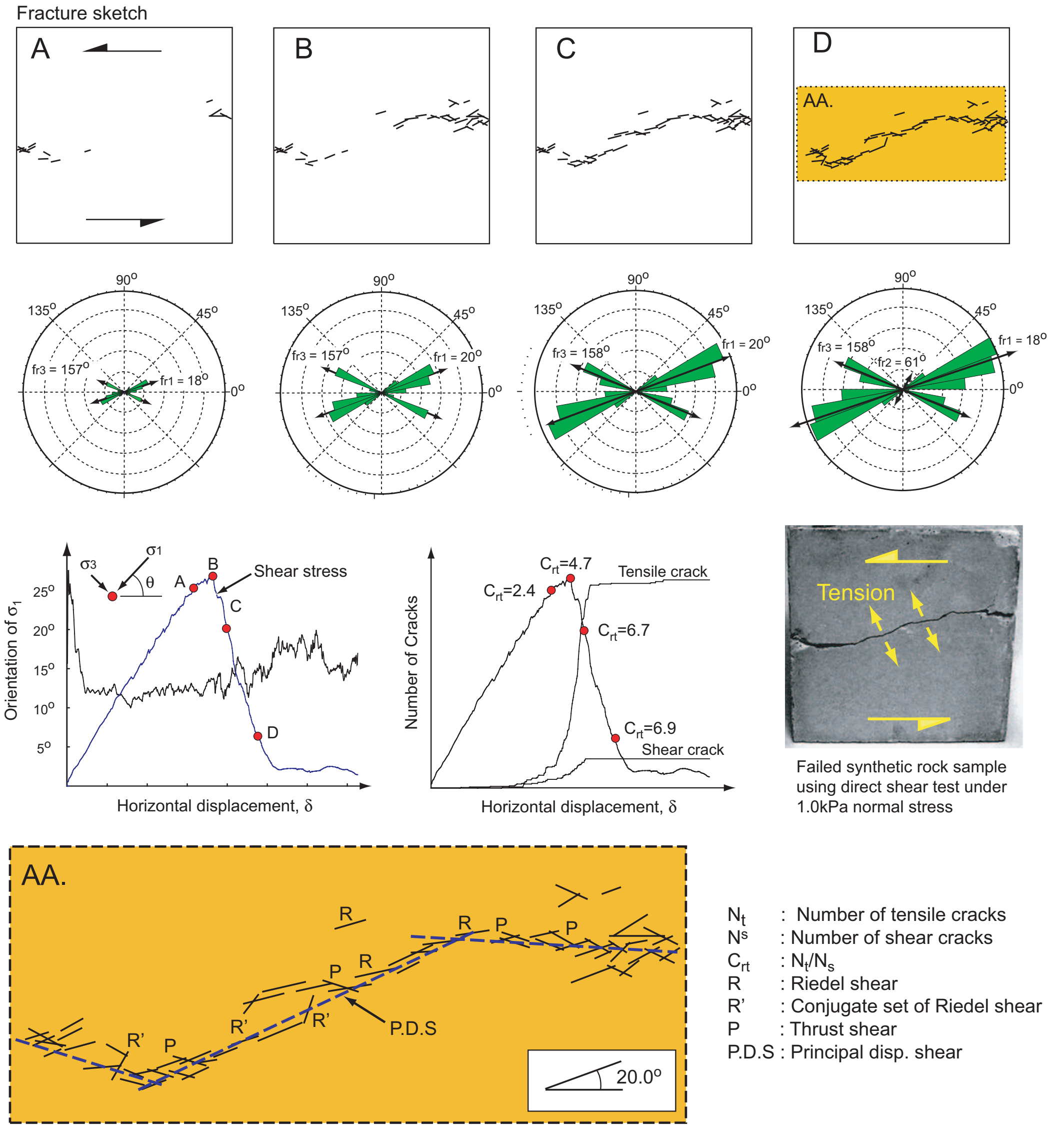

Figure 2.15: Development of fracture on discrete element modeling of synthetic rock (modified from Cho et al., 2008)

2.3 Stability Analysis

The improvements in computers and computational speed in the last three decades have resulted in the development of numerical methods applications in the geotechnical field, for both surface structures and underground excavations. Large rock slopes are in general complex due to the heterogeneity, stress state, discontinuities, coupled processes, geometry, progressive failure, and non-linearity of material behaviour. Due to these complexities, numerical simulation must be used to account for these factors. Moreover, numerical methods are capable of handling the boundary conditions, the constitutive equations of the material, the differential equations of equilibrium, and the strain compatibility equations.

Many numerical methods have been developed and used in the geotechnical engineering field, such as limit equilibrium, continuum, discontinuum, and, more recently, hybrid methods. Stead et al. (2001) discussed the advantages and disadvantages of some of these methods. A brief description of the most important methods is presented in the following sections.

2.3.1 Limit equilibrium analysis

Many limit equilibrium methods have been developed in geotechnical engineering to analyze and design slopes in both soil and rock mechanics. These methods are based on the concept of the factor of safety. In its simplest form, the factor of safety is the ratio between the sum of the forces resisting failure, and the sum of the forces driving failure. A factor of safety greater than unity implies stability while a factor of safety of less than unity implies failure.

In general, to solve a geomechanical problem and achieve an exact solution, the differential equations of equilibrium, the strain compatibility equations, the constitutive equations for the material, and the boundary conditions of the problem must be solved. The methods of limit equilibrium analysis attempt to achieve a solution by making a number of assumptions to simplify the problem (Krahn, 2003). First, the location and shape of the failure surface must be known, although search techniques for the critical factor of safety can be used. Second, the moving mass is assumed to be rigid, but this assumption violates the strain compatibility equations. Third, the shear strength is simultaneously mobilized over the entire failure surface, although this assumption ignores the progressive failure that exists naturally in geological materials. Fourth, the tensile failure is ignored, and tensile fracturing is not allowed to occur inside the rock mass. These assumptions are acceptable when the deformation is not important and when they are used for simple failure modes such as the plane and wedge modes. In the case of large rock slopes, the validity of this method becomes questionable because it ignores the non-persistent nature of the joints, the tensile strength, and the progressive nature of failure in rock masses

The most popular limit equilibrium method is the method of slices. A slip surface is assumed, and then the moving mass is divided into slices. At each slice, the force and/or moment equilibrium equations are solved to determine the interslice normal and shear forces. Figure 2.16 illustrates a slope stability analysis using the SLIDE limit equilibrium program and incorporating a water table analysis.

The major differences among the various "method of slices" techniques depend on which equations of statics are satisfied and the assumption regarding the interslice forces. For example, while the Ordinary method satisfies only moment equilibrium, the Morgenstern-Price method (Morgenstern and Price, 1965) satisfies the moment and force equilibrium and includes both normal and shear interslice forces. Fredlund and Krahn (1977) developed the General Limit Equilibrium method (GLE), which is based on two factors of safety: one with respect to the moment equilibrium and one with respect to the horizontal forces. Understanding the limitations and assumptions included in each method of slices is necessary prior to using any method of slices in rock slope analysis.

Jennings (1970) tried to analyze rock slopes with non-persistent rock joints by using the limit equilibrium method. He assumed a uniform distribution of the normal stresses along both the joints and the intact bridges, but this assumption was questionable due to the stiffness difference between the joints and the bridges. Jennings (1970) also ignored the progressive failure phenomenon and assumed a simultaneous mobilization of the strength parameters of the rock mass. As well, he

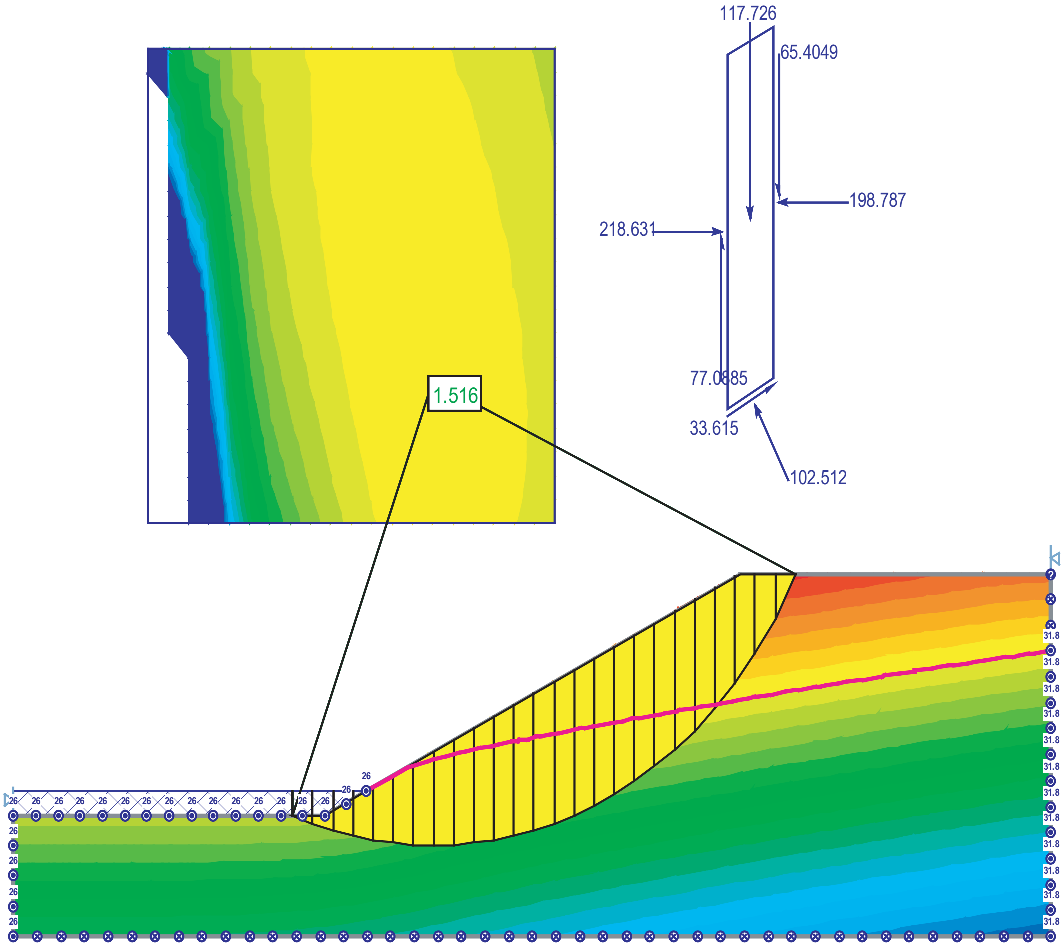

Figure 2.16: Slope stability analysis using the general limit equilibrium method using the SLIDE program, (Rocscience, 2006)

ignored the tensile strength effect on the rock slopes' instabilities. To allow for a kinematic release surface between two sets of joints Jaeger (1971) incorporated the tensile stress fracturing. Jaeger's approach is over-simplified for analyzing rock slopes, may be applicable only to very simple cases, and also assumes simultaneous mobilization of the strength parameters. Barton (1971) used the limit equilibrium method to analyze rock slopes by dividing the planer slope into slices. He allowed the excess forces from the overstressed blocks/slices to be transferred to the lower ones to allow for progressive failure. However, Barton's analysis was limited to the continuous joints and ignored the tensile strength effect.

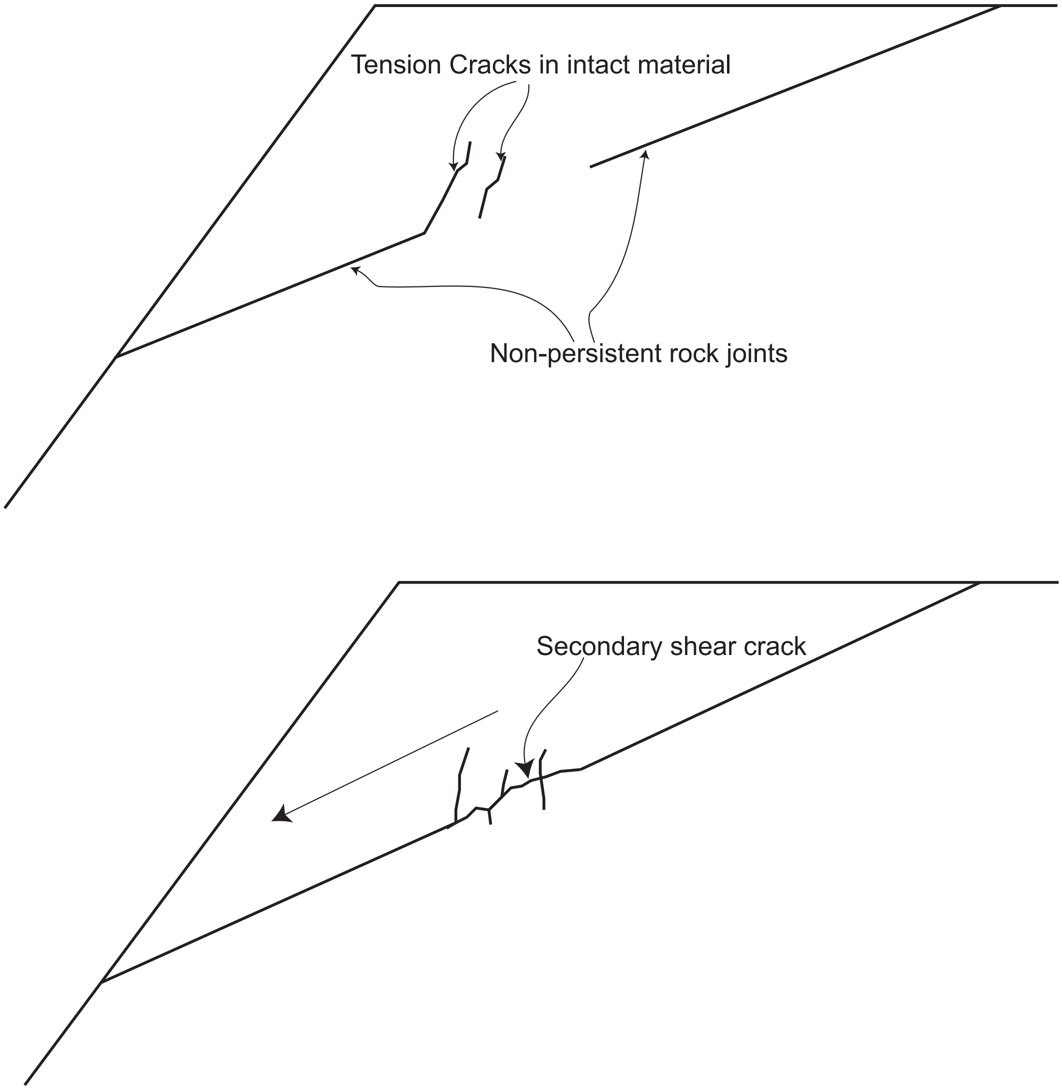

Figure 2.17: Failure in non-persistent joints (modified from Einstein et al., 1983)

Einstein et al. (1983) used a probabilistic approach to account for the continuity of the joints in the field. These researchers emphasized that, in non-persistent rock joints, the failure initiated by tensile fracturing at the rock bridge allows for the connectivity of the natural pre-existing joints. In some cases, the tensile failure followed by secondary shear failure depends on the angle between the joints (see Figure 2.17). This approach is limited to simulating the progressive development of the failure surface inside large rock slopes and also to one parallel joint set.

Using the limit equilibrium method proposed by Sarma (1979), Martin and

Kaiser (1984) found that internal shears formation and internal distortion were necessary to accommodate failure along the basal shear surface. These internal shears indicate the progressive nature of the failure of rock slopes, but do not include the tensile fracturing.

2.3.2 Continuum modeling

Continuum modeling assumes that the displacement field is continuous and results in a small displacement, that shear failure occurs by sliding along the maximum shear strain zone, and that the tensile strength plays a minor role. The actual rupture surface does not form in the continuum modeling, so after-failure analysis is not possible. Also, except for a few major ones, the discontinuities inside a rock mass cannot be modeled explicitly.

To overcome some of the shortcomings of continuum modeling, new approaches have been developed, such as introducing new constitutive models and simulating the localization of the shear bands in the intact material. For example, Adhikary et al. (1996) used the Cosserat medium to simulate rock slopes, but the actual rupture surface did not form. The strain-softening model, in which the material is given a peak and residual strength property, was developed to simulate the localization of the shear band on the intact material, but this approach, according to Sjoberg (1996) and Schlangen (1995), is mesh-dependent, and the shear band tends to follow the pattern of the descretized mesh. Some constitutive models such as the ubiquitous joint model can simulate implicitly the behaviour of the jointed rock mass.

Two continuum methods have been used in geotechnical engineering: the finite element method and the finite difference method. One of the advantages of the finite element over the finite difference method is that the mesh generation is more flexible. For example, FLAC (Itasca, 2000) is a finite difference code developed by the Itasca group, while PHASE2 is a finite element code developed by the Rocsience group (Rocscience, 2006). Benko and Stead (1998) analyzed the Frank slide by using the finite difference method. They divided the Frank slide section into two geotechnical units, one above the Turtle Mountain Fault and the other below it. Figure 2.19 shows the deformed mesh as failure occurred.

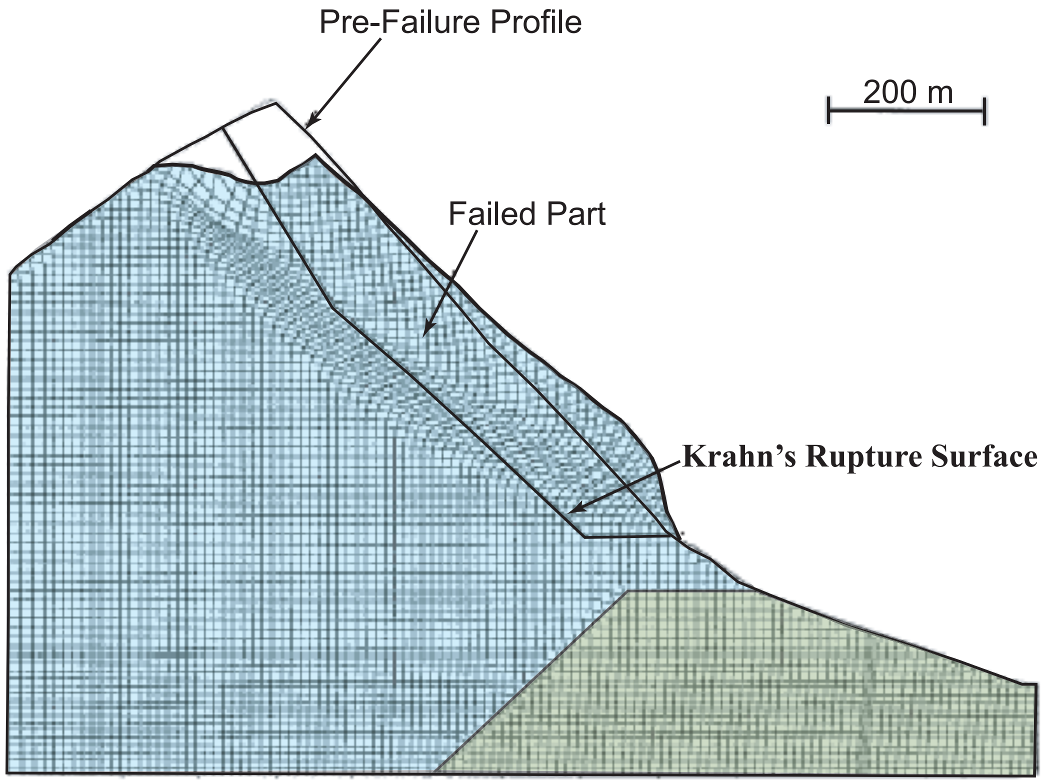

Figure 2.18: Finite difference model using the FLAC program of the Frank slide of Alberta, Canada, (modified from Benko and Stead, 1998)

Cruden and Martin (2007) used the finite element method to model the Frank slide of Alberta (Figure 2.19).

Stacey et al. (2003), in a continuum numerical study of rock slopes, changed the horizontal to vertical stress ratio along with the slope geometry on elastic slopes. These researchers found that the slope geometry and the horizontal stress ratio affected the tensile stresses developed in the slope. Their study also examined the extensional strain inside the rock mass. The slope geometry and the horizontal

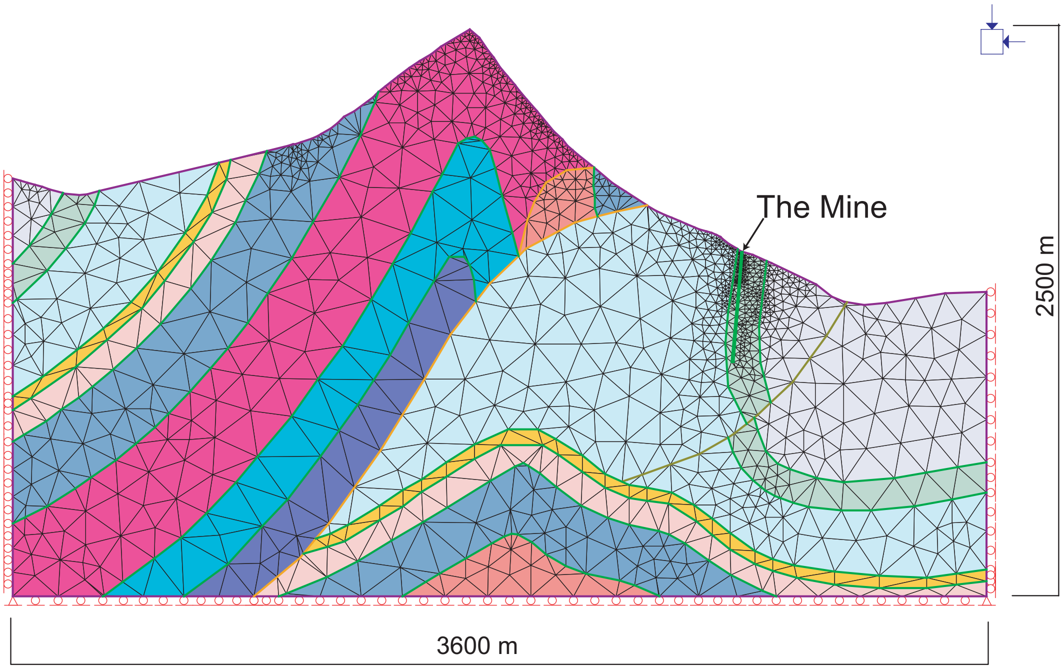

Figure 2.19: Finite Element model using the PHASE2 Program of the Frank slide of Alberta, Canada, (modified from Cruden and Martin, 2007)

stress ratio affected the amount and the extent of the extensional strain. Stacey et al. (2003) used the finite element approach and did not conduct a stability analysis to find the effect of either the tensile strength or the extensional strain on the slopes' stability. The tensile stresses in their study concentrated at the edges of the slope, no tensile stresses developed inside the rock mass, and the joints were not included in the analysis (Figure 2.20).

To model the effect of discontinuities on rock mass behaviour in a continuum modeling framework, two approaches have been used, the Hoek-Brown failure criterion and the cohesion weakening friction strengthening model. A brief description of the two approaches is provided in the following.

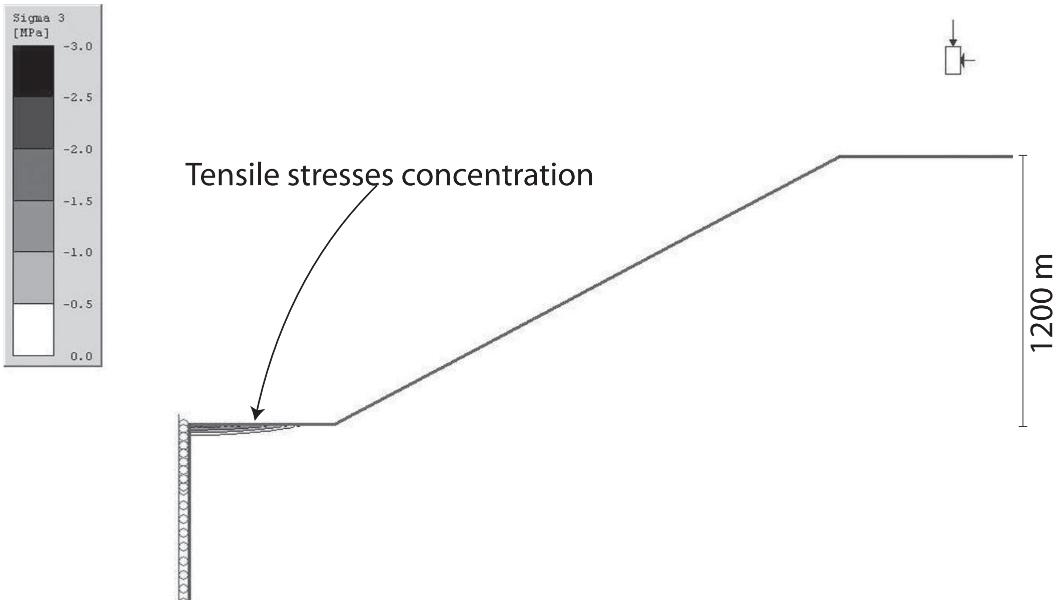

Figure 2.20: Tensile stresses generated using the Finite Element Method (modified from Stacey et al., 2003)

Hoek-Brown failure criterion

The Hoek-Brown failure criterion, one of the most used failure criteria in the rock mechanics literature, is based on a curve fitting for triaxial test data by using trial and error (Hoek and Brown, 1980). This non-linear failure criterion does not incorporate the joint parameters such as the orientation, spacing, and persistence explicitly, but takes general descriptions of these parameters and includes them in the Geological Strength Index (GSI) (Hoek et al., 2002). Hoek et al. (2002) introduced the General Hoek-Brown criterion for jointed rock masses, which is defined by

$$\sigma'_1 = \sigma'_3 + \sigma_{ci}(m_b\frac{\sigma'_3}{\sigma_{ci}} + s)^a, \tag{2.1}$$

where

σ'_1 = the maximum effective principal stresses at failure,

σ'_3 = minimum effective principal stresses at failure,

m_b = value of the Hoek-Brown constant m for the rock mass, s and a = constants which depend upon the rock mass characteristics,

σ_{ci} = uniaxial compressive strength of the intact rock pieces.

m_b, s and a can be calculated as

$$m_b = m_i e^{(\frac{GSI-100}{28-14D})} \tag{2.2}$$

$$s = e^{\frac{GSI-100}{9-3D}} \tag{2.3}$$

and

$$a = \frac{1}{2} + \frac{1}{6}(e^{\frac{-GSI}{15}} - e^{\frac{-20}{3}}), \tag{2.4}$$

where the GSI is the geological strength index, and D is a factor which depends upon the degree of disturbance due to blast damage. The graphs used to determine the GSI value, m_i and D can be found in Hoek et al. (2002) .

The uniaxial compressive strength of the rock mass is obtained by setting σ_3'=0 in equation 2.1, giving

$$\sigma_c = \sigma_{ci} s^a. \tag{2.5}$$

By setting σ_1'=σ_3'=σ_t, the tensile strength of the rock mass is

$$\sigma_t = -\frac{s\sigma_{ci}}{m_b}. \tag{2.6}$$

The program ROCLAB of the Rocscience group (Rocscience, 2006) provides an estimation of the friction angle (ϕ) and cohesion (c) for use in the more commonly used failure criterion of Mohr-Coulomb. Figure 2.21 shows the relation between the Hoek-Brown failure criterion and the equivalent Mohr-Coulomb criterion.

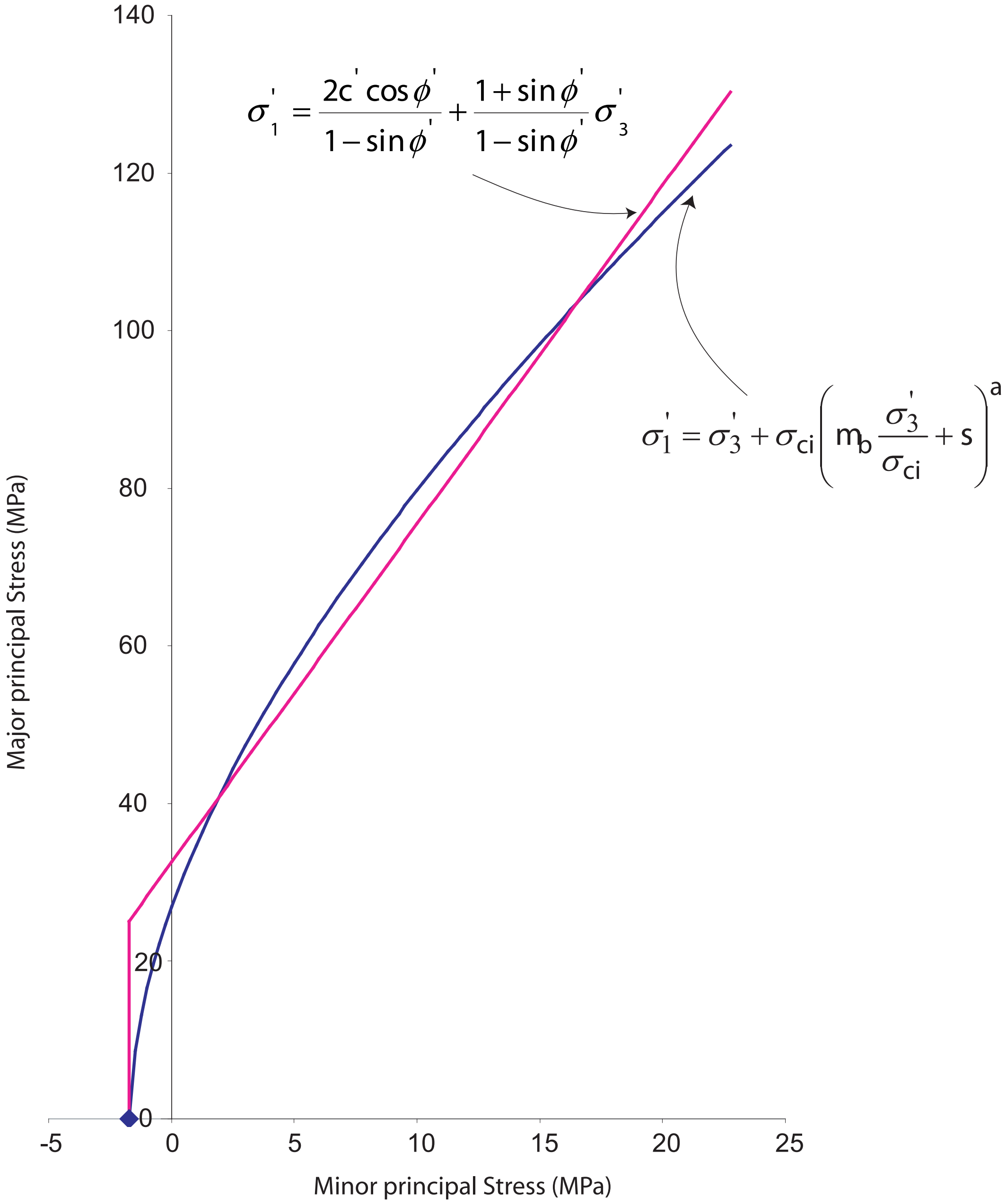

Figure 2.21: The relationship between the Hoek-Brown and Mohr-Coulomb failure criterion (modified from Hoek et al., 2002)

For example, in order to establish the shear strength parameters of the different geological units, Cruden and Martin (2007) utilized the Hoek-Brown criteria and the GSI. Table 2.1 shows Mohr-Coulomb and deformations properties determined by using the Geological Strength Index for the rock units encountered on Turtle

Mountain. It is expected that the GSI values decrease as the structures on fold increase, which was not taken into consideration in Cruden and Martin's (2007) analysis.

Table 2.1: Frank Slide rock mass properties used in the Numerical Model determined using Hoek-Brown Failure Criteria, (modified from Cruden and Martin, 2007)

The Formation	GSI	E(MPa)	μ	$\gamma (MN/m^3)$	ϕ (°)	C(MPa)
Blaimore group	73	25000	0.3	0.026	34	4.5
Kootenay group	73	25000	0.3	0.022	36	4
Fernie Formation	73	25000	0.3	0.025	35	4
Misty Formation	65	18300	0.3	0.023	33	3
Etherington Formation	80	47000	0.3	0.026	40	5.71
Mount head Formation	80	47000	0.3	0.027	42	5.73
Livingstone Formation	80	47000	0.3	0.026	42	3.76
Banff Formation	60	13700	0.3	0.027	36	3.42
Palliser Formation	80	47000	0.3	0.029	40	5.79
Coal	68	8000	0.3	0.022	18.2	0.99

Ignoring the joint persistency, orientation, and spacing might result in limiting the tensile stresses arising inside the rock mass and, thus, neglecting the tensile fracturing role inside the rock mass; however, such a failure criterion is extremely important in characterizing the rock mass and obtaining important parameters such as the friction and cohesion, which are needed to analyze rock masses. Moreover, Hoek-Brown failure criterion was developed for isotropic material and used into continuum model framework. In rock slopes, due to the existence of rock discontinuities, the rock mass is anisotropic. For example, in toppling movement, the indipping discontinuities create anisotropy in the direction of the joints. The use of this criterion smeared the effect of the rock mass non-continuous discontinuities and anisotropy. Brown (2008) stated that Hoek-Brown failure criterion is intended for use with isotropic rock masses and it should not be used in cases in which the strength of the rock mass is dominated by one or two sets of discontinuities.

Diederichs et al. (2007) concluded that the application of equation 2.1 is of limited reliability when used for hard undisturbed rock masses with GSI>75. For low GSI and low strength rocks, the Hoek-Brown criterion should be applied with extreme caution, Carvalho et al. (2007) proposed modifications for a,s, and m_b in low strength rocks at which the UCS is ranging between 10 to 15 MPa. Brown (2008) suggested that, in rock slopes, care must be taken to ensure that he estimated shear strengths of rock masses are not below those of the weakest constituent discontinuities. He also pointed out that the Hoek-Brown criterion is empirical method of estimating rock mass properties and not intended to replace careful site characterization and laboratory tests.

CWFS constitutive model

In order to model the progressive failure in rocks and to model joints, Hajiabdolmajid (2001) proposed the cohesion weakening-frictional strengthening constitutive model. He argued that the cohesion and friction of rock mobilized at different strain levels and caused the progressive failure of rocks (see Figure 2.22). In his analysis, he used the finite difference method to allow for the mobilization of the strength component at different strain levels. Later, Hajiabdolmajid and Kaiser (2002b) tried to model the Frank Slide by using the FLAC finite difference program to simulate progressive failure. This model was developed in a continuum modeling framework and generating tensile stresses and allowing fracturing in the continuum modeling approach is difficult.

The continuum method is limited in generating tensile stresses inside the rock mass due to the method's limited ability to include the joints, flaws, and fractures, especially if these discontinuities are non-persistent closed joints, as is the case in most rock masses. Also, when using the continuum methods, the heterogeneity of the rock mass is difficult to model. Moreover, the formulation may be limited

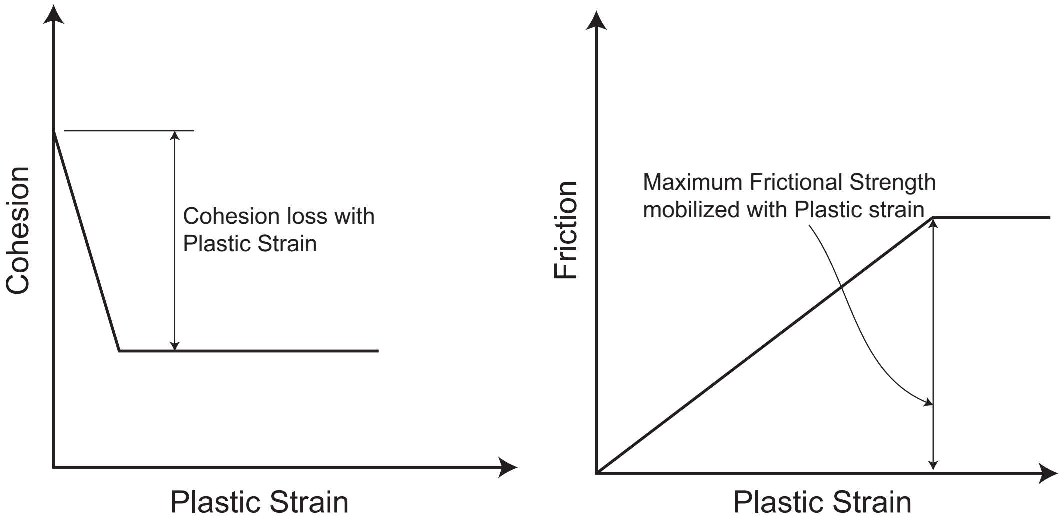

Figure 2.22: Cohesion weakening and friction strengthening as a function of plastic strain (modified from Hajiabdolmajid et al., 2002c)

to small displacements and/or rotation and did not allow for complete detachment. These limitations did not allow the researchers to track the tensile strength and fracturing effect on rock slopes.

2.3.3 Discontiuum modeling

Rock masses are generally characterized by their block nature and a network of discontinuities that, in most cases, dominate the behaviour of a slope or, for that matter, of underground excavations. Including the structures in rock slope modeling is essential. Cundall (1971) introduced the distinct element modeling approach in which the discontinuities can be modeled explicitly in the model.

The blocks forming the model are free to move and rotate, and completely detach from the rock mass body as failure occurs. The blocks in this modeling approach are discretized into a finite difference mesh in which failure can occur in the same manner as that in the continuum modeling approach.

Cundall (1971) proposed the discrete element numerical modeling method, which allows for the finite displacement and rotations of discrete deformable or rigid blocks and complete detachment. The calculation alternates between the application of a force-displacement law at the contacts and Newton's second law at the blocks. Local and global damping is necessary to keep the model under control. This logic is used by the Universal Distinct Element Code (UDEC, Itasca, 2004b), which is a commercially available distinct element programs made by the Itasca Consulting group. Rock slope stability problems can be modeled reasonably well by using the UDEC code. It can handle complex geometries along with a number of material types and complex constitutive models. UDEC especially allows for the development of models that more accurately reflect than other models the rock mass conditions encountered in the field. Any number of discontinuity sets and orientations can be included, all with different strength characteristics, but the conventional discrete element methods require a defined failure surface, and the actual rupture surface is not free to develop inside the rock mass. Figure 2.23 shows a discrete element model for the Frank slide in Alberta (Benko and Stead, 1998).

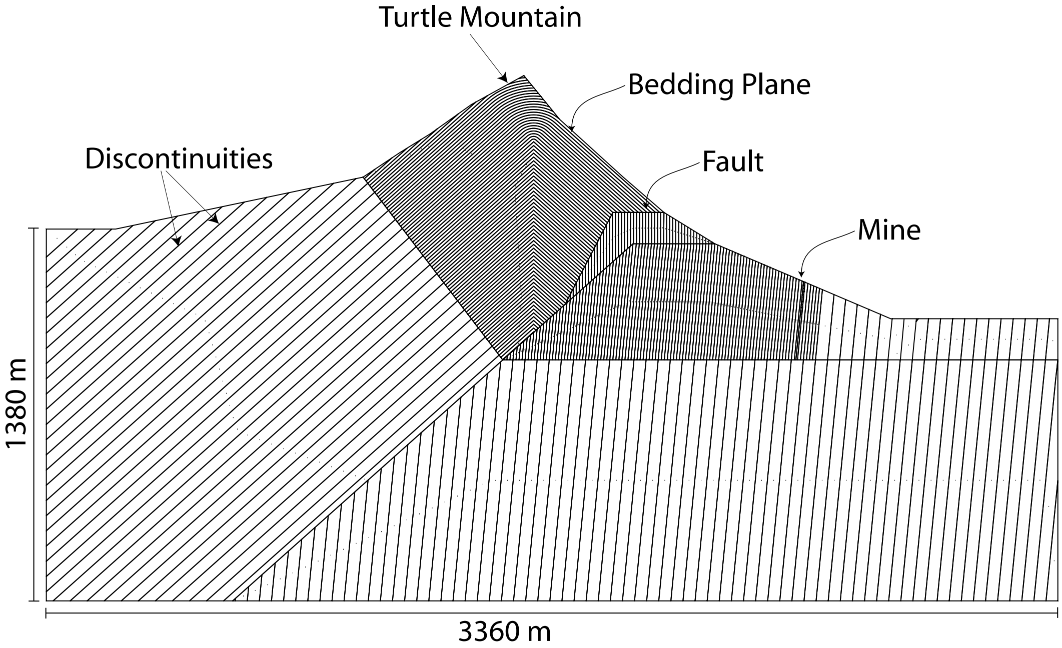

Figure 2.23: Discrete Element model of the Frank slide (Alberta, Canada) by using the UDEC Program (modified from Benko and Stead, 1998)

Nichol et al. (2002) used the conventional discrete element method to model block topple in strong granitic rocks that had failed catastrophically and produced a high velocity rock avalanche in British Columbia, Canada. To allow failure to occur, continuous discontinuities were used in the model as shown in Figure 2.24, which reveals that, failure occurred by sliding along the continuous joints and that the direction of the sliding and the rupture surface is pre-defined and confined to joints.

With the conventional discrete element methods, failure is controlled by the pre-existing continuous joints, and failure occurs along these continuous joints. The inclusion of the closed non-persistent joints is not possible. Conventional UDEC underestimates the role of tensile fracturing inside the rock mass due to the limited ability to generate tensile stresses at the joint tips and/or the intact rock bridges. Intact material in this modeling approach is handled in the same way as in continuum modeling.

2.3.4 Hybrid methods

The previously mentioned methods are not capable of handling fracturing through intact material from the pre-existing structures inside a rock mass. Terzaghi (1962) stated that most rock masses include non-continuous rock joints and that the strength must be derived from both the joints and the intact rock between the joints.

To simulate this effect, different methods have been developed based on the fracture mechanics principles; failure between rock joints can occur through either tensile failure (MODE I), shear failure (MODE II) and/or tearing (MODE III). Fracture Mechanics (the Griffith theory), proposed by Griffith (1920), has been used as an engineering approach to optimize the calculation of the strength of non-persistent rock joints. The use of this approach requires knowledge of the process of the initiation, propagation, and coalescence of the cracks from the offset pre-existing rock

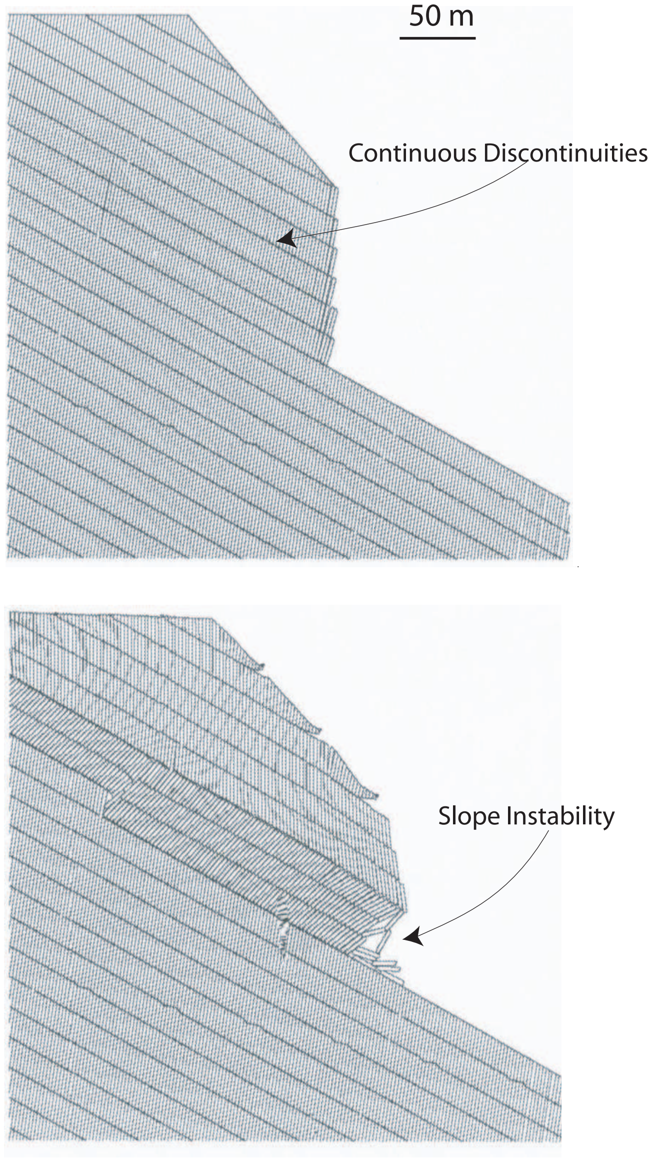

Figure 2.24: Rock slope simulation by using Discrete Element method (modified from Nichol et al., 2002)

joints. Fracture mechanics has its own disadvantages: Griffith's theory has been developed for material under tension loading, whereas geomaterials are subjected mainly to compressive stresses, which produce stress heterogeneity and lead to a complex failure process in the rock masses. These factors do not mean that tensile stresses are not present or that they can be ignored. As a result, several attempts have been made to modify Griffith's theory to handle the compression stress state which is experienced in geotechnical engineering.

In rock slopes, Scavia (1995) used the displacement discontinuity method and fracture mechanics principles to model fracture initiation and development through a network of pre-existing joints and to form a failure surface. He used the linear elastic stress intensity factor at the joint tip to initiate the fractures. Kaneko et al. (1997) used the same principals to simulate a homogeneous rock slope, but this simulation did not consider the heterogenous nature of rock masses. The failure was initiated at the toe and incorrectly propagated to the upper face of the slope, not to its crest, as is the case in rock slopes.

The Particle Flow Code (PFC2D) (Itasca, 2004a) is a discrete element code by which the rock mass is simulated by circular particles that can be bonded together to represent intact rock. Wang et al. (2003) used discrete elements to analyze a jointed rock slope by bonding circular disks (Figure 2.25). However, it is not clear how spheres should be calibrated to represent discontinuities, as the spheres create very irregular surfaces; i.e., the joints are not smooth. In Wang et al.'s (2003) analysis, the presented model did not use any bond for the joints, and the particles directly adjacent to the joint were assigned zero friction. Potyondy and Cundall (2004) concluded that extensive numerical calibration is needed to to use bonded particles to simulate intact rock. It is also difficult to simulate the geometrical heterogeneity of the rock masses by using the PFC code.

More recently, Pierce et al. (2007) introduced a synthetic rock mass model for jointed rock by using PFC3D in which a new sliding joint model has been used. The new sliding joint model allows for large volumes containing non-persistent or persistent joints to be modeled . This approach is capable of modeling Discrete Fracture Network, which is a step forward in modeling rock masses behaviour and heterogeneity.

Eberhardt et al. (2002) and Eberhardt et al. (2004) used a hybrid technique (the

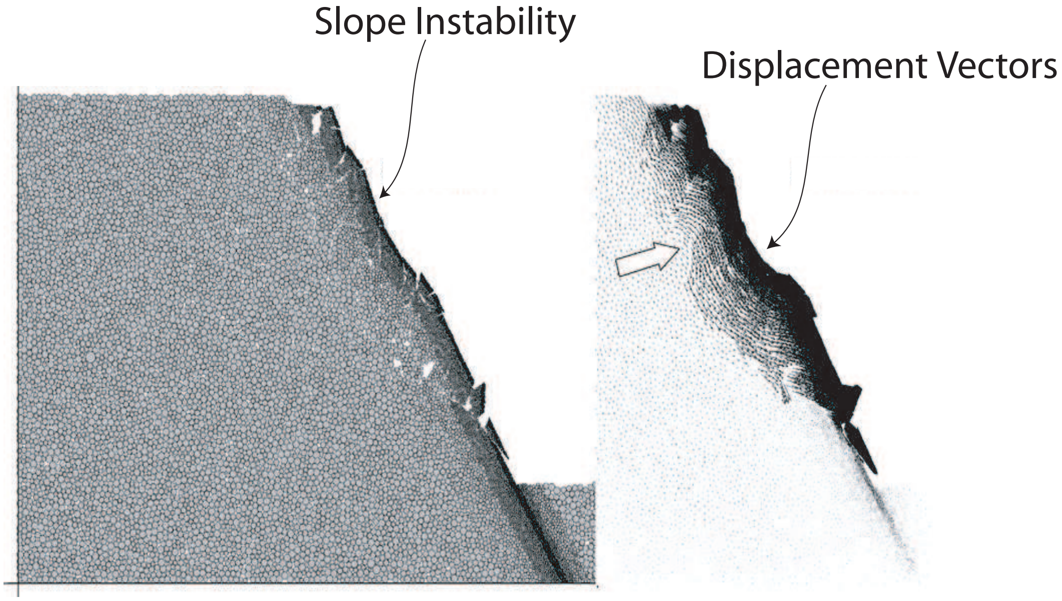

Figure 2.25: Rock slope failure simulation by using the PFC program (modified from Wang et al., 2003)

ELFEN program) with remeshing capabilities to simulate the 1991 Randa rock slide in Switzerland (Figure 2.26). This method allowed for the movement from the continuum to the discontinuum through the re-meshing techniques to form new cracks. This method is promising and can give good results. The researchers adapted the cohesion weakening-frictional strengthening constitutive model proposed by Hajiabdolmajid and Kaiser (2002b). In their analysis, Eberhardt et al. (2004) did not include the natural pre-existing joints in the rock mass, yet were able to model the failure initiation and propagation through the slope. These researchers did not compare the deformation prior to failure with the deformation predicted by the numerical model, so the validity of the numerical model in this context still needs to be proved.

ELFEN uses a finite/discrete element code and fracture mechanics principles to initiate cracking. In ELFEN, the sliding crack model is used to initiate tensile

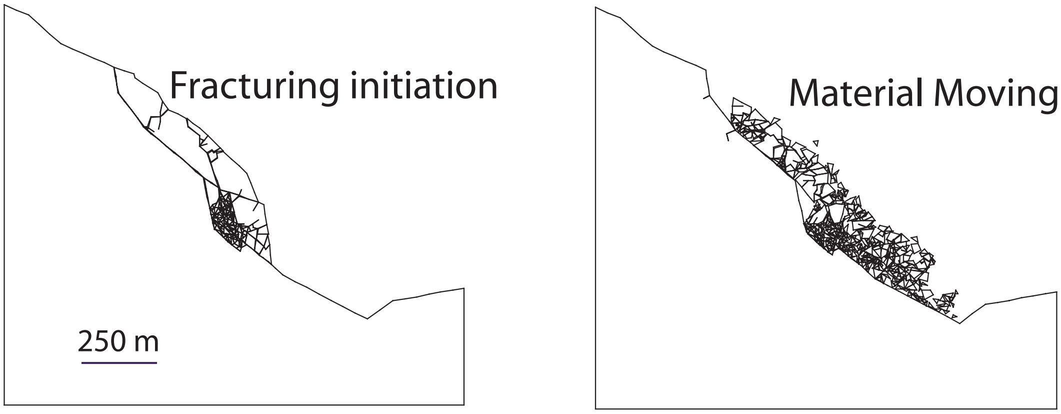

Figure 2.26: Randa rock slope failure simulation by using the ELFEN program (modified from Pine et al., 2007)

fracturing in rock mass. As sliding occurs along the main crack, the wing cracks nucleate and propagate. Plasticity evolves through degradation of the elastic modulus in the directions of the principal strains. Pine et al. (2006) pointed out that the material strain softening in ELFEN is fully governed by the fracture energy parameters and tensile strength. The fracture extensions and new fractures develop in Mode I. All existing fractures and new fracture surfaces are given Mohr-Coulomb shear strength parameters. The remeshing technique allows the crack initiation to be modelled. Stead et al. (2004a) and Stead and Coggan (2006) used the ELFEN hybrid method to simulate other rock slopes. This technique is promising, but further comparison with deformation patterns might be needed. Figure 2.27 shows an example from these studies.

Vyazmensky et al. (2007) used ELFEN to simulate block caving and surface subsidence. In their analysis, a Discrete fracture network model has been included in models with ELFEN to simulate the rock mass behaviour. The results are encouraging and showed the ability of including non-persistent joint sets in large pits (Figure 2.28). Pine et al. (2007) showed that non-persistent rock joint sets and realistic complex failure mechanisms can be modelled. Pine et al. (2007) presented several applications, such as hangingwalls, block caving, mine pillars and rock slopes. Yan

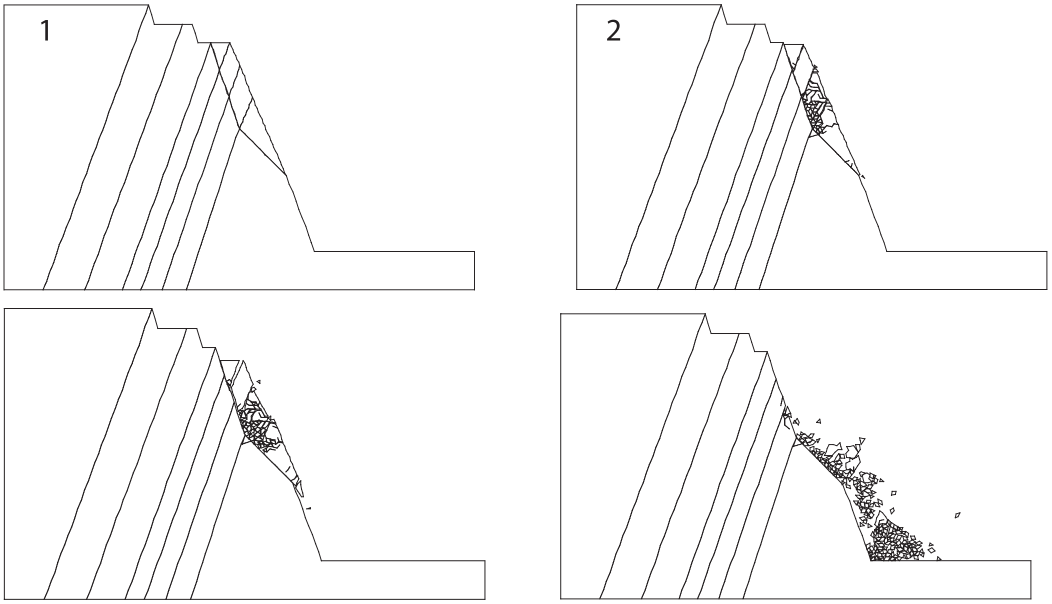

Figure 2.27: Rock slope failure simulation by using the ELFEN program (modified from Stead and Coggan, 2006)

et al. (2007) used ELFEN to simulate step-path failure in rock slopes, They incorporated non-persistent rock joints in the simulation and showed good results. Yan et al. (2007) simulated step-path failure in 800 m large open open pit that contained two sets of joints.

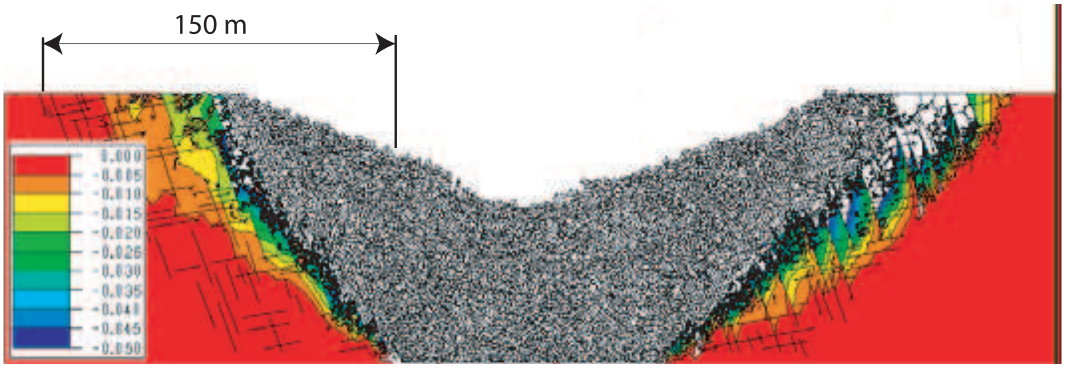

Figure 2.28: Block caving by using the ELFEN program (modified from Vyazmensky et al., 2007)

2.4 Summary

The overall conclusion from laboratory tests and physical models is that tensile failure is a dominant process in the development of discontinuous rupture surfaces. Laboratory and numerical tests results showed that, at low normal stress, which is the case in most rock slopes, tensile fracturing controls the formation of the shear zones in rock masses. The discontinuities must also be incorporated into any rock slope analysis. The most common methods used in analyzing rock slopes are the limit equilibrium methods, continuum and discontinuum modeling methods. These methods have common limitations in their ability to simulate the non-continuous nature of rock rock joints. Moreover, tensile strength and tensile fracturing is underestimated, due to ignoring the rock mass heterogeneity and anisotropy. In the following chapters, a numerical methodology is developed for modeling the role of tensile strength in rock slopes failure.

Chapter 3

A discrete element damage model for rock slopes

3.1 Introduction

Cundall (1971) proposed the discrete element numerical modeling method to allow for the finite displacement and rotations of discrete deformable or rigid blocks, as well as for complete detachment. In the discrete element method, a rock mass is represented as discrete blocks, and discontinuities are treated as interfaces between bodies. The contact displacements and forces at the interfaces are calculated by tracing the movements of the blocks. Applied loads or forces to a block system can cause disturbances that propagate and result in movements. The propagation speed in this dynamic process depends on the physical properties of the blocks and the contacts (Itasca, 2004b). The behaviour of the solid material and the discontinuities must be considered.

A time-stepping algorithm must be used to represent the dynamic behaviour, and within a time-step, the velocities and accelerations are assumed to be constant. The time-step is small enough to prevent the propagation of disturbances between one block and its neighbors. This explicit time marching solution scheme is identical to that used by the explicit finite-difference method for continuum analysis. The time-step restriction applies to both blocks and contacts as follows. For deformable blocks, the size of the zone is used, and the stiffness of the system includes contributions from both the intact rock modulus and the stiffness at the contacts. For rigid blocks, the block mass and interface stiffness between blocks define the time-step limitation.

The discrete element method calculation step alternates between application of a force-displacement law at the contacts and application of Newton's second law at all blocks. Local and global damping is necessary to keep the model under control. This logic is used by the Universal Distinct Element Code (UDEC) (Itasca, 2004b). Figure 3.1 presents a schematic diagram of a one time-step cycle. The force-displacement law is used to find the contact forces from the known displacements. Newton's second law gives the motion of the blocks resulting from the known forces acting on them. If the blocks are deformable, the motion is calculated at the gridpoints of the triangular finite-strain elements within the blocks. Then, the constitutive relations are applied to the block material to obtain the new stresses within the new elements.

In UDEC, a rock joint is represented numerically as a contact surface formed between two block edges. In general, to detect and identify a contact, for each pair of blocks that touch (or are separated by a small enough gap), data elements are created to represent the point contacts. The adjacent blocks can touch along a common edge segment or at discrete points where a corner meets an edge or another corner (Itasca, 2004b). Thus, the number of contact points is increased as a function of the blocks, thereby in increasing the cycle time. A number of different constitutive models can be applied to the contacts and the solids, such as the Mohr-Coulomb failure criterion, which is one of the most acceptable failure criterion in rock mechanics (Figure 3.2).

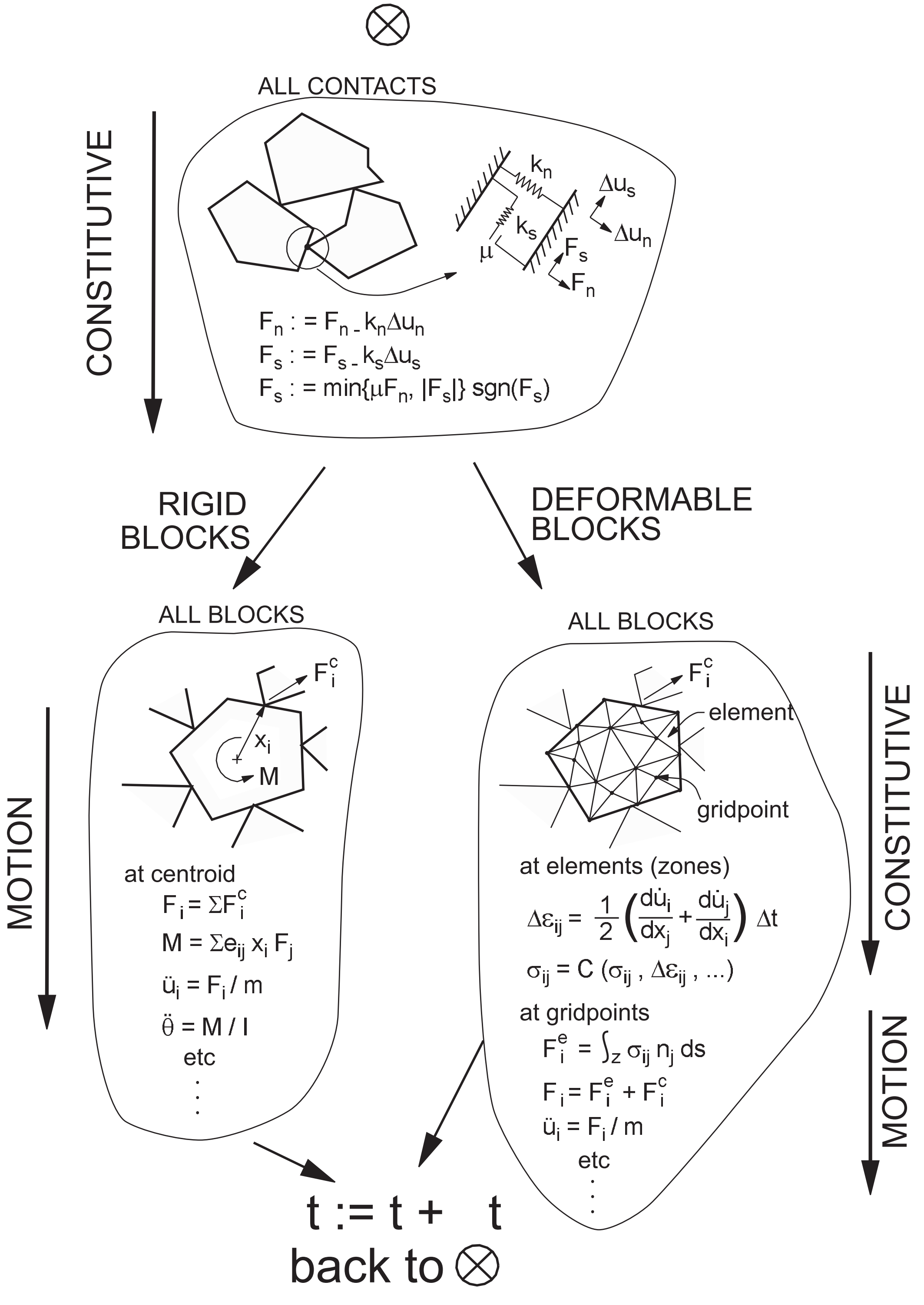

Figure 3.1: Calculation step in discrete element method (modified from Itasca, 2004b)

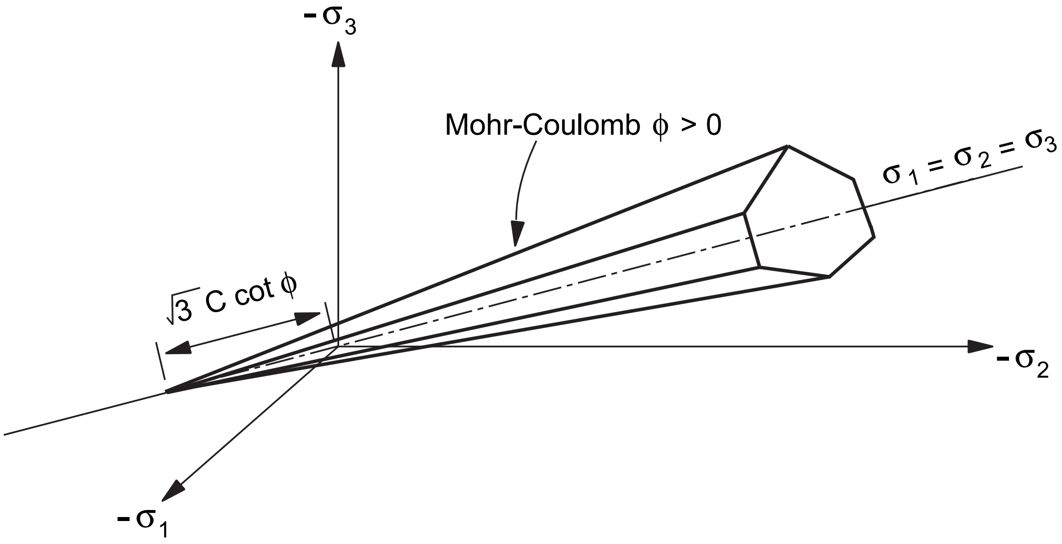

Figure 3.2: Mohr-Coulomb surface in principal stress space

3.2 Damage Model

The progressive failure of geo-materials is a gradual and time-dependent failure process at localized areas, followed by the redistribution of the stresses in the slope. These new stresses build up and cause the propagation of the failure. If this fracturing continues, a rupture surface connecting all the failed parts will form. Many factors can cause progressive failure, such as the time-dependent degradation of the strength parameters, increasing pore pressures, and/or thermal stresses. In addition, the presence of non-persistent joints and the heterogeneity of the rock mass might cause tensile stresses inside the rock mass and also the initiation and propagation of cracks that might lead to failure. Figure 3.3 presents a conceptual diagram of the tensile stresses resulting from the compression forces in a block assembly. Cho et al. (2008) showed that the development of the through-going rupture surface through intact material is preceded by tensile fracturing.

To simulate the rock failure processes by using discrete element modeling, a polygonal block component is added to the usual capability of UDEC (Itasca,

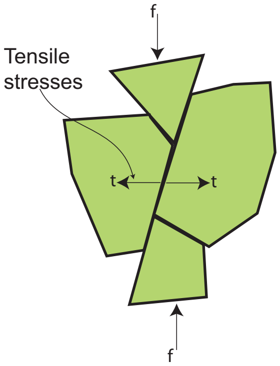

Figure 3.3: Block assembly subjected to compression forces and the resulting tensile stresses at the bond (Modified from Potyondy and Cundall, 2004)
.

2004b) to model discrete fractures by using the Voronoi tessellation generator command, which creates randomly sized polygonal blocks. The Vornoi tessellation creates random points within the specified region. Points are also distributed uniformly along each edge. The position of interior points may be relaxed by iteration to create more uniform block distribution. The line segments forming the Voronoi polygons are then generated by constructing perpendicular bisectors of all triangles which share a common side. The randomly sized polygons are analogous to the flaws in the intact rock that can represent grain-boundary flaws or larger-scale internal flaws (Figure 3.4). The size, seed and number of iterations can be varied to generate randomly sized blocks. For example decreasing the number of iterations to generate the blocks in Figure 3.4 will result in less unform blocks. These flaws are defined such that they have intact rock properties and do not contribute additional jointing to the joint system of the rock mass. It should be noted that the term ”Damage” is used to describe fracturing of flaws and joint, not plasticity damage.

Lorig and Cundall (1987) introduced the Voronoi tessellation to model a concrete member as assemblage of blocks bonded at common boundaries. Failure is simulated by progressive breakage of bonds, Lorig and Cundall’s (1987) simulation showed the ability to visualize deformed shape and crack development with

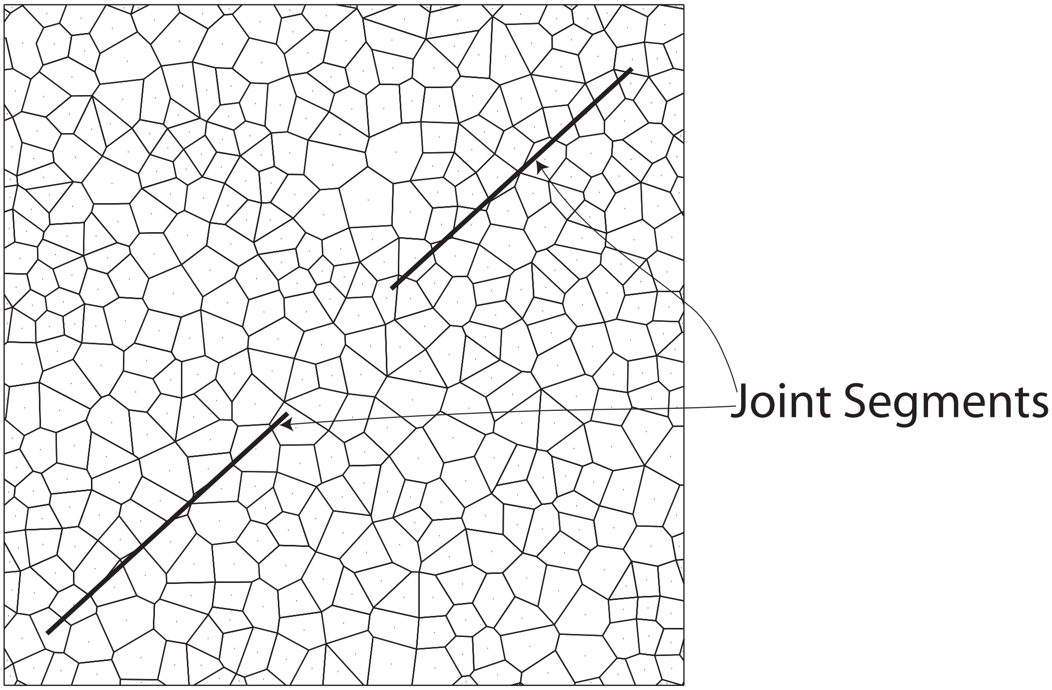

Figure 3.4: Illustration of the polygonal structure used to simulate intact rock using 100 iterations to generate the flaws.

displacement . Watson et al. (2006) used the Voronoi joint to simulate material flow toward dam reservoir in the Checkerboard Creek rock slope, British Columbia, Canada. Alzo'ubi et al. (2007) used this approach to model rock slopes that include persistent and non-persistent smooth rock joints. This polygonal block model will be referred to as the UDEC damage model (UDEC-DM) in this thesis. This polygonal block pattern provides a unique method for simulating tensile and/or shear fracturing through intact rock. Cohesion, friction, and tensile strength can be assigned to the boundaries of these polygonal blocks such that the strength is the same as that of intact rock. Local variation in strength and stiffness can also be applied if required. While the polygonal flaw structure shown in Figure 3.4 may represent the flaws found in crystalline rocks, these discontinuities are not commonly observed in sedimentary rocks. For sedimentary rocks, the main set of joints should be generated first and then the flaws generated next inside the major bedding units. This approach produces polygonal shapes that are more representative of the cross-cutting joints observed in sedimentary rock than other shapes. Hence, in the UDEC-DM, the user has control over the creation of the internal flaws to match the geological conditions of the rock mass being analyzed.

The blocks created in this approach assigned the elastic, isotropic model of material behaviour. This model exhibits linear stress-strain behaviour with reversible deformations upon unloading. In this model, the relation of stress to strain in incremental is expressed by Hookes law. The blocks can be attached together by specifying the friction, cohesion, and tensile bond strength. The values assigned to these strengths influence the strength of the synthetic rock and the nature of cracking and failure. Once the shear stresses exceeds the strength, the shear strength is set to its residual value as long as blocks stay in contact, which is a function of compressive normal stress and the friction angle at the contact. However, once a tensile bond fails the tensile strength of the contact is set to zero. This flaws pattern provides an extra degree of freedom that is useful to simulate the fracturing of the rock masses through intact material. Thus, failure is not restricted to the joints but, rather, can be developed simultaneously and/or progressively in both intact and joint segments. The random shape of the blocks generated in the modeling approach can allow tensile stresses to arise and produce tensile fracturing throughout the intact material. This approach is not based on a fracture mechanics approach where fracture propagation is controlled by the fracture toughness and the stress intensity factor at the crack tip. Instead a failure approach is adopted in the UDEC-DM where fracturing occurs when the stress level exceeds the strength in any flaw inside the model. In the present study, the Mohr-Coulomb criterion with a tensile cut-off is used, and the flaws may fail either in shear or in tension based on the stresses to cause failure.

3.3 Flaw patterns in rock

In addition to the geomechanical properties of rock mass flaws, the geometrical properties are of great concern in characterizing a rock mass. The blocks in a rock mass are formed by flaws with different patterns formed in nature under different geological circumstances. Understanding the origin of a rock mass would help to have a general idea about the pattern of those flaws. For example, in sedimentary rocks, flaws are generally three perpendicular sets with different degree of persistency. In plutonic rocks, these flaws have irregular shape that intersect each other at different angles.

Dershowitz and Einstein (1988) pointed out that two main approaches have been used to describe the assemblage of geometric flaw characteristics in a rock mass: the disaggregate characterization in which each flaw is described separately, for example, through spacing distribution, and the aggregate characterization in which the interdependence of the flaw characteristics is captured through the formulation of flaw system models. The models can represent real flaw geometries and, as a result, can represent the rock mass geometry. Examples of these flaw model systems are the orthogonal system, which consists of three sets of orthogonal flaws, and the mosaic block tessellation models. According to Ambarcumjan (1974) the mosaic tessellation randomly subdivides of the plane into non-overlapping convex polygons. The block shapes can vary and be irregular, and the flaws are the faces of those blocks.

Dershowitz and Einstein (1988) stated:

> Since jointing in Mosaic Block Tessellation models is defined by the faces of a process of non-overlapping blocks completely containing the rock mass, they are appropriate for joint systems which are actually the result of a process of block formation in a rock mass. One example of

> such a joint system is jointing in columnar Basalts. (p. 26).

One of the mosaic block tessellation models is the Voronoi tessellation, which can be utilized in the discrete element modeling approach and used to create realistic rock mass simulation.

Dearman (1991) discussed the types of blocks formed in natural rock masses. He stated that flaws' patterns and the difference in spacing and degree of persistency within each flaw set determined the shape of the resulting blocks. For example, these blocks can be described in three dimensions as polyhedral, cubic, etc. (see Figure 3.5)

3.4 Failure criterion of the flaws

In UDEC, the numerical contacts are of two types: corner-to-corner contacts and edge-to-corner contacts. However, in rocks, edge-to-edge contact is important because it corresponds to the case of a rock joint closed along its entire length. A physical edge-to-edge contact corresponds to a domain with exactly two numerical contacts. The joint is assumed to extend between the two contacts and to be divided in half, with each half-length supporting its own contact stress. Incremental normal and shear displacements are calculated for each point contact and associated length (Itasca, 2004b).

In the normal direction, the stress-displacement relation is assumed to be linear and controlled by the constant normal stiffness (k_n) such that

$$\Delta\sigma_n = -k_n \Delta u_n, \tag{3.1}$$

where $\Delta\sigma_n$ is the effective normal stress increment, and Δu_n is the normal displacement increment. There is also a limiting tensile strength, T, for the joint in the normal direction. If the tensile strength is exceeded (if $\sigma_n < -T$), then σ_n = 0. In the shear direction, the response is governed by a constant shear stiffness (k_s). The

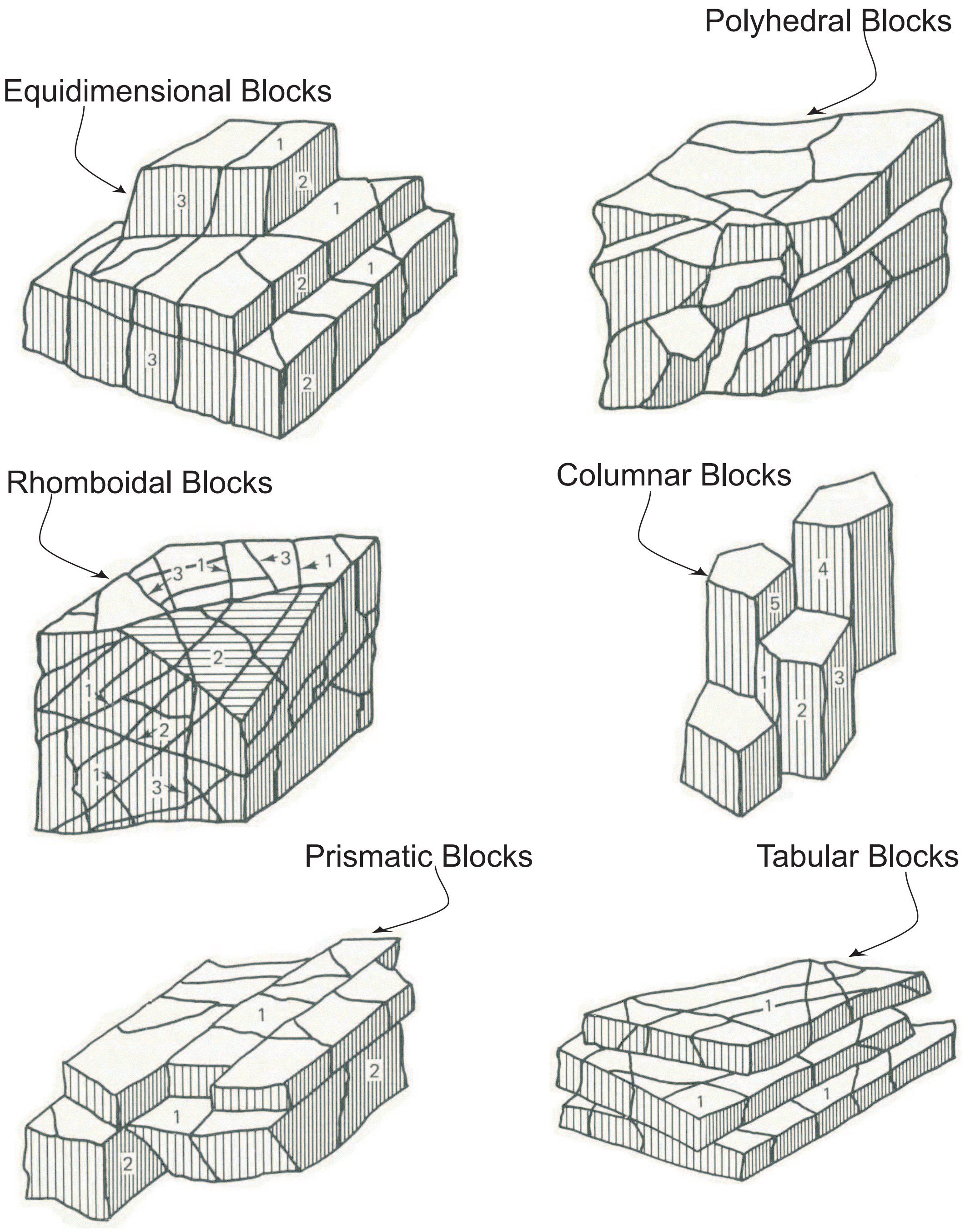

Figure 3.5: Rock mass block shape, The numbers refer to various flaw sets (modified from Dearman (1991))

shear stress, τ_s , is controlled by a cohesive (c) and frictional (ϕ) strength according to the Coulomb slip model (Itasca, 2004b), such that

$$\mid \tau_s \mid \leq c + \sigma_n \tan \phi = \tau_{max}, \tag{3.2}$$

then

$$\Delta \tau_s = -k_s \Delta u_s^e, \tag{3.3}$$

or else, if

$$\mid \tau_s \mid \geq \tau_{max}, \tag{3.4}$$

then

$$\tau_s = \text{sign}(\Delta u_s) \tau_{max}, \tag{3.5}$$

where Δu_s^e is the elastic component of the incremental shear displacement, and Δu_s is the total incremental shear displacement (Itasca, 2004b).

The basic joint model used in UDEC that captures several of the features in the normal and shear direction is the Coulomb slip model with tension cut-off. The Coulomb slip model is an elastic-perfect plastic model (Figure 3.6). Notice that in Figure 3.6, σ_t should be drawn in $\sigma_1 - \sigma_3$ space not shear-normal stress space and this diagram is only for demonstration purpose. The Coulomb model can also be used to approximate a displacement-weakening behaviour by setting the joint cohesion, friction, and tensile strength to reduced values whenever either the tensile or shear strength is exceeded.

Lajtai (1969b) stated that at low normal stress the rock mass strength is totally controlled by the tensile strength (Equation 3.6). The tensile stresses cause non-linearity in the failure envelope in the Mohr-Coulomb space. Moreover, Cho et al. (2008) found that the formation of the shear zone was preceded by tensile fracturing aligned with the major principal stress direction. In addition, in rock slopes, the majority of the back-calculated cohesion is mostly apparent cohesion due to asperities and interlocking but not true cohesion. Moreover, Skempton (1964) showed that the long-term (decades-long) stability of slopes in stiff overconsolidated clay

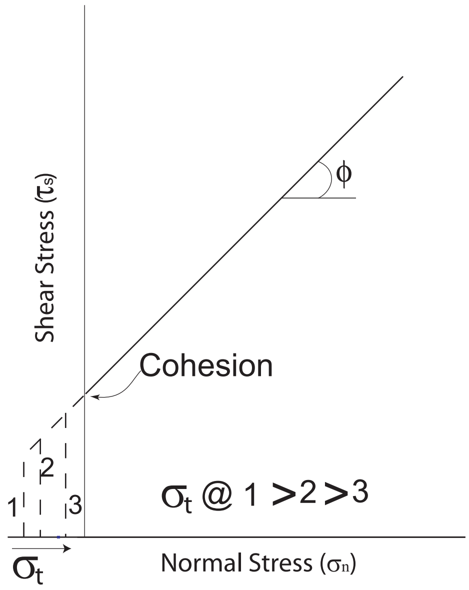

Figure 3.6: Coulomb-slip model used to simulate the flaws behaviour

was a function of the loss of cohesion with time. In soils, cohesion is a function of Van de Vaals' bonding forces which are influenced by environmental factors such as water content. In many rocks, the cohesive forces are dominated by ionic and covalent bonds, which are not readily susceptible to environmental factors. However, these bonds are weaker in tension than in shear. Hence, if tensile stresses exist, these bonds may break at relatively low stress magnitudes. Aydin and Basu (2006) showed, using Brazilian tensile tests that the tensile strength of a rock is extremely sensitive to the degree of weathering. They found that the tensile strength could decrease by an order of magnitude depending on the extent of weathering, and that the stiffness of the rock decreased as the tensile strength decreased. In other words, weathering may be a significant factor in controlling the behaviour of rock slopes, if the stability of the slope is controlled by the tensile strength. Hence, in this study, the tensile strength of the flaws was decreased gradually to study the effect of tensile strength degradation on rock slopes, while, cohesion and friction angle were kept constant, Figure 3.6 presents the modeling procedure used in this study.

$$\tau = \sqrt{\sigma_t(\sigma_t - \sigma_n)}, \tag{3.6}$$

where σ_t is the tensile strength, and σ_n is the normal stress.

The normal stiffness of the flaws is calculated from Equation 4.9. At the beginning of each simulation, the shear stiffness is assumed to be equal to the normal stiffness, and then the response of the model is examined. Next, a trial-and-error procedure is adopted to match the deformation of the numerical model with the actual measured deformation, if any. If the measured deformation is not available, the shear stiffness is changed to match the expected behaviour of the model. According to Itasca (2004b), up to ten times the normal stiffness calculated from Equation 4.9 can be assigned to the flaws. If the joint stiffnesses are greater than 10 times the equivalent stiffness, the solution time of the model will be longer than for the case in which the ratio is limited to ten, without a significant change in the behaviour of the model:

$$\mathrm{k}_n = \max\left[\frac{(K + \frac{4}{3}G)}{\Delta Z_{min}}\right], \tag{3.7}$$

where k_n= normal stiffness, K is the bulk modulus, G is the shear modulus, and Z_{min} is the smallest width of an adjoining zone in the normal direction (see Figure 3.7).

Small scale flaws can be very stiff i.e., relative to the size of the model, as the flaws can represent grain-boundary flaws or larger-scale internal flaws which have a very small aperture and that justify the relatively high normal and shear stiffness used in some models.

3.5 Damage Model on direct shear tests

Lajtai (1969c) conducted a series of tests using plaster of Paris to simulate intact rock blocks. The blocks, containing rectangular voids to represent the discontin-

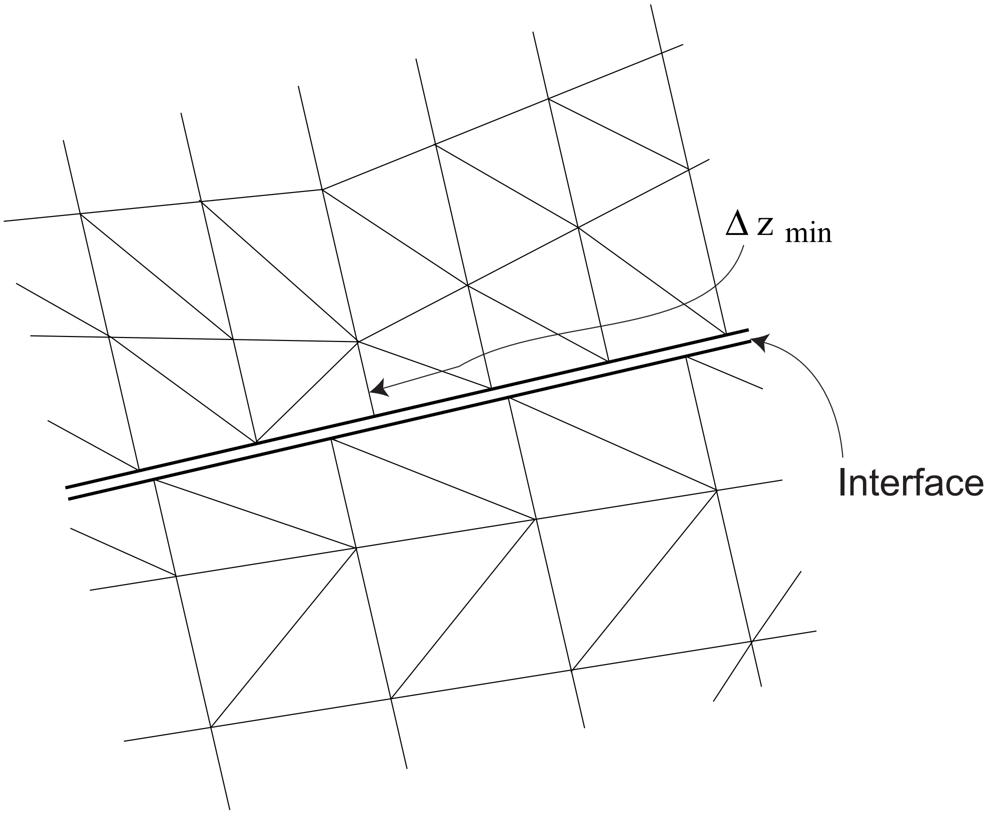

Figure 3.7: Definition of zone dimension used in stiffness calculation, Equation 4.9

uous nature of the joints, were subjected to direct shear stress at various normal stresses. Lajtai argued that for non-continuous joints, the minor principal stress in the rock bridge is tensile even if the all-around stresses are compressive, and that these tensile stresses are responsible for forming the fractures in the rock bridges. Lajtai concluded that at low normal stress, tensile fracturing in the rock bridge was the dominant mode of failure, but that as the normal stress increased, the failure mode progressively became dominated by shear mechanisms. Based on his finding, Lajtai suggested that the failure of rock containing intact rock bridges between joints could be represented by a nonlinear envelope whose nonlinearity occurred because of the nonuniform mobilization of friction (Hajiabdolmajid et al., 2003). At low normal stress, the tensile strength controlled the failure while at high normal stress, the frictional strength dominated the failure process.

The properties of the plaster of Paris used by Lajtai (1969c) were as follows: unconfined compressive strength of 4.1 MPa, a friction angle of 37°, tensile strength of 1.1 MPa, and an estimated cohesion of less than twice the tensile strength. The Mohr-Coulomb failure criterion with tension cut-off was used to control the flaws' behaviour in this modeling approach.

To model the direct shear test, the cohesion, the friction angle and the tensile strength needed to be known prior to conducting the analysis. However, the tensile strength and the friction angle were known while the cohesion was unknown, so the UDEC-DM was utilized to back-calculate the unconfined compressive strength. A two-to-one model was prepared with an edge length of 7 mm, which is the same edge used in the direct shear model. The model was subjected to a constant displacement rate to induce stresses until failure was achieved. The axial stress and vertical strain were monitored by using Fish functions. A trial-and-error study was conducted to match the unconfined compressive strength of 4.1 MPa by varying the cohesion of the flaws while keeping the tensile strength and friction angle constant, Table 3.1 shows the flaws' properties used in the unconfined compressive strength model. Figure 3.8(a) shows the stress-strain curve resulting from this test. The failed sample is shown in Figure 3.8(b).

At σ_{ucs} of 4.1 MPa, the back-calculated cohesion was approximately 1.2 MPa. Figure 3.9 shows the variation of the unconfined compressive strength as the cohesion of the flaws varied. As the cohesion increased, the (σ_{ucs}) increased. This value, along with the properties shown in Table 3.1, was used to model Lajtia's direct shear test.

The UDEC-DM model was used to simulate Lajtai's direct shear experiments (Figure 3.10). The tensile strength of the plaster of Paris was approximately 1.1 MPa, and the friction angle was 37°, these values assigned to the flaws in the model.

The plaster of Paris Young's modulus can range between 2-10 GPa (Vekinis

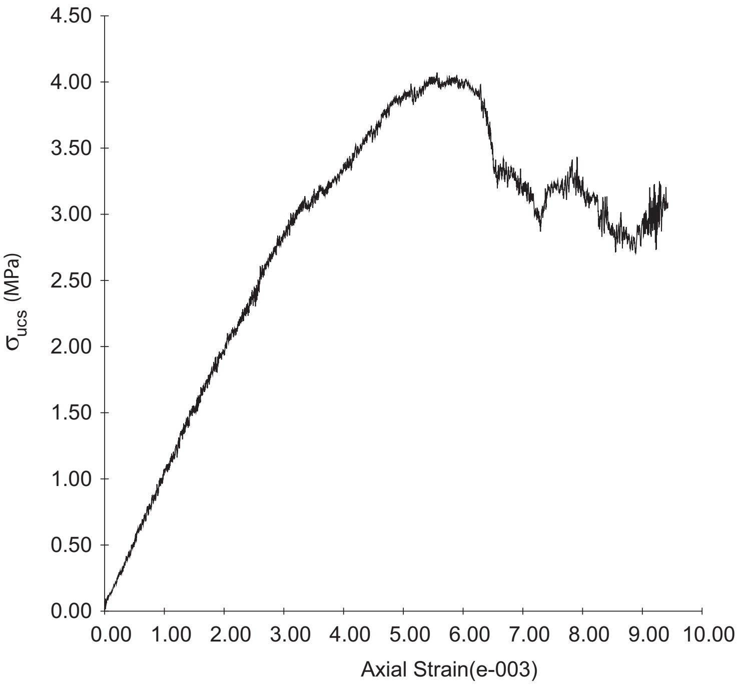

(a) Stress-strain response

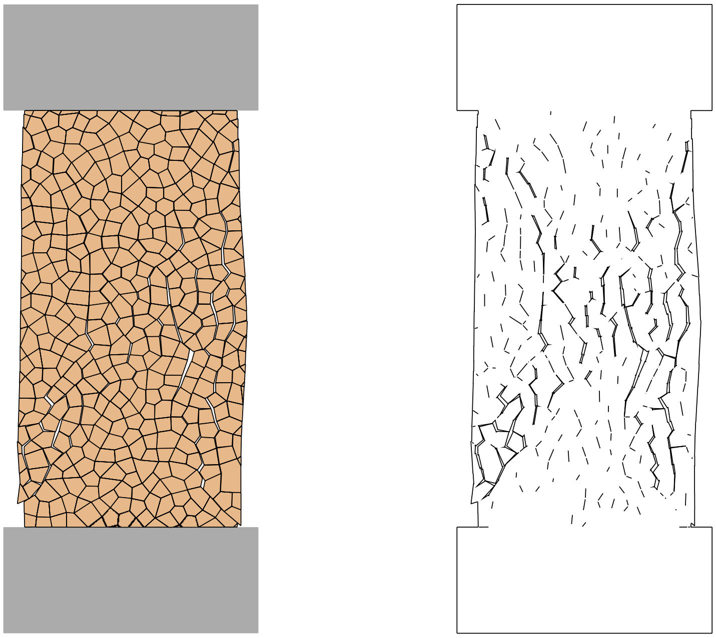

(b) Model of the intact rock after failure

Figure 3.8: The unconfined compressive strength of plaster of Paris

et al., 1993). In this model, the blocks had a Young's modulus of 4.5 GPa. The UDEC-DM model was calibrated to these properties such that the uniaxial com-

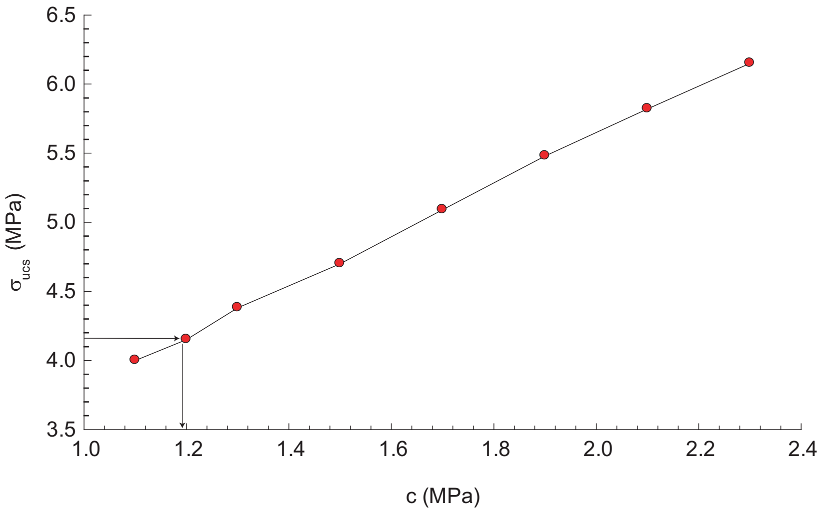

Figure 3.9: Effect of cohesion on the uniaxial strength

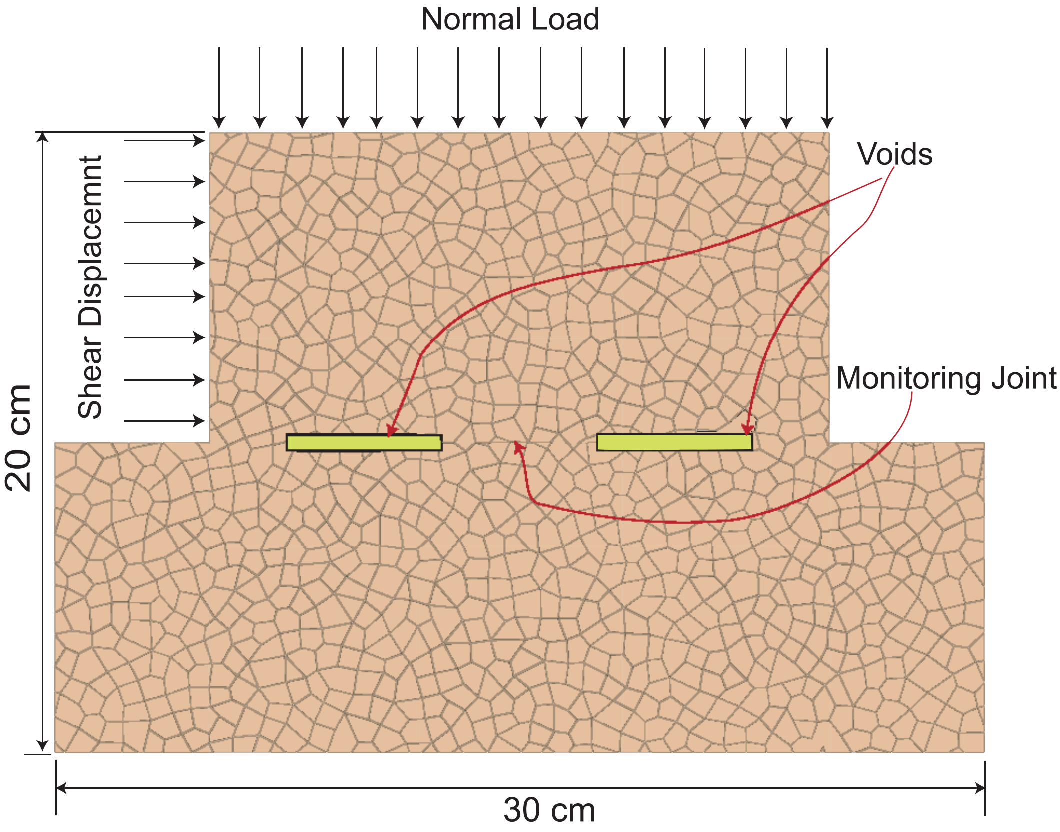

Figure 3.10: The UDEC-DM model used to simulate Lajtai's direct shear experimental results.

Table 3.1: Comparison between Lajtai's plaster of Paris model properties and those used in the UDEC-DM

Properties	UDEC-DM	Lajtai
Friction angle(°)	37	37
σ_t(MPa)	1.1	1.1
C(MPa)	1.2	$< 2\sigma_t$
Normal Stiffness (GPa/m)	40	-
Shear Stiffness (GPa/m)	20	-
Joint aperture (mm)	0.1	-

pressive strength was captured as mentioned above (Table 3.1). In these simulations, the flaw size in the plaster of Paris was very small, i.e., sub mm scale. However, in the UDEC-DM model, the length of the polygonal block was limited to 7.0 mm. Different block lengths were evaluated ranging from 5 mm to 11 mm, and the length used in this study (7 mm) provided a reasonable compromise between accuracy and simulation time. A total of 23 UDEC-DM models were carried out, Figure 3.11 compares the UDEC-DM model results with those obtained by Lajtai. These results suggest that this approach is capable of capturing the behaviour of discontinuous rock joints subjected to direct shear and automatically captures the nonlinear failure envelope commonly observed in rock testing. Lajtai (1969c) also presented a direct shear test results from samples with closed joints. The direct shear experiment were also modeled numerically by using the UDEC-DM in the same manner for the model with the open joints and the same properties shown in Table 3.1 . A close agreement was achieved between the experimental results and the numerical simulation (see Figure 3.12). Notice that the direct shear tests were performed under a limited range of normal stress.

3.6 The effect of discontinuity persistence

The effect of discontinuity persistence has been investigated by using numerical modeling of the direct shear test. The degree of persistence (k) is equal to the ratio

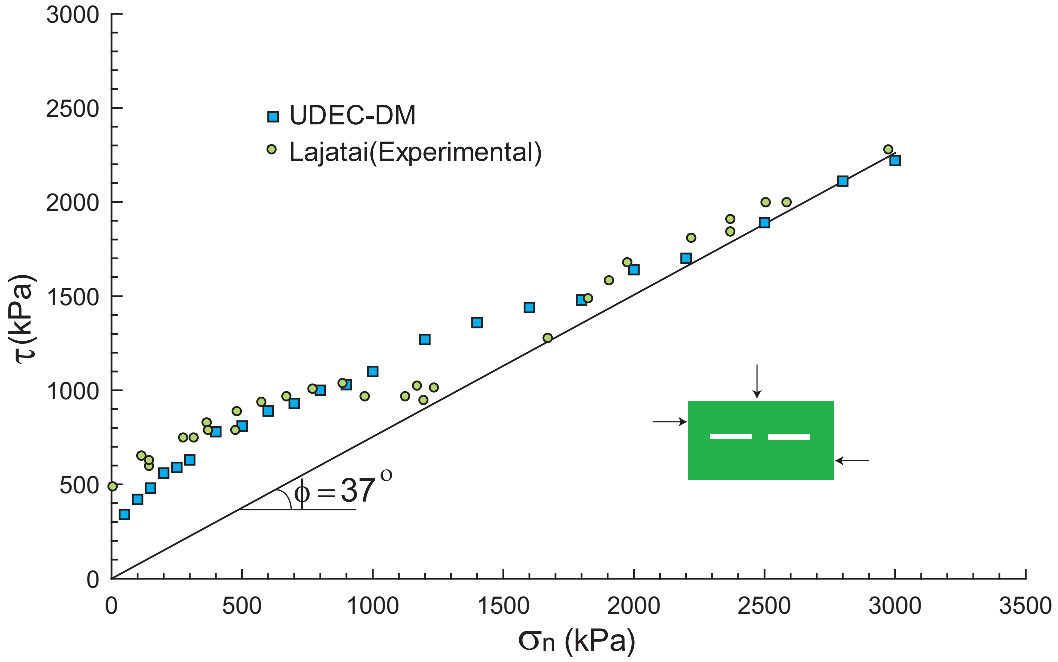

Figure 3.11: Comparison of UDEC-DM model results with the results from direct shear tests on plaster of Paris and open joints (data from Lajtai, 1969c)

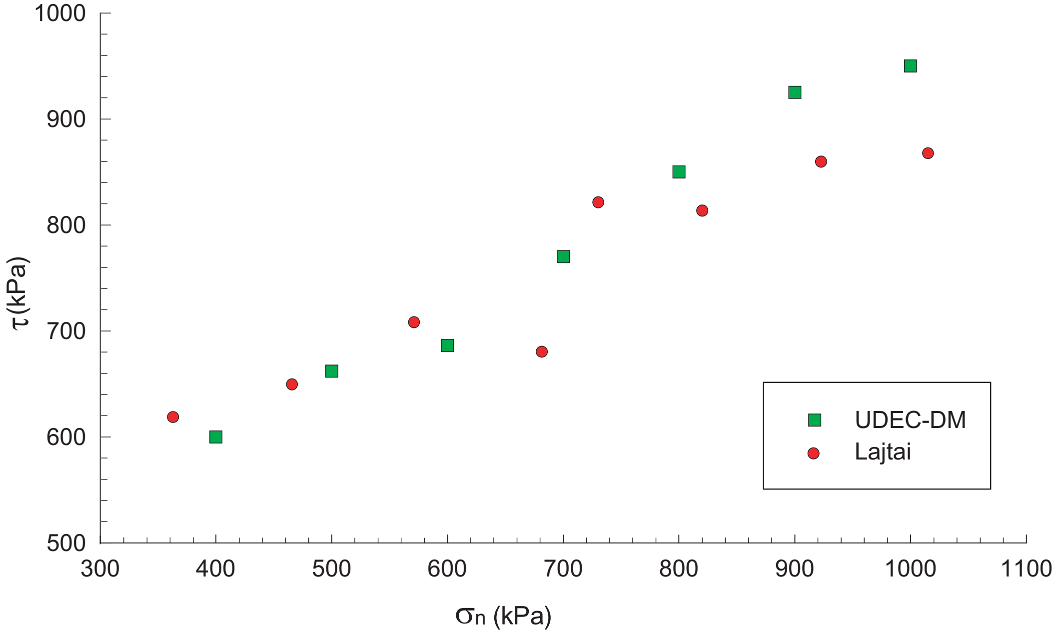

Figure 3.12: Comparison of UDEC-DM model results with the results from direct shear tests on plaster of Paris and closed joints (data from Lajtai, 1969c)

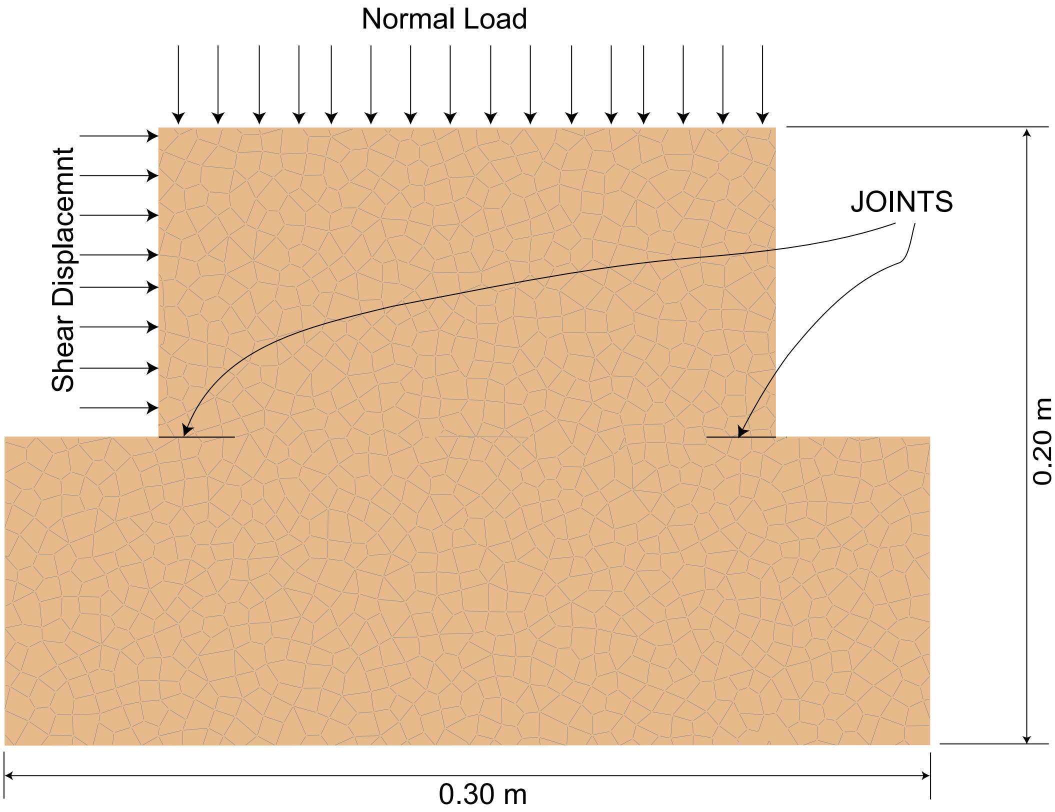

Figure 3.13: Non-persistent joints direct shear model

between the total lengths of the joint segments to the total length of the model in the direction of shearing. Five models with $k = 0, 0.25, 0.5, 0.7$ and 1.0 were simulated. Joints were inserted at each side of the model (see Figure 3.13). A friction angle of 30° was used for both the flaws and the joint segments. The flaws was assigned a tensile strength of 1.0 MPa, while the tensile strength and the cohesion for the joint segments were equal to zero. Table 3.1 shows the properties used in this model with a friction angle of 30° for the intact rock and the joints to allow shear failure at low (k). The normal and shear stiffness of the joints were the same as the flaws in table 3.1.

Normal stress was applied, and the model was subjected to shear displacement from left to right (see Figure 3.13). The shear stresses were monitored along the forced shear plane. For each model, the normal stress was varied between 0.3 to

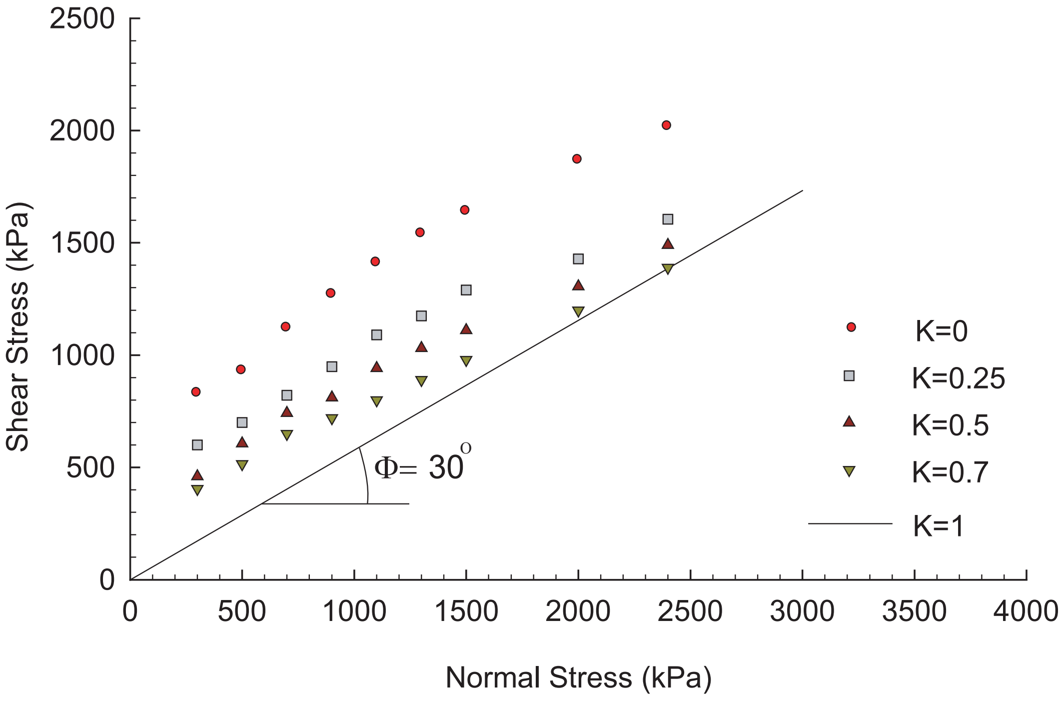

Figure 3.14: Failure envelope of non-persistence joint direct shear model

2.4 MPa. Figure 3.14 shows the failure envelope for the five models. As the length of the joints increased, the rock became weaker in the shear, and the shear strength decreased as a sign of the progressive failure effect due to the presence of the joints.

If $k > 0$, i.e., if the rock is jointed, the strength of the rock is controlled by both the joints and the intact material. At $k = 1.0$, the strength was totally controlled by the basic friction angle of the rock (30°). As the normal stress increased, the shear strength decreased to the ultimate strength at a normal stress lower for high k than for low k. As the normal stress approached or exceeded the unconfined compressive strength of the rock material, the degree of discontinuity had no effect as the strength of the rock was controlled by the friction angle of the crushed material (the basic friction angle). In order to clarify this point, the shear strength of the jointed models was normalized to the intact material strength derived from the UDEC-DM direct shear model. The results are plotted against the normal stress in Figure 3.15.

As this figure shows, the difference between the normalized strength and the

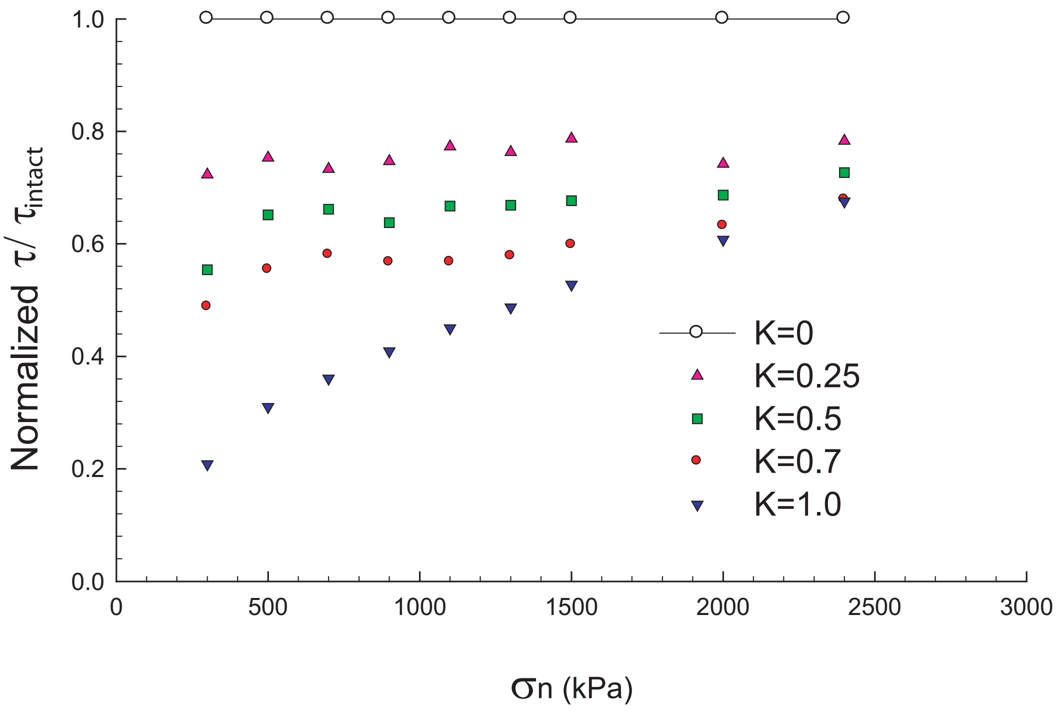

Figure 3.15: Normalized shear strength of jointed rock to the strength of the intact material

frictional strength decreased as the normal stress increased, and eventually at high normal stress, the strength of the partially jointed rock ($k < 1$) became equal to the ultimate strength derived from the basic friction angle. These results support the importance of the joints in rock mass analysis, especially in low-stress environments such as those involving slope stability problems. To build a complete geological model for a rock mass, the planes of weakness must be included to contribute to the rock mass's total strength. This modeling approach can explicitly model the joints and allow fractures to initiate and propagate and cause coalescence between the pre-fractured joints. The existence of joints inside the rock mass will introduce weakness planes and reduce the shear strength of the intact rock. The direct shear model using the UDEC-DM provides insights into the effect of the planes of weakness on the rock mass strength envelope and the progressive failure.

3.7 Effect of tensile strength in the direct shear test

The model shown in Figure 3.13 represents a direct shear test model. If $k = 0$, the direct shear for the intact material is obtained. The advantage of this damage model is that it provides heterogeneity and interlocking inside the rock mass, and the failure path is not predetermined; i.e., the failure can follow any arbitrary path, and the material can also fail in different mechanisms.

To examine the ability of the UDEC-DM to capture the tensile strength in the direct shear model, two models with a friction angle of 30° and tensile strengths of 0.5 MPa and 1.0 MPa were numerically simulated. Non-linear failure envelopes were obtained by using this modeling approach. Figure 3.16 shows the failure envelope for both cases. These results indicate that the UDEC-DM captured the non-linearity in the failure envelope predicted in the experiments and also captured the tensile strength effect as shown in Figure 3.16. The normal and shear stiffness and the cohesion of the flaws used in this model are shown in Table 3.1.

3.8 Scale effect in UDEC-DM

To study the scale effect on the UDEC-DM, four models with edge lengths of 0.5, 0.7, 0.9, and 1.1 cm long were studied. The models was similar to the one shown in Figure 3.13 with no joint segments. The size of the models was kept constant throughout the modeling process. The joint normal and shear stiffness were varied according to Equation 4.9. The models were tested under direct shear loading; a range of normal stress was applied to the model, and shearing started. The peak shear stress was monitored and plotted against the applied normal load in Mohr-Coulomb space, (see Figure 3.17). The results in this direct shear simulation showed that within the range of the edge lengths used in this study, the scale effect was minimal, and the failure envelopes for the four models were reasonably close.

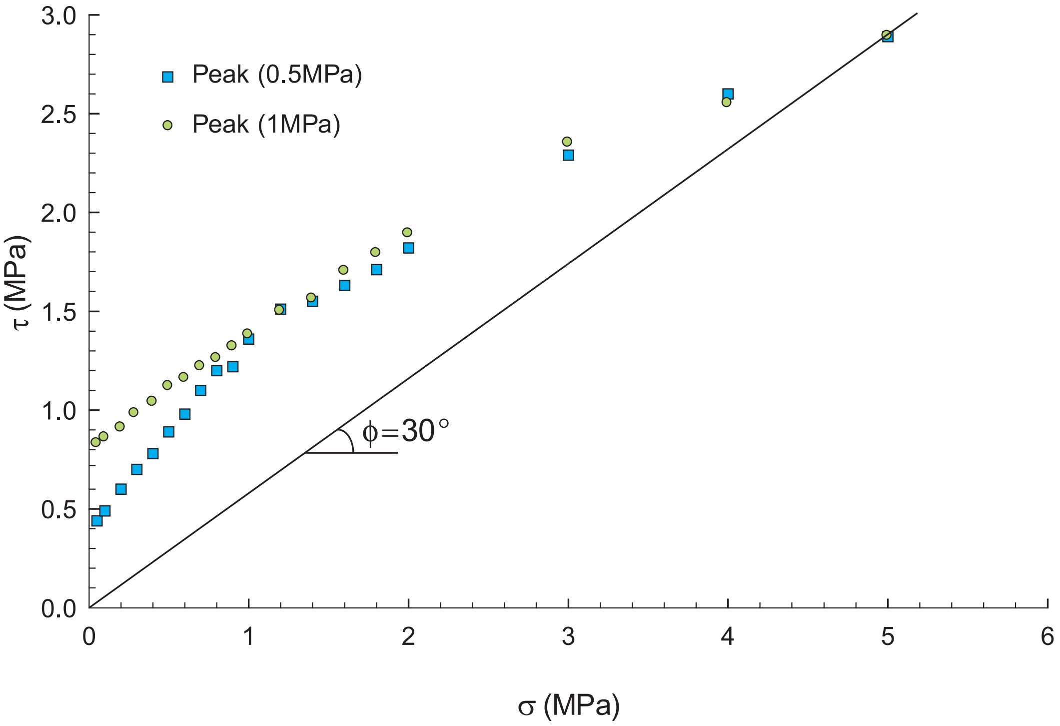

Figure 3.16: Failure envelope and the tensile strength effect on direct shear discrete element damage model simulation

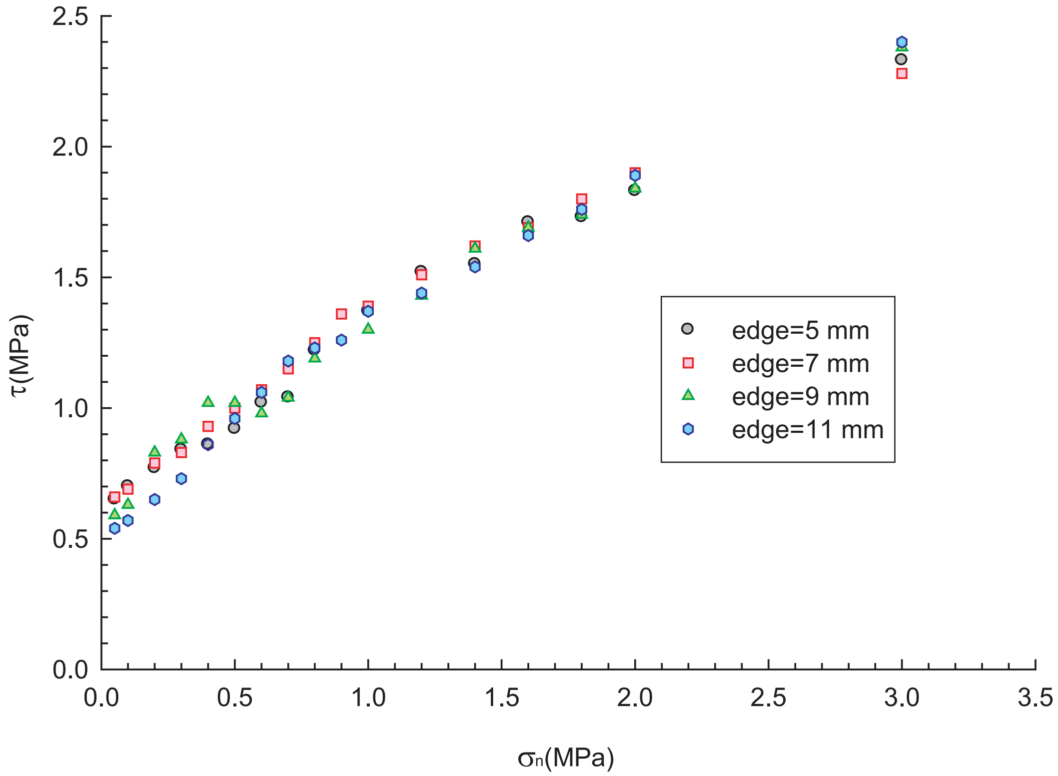

Figure 3.17: Direct shear results for different edge lengths

In the following chapter, the discrete element damage model is applied to experimental toppling examples to examine the effect of tensile strength on rupture surface formation.

3.9 Summary

The discrete element formulation in UDEC was used to create a damage model (UDEC-DM) that can simulate a jointed rock mass and accommodate both continuous and discontinuous joints. The intact rock between the joints are assigned internal flaws and the flaw properties can be adjusted to simulate a rock mass that varies from a strong brittle rock mass to a very weak one. The UDEC-DM was successfully used to model direct shear tests of discontinuous joints. The resulting failure envelope was nonlinear and was found to be in general agreement with experimental results.

Chapter 4

Toppling Failure in Centrifuge Models

4.1 Introduction

Toppling failures of rock slopes are common in natural or excavated slopes. Understanding the toppling movements' mechanisms is an essential step for carrying out back analysis, designing rock slopes, or predicting the rock slopes' behaviour. Goodman et al. (1968), Goodman and Bray (1976), recognized three types of toppling failures: flexural, block, and block-flexural. In these types, the main set of joints dip into the slope. Later, Cruden (1989) identified underdip slopes in which the main set of joints dip more steeply and in the same direction as the slope face. In the underdip topples, Cruden and Hu (1994) found examples of block and block-flexural topples but not of flexural toppling because of the existence of fractures perpendicular to the bedding at all their sites. Figure 4.1 illustrates the different types of toppling. However, topples where beds dip into the slope are more common in natural and man-made slopes with one set of discontinuities dipping steeply into the rock slope than the underdip topples.

This chapter concentrates on slopes with joints dipping into the slope and, more specifically, on flexural toppling, which involves the bending of intact rock columns, fracturing, and, finally, the forming of a rupture surface.

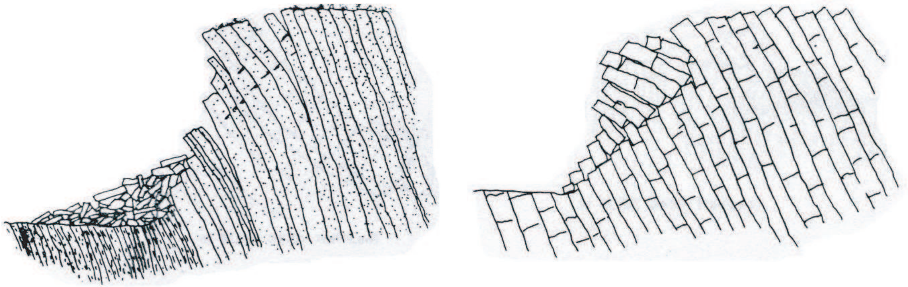

a) Flexural toppling

b) Block toppling

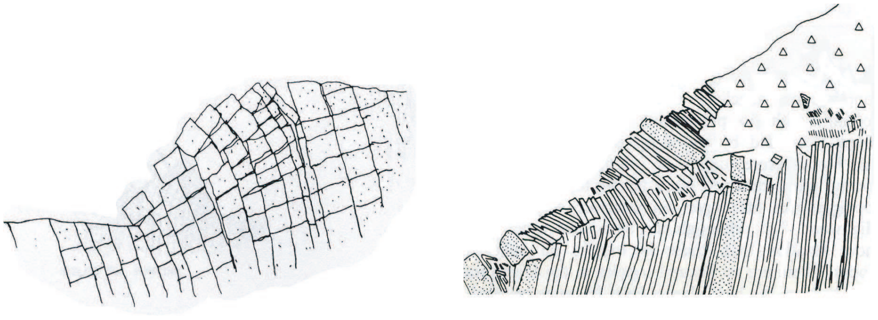

c) Block-Flexural toppling

d) Underdip Toppling

Figure 4.1: Toppling modes observed in the field, (a) Flexural Toppling, (b) Block toppling, (c)Block-flexural toppling (modified from Goodman and Bray, 1976) (d) underdip toppling (modified from Cruden and Hu, 1994)

As sliding between the rock columns occurs along the steeply dipping bedding planes, the rock columns start to bend over into the excavation; these bending movements create bending stresses inside the rock mass. These bending stresses subject the rock columns to tensile stresses. If these exceed the tensile strength of the rock mass, the rock columns fracture.

Thus, tensile strength plays an important role in flexural toppling failure and needs to receive more attention. Although the sliding mechanism is important in flexural toppling, failures due to bending stresses are also important, and are required to form a rupture surface inside the rock mass. I use ”failure” to indicate that a discrete rupture surface forms inside the model.

The following sections introduce the experimental results, examine flexural toppling failures in a discrete element frame using the conventional UDEC and UDEC-DM approaches, and discuss the effect of tensile strength on the toppling mechanism. Two centrifugel tests were simulated, the results showed good agreement with the laboratory results in terms of predicting the load at failure and the rupture surface location.

4.2 Adhikarys's centrifuge experimental results

4.2.1 Introduction

Adhikary and Dyskin (2006) conducted a series of centrifugel experiments on models made of two types of materials: an ilmenite-gypsum mixture and fibre-cement sheeting. Because of its properties, the ilmenite-gypsum mixture is more likely to behave like a rock. Thus, I used the ilmenite-gypsum results to verify the UDEC-DM numerical modeling approach. Table 4.1 shows the material properties of the ilmenite-gypsum (IGM-01) used by Adhikary and Dyskin (2006).

Table 4.1: Properties of the ilmenite-gypsum material, (modified from Adhikary and Dyskin, 2006)

Model parameters	IGM-01(ilmenite-gypsum)
Slope height(mm)	330.0
Slope dip angle	61.0°
Joint spacing (mm)	10.0
Joint dip angle	80.0°
Modulus of elasticity(GPa)	2.2-2.6
Poisson's ratio	0.16
Unit weight (kN/m^3)	23.8
Tensile strength (MPa)	1.1-1.4
Joint friction angle	22.0°-26°

The manufactured models were subjected to incremental gravity loading to simulate increases in the slope height. The displacements were monitored at two different points in the physical model (see the insert in Figure 4.2). Figure 4.2 illustrates the horizontal displacements as the gravity level increases in the experiment.

Adhikary and Dyskin (2006) reported that the physical model failed at a gravity level between 80g and 85g. Figure 4.3 shows the physical model after testing under

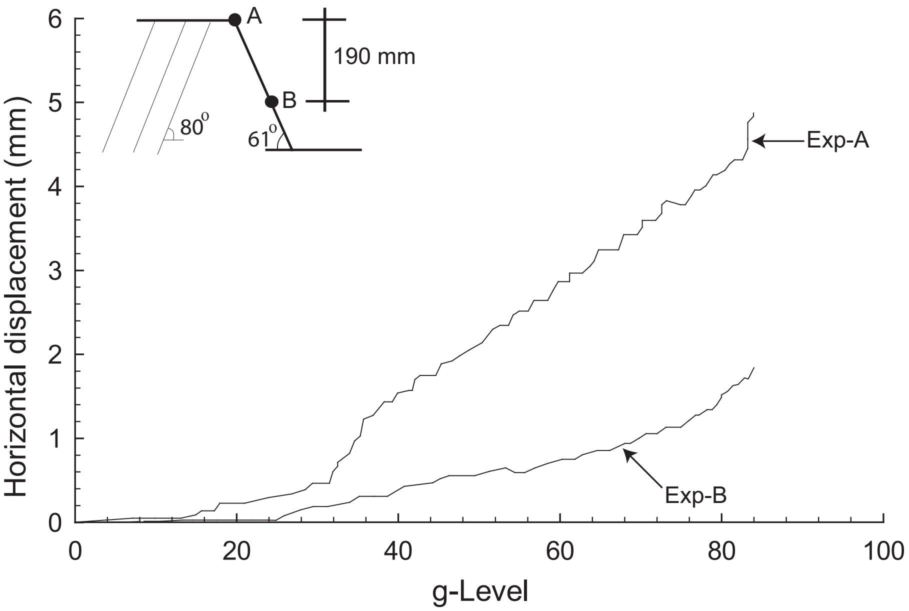

Figure 4.2: Centrifugal experimental results, g is gravity, (modified from Adhikary and Dyskin, 2006)

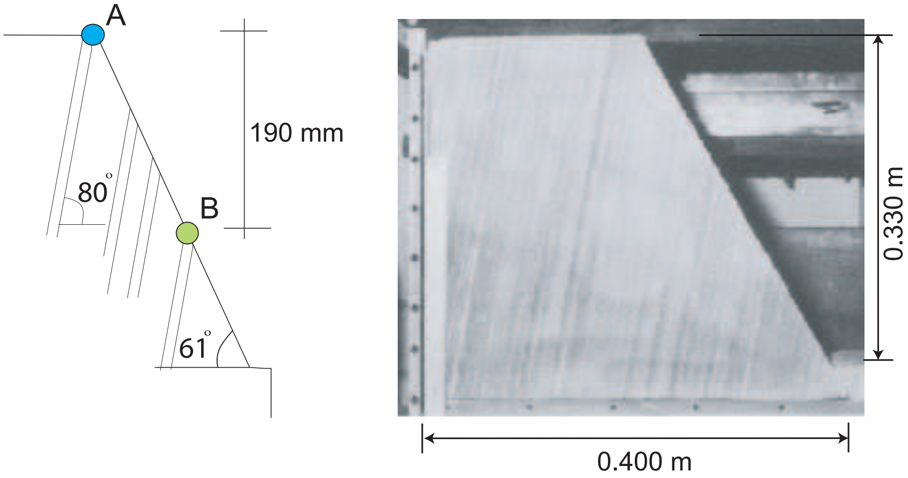

Figure 4.3: The physical model after testing (modified from Adhikary and Dyskin, 2006)

gravity acceleration. Adhikary and Dyskin (2006) also presented a numerical model based on the Cossart medium. To match the experimental results with the numerical model results, these researchers changed the cohesion of the bedding planes. A good agreement was achieved between the deformation patterns at a cohesion of 15 kPa, and the G-level at failure was 76g. No actual rupture surface was developed in their numerical modeling approach.

4.2.2 Numerical modeling: conventional UDEC

The distinct element code, UDEC (Itasca, 2004b) was used to model Adhikary's experimental results by gradually increasing the gravity level to failure. The IGM-01 results (see Table 4.1) were used in this simulation.

Figure 4.4 shows the conventional UDEC numerical model used in this study. Table 4.1 shows the properties of both the intact material and the bedding planes. The cohesion and the friction of the bedding plane are the same as that used by Adhikary and Dyskin (2006), a cohesion of 15 kPa and a friction angle of 23°. Figure 4.5 shows the displacements from both the experimental results and the UDEC model.

These results show that the conventional UDEC underestimated the displacements and overestimated the failure load (failure load = 115g). At a second stage, the cohesion of the bedding planes was reduced gradually to 5 kPa. Figure 4.6 presents the experimental results along with the UDEC results at a cohesion of 5kPa.

Although the results show good agreement between the results at this low cohesion value, the conventional UDEC could not capture some essential aspects of the model's behaviour during testing. The first of these aspects is the transitional point of the deformation patterns that occurred between 20g and 40g, as found in the experiments. Moreover, the conventional UDEC was not able to predict accurately the location of rupture surface. Adhikary et al. (1997a) pointed out that the main fracture path was found to be oriented at an angle of 12° to 20° above the normal to the joint dip angle. The conventional UDEC predicted a deeper failure surface than anticipated. Figure 4.7 shows the plasticity indicators inside the UDEC model and

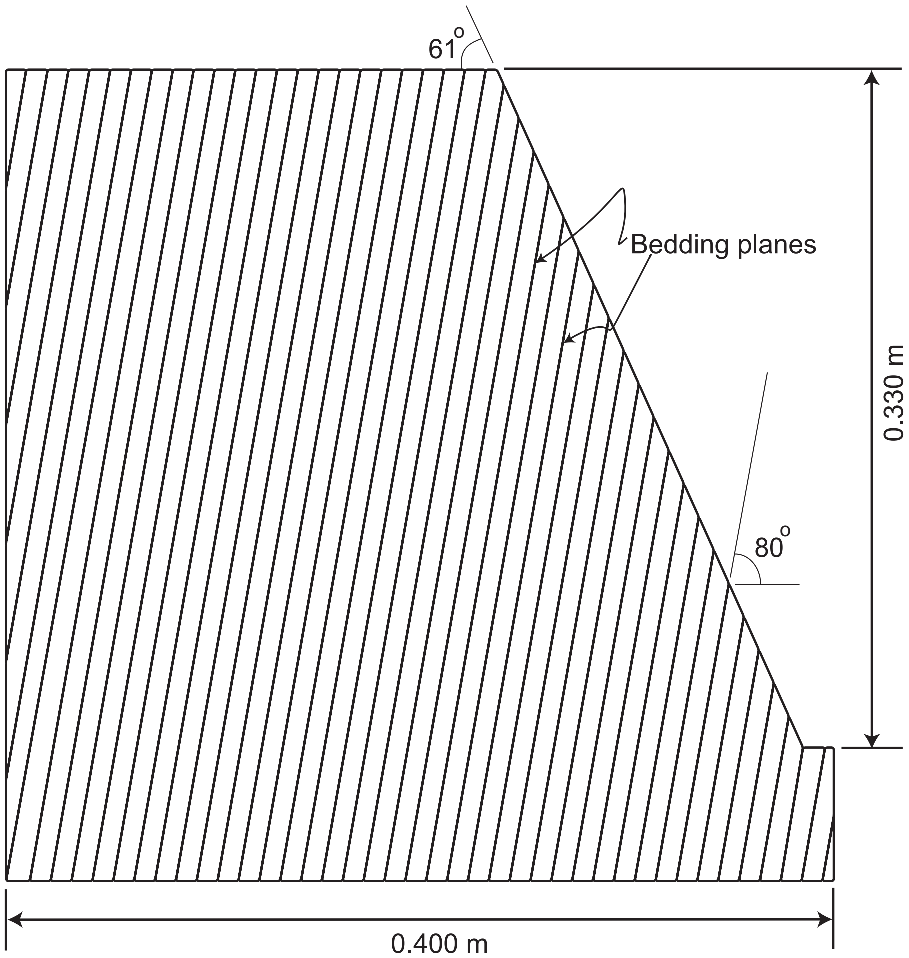

Figure 4.4: Conventional UDEC numerical model, 40 beds across base

the failure surface from the experimental study . The failure surface is found to be oriented at an angle of 0° to 4° above the normal to the joint dip angle.

4.2.3 The Damage Model toppling simulation

The UDEC-DM was used to model the centrifugel experimental results. This model was created by first generating the main set of joints and then implementing the flaws. Figure 4.8 shows the UDEC-DM model used in this example.

The size of the model is the same as that in Adhikary's experiments, and the main set of joints dip into the model at an angle of 81°. The horizontal displacement was monitored for each gravity level at points A and B (see Figure 4.8). The shear

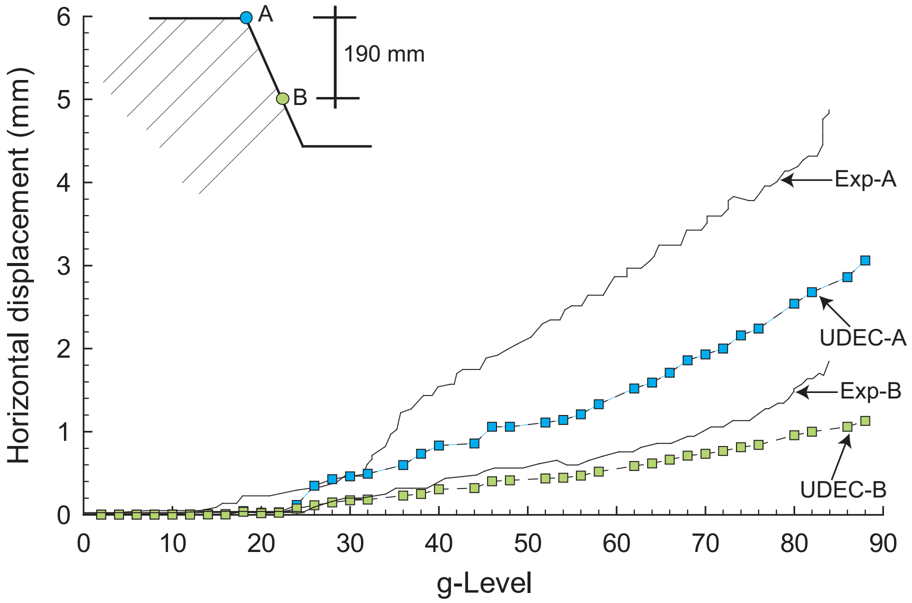

Figure 4.5: Comparison between conventional UDEC and the experimental results, c=15kPa

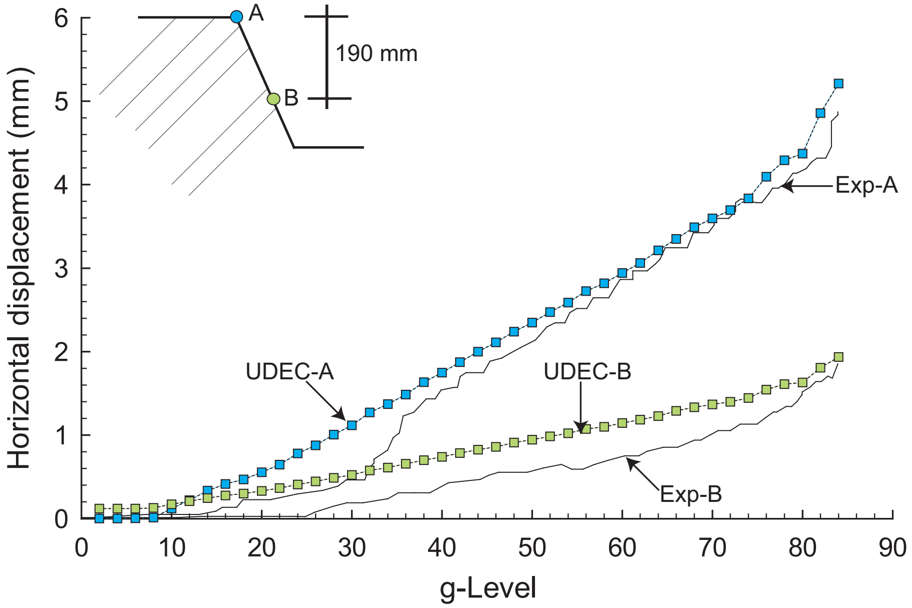

Figure 4.6: Comparison between conventional UDEC and the experimental results, c=5kPa

strength and deformation properties are the same as those in Adhikary and Dyskin (2006) for the IGM-01. The bedding planes had 15 kPa of cohesion, and 23° of

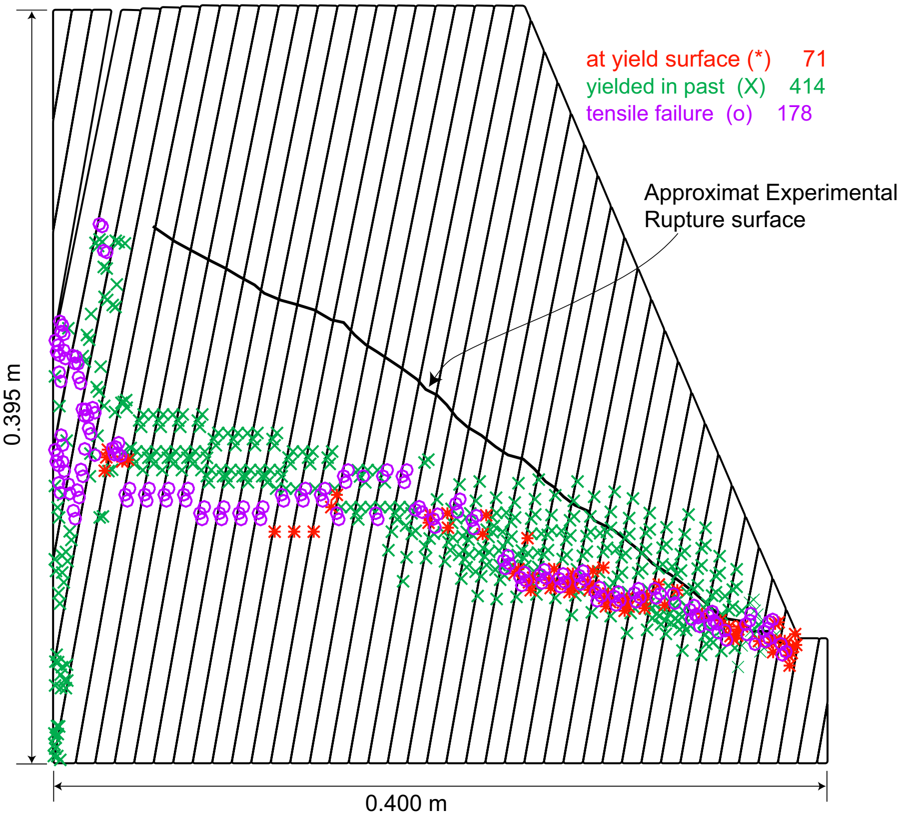

Figure 4.7: The plasticity indicators in conventional UDEC compared to the actual failure surface

friction. The following intact material properties were assigned to the internal flaws: the tensile strength was 1.1 MPa, the friction angle was 37° and the modulus of elasticity was 2.6 GPa, cohesion of the flaws was 1.6 MPa. The Coulomb slip model (Elastic-plastic)was used to simulate the flaws behaviour.

Calibration of the Model

The normal stiffness of the flaws was calculated by using Equation 4.9. At the beginning of each simulation, the shear stiffness is assumed to be equal to the normal stiffness, and then the response of the model was examined. Next, a trial-and-error procedure was adopted to match the deformation of the numerical model with the actual measured deformation.

In this model, normal (k_n) and shear (k_s) stiffnesses were varied while moni-

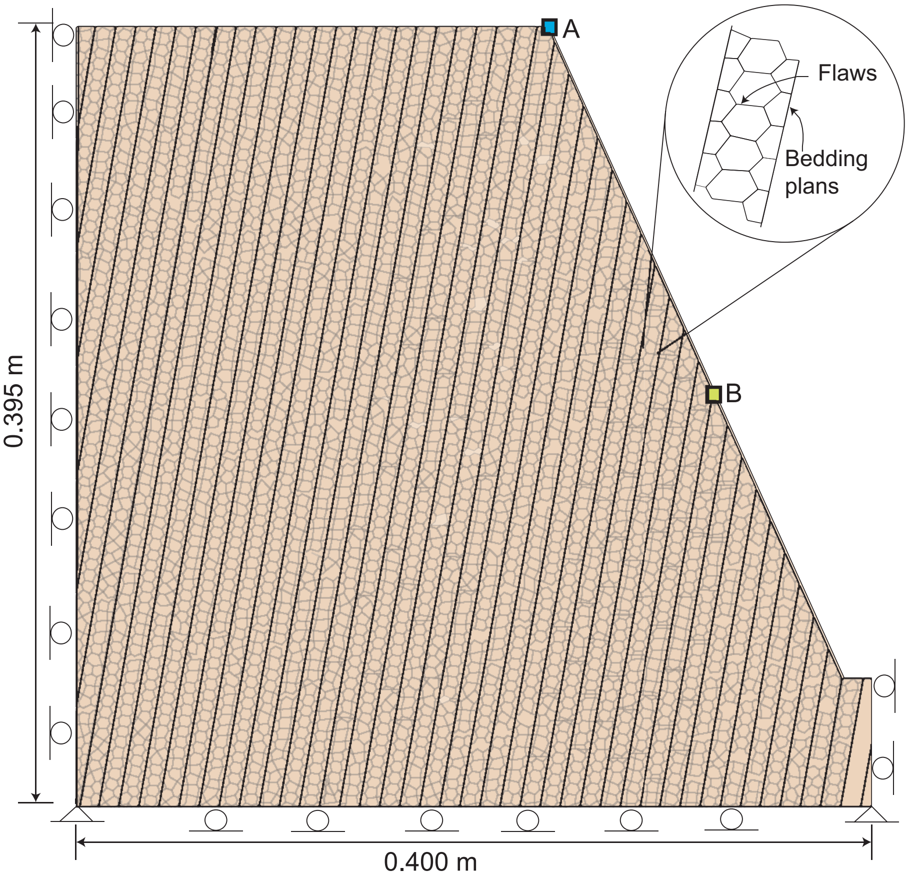

Figure 4.8: The UDEC-DM model used to model Adhikary's experiments and the boundary conditions

toring the horizontal displacement at points A and B. Figure 4.9 shows the effect of changing the flaws' normal and shear stiffness with the experimental results. A good match between the results was obtained at a k$_n$ of 700 GPa/m and a k$_s$ of 600 GPa/m. These values were used through out the rest of the simulations in the Adhikary's simulation. Moreover, these values of stiffnesses were relatively high to control the model and prevent overlaping between the internal blocks due to the existence of sharp corners. Although these stiffnesses values are not a unique solution, they assumed to be constant throughout the rest of the modeling.

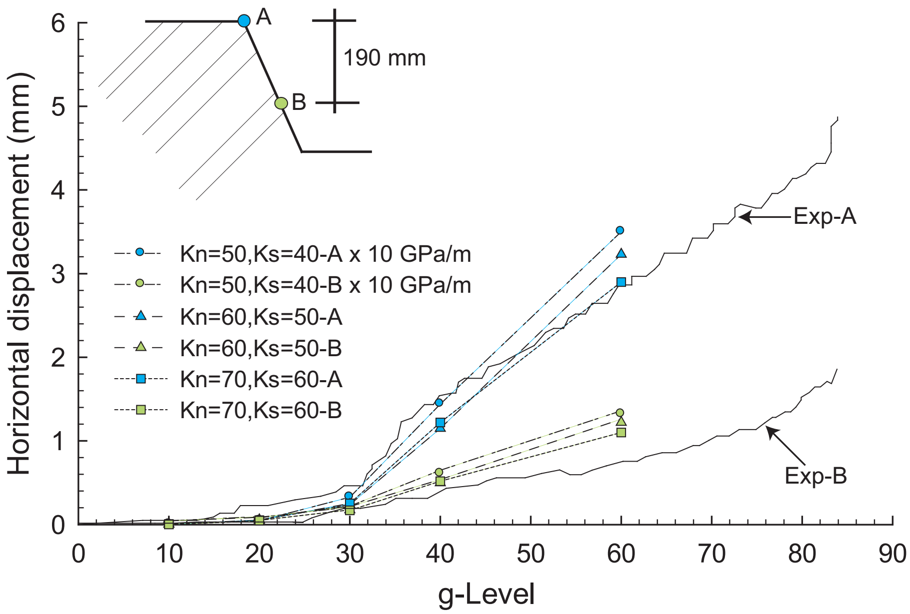

Figure 4.9: The effect of normal and shear stiffness at the deformation pattern, x10 GPa/m

Modeling Results

To model the centrifugel experiments, the gravity acceleration was increased gradually in 1g increments, and the horizontal displacements were monitored at points A and B (see the insert in Figure 4.2). As the gravity acceleration increased, the horizontal displacements increased. Figure 4.10 shows a comparison between the horizontal displacement predicted by the UDEC-DM model and that predicted by Adhikary's test as the gravity acceleration increased. While Figure 4.11 shows the deformation at both monitoring points when the model failed at 70g.

The simulation shows a good agreement between the results prior to failure. In contrast to the conventional UDEC model, the UDEC-DM was able to capture the transitional point of the deformation between 20g to 40g, but this model was not able to capture correctly the load at failure as predicted in the experiments. This transitional point of the deformation was attributed to initiation of shearing between the beddings along with initiation of fracturing in the model. The model in the ex-

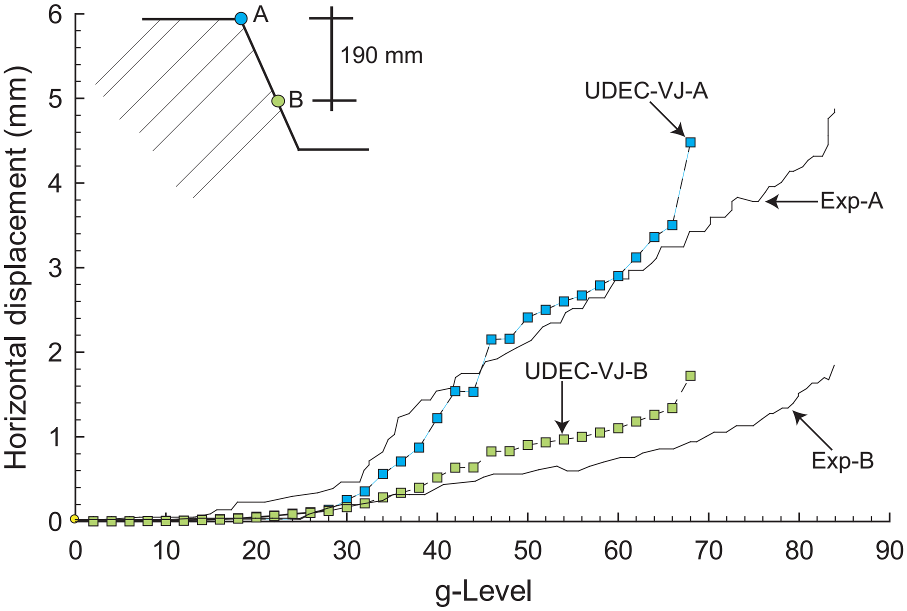

Figure 4.10: Comparison between the horizontal displacement between Adhikary's results and those from UDEC-DM model

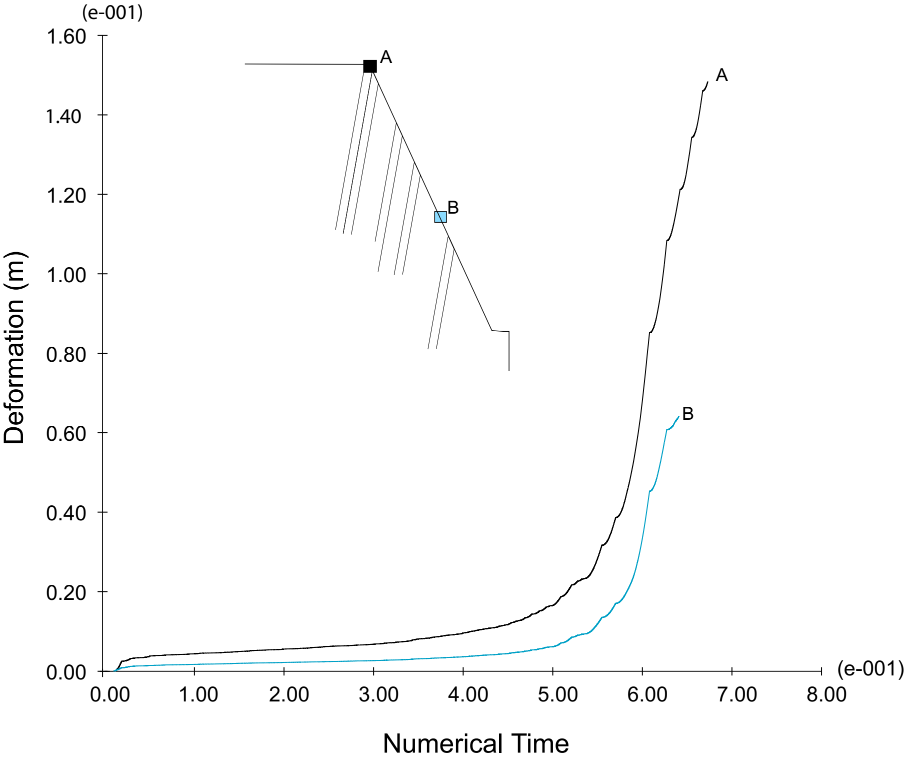

Figure 4.11: The deformation at the monitoring points at failure

perimental study failed at 80g to 85g (see Adhikary and Dyskin (2006)), while in the numerical study, the model failed at 70g. The UDEC-DM was able to predict the failure surface more accurately and in good agreement with that observed in Adhikary's experiments. Figure 4.12 shows the model at failure, in this figure another rupture surface formed at the upper part of the model because the model was allowed to deform numerically. This secondary rupturing was also observed in the physical model. Figure 4.13 shows the rupture surfaces formed inside the model as a result of this simulation.

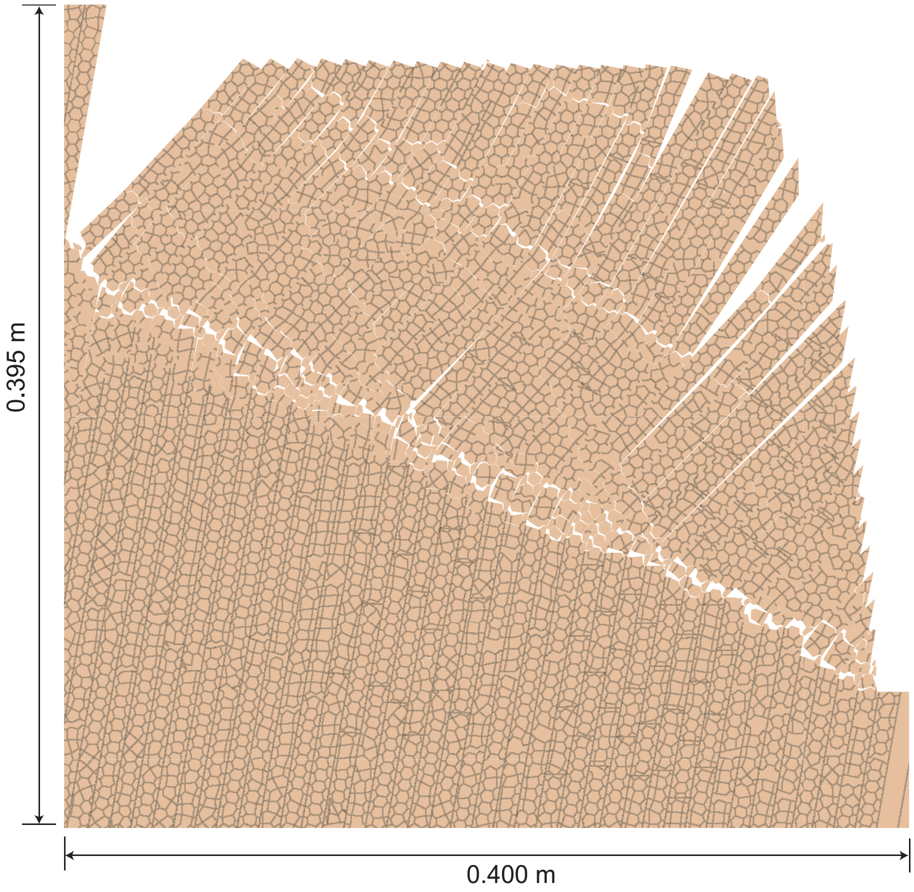

Figure 4.12: UDEC-DM simulation at failure

As was pointed out earlier, flexural toppling involves tensile (bending) stresses acting inside the rock columns. The next section discusses the tensile strength effect in further detail.

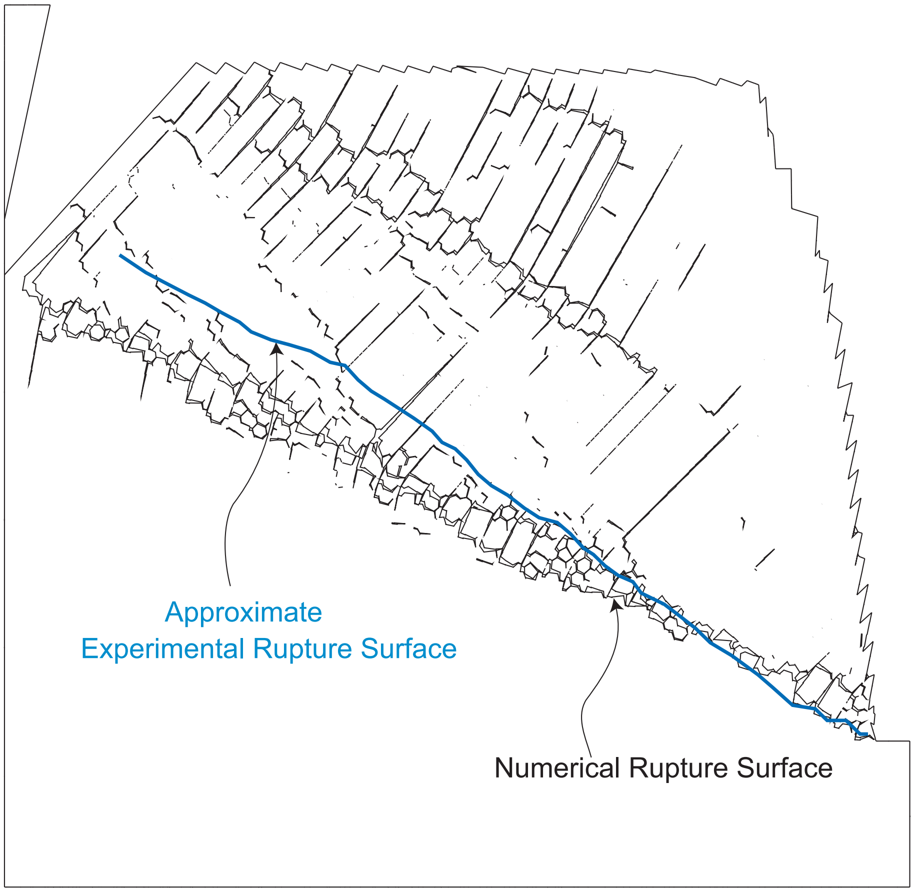

Figure 4.13: Rupture surface as predicted by the UDEC-DM model

Tensile strength's effect on the flexural toppling

Adhikary and Dyskin (2006) indicated that the tensile strength of the ilmenite-gypsum material has a range between 1.1 MPa to 1.4 MPa. To examine the tensile strength's effect on the flexural toppling, the tensile strength of the flaws was varied between 0.8 MPa and 1.4 MPa in 0.1 MPa increments.

Due to bending of the rock columns, the tensile stresses were concentrated on a hinge surface inside the rock slope. It was hypothesized that if these tensile stresses exceeded the tensile strength of the material, failure would be initiated and propagate to form the rupture surface. This hypothesis was examined by using the UDEC-DM modeling approach. Figures 4.14 and 4.15 show the horizontal displacement of the numerical models, the experimental results at different tensile strengths, and the effect of tensile strength on the failure load, respectively. As these figures show, increasing the tensile strength of the flaws caused the failure load to increase; *i.e.*, increasing the tensile strength delayed the failure, and the gravity load had to be increased to cause the failure. At a tensile strength of 1.4 MPa, the results show excellent agreement with the experimental results in terms of both the deformation patterns and the failure load. At this tensile strength, which is equal to the maximum tensile strength found experimentally by Adhikary and Dyskin (2006),the model failed at a gravity level of 82g-83g, which is within the range found in the experiments. These results show that the tensile strength is important for the flexural toppling mechanism and also that the tensile strength of the material controlled the flexural toppling failure. On the other hand, the deformation patterns remained the same, the tensile strength did not affect the deformation path. The effect of the tensile strength on the location of the failure surface was not significant and only a small difference was observed. As the tensile strength increased, the failure surface became deeper. This observation was not significant and is discussed in more detail in the next sections.

Effect of friction angle

The friction angle of the rock masses is a fundamental shear strength parameter. Jaeger (1971) in his Rankine lecture discussed the friction of rock in detail, arguing that the frictional behaviour of rocks is best described by a non-linear law. Jaeger also concluded that the primary mechanism of distortion in rock slopes is the sliding mechanism. This conclusion does not apply to toppling failure. I suggest that the primary mechanism in toppling is the bending mechanism and that the friction angle does not play an important role in the toppling mechanism. This hypothesis was tested in the discrete element damage model by varying the friction angle of the

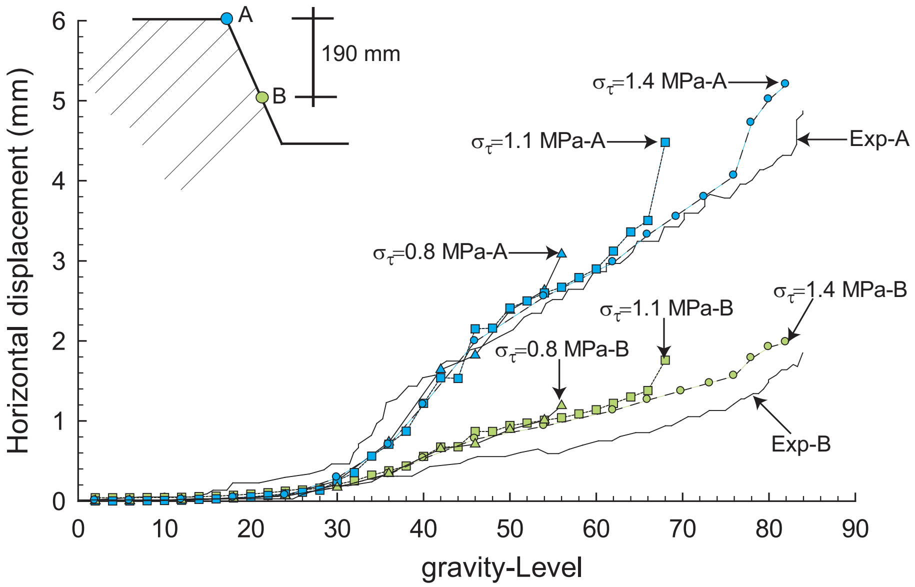

Figure 4.14: Horizontal displacement patterns with variations in the tensile strength

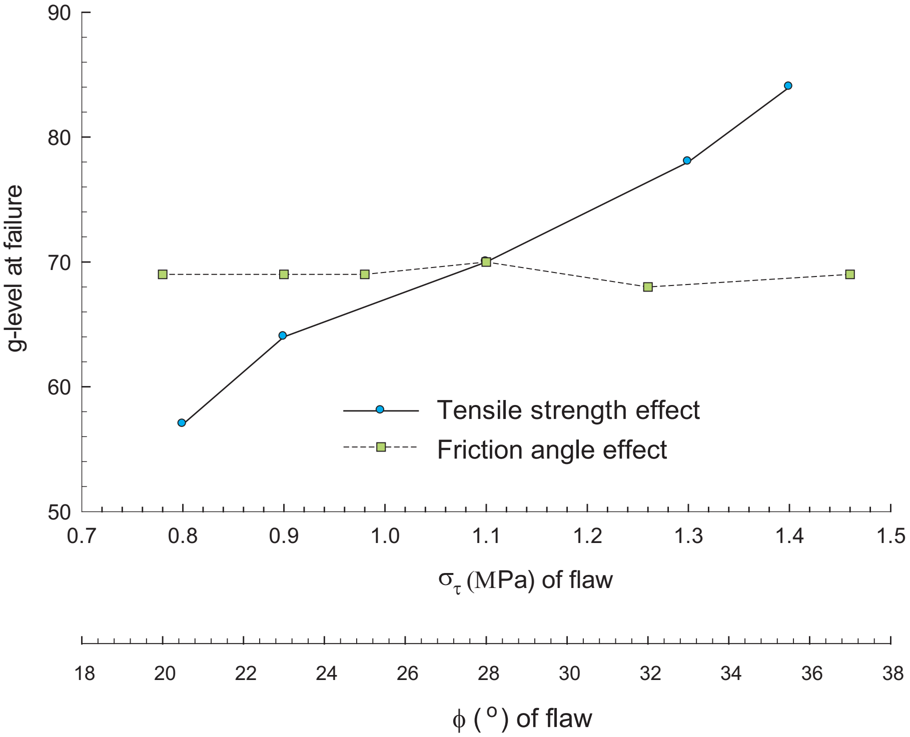

Figure 4.15: Tensile strength and friction angle of the flaws effects on the failure load

flaws.

The friction angle of the intact material (the flaws' friction angle) was assumed to be 37° throughout the previous modeling. In the modeling discussed in this section, the friction angle of the flaws was varied from 37° to 20°, and both the deformation and the failure loads were monitored to examine any effect of the friction angle on the failure mechanism. Adhikary et al. (1997a) performed direct shear tests on the bedding planes and reported that the friction angle was between 22° and 26°; thus, the friction angle of the ilmenite-gypsum mixture was more than 20°. Figure 4.16 shows the deformation pattern at three different friction angles of 37°, 32° and 25°. The deformation patterns shown in the figure are almost identical provided that k_n and k_s were kept constant. This result indicates that in toppling failure, the friction angle of the intact rock does not have a significant effect on either the deformation patterns or the failure load. Figure 4.15 shows the failure load at different friction angles. In Figure 4.15, the results show unambiguously that the tensile strength of the intact rock is of great importance and the friction angle of the intact rock does not make an important contribution to the toppling mechanism; i.e., the tensile stresses and strength control this failure mechanism. The figure also shows that the friction angle of the intact rock does not make an impact on the early stages of deformations. Although the bedding plans friction was not varied in this study, this effect should be studied in details as sliding along the beddings is essential to promote tensile stresses.

Rupture surface

In slope stability, the rupture (failure) surface is important for both back analyzing a failed slope or predicting the depth of failure in design problems. In back analysis, the failure surface has been used to compare the modeling results with the actual failure surface and to increase confidence in the numerical model. Benko and Stead

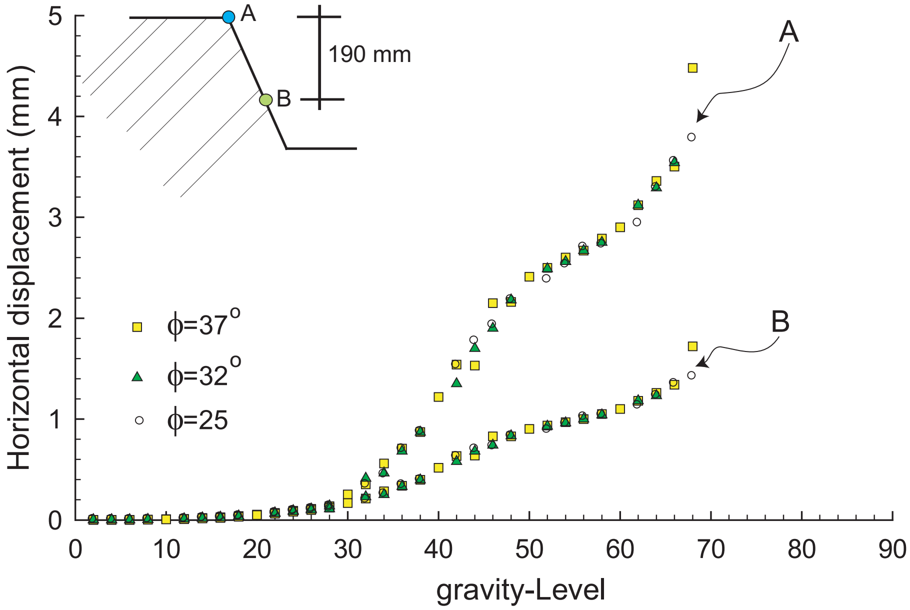

Figure 4.16: The flaws' friction angle effect on the deformation pattern

(1998), Sjoberg (1999), and Eberhardt et al. (2004) have used this approach in numerical modeling. In the limit equilibrium method, the importance of the failure surface in design problems has also been long recognized; that is, in order to install a support system for a slope, the location of the future possible failure surface should be approximately determined.

The failure surface in discontinuum modeling used to be pre-determined by the pre-existing continuous joints required to perform the conventional discontinuum analysis, this requirement is a major shortcoming of the conventional discontinuum approach. The UDEC-DM approach allows for an arbitrary failure surface to be formed and for failure to be initiated based on stresses. As the stresses exceed the strength along any flaw, failure is initiated along that flaw. The failed flaws may coalesce and form a continuous rupture surface inside the rock mass. During the use of the numerical modeling discussed in this chapter, the failure surface was continuously monitored and compared to the actual rupture surface from the centrifugel experiment. When the tensile strength changed, as mentioned before, no significant effect was found; the failure surface became insignificantly shallower as the tensile strength decreased. In all cases, the rupture surface passed through the toe of the slope. Figure 4.17 shows the failure surfaces at different tensile strengths as plotted from the opened joints and the boundary at failure. These rupture surfaces are approximate ones and do not reflect the exact match of the polygonal variation in the rupture surface.

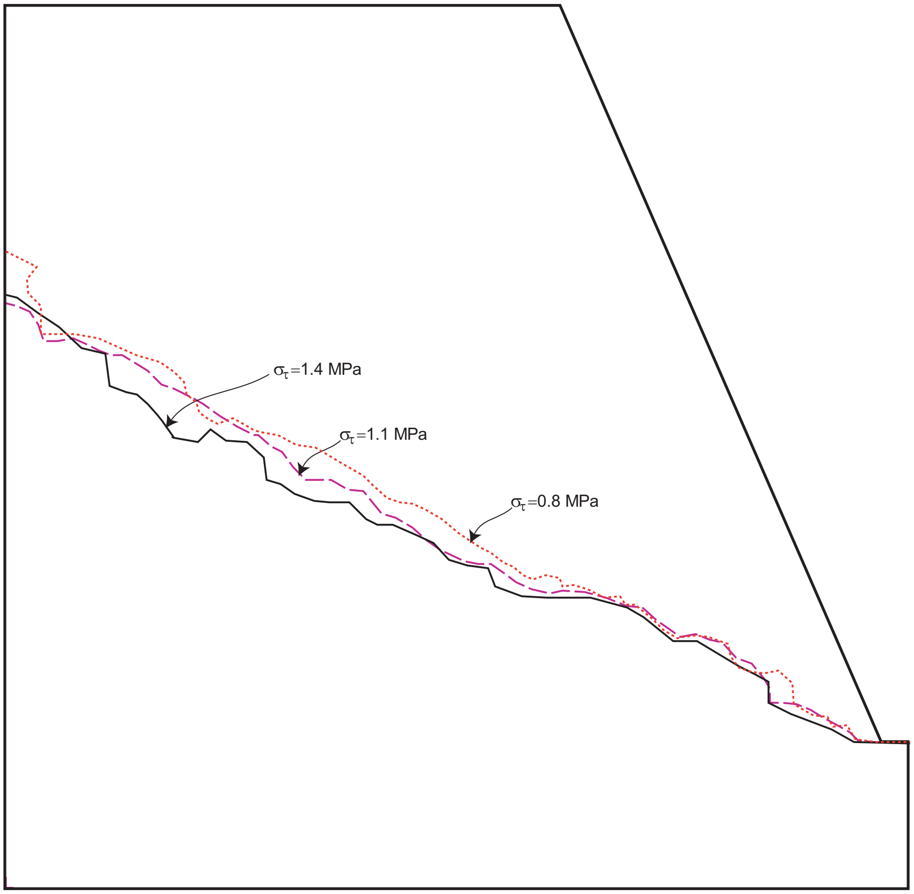

Figure 4.17: Comparison of failure surfaces at different tensile strength values (failure surface drawn based on the open joints)

In order for flexural toppling to occur, sliding of the rock columns is essential (Goodman and Bray, 1976, Adhikary et al., 1996 and Nichol et al., 2002). The cohesion of the bedding planes in this numerical model was based on the numerical modeling conducted by Adhikary and Dyskin (2006). These researchers showed that at 15 kPa of cohesion, an excellent agreement between the numerical model and the experimental results was achieved. To examine the effect of the cohesion of the bedding planes on the failure mechanism, the cohesion was varied between 15 kPa and 5 kPa at the same tensile strength of 1.1 MPa, this tensile strength was chosen for comparison purposes. This cohesion variation affected the deformation patterns, the failure load and also affected the rupture surface location. Figure 4.18 illustrates the effect of the bedding planes' cohesion on the deformation patterns compared to the actual deformation along with deformation at a bedding plane cohesion of 15 kPa. For the rupture surface at a cohesion of 15 kPa, the failure surface predicted by the numerical model was closer to the actual failure surface than the rupture surface at 5 kPa, especially at the upper portion of the failure surface. Figures 4.19 and 4.20 show the rupture surfaces formed inside the model at both cohesion values and the model at failure, respectively. The model in Figure 4.20 was not allowed to deform as much as the model in Figure 4.12 and thats why no clear secondary rupturing is observed.

As the cohesion of the bedding planes decreased, the rupture surface became deeper. A possible explanation of these results is that when the cohesion of the bedding planes decreased, the sliding occurred over more of the bedding planes and pushed the rupture surface deeper than the case when the bedding planes had a higher cohesion value, that changed the tensile stresses distribution inside the model and resulted in different locations of the failure surface. The failure load at 5 kPa, low cohesion, is around 50g, which is much lower than the failure load of 70g at 15 kPa of bedding plane cohesion. As the cohesion decreased, the sliding became easier and allowed failure to be initiated at a lower gravity level and caused higher deformation at the same gravity level compared to what occurred at the higher bedding planes cohesion. These results support the use of 15 kPa of bedding plane cohesion due to the better agreement between the failure surfaces and the defor-

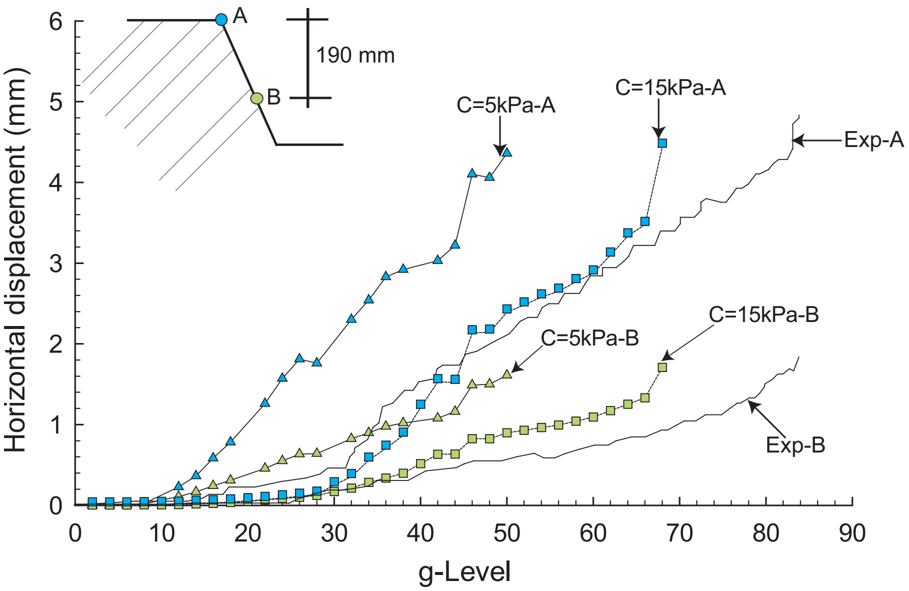

Figure 4.18: Deformation patterns from the numerical models at 15.0 kPa and 5.0 kPa of bedding planes' cohesion, along with the actual deformations from the centrifugel experiments

mation patterns . In addition, this value was used by Adhikary and Dyskin (2006), Adhikary et al. (1997a) reported their inability to determine the exact cohesion of the bedding planes experimentally, the cohesion in their model was attributed to the roughening and bonding of the paper separation sheets during sample preparation.

4.3 Longtan Hydropower Project centrifuge model

4.3.1 Introduction

Another centrifugel toppling example from the intake structure of the Longtan hydropower project was modeled numerically by using both conventional UDEC and the UDEC-DM. The centrifugel model was made of a mixture of cement, sand, water and iron-powder (Zhang et al., 2006). The natural rock slope is interbedded sandstone, argillite and siltstone. To model the geological structures, two sets of joints were used, the first one is a continuous set, dipping into the rock slope at an angle of 60°, the second set of joints is an open non-continuous one dipping in the

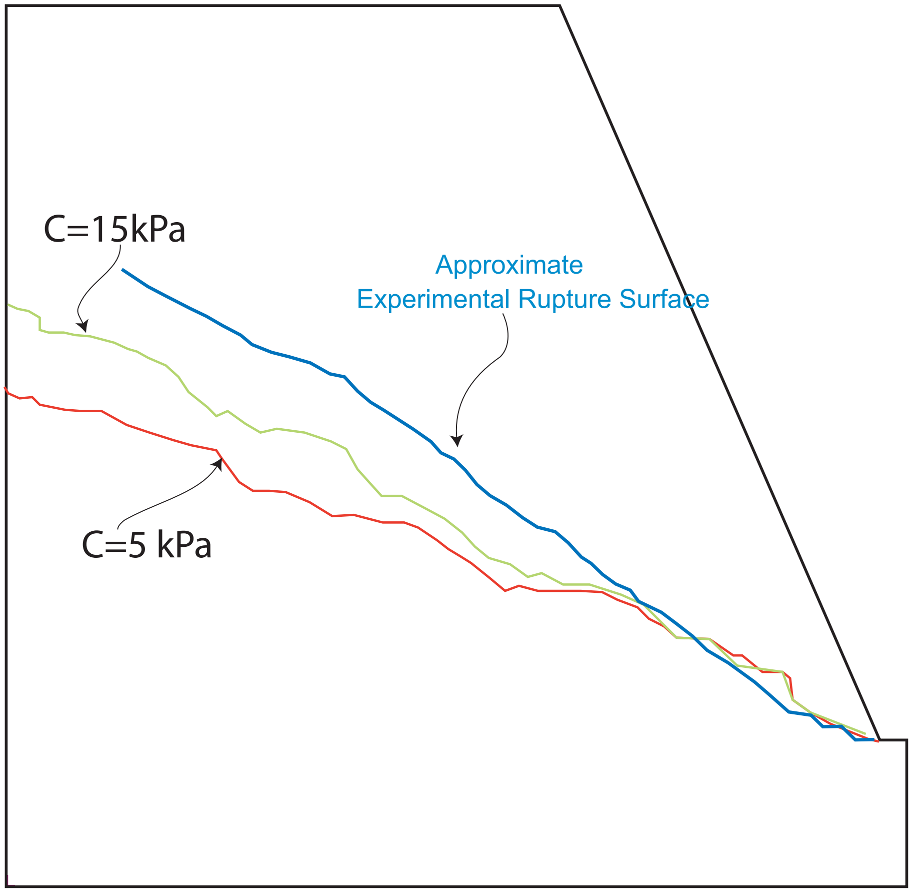

Figure 4.19: Failure surfaces at cohesions of 15 kPa and 5 kPa, along with the actual rupture surface, Tensile strength= 1.1MPa

same direction as the slope face at an angle of 60°.

Zhang et al. (2006) conducted a laboratory tests to determine the strength properties of the intact artificial rock. Table 4.2 shows the strength properties of the sand-cement mixture. The synthetic model was then subjected to gravity acceleration until failure was achieved. The model failed at a gravity level of 130g and formed a rupture surface. Figure 4.21 shows the failed model and Figure 4.22 shows a sketch of the rupture surface as a result of increasing the gravity loading. Both the conventional method and the damage model approaches were used to simulate the Longtan centrifugel experiment, to examine the gravity level at failure, and to determine the rupture surface location. The numerical results were compared to

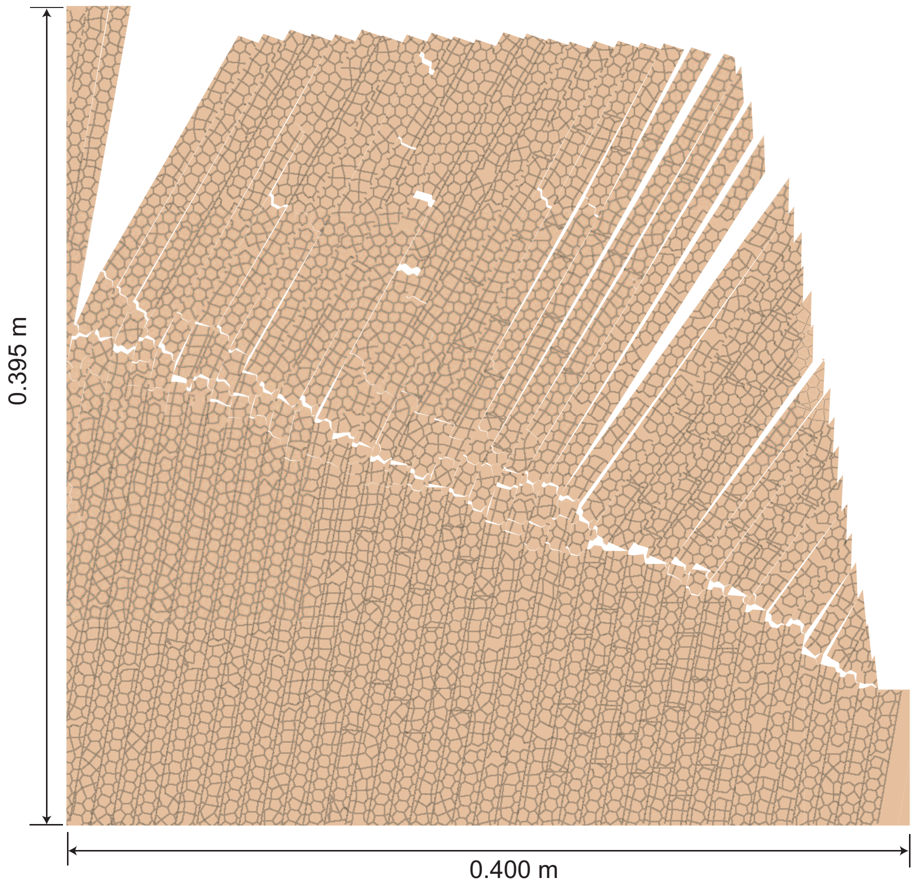

Figure 4.20: The model at failure, bedding planes' cohesion = 5.0 kPa

those from the laboratory. In this centrifugel experiment, the actual displacements in the laboratory were not measured.

4.3.2 Conventional UDEC

The conventional UDEC with both sets of joints modeled explicitly was used to simulate the centrifugel experiment. Figure 4.23 shows the geometry of the slope.

Table 4.2 shows the properties used in the simulation for both the intact material and the joints. The gravity loading was increased gradually until failure occurred at gravity level of 146g. To determine the failure load, the displacement, unbalanced forces, and the yielded elements were monitored. At 146g, the slope did not come to equilibrium and the yielded elements formed inside the model. Figure 4.24 shows

Table 4.2: Properties of the artificial rock (modified from Zhang et al., 2006)

Parameter	Column at the toe	The remaining columns
Joint persistence ratio k	0.8	0.7
Tensile strength of the jointed rock (MPa)	4.81	4.81
Friction angle of the column side (°)	37	37
Cohesion of the column side (MPa)	0	0
Friction angle of the column base (°)	0	0
Cohesion of the column base (MPa)	0.316	0.474

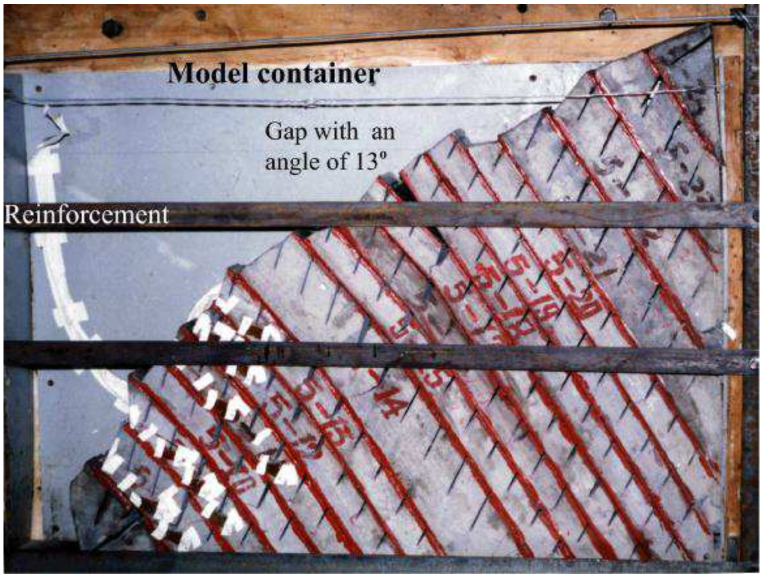

Figure 4.21: Failure of the model at 130g (modified from Zhang et al., 2006)

the model at failure, the yielded elements inside the model, and the experimental rupture surface. Notice that, the failure surface formed by the yielded elements is deeper than the experimental rupture surface. The conventional UDEC did not predict accurately the failure surface or the load at failure which was 130g. In the next section, the same experiment is simulated by using the damage model approach to examine both the load at failure and the location of the rupture surface.

4.3.3 UDEC-DM simulation

The discrete element damage model was utilized to simulate the centrifugel experiment in order to compare the results with the experimental results and the conven-

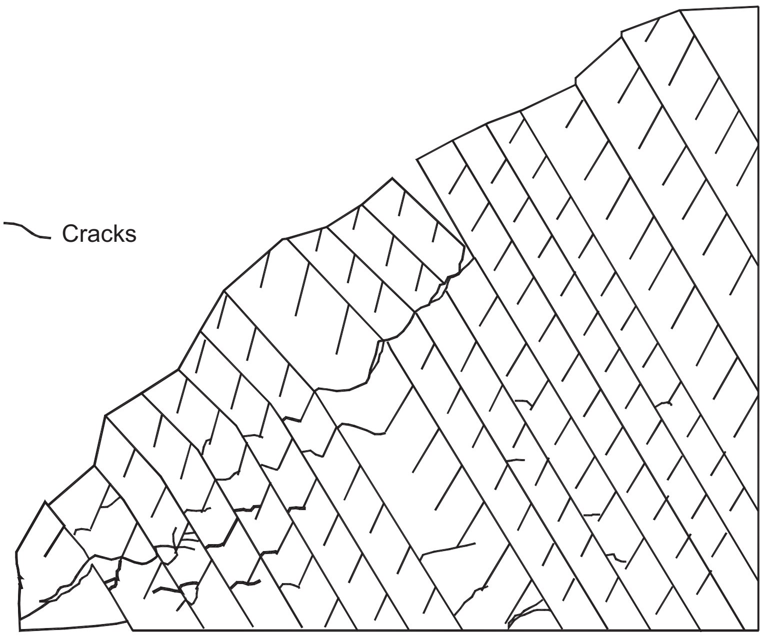

Figure 4.22: Sketch of the centrifugel model at failure (modified from Zhang et al., 2006), scale is shown in Figure 4.23

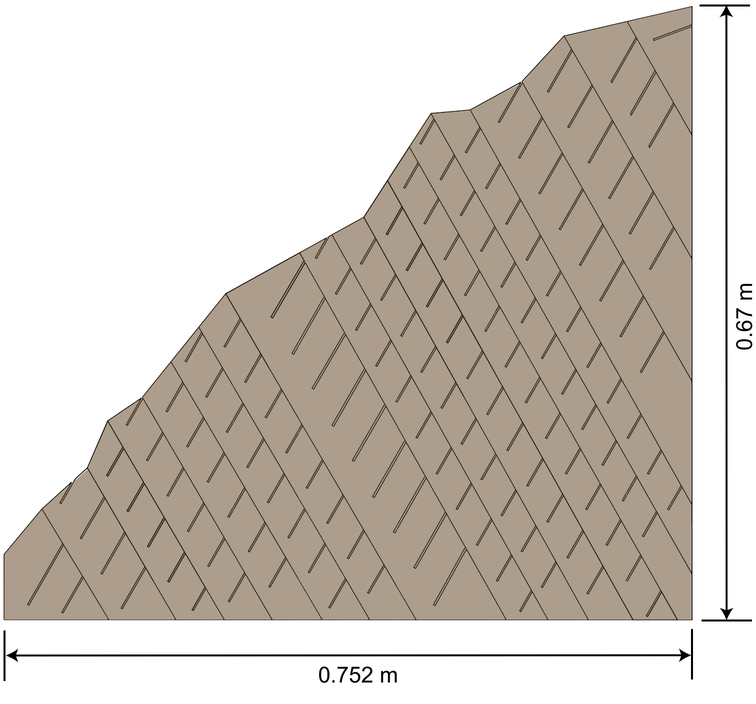

Figure 4.23: The conventional UDEC model

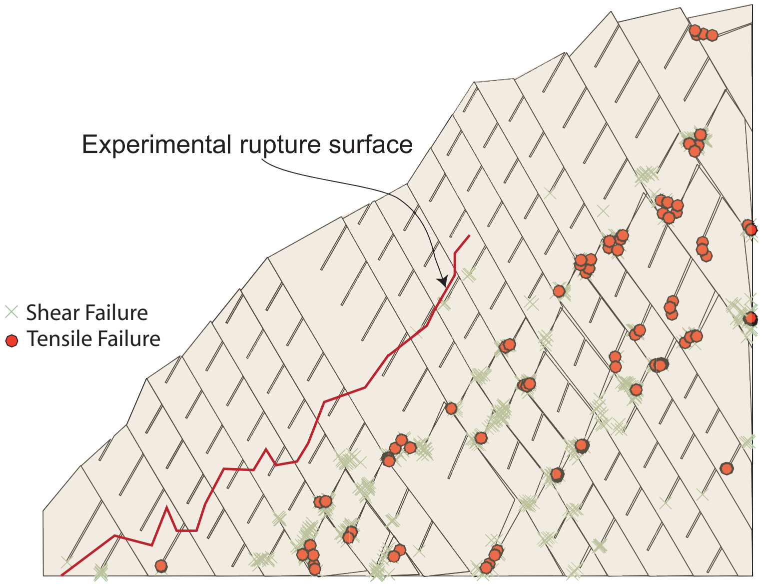

Figure 4.24: Conventional UDEC model at failure

tional UDEC results. Figure 4.25 shows the model with the flaws generated inside the artificial rock columns. The open joints were included in the model explicitly, the insert in Figure 4.25 show the details of the model and the flaws.

Table 4.3 shows the properties of the blocks and the flaws used in the UDEC-DM simulation. The normal stiffness of the flaws were derived from equation 4.9 while the shear stiffness were assumed to be 400 GPa/m. Due to lack of deformation measurements during the experimental program, these values were used and no further calibration was attempted. However, the k$_n$ and k$_s$ values in this damage model are within the same range of the values in the first toppling UDEC-DM.

Table 4.3: Elastic properties and the flaws properties used in the simulation

Parameter	
Normal Stiffness (GPa/m)	600
Shear Stiffness (GPa/m)	400
Flaws aperture (mm)	0.1
Poisson's ratio	0.25
Modulus of elasticity (GPa)	2.0
Unit weight (kN/m^3)	23.5

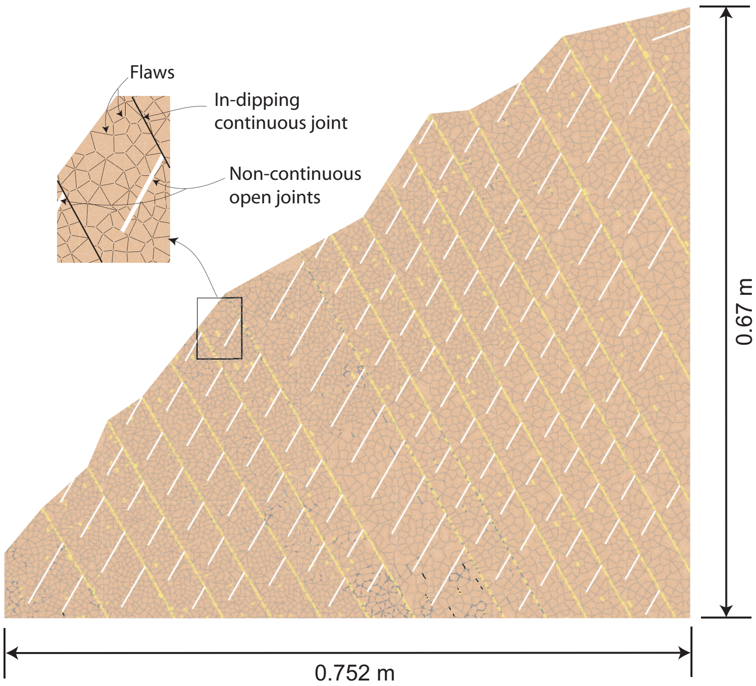

Figure 4.25: The UDEC-DM model used to simualte the centrifugel experiment

As in the conventional discrete element model, the gravity acceleration was increased gradually until failure. The model failed at a gravity level of 134g and a rupture surface was formed. At this gravity level, the damage model did not come to equilibrium and the unbalanced force increased. Figure 4.26 shows the rupture surface predicted by the damage model along with the approximate rupture surface from the experimental study. Both the rupture surface and the load at failure were in good agreement with the ones predicted by the centrifugel laboratory experiment. Notice that the rupture surface is shallower than the one predicted by the conventional discrete element model which coincides with the experimental results. As a result of stress concentrations at the joints' tip, the damage in this numerical model initiated at the pre-existing joints and propagated to form a continuous rupture surface (Figure 4.26). The degree of freedom added to the conventional discrete element method allowed initiation and propagation of non-directional rupture surface throughout the model.

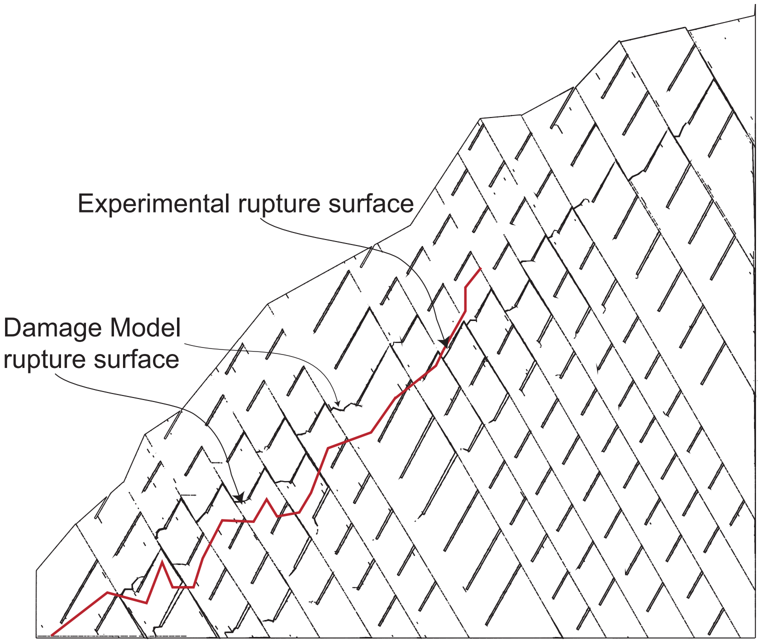

Figure 4.26: Rupture surface formation based on the UDEC-DM and the experimental one

4.4 Conclusions

The fracturing of the intact rock inside the rock masses is essential to form a kinematic admissible rupture surface. By adding a new degree of freedom to the conventional discrete element method, the rock mass was allowed to fracture and form a non-directional rupture surface.

Flexural toppling failure was investigated to verify the modeling approach and to determine the most important factors in this failure mechanism. The rock columns bent over and caused high tensile stresses inside the rock mass, in other words, as the tensile strength of the intact material increases the tensile stresses required to cause failure increases. These stresses caused flexural toppling and formed a rupture surface at a relatively high deformation, this process of rupture surface formation due to bending stresses might also occur in natural toppling slopes with few joints perpendicular to bedding. In the flexural toppling, the tensile failure mechanism is an important mechanism and should be always considered; i.e., the tensile strength should be incorporated into the design and analysis of the rock slopes at which toppling might occur.

The discrete element damage model was able to capture the toppling failure mechanism, the rupture surface formation, and the effect of tensile strength on the toppling movement. Although the conventional discrete element method gave good results, it could not capture the actual failure surface. As well, the conventional discrete element method (UDEC) was not able to capture the deformation pattern observed in the experiments. The discrete element damage model captured the transitional point of the horizontal displacement and the failure load observed in the experimental study. The discrete element damage model (UDEC-DM) also predicted the failure surface more accurately than the conventional discrete element method. The friction angle of the intact material was varied and found to have little effect on the toppling mechanism. The bedding planes' cohesion affects the deformation patterns, the load at failure, and the depth of the rupture surface.

The pre-existing joints in the Longtan Hydropower Project centrifugel model, caused stress concentrations which resulted in damage nucleation near the joints' tip and eventually formed a continuous rupture surface across the model. This numerical model presents a general approach to toppling problems in both natural and man-made rock slopes.

Chapter 5

Toppling and Buckling in Rock Slopes

5.1 Introduction

In layered rock masses, the orientation of the main set of discontinuities relative to the orientation of slope face might control the mode of movement. Different modes of rock slope movement have been observed in the field on both anaclinal and cataclinal slopes in sedimentary rocks. Cruden (2003) identified different modes of movements such as, underdip toppling, common toppling, sliding, and buckling that occurred in sedimentary rocks in the Rocky Mountains. He used a friction angle of 30° to build a process diagram to describe the type of slope movement based on the slope face and the beds' orientation.

In the following, rock slopes susceptible to underdip toppling, common toppling, and buckling are examined by using the discrete element damage model approach. The groundwater effects are not included in the following analyzes and the rock slopes are assumed to be dry. To simulate the effect of long-term processes, only the intact tensile strength is changed, and the impact of this change is tracked.

5.2 Toppling

Topples are common in steeply dipping natural and excavated slopes with distinctive layering. De Freitas and Watters (1973) introduced the term ”toppling” to describe the movements of rock slopes in rotation with steeply dipping beds. Goodman and Bray (1976) recognized three types of toppling failures: (1) flexural, (2) block, and (3) block-flexural,. In these topples, the main set of joints were thought to dip into the slope. More recently, Cruden (1989) identified underdip topples. This mode of toppling occurs when the main set of joints dip in the same direction as the slope face (see Figure 5.1). In the underdip topples, Cruden and Hu (1994) described several examples of block and block-flexural topples, concluding that in the underdip slopes, the toppling type is controlled by the discontinuity spacing and the ratio between the joint spacings of the strike joints to the bedding thickness (block ratio). Later, McAffee and Cruden (1996) discussed the effect of the block ratio and concluded that using the block ratio to identify the toppling style is very difficult due to the overlap between the different modes of toppling. McAffee and Cruden (1996) concluded that weathering, which is a time dependent process, caused the toppling to occur at the Highwood Pass (Figure 5.2).

5.2.1 Underdip toppling

Cruden and Hu (1994) reported that these topples occur mainly in bedded sandstones such as those shown in Figure 5.1. The tensile strengths of these sandstones range widely, depending on the clay and quartz contents. While no tensile testing was carried out on the Sandstones described by Cruden and Hu, tensile strengths for these rocks can be expected to range between 0.5 to 3 MPa, depending on the extent of weathering (Lockner, 1995). A slope similar to that described by Cruden and Hu with a height of 75 m was used to develop a UDEC-DM model to explore the mechanism of failure and the effect of cohesion and tensile strength degrada-

Figure 5.1: Example of an under-dip topple described by Cruden and Hu (1994). The beds are approximately 5 to 20 cm thick

tion on this mode of slope instability. The main set of joints dipped at 80°, and the slope face dipped at 61° in the same direction (see Figure 5.3). Initially, the model contained a single bedding joint set with a uniform thickness of 0.75 m. The flaws were then generated inside each bed to make the polygonal shape of the blocks more brick-like. Table 5.1 shows the assumed strength properties used in this model as no experimental studies were conducted to on these rocks to determine the tensile strength or the cohesion. Cruden and Hu (1988) tested the friction angle of these rocks and found that the friction angle can vary from 25-35°, the kn and ks were assumed the same for the flaws and the bedding.

The model was brought to equilibrium under gravity loading and then the tensile strength was decreased gradually. Griffith (1920) suggested that the cohesion of a rock was related to the tensile strength based on his experiments on brittle materials

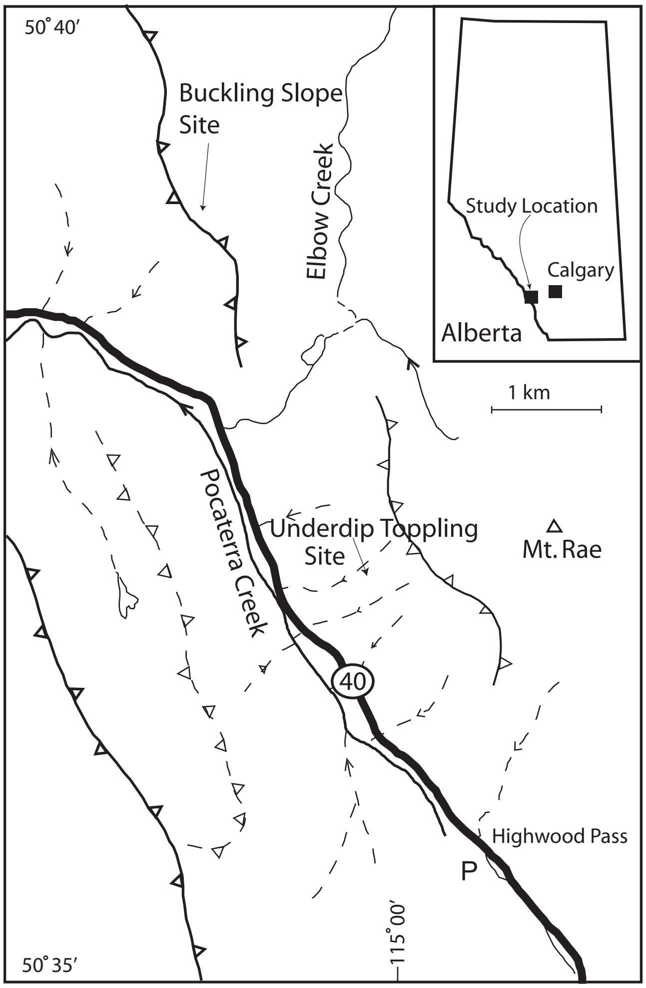

Figure 5.2: Locations in the Highwood Pass (modified from Cruden and Hu, 1994)

containing flaws. For the purposes of this underdip example, the tensile strength was decreased to trigger the failure. When the tensile strength was reduced to 10 kPa, the slope collapsed with the toppling starting at the toe of the slope and gradually extending back into the slope (see Figure 5.4), notice the amount of dilation in at the toe of the slope which indicates that dilation in essential in the rock masses movements to allow the development of rupture surface, the flaws were important to allow this dilation.

Cruden and Hu (1994) suggested that the block ratio in the underdip slope plays an important role in the toppling mechanism. Figure 5.4 shows the results with

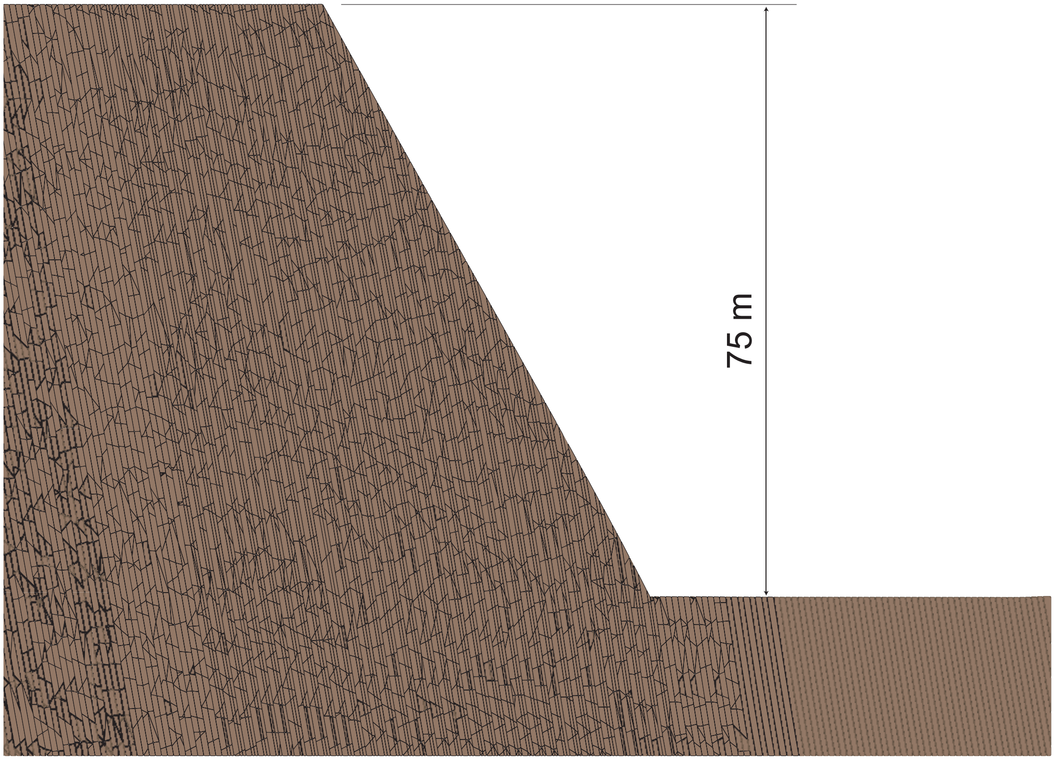

Figure 5.3: Geometry of the underdip toppling example

a constant block ratio. Figure 5.5 shows the underdip toppling failure with non-uniform bedding. With non-uniform bedding, the resulting failure is more comparable to the actual failure observed in the field and shown in Figure 5.1. Cruden and Hu (1994) reported that in these underdip topples, the thickness of the toppling is in the order of 15-m, this thickness was also observed in this UDEC-DM example.

Table 5.1: Material properties used in modeling of the underdip example

Property	Underdip Topple
$\phi(^{\circ})$ of beddings	25
Tensile strength (kPa)	60
Cohesion (MPa)	0.6
$\phi(^{\circ})$ (intact material)	30
Kn (GPa/m)	1
Ks (GPa/m)	0.1

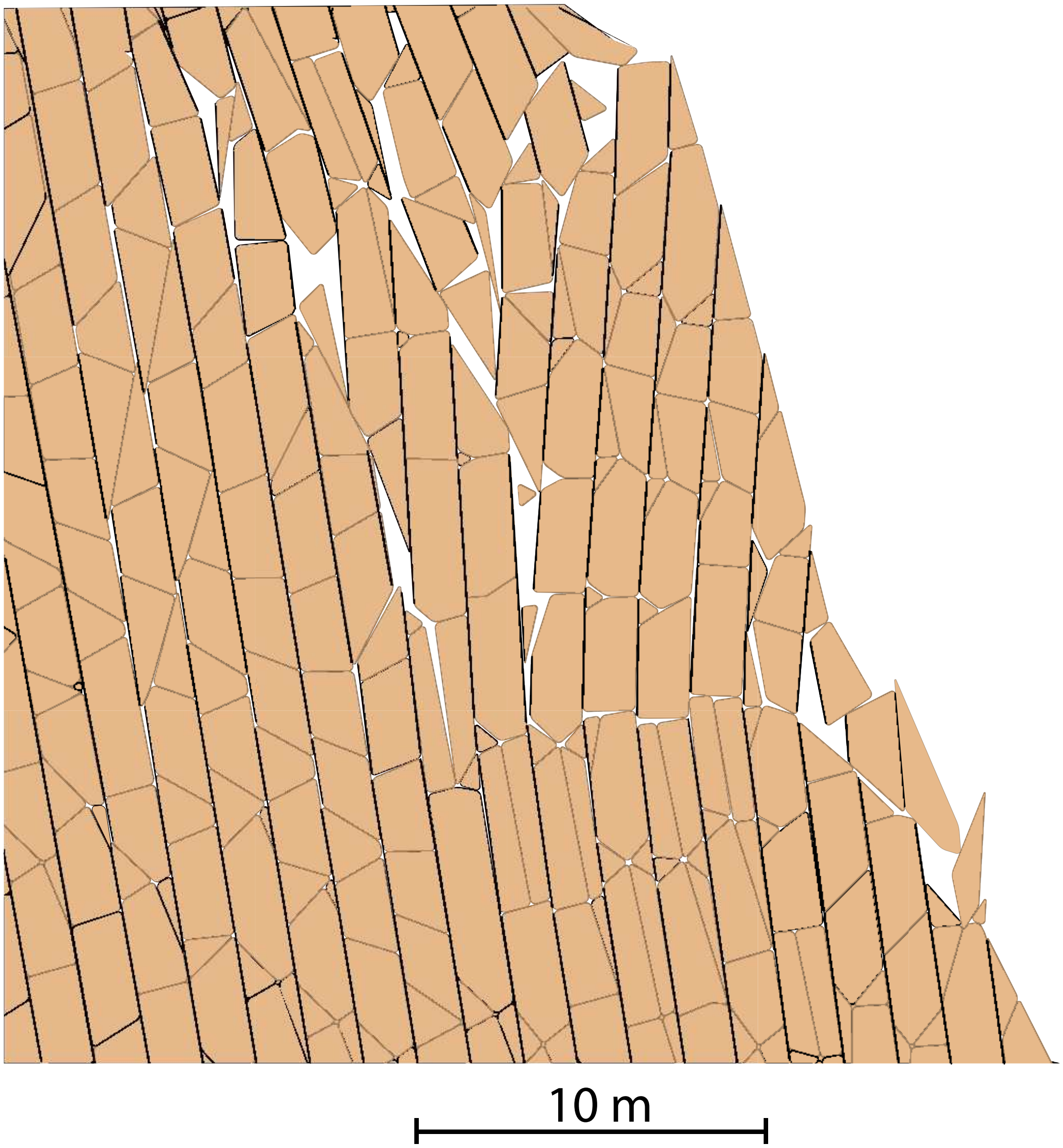

Figure 5.4: Initiation of toppling at the slope's toe (uniform bed thickness)

5.2.2 Common toppling

Topples where beds dip into the slope are more common in natural and man-made slopes with one set of discontinuities dipping steeply into the rock slope than the underdip topples discussed above . Topples of this nature have been reported at scales ranging from several metres high to several hundred metres high in large open-pit mines (Tosney et al., 2004, Sjoberg, 1999). The simulations by Tosney et al. (2004)

Figure 5.5: Underdip slope failure using the UDEC-DM (non-uniform beds)

and Nichol et al. (2002), using conventional UDEC, required the placement of discrete cross joints as well as the bedding joints to simulate toppling failure. Using their approach, the movement kinematics are defined by the geometrical constraints built into the model. In the UDEC-DM the failure mode evolves with deformation and does not follow a predefined failure surface constrained by the input geometry. As Cundall (2001) noted, the major advantage of the discrete element logic is that the failure process does not have to be constrained by the model geometry or complex constitutive models. If properly formulated, the failure process and rupture surface should develop unconstrained as deformations occur. Toppling occurs in slates, schists, regularly-jointed granites, phyllites, sedimentary rocks and others. As shearing and sliding along the steeply inclined discontinuities start, the rock layers bend and tilt, forming tension cracks at the crest of the slope and obsequent scarps at the surface of the slope. The effect of tensile strength versus the effect of the frictional strength is examined by using the UDEC-DM approach. The effect of the layer thickness and slope height on the tensile strength at failure is also discussed.

The Numerical Model

Figure 5.6 shows the UDEC-DM model used to simulate common toppling, and the material properties used in the analysis are provided in Table 5.2. In the model only the bedding planes are provided as through-going discontinuities. The cross-cutting joints are treated as internal flaws with the same properties as intact rock. The numerical model in this section is based on the general toppling model proposed by Nichol et al. (2002). Figure 5.6 shows the model, in which one set of discontinuities dipping into the slope at an angle of 80° from the horizontal were installed. To produce the three different models analyzed in this study, three discontinuity spacings (6m, 3m, and 1.5m) were used to vary the rock layers' thickness. The material was simulated as network of flaws inside the rock layers. The edge length of the flaws was the same for all three numerical models. As shown in Figurer 5.6, the flaws were implemented in the dark shaded area as shown in the same figure. The flaws were generated inside this zone to study the intact rock tensile strength effect and not to study the extension of toppling at the back of the slope. Moreover, generating more flaws inside the model was time consuming which is one of the limitations of this approach. Although in nature cross-joints would be expected, these cross-joints might be widely spaced. So fracturing through intact material would be essential to form admissible rupture surface. The Coulomb-slip model were used to control the flaws' behaviour, and the blocks formed by the flaws were assigned the following elastic properties: *modulus of elasticity* (E) = 20 GPa and *Poisson's ratio* (ν) = 0.25. Numbers 1 to 12 in the figure are the excavation stages used to increase the height of the slope. This aspect of modelling will be discussed later in the layer thickness versus tensile strength section. In the following, the effect of the intact rock tensile strength on the formation of rupture surfaces is discussed.

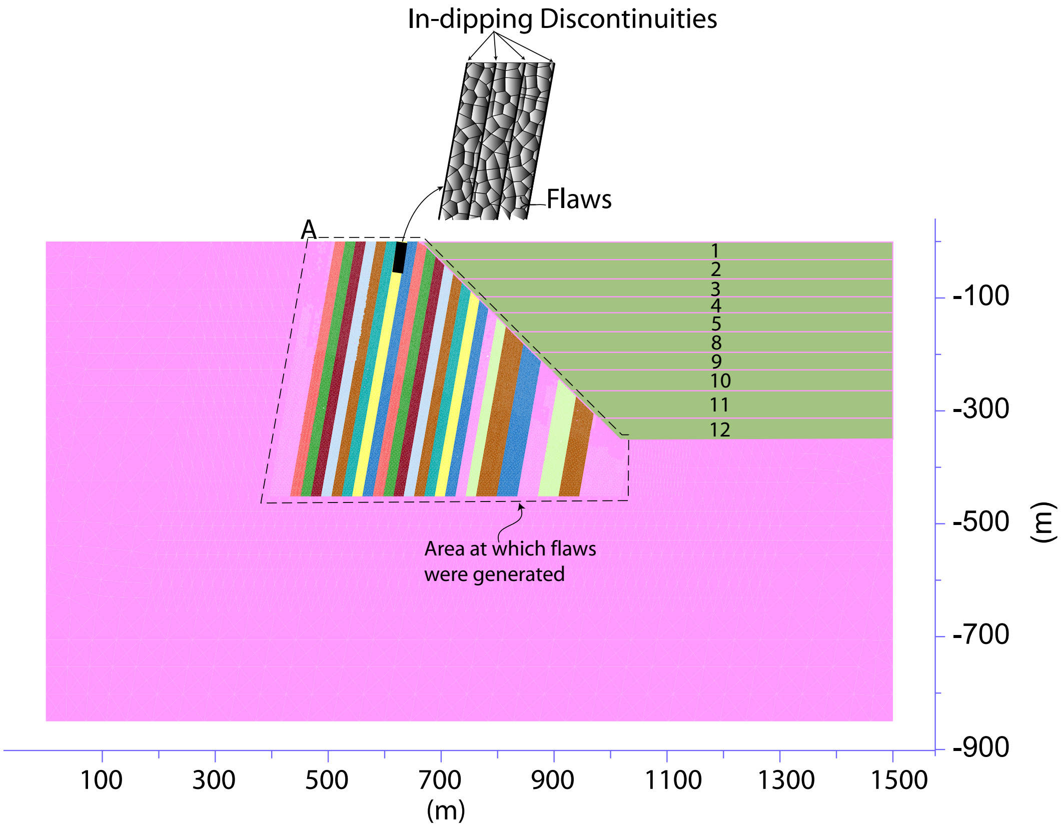

Figure 5.6: The model used for common toppling failure analysis using the UDEC -DM model

Tensile strength versus frictional strength of the rock layers

To bring the numerical model (6m-model) to equilibrium under gravity loading, high strength values were assigned to prevent yielding at the early stages of the modeling process. The slope was then excavated (1-12 blocks in Figurer 5.6 re-

Table 5.2: Initial strength and deformation properties used in the UDEC-DM

Property	Flaws	indipping discontinuities
$\phi°$	30	30
C (MPa)	5	0
σ_t (MPa)	1	0
Kn(GPa/m)	40	10
Ks(GPa/m)	20	1

moved together), and more realistic properties were assigned to the model. Table 5.2 shows the strength and deformation properties for the flaws and the joints. This model was analyzed to back-calculate the strength properties required to stabilize the model (to prevent a continuous rupture surface formation). As a result of using the properties in Table 5.2, the rock columns bent forward, and a rupture surface formed inside the rock mass. Figure 5.7 shows the rupture surfaces inside the model. A principal rupture surface formed at the base of the topple and several secondary rupture surfaces formed as toppling progressed. Small roughness in the rupture surface due to the polygonal nature of the blocks was noticed, smaller polygonal blocks would probably produce less rough rupture surface. It is important to investigate this factor in future researches.

To stabilize the model and prevent rupture surface formation, the friction angle of the flaws was increased from 30° to 50° in 5° increments, and the model was re-run from stable status. Increasing the intact material friction angle did not prevent the rupture surface formation, i.e., changing the friction of the intact rock had essentially no effect on the rock mass toppling strength. It is important to realize that the friction angle of the bedding is a key factor in this sliding mechanism unlike the intact rock friction angle. For example, increasing the friction angle of the bedding to 40° would prevent toppling to initiate, because sliding along these bedding is the driving mechanism and it is not allowed at this relatively high friction angle. Another attempt was made by increasing the cohesion of the flaws from 5MPa to 15 MPa in 1 Mpa increments and re-running the model from stable status. This attempt

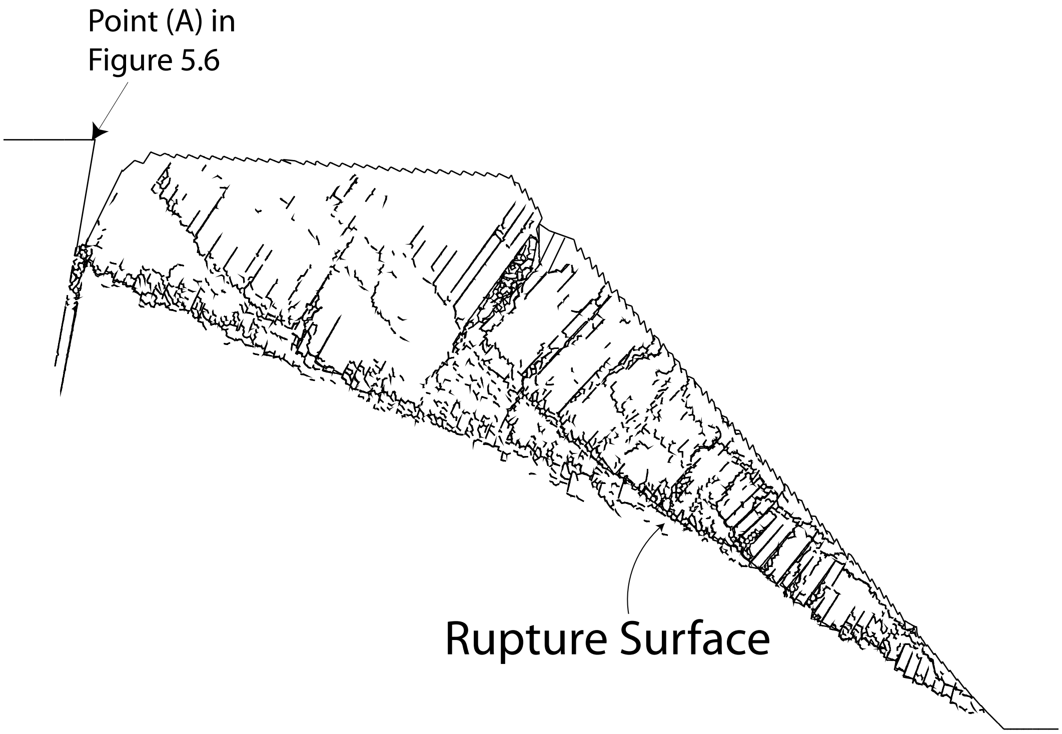

Figure 5.7: Rupture surfaces formation inside the UDEC-DM

was also not successful in preventing the rupture surface from forming inside the model. The final attempt was made by increasing the tensile strength of the flaws from 1 to 7 MPa. At a tensile strength of 7 Mpa, no rupture surface formed inside the model and the slope had a state of limiting equilibrium. The tensile strength of the intact rock was then degraded from 7 MPa to 6.8 MPa. When the intact rock reached a tensile strength of 6.8 MPa, a through-going rupture surface formed (see Figure 5.8), and the rock slope moved in the toppling mode. Notice the formation of obsequent scarps at the slope surface as a result of the toppling movement which has been reported in the literature (i.e.,Tosney, 2001) . According to Cruden and Varnes (1996) classification, this toppling movement might be called a ”Chevron topple”. This extensive numerical modeling parametric study showed that if sliding along the steeply dipping discontinuities is allowed, the block-flexural toppling behaviour is dominated by the tensile strength and a continuous rupture surface was formed as the stresses inside the rock slope exceeded the tensile strength. Cho et al. (2008) shows that the development of a shear zone inside a rock mass is controlled by tensile fracturing.

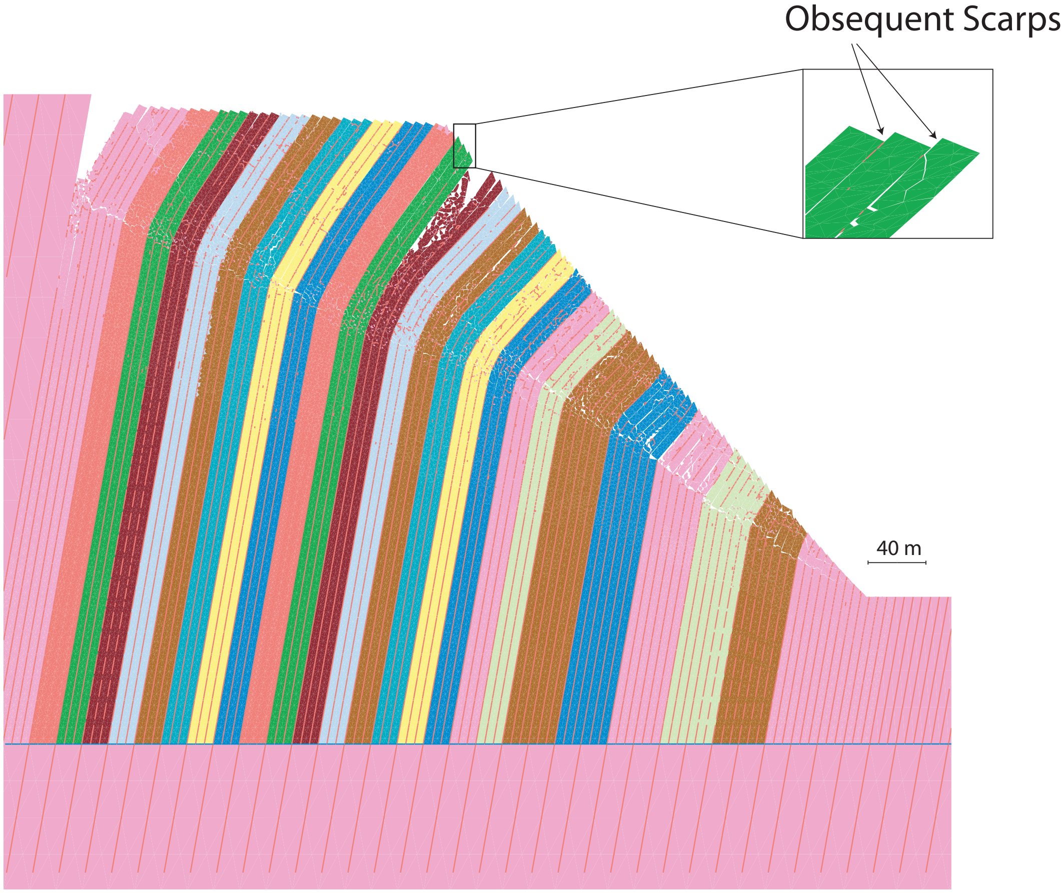

Figure 5.8: Common toppling failure using the UDEC-DM model

Figure 5.8 shows an advance stage for common toppling in the UDEC-DM, in the upper part of the slope a zone of extensive fracturing formed due to the progressive nature of this toppling mode at which the lower rock layers topple and then followed by the upper layers. As is commonly associated with toppling, the model shows extensive dilation before complete collapse and this is one of characteristics of rock mass movements. This result is also reflected in the monitored displacements shown in Figure 5.9. The displacements were monitored at two points in the model: (1) the top of the slope and (2) the toe of the slope. These points were chosen to understand the movement trend and not for comparison purposes as no real data was available. The displacements associated with these monitoring points once the tensile strength reached 6.8 MPa are shown in Figure 5.9, which shows that the displacements at the top of the slope were considerably larger than the displacements at the toe of the slope. This finding is consistent with a toppling mode of movement. The deformation pattern in the previous figure is not related to excavation stages but rather to the nature of toppling movements development and the progressive nature of the failure. The effect of the layer thickness on the tensile strength at failure is discussed in the following.

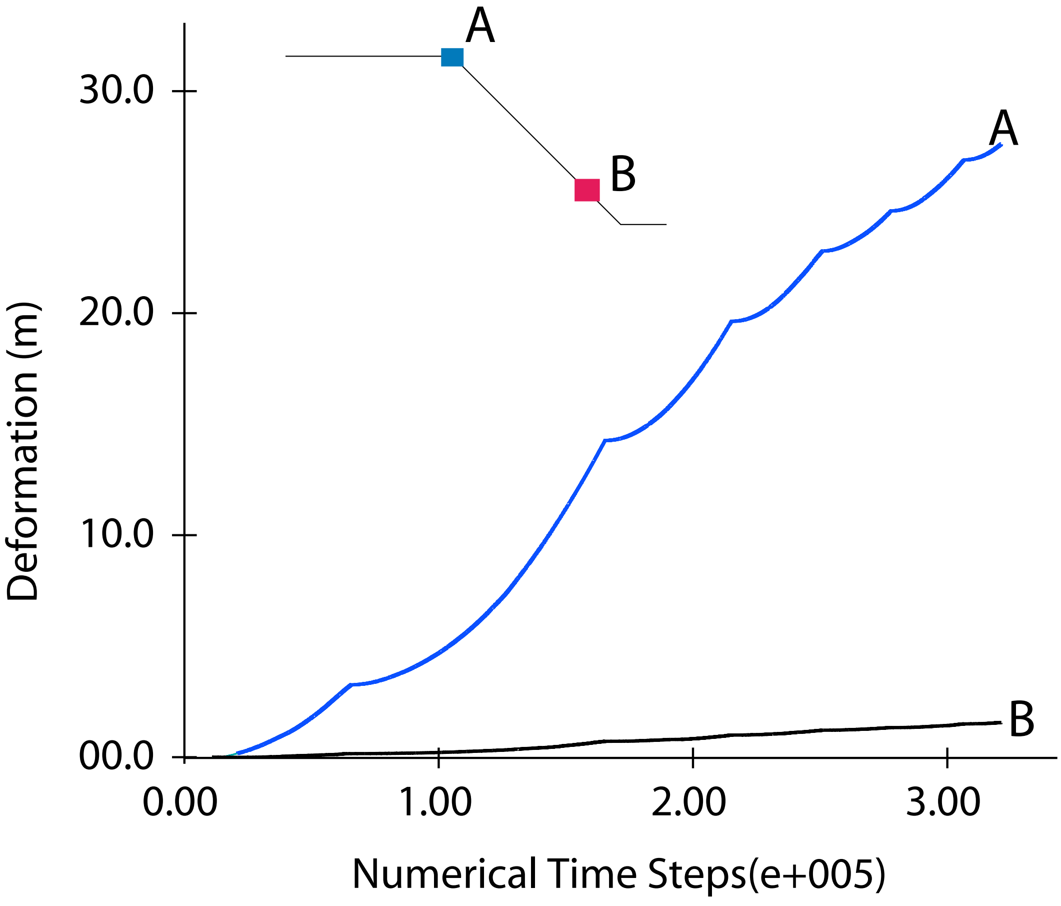

Figure 5.9: Deformation pattern observed in the block-flexural model for two points

Tensile strength and the layer thickness

As mentioned earlier, three models with three layer thicknesses (6m-model,3m-model, and 1.5m-model) were prepared to examine the layer thickness effect on the tensile strength required to prevent formation of a rupture surface inside the model. Figure 5.6 shows the UDEC-DM flexural-toppling model prior to excavation. The modeling process was conducted as follows:

1. High-strength properties were used to bring the numerical model to the equilibrium state under gravity loading.
2. The properties shown in Table 5.3 were assigned to the model based on the analysis in the previous section.
3. The model was allowed to cycle until the new equilibrium state was reached.
4. The slope was excavated block by block (blocks 1 to 12 in Figure 5.6). After each block was removed, a search for a new equilibrium state was conducted while monitoring the rupture surface formation.

By excavating the slope, the height of the slope was increased gradually. At each new slope height, the model was monitored to detect if a rupture surface had formed. This defines the critical slope height; if not, the subsequent layer was removed. The tensile strength was varied between 1 MPa to 5 MPa in 1 MPa increments. The above-mentioned modeling procedure was repeated for each value of the tensile strength and for each model (the 6m-model,3m-model, and 1.5-model). Figure 5.10 shows the results of this parametric study.

As Figure 5.10 shows, as the layer thickness decreases, the tensile strength required to prevent a rupture increases. The gradient of the lines connecting the points of each layer thickness in Figure 5.10 is not the same for different layer thicknesses. The layer thickness is important factor in toppling movement, Tosney et al. (2004)

Table 5.3: Strength and deformation properties used to study the layer thickness effect

Property	Flaws	Joints
$\phi°$	42	30
C (MPa)	14	0
σ_t (MPa)	1	0
Kn(GPa/m)	40	10
Ks(GPa/m)	20	1

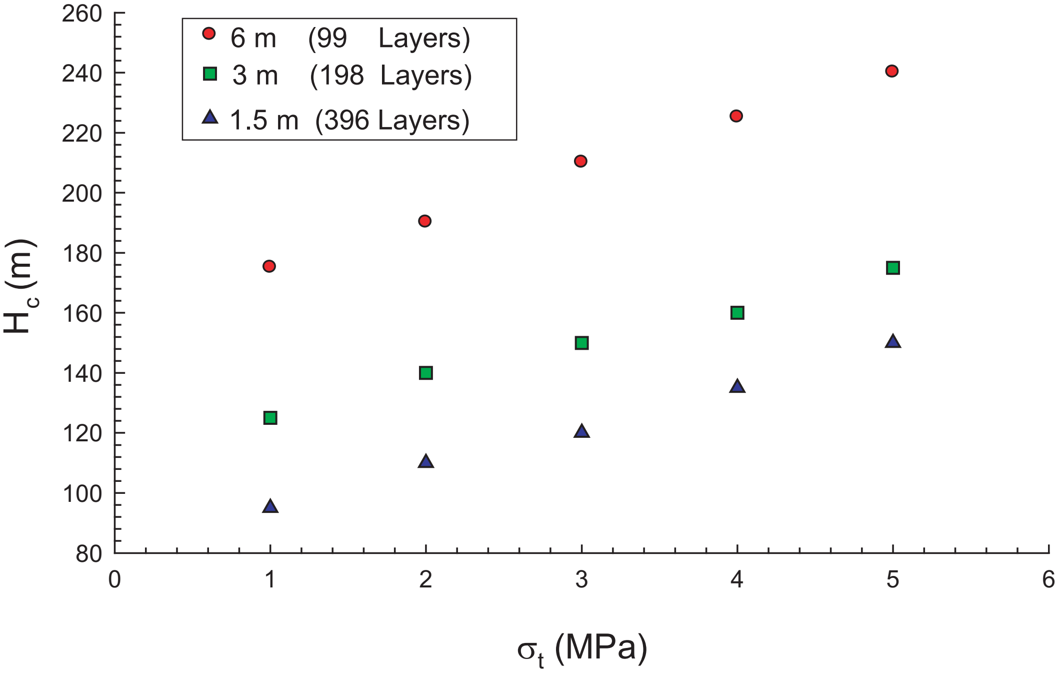

Figure 5.10: Critical slope height (Hc) for rock masses with different layer thicknesses and tensile strengths

showed that rupture surface formation was not observed in Lornex Pit in British Columbia, Canada. The layer thickness in this pit is between 20-40 m, this case history is discussed in Chapter 6 of this thesis. The figure also shows that as the tensile strength increases, a higher slope can be achieved prior to rupture surface formation. The tensile strength delayed the formation of rupture surfaces.

5.3 Buckling failure

5.3.1 Introduction

This type of movement forms folds near ground surfaces. Both natural and man-made slopes experience buckling movement. Harrison and Falcon (1936), Nemcok et al. (1972), Brawner et al. (1971), Cavers (1981), Hu and Cruden (1993), and Cruden and Varnes (1996) have described this type of movement in natural and man-made slopes. Limit Equilibrium methods is usually used to analyze these rock slopes and calculate the factor of safety assuming rigid body movement and no dilation is allowed (see Dawson, 1990). Stead and Eberhardt (1997) described the buckling of footwall slopes in surface coal mining and used discrete element modeling to analyze the footwall slopes. The buckling movements generally occurred in steeply dipping slopes with discontinuities parallel to the slope face.

5.3.2 Buckling failure in open-pit coal mines

One of the commonly observed failure mechanisms in open-pit coal mines in dipping layered rocks is buckling of the layer near the toe of the slope (Stead and Eberhardt, 1997). They reported that the failure is restricted to layers that are less than 10 m thick and suggested that this mode of failure involves both shear and tensile fracturing. Figure 5.11 shows the geometry of the slope used in the UDEC-DM model. The slope is similar to that used by Stead et al. (2004b), with a height of 75 m with a 30° slope angle. A layer with a thickness of 3.5 m was assigned a basal friction angle of 20° based on the suggestions by Stead and Eberhardt (1997). The intact layer had the properties listed in Table 5.4, and the tensile strength was gradually reduced everywhere in the layer until instability occurred. The normal and shear stiffnesses for both the flaws and joints were assumed the same. As observed by Stead and Eberhardt (1997), the instability occurred as buckling at the lower third of the slope face from the toe of the slope.

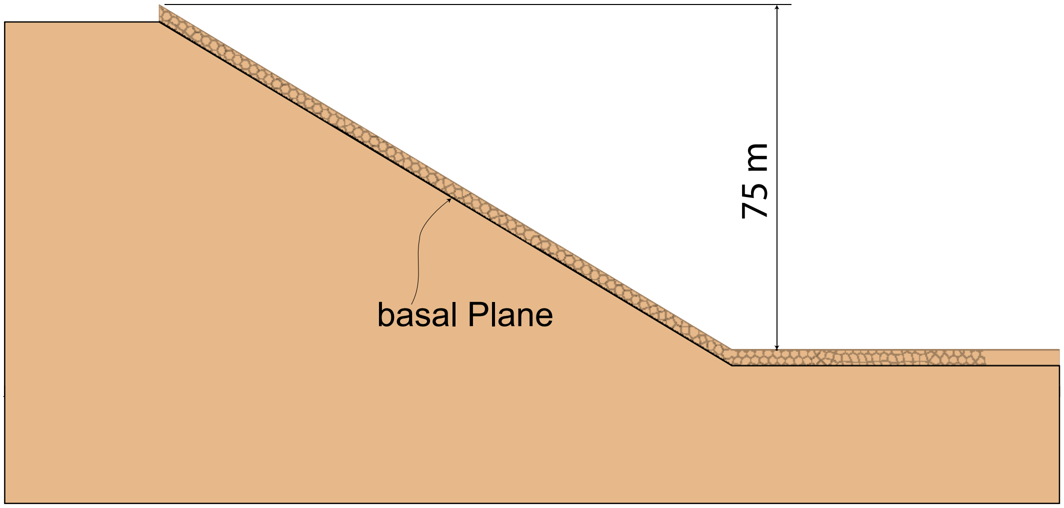

(a) Geometry of the slope

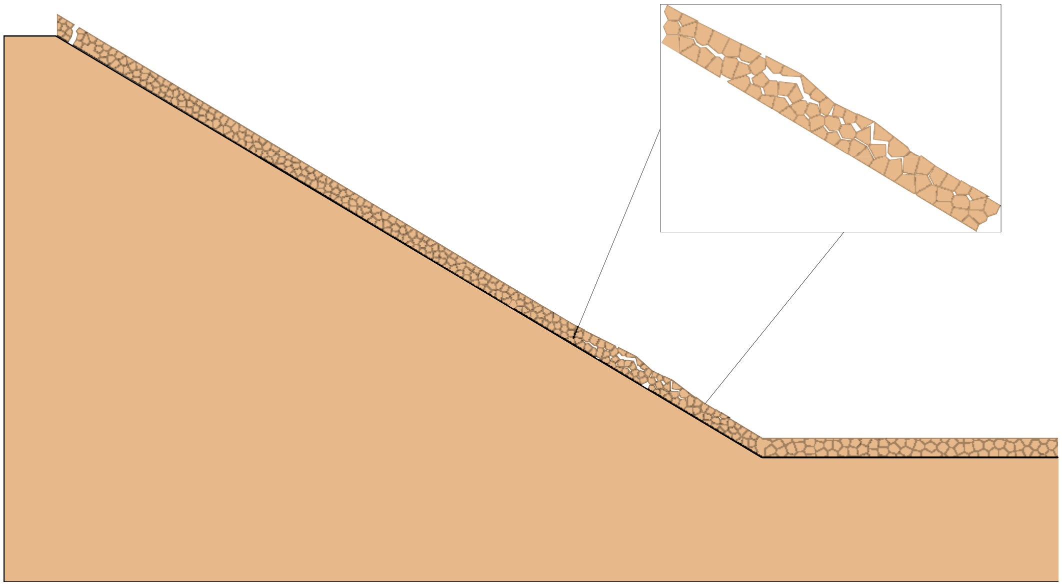

(b) Buckling failure

Figure 5.11: Buckling failure: (a) The Model, (b) failure initiation at the toe of the slope.

Table 5.4: Material properties used in modeling of the open-pit buckling examples.

Property	Buckling
ϕ(°)(basal plane)	20
Cohesion (MPa)	0.3
Kn (GPa/m)	1
Ks (GPa/m)	1
Intact tensile Strength (MPa)	0.03
ϕ(°) (Intact material)	25

Figure 5.11b shows the final failure after the tensile strength of intact rock was reduced from 30 kPa to 10 kPa. The amount of displacement associated with the buckling is directly related to the reduction in tensile strength and hence the process once initiated continues provided the tensile strength continues to degrade. Rupture of the intact rock occurred when the tensile strength reached 10 kPa at the toe as shown in figure 5.11b. This value is within the range of the tensile strength of the coal suggested by Lockner (1995). For the movement to occur as shown in Figure 5.11, the friction angle of the basal shear plane must be sufficiently low to allow sliding to occur once the toe of slope starts to rupture. This complex mobilization of shear strength is similar to that captured by Lajtai (1969c) in his experiments described in Chapters 2 and 3.

In a mining environment, the displacements due to excavation unloading and blasting-induced damage may cause the loss of tensile strength used in the UDEC-DM model. Once the instability is triggered, rupture along the basal slip surface occurs and the buckling of the slope toe is observed. While the complete process involves both shear and tensile strength degradation mechanisms, the process in the UDEC-DM model is controlled by the tensile strength degradation.

5.3.3 Buckling in natural rock slopes

Description of the Site (site 1, Hu and Cruden 1993)

Hu and Cruden (1993) observed buckle strata in the Highwood Pass in Alberta (Figure 5.2) at four buckling locations. These buckles were mainly in the sedimentary rocks of the Mississippian Rundle Group, the Permo-Pennsylvanian Rocky Mountain Group and the Triassic Spray Group (Hu and Cruden, 1993). Hu and Cruden (1993) carried out detailed joint mapping for the four sites and found four joint sets; strike joints, dip joints and two other joint sets, which were perpendicular to the bedding planes (stereonet of the joints is shown in Hu and Cruden, 1993). Figure 5.12 and Figure 5.13 shows a buckling example (site#1, Hu and Cruden ,1993). No experimental programs were conducted to estimate the tensile strength or the cohesion of the intact rock. Although groundwater flow might play a role as driving mechanism in this site, the groundwater effects are not included and the rock slope is assumed to be dry.

This rock slope consists of the Rocky Mountain Group and the Rundle Group. The slope is about 100 m in height, and the beds dip 84° in the same direction as the slope face. The beds buckle at two locations: at the foot and the middle of the slope. According to Hu and Cruden (1993), the slope consists of intact quartzite beds with few cross-joints at the surface, and the buckled beds are around 0.7 m thick. The inner beds are limestone beds with a thickness of about 0.3 m and cross-joints at spacing of about 0.4 m.

The Numerical modeling

The UDEC-DM was utilized to build a geological model of the buckle. Rock columns were generated with spacing between 0.4-1.2 m thick in the surface layers and kept constant at 0.7 m in the inner limestone layers. The beds and the slope face dipped at 84° from the horizontal. To model the intact Quartzite, the UDEC-DM was used to generate blocks inside the surface rock columns with an average edge length of 0.2 m, this value was kept constant regardless of the bedding thickness. The variation in relative edge length to column spacings was not investigated and

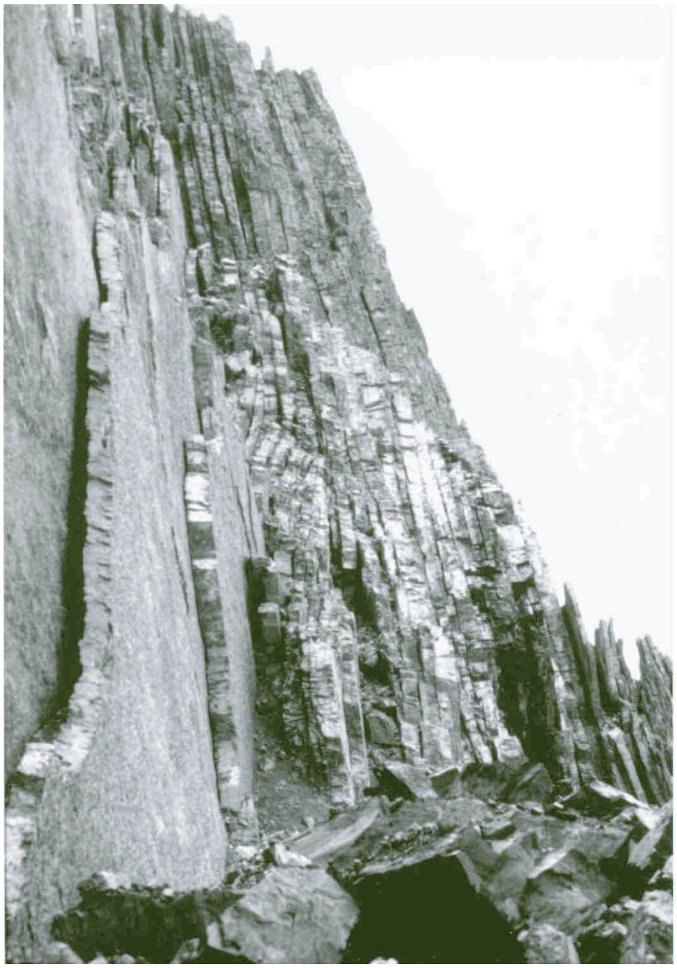

Figure 5.12: Buckling in natural rock slope at the Highwood Pass (modified from Hu and Cruden, 1993, scale shown in Figure 5.13)

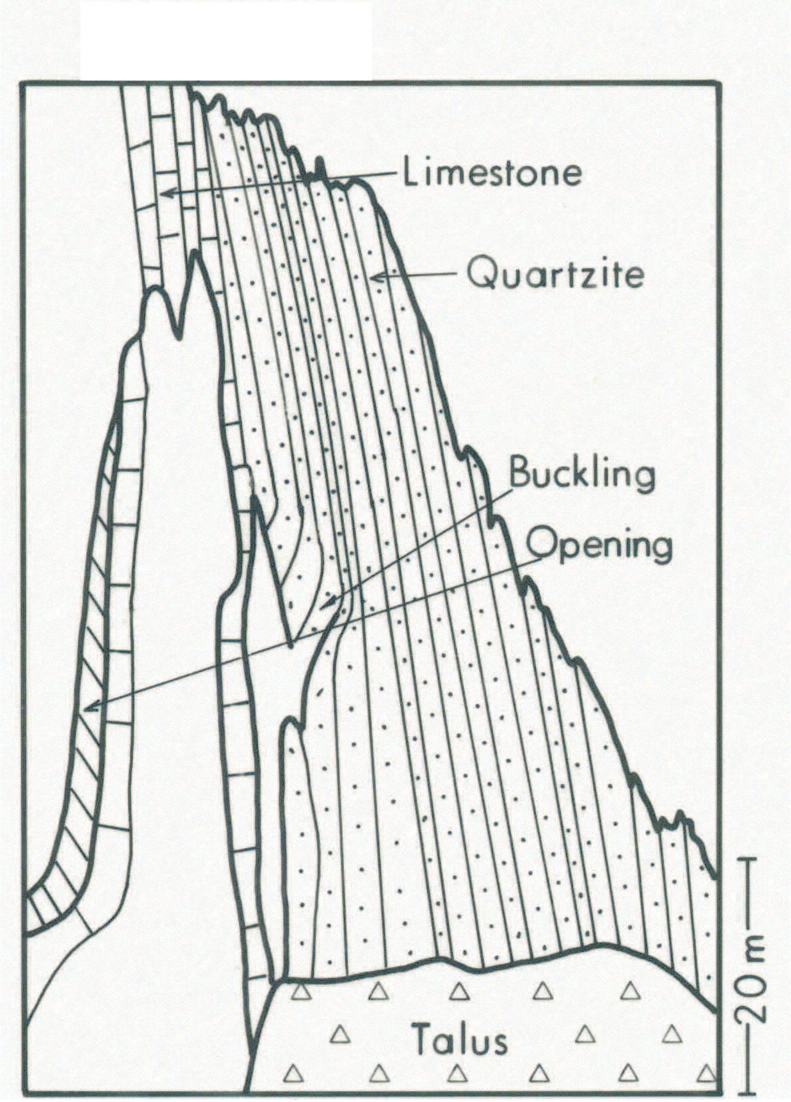

Figure 5.13: Sketch of the Highwood Pass buckling example with different rock units (modified from Hu and Cruden, 1993)

Table 5.5: Buckling numerical model properties

Properties	Joints	Flaws
Friction angle (°)	30	30
σ_t (MPa)	0.0	1.6
Cohesion (MPa)	0.0	5.0
Normal stiffness (GPa/m)	10	400
Shear stiffness (GPa/m)	5	200
Joints aperture (m)	0.001	0.0001

kept constant to model the Quartzite layers. To model the inner limestone beds, cross-joints were generated perpendicular to the beds with average spacing of 0.4 m. Figure 5.14 shows the details of the complete geological model for site#1 in Hu and Cruden (1993).

The insert in the figure shows the flaws and the cross-joints generated in the model in the quartzite and the limestone layers. The blocks were assumed to be elastic, while the flaws, the cross-joints and the beds were controlled by using the Mohr-Coulomb failure criteria. The bedding planes and the cross-joints were assigned a friction angle of 30° and zero cohesion. The flaws inside the intact quartzite columns were assigned the following intact material properties: a friction angle of 30°, cohesion of 5.0 MPa, and tensile strength of 1.6 MPa. Table 5.5 shows the properties of the joints and the flaws. The elastic modulus of the intact rock in this model was assumed to be 20.0 GPa and the unit weight was 25 kN/m^3. The normal and shear stiffnesses of the flaws were high to prevent overlapping of the blocks in the early stages of the modeling. In the following, the tensile strength effect on the formation of rupture surface is discussed.

The tensile strength of the quartzite was reduced gradually in 50 kPa increments for each simulation. At a tensile strength of 200 kPa, buckling was initiated. This low value showed that weathering damaged the rock mass and reduced the tensile strength of the Quartzite which is expected to have higher tensile strength. Failure was initiated at the foot of the slope at which the surface quartzite layers started to

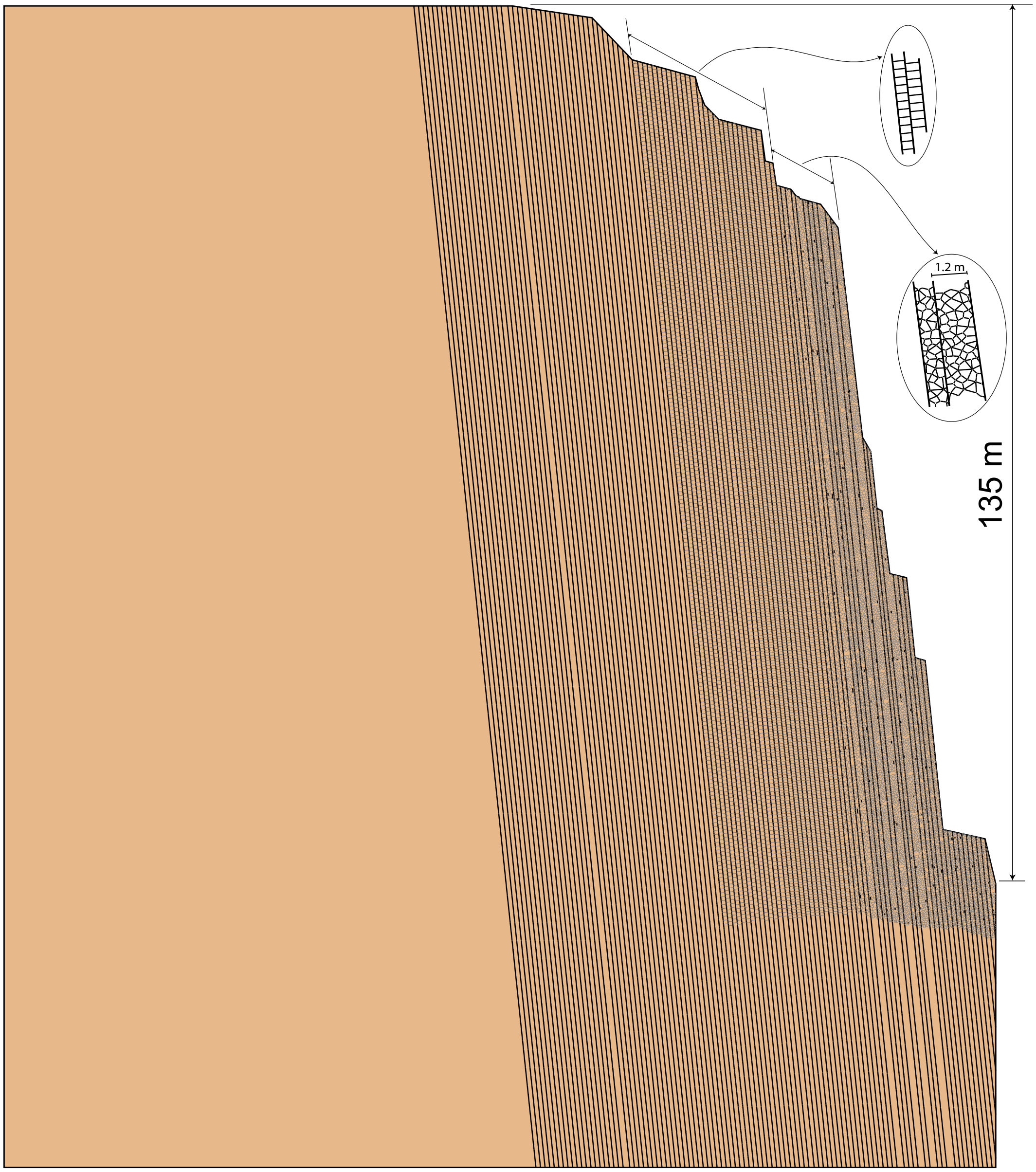

Figure 5.14: Numerical model for buckling site. The insert shows the details of flaws and joints in the model

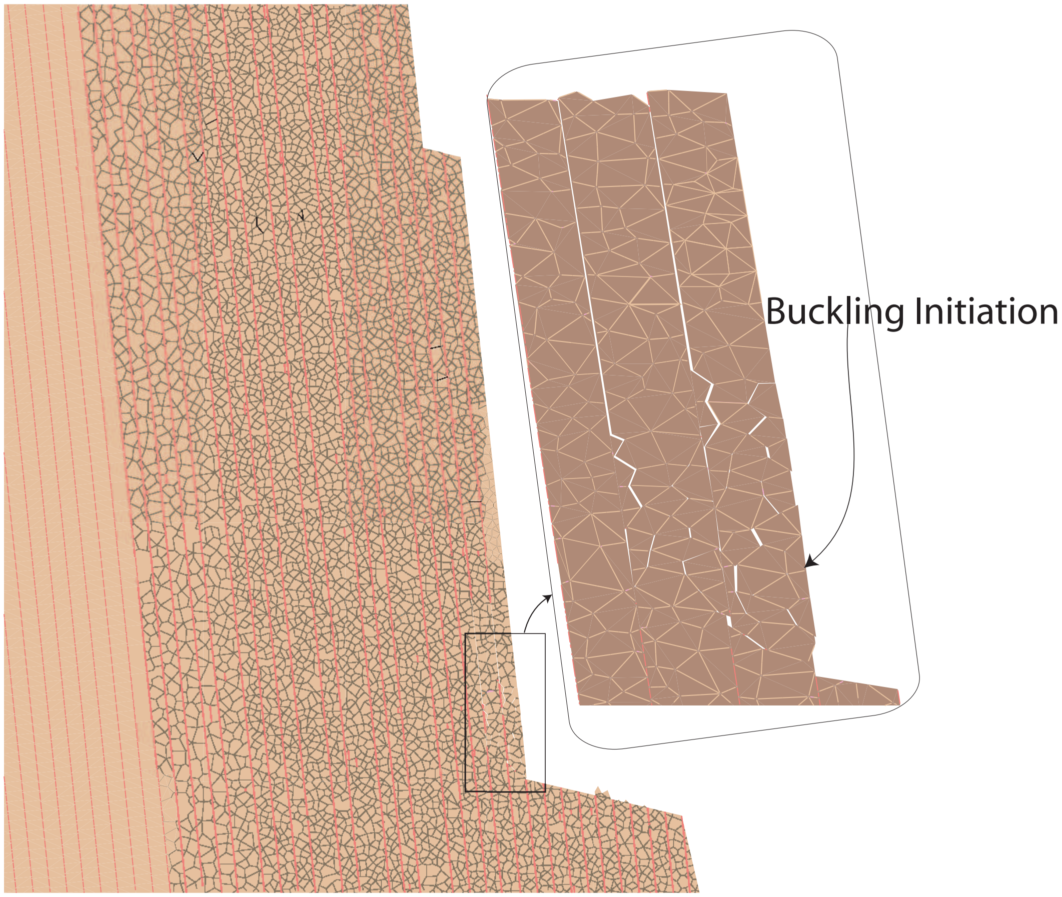

Figure 5.15: Buckling initiation at the toe of the slope

buckle. Figure 5.15 illustrates the buckle initiation at the slope foot.

The failure progressively propagated up the slope by fracturing the intact material due to tensile strength destruction. The displacement of the slope was monitored at two points on the slope face. Figure 5.17 shows the displacement in the X and Y directions. Points A and B (Figure 5.17) showed almost equal vertical displacement in the Y-direction. In contrast, points A and B experienced very different amounts of displacement in the X-direction. Point A (slope crest) showed sliding along the bed while Point B (slope toe) experienced significant displacement in the X-direction associated with buckling deformation. Figure 5.16 shows extension of buckling failure toward the middle of the slope.

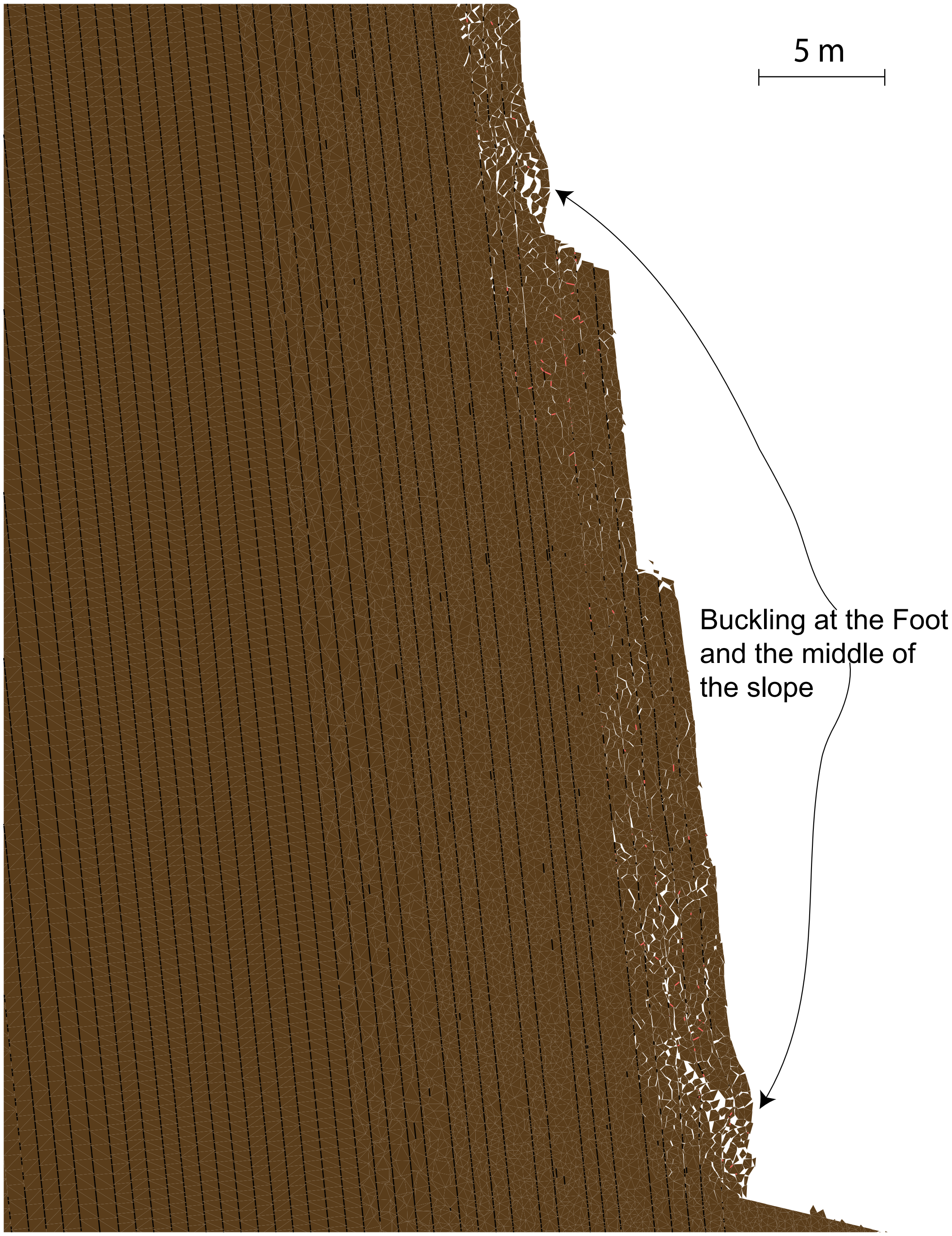

Figure 5.16: Buckling deformation at the toe and the middle of the slope

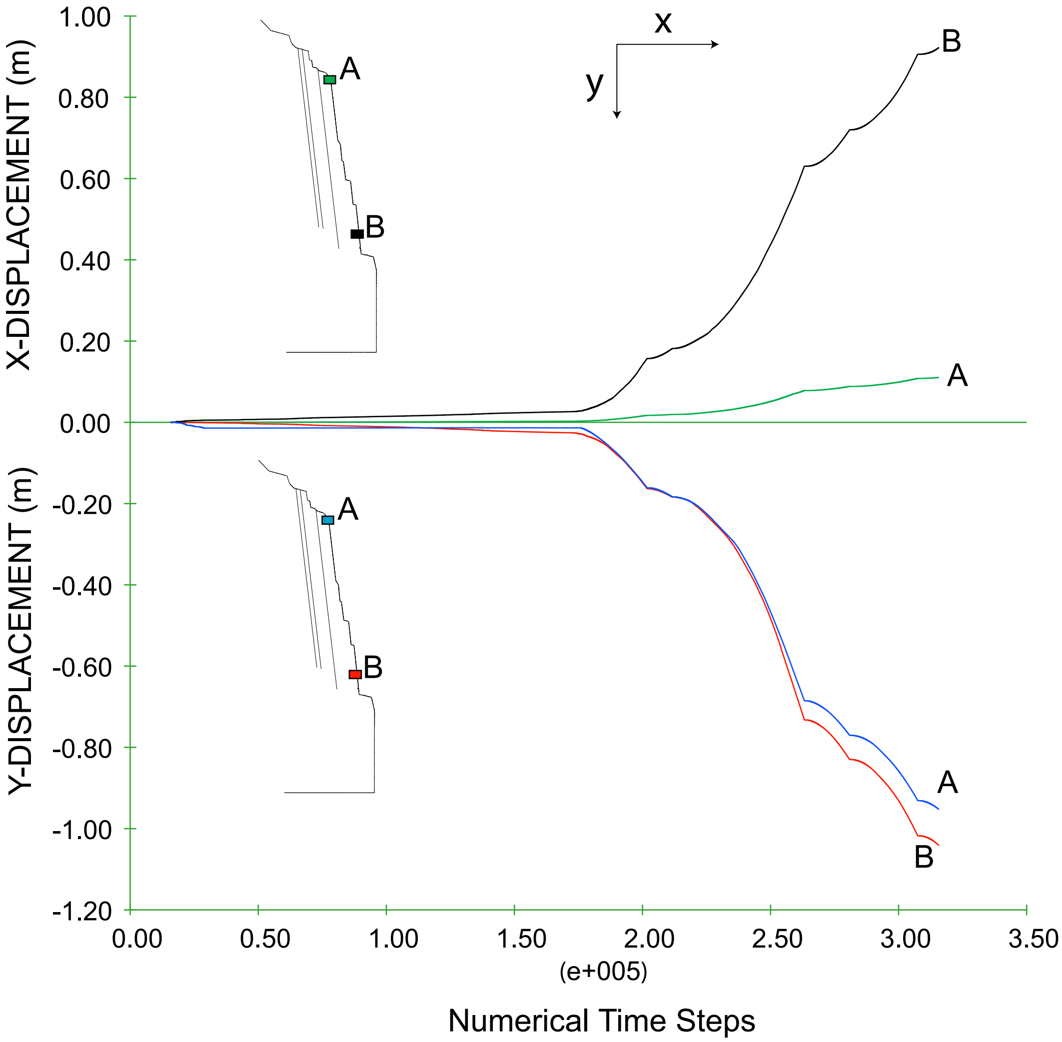

Figure 5.17: The displacement pattern in the buckling example at two points. See the insert for the points' location

Effect of the horizontal to vertical *in situ* stress ratio

This site is in high mountains, susceptible to significant topographic and tectonic stresses responsible for the mountains' formation. A high horizontal to vertical *in situ* stress ratio is expected in such high-mountain areas. Arjang (2006) presented a database for the Canadian crustal stresses which suggested a high horizontal to vertical stress ratio in the Canadian Shield. The *in situ* stress ratio had a range between 0.5 to 6 near the surface and decreased with depth. The high *in situ* stress ratio might have an effect on the stability of the slopes in the high mountains in western Canada. Stacey et al. (2003) using a elastic finite element analysis to explore the tensile stresses and the extensional strain in large open pits, concluded that at higher horizontal to vertical *in situ* stress, high tensile stresses occurred, especially at the crest of the slope. Stacey et al. (2003) showed that the horizontal to vertical *in situ* stress ratio generated high tensile stresses if the *in situ* stress ratio > 2. Stacey et al. (2003) also showed that the slope geometry affects the amount of the tensile stresses and their distribution in the slopes. Moreover, it is worth noting that this buckle is a local portion of a much larger slope (Figure 5.18), which might cause high horizontal stresses at the buckle.

The buckling example used in this study was tested under four horizontal to vertical *in situ* stress ratios of 0.5,1.0,2.0,3.0, and 5.0 to examine the tensile strength at failure. Figure 5.19 shows the effect of the horizontal to vertical *in situ* stress ratio on the tensile strength at failure. The results show that as the *in situ* stress ratio increased, the tensile strength required to prevent failure increased. At $k = 5$ failure occurred at a tensile strength of 1.15 MPa. Buckling occurred at the toe and the middle of the slope and propagated throughout the slope. Figure 5.20 shows the buckling failure at *in situ* stress ratio of 2.0 and a tensile strength of 0.25 MPa, no significant fracturing has been observed at the crest of the slope, while more fracturing occurred in the middle of the slope as shown in Figure 5.20.

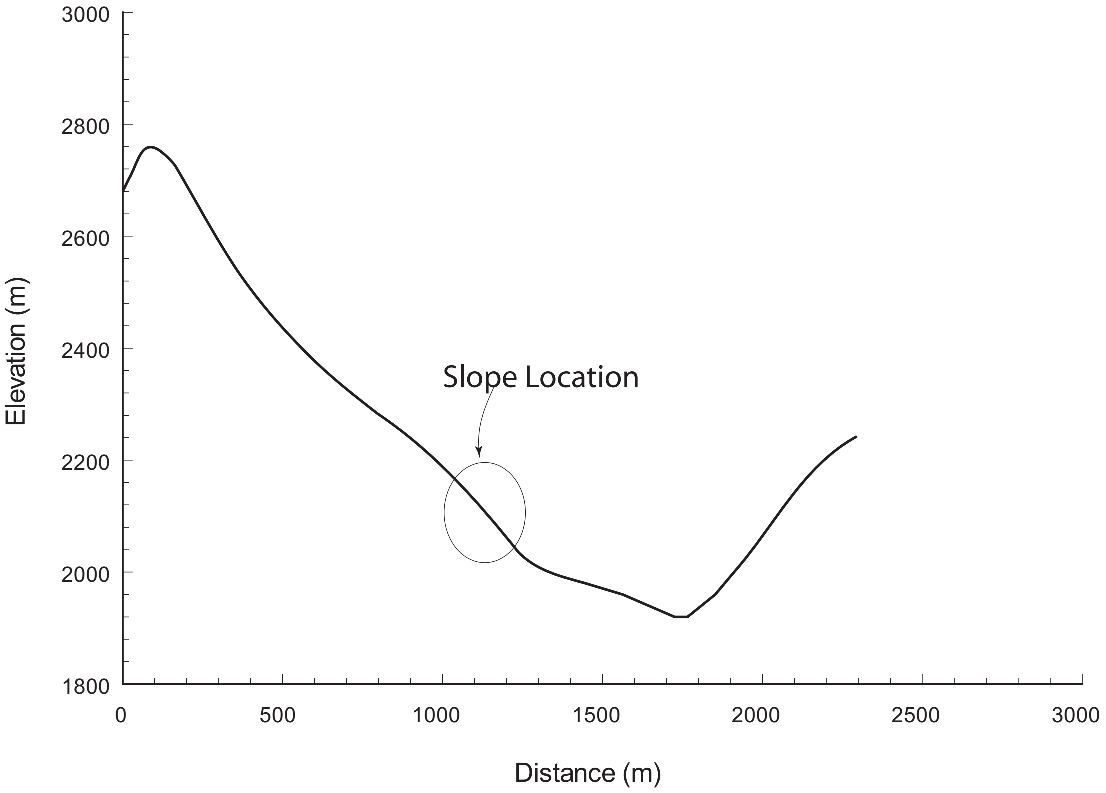

Figure 5.18: General cross-section through the buckling site location, notice the location of the buckle

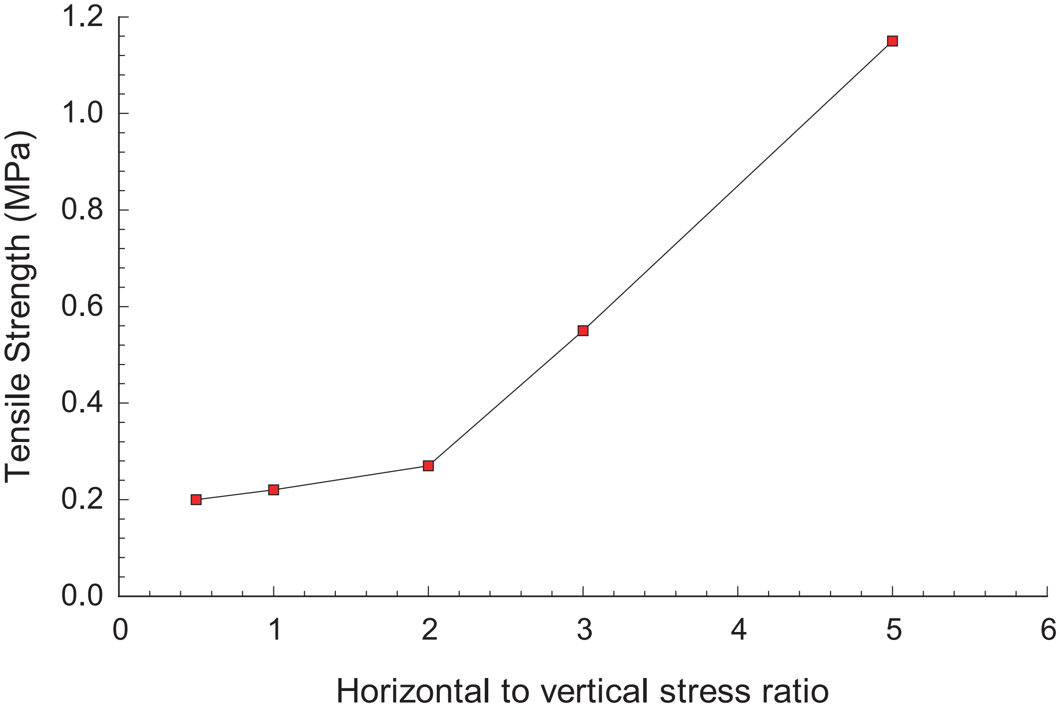

Figure 5.19: Horizontal to vertical stress ratio effect on the tensile strength at failure

5.4 Conclusion

The UDEC-DM was applied to different rock slopes, the results showed that rock's tensile strength is a key factor in the critical height of slopes that topple or buckle. In buckling, as horizontal to vertical stress ratio increased the tensile strength required to prevent failure increased. The formation of a rupture surface inside a toppling slope is controlled by the tensile strength of the flaws. The critical slope height increased as the tensile strength increased. Moreover, as the number of layers in a slope that were susceptible to toppling increased, the tensile strength required to stabilize the slope also increased. The friction of the flaws was also reduced to examine its effect on the toppling failure in the UDEC-DM. Reducing the friction of the flaws had essentially no effect on the rock mass toppling strength.

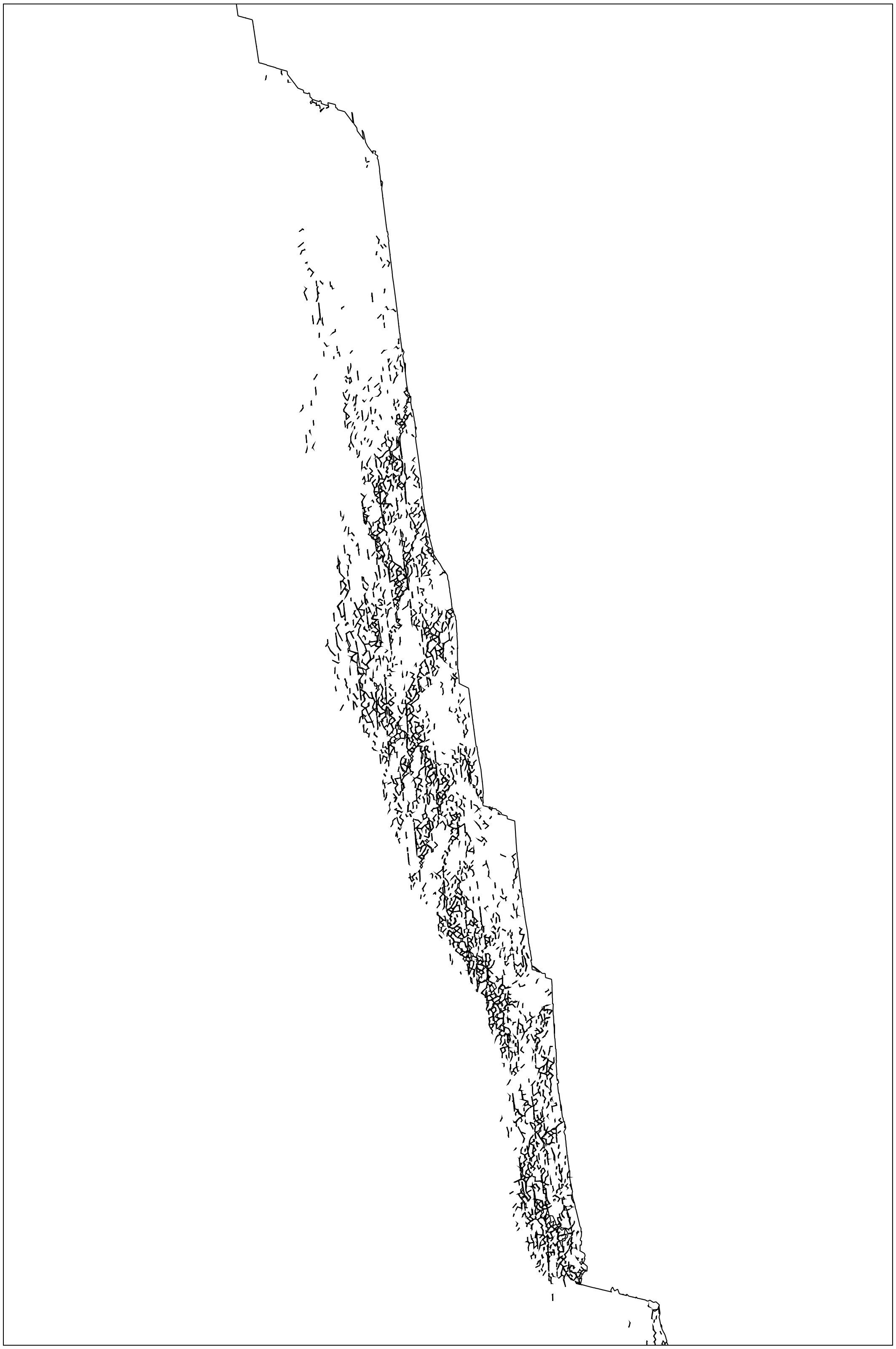

Figure 5.20: Buckling failure at the slope. Tensile strength=0.25MPa

Chapter 6

Toppling at Highland Valley Copper Mine

6.1 Introduction

Block toppling in natural rock slopes has been under investigation since the 1970's. De Freitas and Watters (1973) introduced the term "toppling" to describe the movements of rock slopes by rotation in steeply dipping beds. Goodman and Bray (1976) defined block toppling as the overturning and toppling of rock blocks formed mainly by two sets of discontinuities: a penetrative continuous discontinuities following bedding surfaces into the rock mass, and discontinuous sets of joints perpendicular to bedding. According to Terzaghi (1962), these characteristics are associated with the sedimentary rocks in which the cross-joints are perpendicular to the bedding. The thickness of the beds in sedimentary rocks ranges from centimetres to metres.

Terzaghi (1962) also described a geological model for crystalline rocks such as marble or granite as irregular-shaped crystalline particles. The jointing is a random joint pattern in which the cross-joints are not perpendicular to the main set of joints. Nichol et al. (2002) investigated rock slope toppling in natural rock slopes and found topples where the secondary joint set is not perpendicular to the inward dipping main joint set. The thickness of the rock columns susceptible to toppling is considerably smaller in sedimentary rock than in plutonic rocks. Tosney (2001) pointed out the thickness of rock columns in plutonic rocks can be as much as 40 metres as in the case of Highland Valley Copper Mine, no clear rupture surface has been observed throughout the slope.

The Highland Valley Copper (HVC) mine is located in British Columbia 75 km southwest of Kamloops, Figure 6.1. It is the largest copper mine operation in Canada and consists of two pits; the Lornex Pit and the Valley Pit. The two pits are currently being mined and are scheduled to end operation in 2009. Figure 6.2 presents an aerial view of the pits.

Figure 6.1: The location of the Highland Valley Copper Mine in British Columbia, Canada

The southeast wall of the Lornex Pit (Figure 6.2) suffered deformation by top-

Figure 6.2: Overview of the Lornex Pit and the Valley Pit and the location of the instability location (modified from Newcomen et al., 2003b)

pling, sliding and raveling in the order of 20 metres. Complex ductile movement and instability have been observed and monitored to insure the safety and continuity of the mining operations in the area of instability. The movement mode observed in the field was compared to the movement characteristics predicted by the numerical model. During the mining operation, an extensive displacement monitoring program was carried out using slope-monitoring prisms (SMP's). The displacement due to the mining operation was compared to the displacement predicted by the UDEC-DM simulation after carrying out an intensive calibration process by utilizing the actual measured displacement in the field. A good agreement with field observation has been achieved.

6.1.1 Geology of the Site

The rock mass characteristics of the southeast wall at the Lornex Pit vary widely and range from strong rock to a very weak rock mass. The Lornex Pit is approximately 1900 m in length, 750 m depth and 500 m wide. Three main geological units occur in the Lornex Pit: Skeena Quartz Diorite, the Bethsaida Granodiorite and the Quartz Porphyry Dyke (Newcomen et al., 2003a). Extensive alteration zones have been identified throughout the Lornex Pit. These alteration zones are mainly structurally controlled with weak to moderate chloritic and serictic alteration zones around shears and faults.

The geological discontinuities analysis of the Lornex Pit identified two major sets of discontinuities: the first set of faults is continuous and dips into the slopes at angles between 70° to 80° with a spacing between 20-40m; the second set is less continuous and dips in the same direction as the slope at angles ranging between 50°to 60°from the horizontal with an average spacing between 10-20m. The two sets of joints contain infilling that controls their shear strength properties (Tosney et al., 2004). Waldner et al. (1976) discussed the discontinuity's distribution in the Lornex Pit based on 11,000 mapped discontinuities.

6.2 Movement mode at Lornex Pit

The movement at the southeast wall of the Lornex Pit is a composite mode involving sliding along the secondary joint set at the crest of the slope, forming a normal scarp facing in the same direction as the slope face. Toppling in middle parts of the slope, which is driven by sliding along the in-dipping discontinuities of the slope and forming obsequent scarps (Figure 6.3). Bulging at the toe of the slope as a result of stress concentrations. According to Cruden and Varnes (1996) classification, the movement at the Lornex pit is a composite rock slide-rock topple or a slide toe topple, and it is driven by the movement of the actively sliding block at the crown of the slope. Tosney et al. (2000) presented a conceptual model of the movement mode at the HVC mine. Figure 6.3 illustrates the movement mode observed at the southeast wall of the Lornex Pit. Goodman and Bray (1976) showed that toppling in rock slopes is possible according to

$$\beta \geq \phi + (90 - \Psi), \tag{6.1}$$

where β is the inclination of the slope face, ϕ is the friction angle, and Ψ is the dip of the main set of joints. With β around 35°, ϕ of 12° (Fault gouge sample, residual), and Ψ between 70° and 80°, toppling at the Lornex Pit is kinematically possible.

The block toppling observed at the southeast wall was different from the block toppling proposed by Goodman and Bray (1976). Tosney et al. (2004) discussed in detail the main differences between the two, which involved the formation of normal scarps at the crest of the slope and the formation of tension cracks at the crest of a slope in topples described by Goodman and Bray (1976). In addition, the scale of the block toppling described by McAffee and Cruden (1996), Goodman and Bray (1976) averages 1:100 to 1:150 (scale is set by the thickness of the layers relative

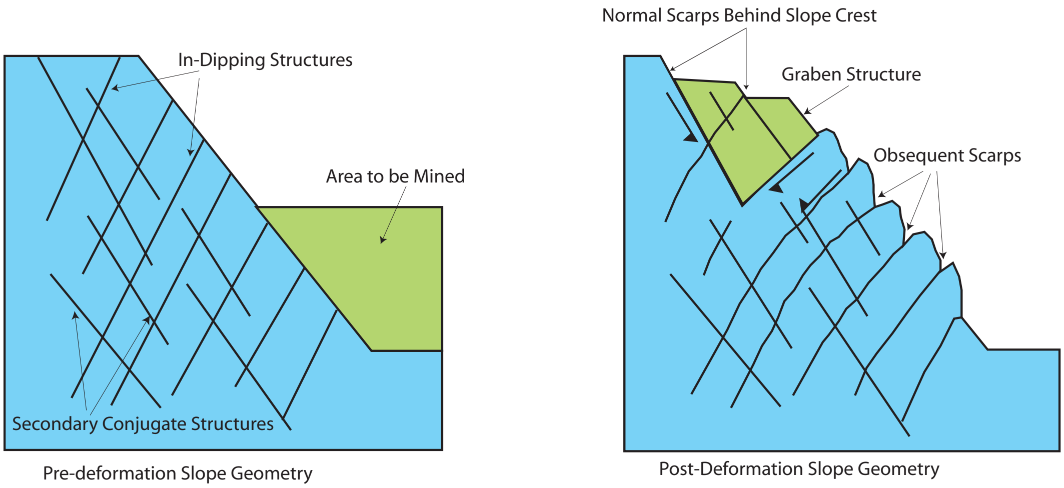

Figure 6.3: Conceptual toppling movement mode observed at HVC (modified from Tosney et al., 2000)

to the height of the slope). While at the HVC mine, this scale averages 1:7 to 1:11. Also, while the cross-cutting joints are perpendicular to the bedding in the block toppling (McAffee and Cruden, 1996, Cruden and Hu, 1994, Goodman and Bray, 1976) because these topples are in sedimentary rocks, the secondary joint set at the Lornex Pit is not perpendicular to the main inward dipping discontinuities because this topple is in granite. The block toppling observed at the HVC mine resulted in a large displacement of up to 20 metres with no rupture surface development.

The displacement the the Lornex pit were triggered by the excavation at the toe of the slope accompanying the background movement. As the confinement (provided by the benches) was reduced by the mining, the mining-induced deformation accelerated. Figure 6.4 shows somr surface expression observed at the southeast wall of the Lornex Pit. Similar behaviour was also observed at the southwest wall of the Lornex Pit (Newcomen et al., 2003a).

The complexity of the slope at the HVC mine was increased by the presence of infilling material in the faults and the presence of high pore-water pressure inside the slope.

Figure 6.4: Surface expression of the movement mode at Highland Valley Copper Mine (modified from Tosney, 2001)

6.3 Material testing

Geotechnical testing for the intact rock and discontinuities is essential to determine the material properties needed for numerical modeling to be reliable. Tosney (2001) conducted a series of point load tests on intact material from the southeast wall to determine the unconfined compressive strength (UCS) of the intact material. The results indicated that the average UCS is between 37 MPa and 103 MPa. Basic geotechnical tests were also performed to determine the strength parameters of the faults' gouge samples. According to the Unified Classification System, the gouge material contains montmorillonite clay mineral that has swelling potential and may affect the slope behaviour in the presence of water. The direct shear test was used to determine the shear strength properties of the fault gouge material. The friction angle had a peak value of 18° and a residual value of 12°, while the peak cohesion was 20 kPa, and the residual cohesion was 6 kPa (Tosney et al., 2000).

6.3.1 Hydrology of the Site

The flow of the water and pore-water pressure should be assessed and incorporated in the numerical modeling to take their effect into account. The Lornex Pit is fully or nearly fully saturated, and groundwater seepage along the slope's face has been observed by the site engineers (Tosney et al., 2004). To establish the groundwater profile, a number of piezometers have been installed and monitored. The readings show that the groundwater table is near the slope surface. Seasonal variation has also been detected by the piezometers. Figure 6.5 shows the groundwater profile used in the numerical model to simulate the slope realistically.

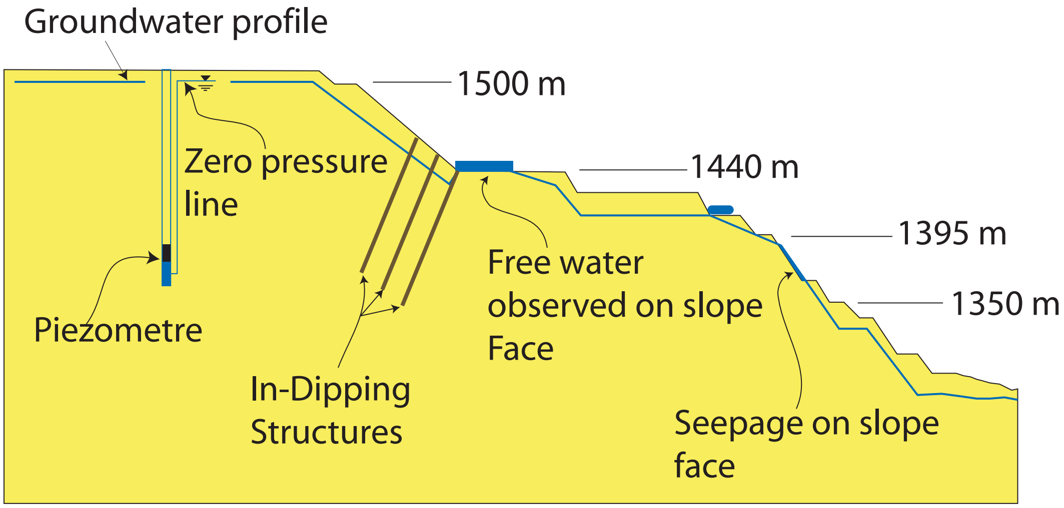

Figure 6.5: Groundwater profile at southeast wall of Lornex Pit (modified from Tosney, 2001)

Many attempts have been made to lower the groundwater table to stabilize the slope; deep groundwater wells and horizontal drains have been installed in several locations throughout the slope. These techniques have been used in the southeast wall with limited success in lowering the displacement rate or lowering the water table. In the following section, the rock mass classification of the Lornex Pit is discussed.

6.4 Geomechanics assessment and strength properties

A backpack-mounted GPS receiver was used to map the large-scale discontinuities in the southeast wall. Information on faults and surface scarps was logged as either a line or a point feature. Attribute data including continuity and gouge thickness, the location, water presence, infilling, and strike and dip were attached to each large-scale discontinuity and stored in a computer (Newcomen et al., 2003b). Line mapping by using a 30 m long tape was carried out to map the small discontinuities and their geotechnical characteristics. As a result of the mapping, two major discontinuities sets were determined: the in-dipping faults and the out-dipping structure. These two sets are believed to be the controlling factor of the slope behaviour and to develop the movement mode observed at the southeast wall.

The Highland Valley Copper Engineers used the RMR classification system (Bieniawski, 1976) to characterize the geological units of both the Valley Pit and the Lornex Pit. To estimate the RMR for a geological unit, the following factors were estimated and attached to each location:

1. Uniaxial Compressive Strength.
2. Rock Quality Designation (Deere, 1963).
3. Spacing of discontinuities.
4. Condition of discontinuity.
5. Groundwater conditions.

6. Discontinuities orientation.

The results of the mapping are summarized in Figure 6.6, which shows the RMR for different areas of the Lornex southeast wall. The non-linear failure criterion proposed by Hoek and Brown (1988) was used by Tosney (2001) to estimate the Mohr-Coulomb strength parameters necessary to develop the numerical model. Table 6.1 shows the strength properties used in the numerical model. The site engineers estimated the tensile strength at 0.1 MPa for all the geological units (Tosney (2001)).

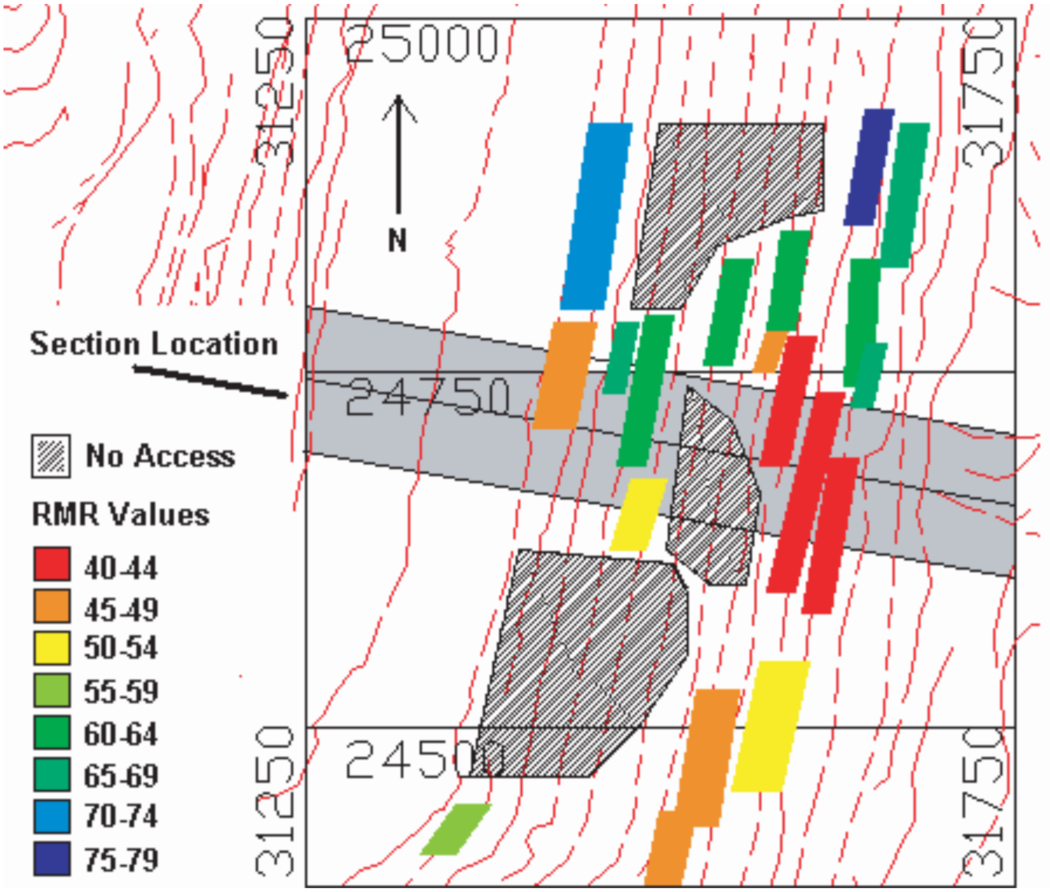

Figure 6.6: Lornex southeast wall RMR rating (modified from Tosney et al., 2004)

The RMR 1976 was also used to estimate the elastic properties of the southeast wall geological units (Table 6.2) based on Hoek-Brown's 1988 criterion, equa-

Table 6.1: Strength properties of the geological units used in the model, modified from Tosney (2001)

RMR 76	H-B (m)	H-B (s)	UCS (MPa)	H-B (mi)	ϕ(°)	C (MPa)
40	0.39	4.54e-5	65	28	29	0.7
45	0.55	1.04e-4	65	28	33	0.7
50	0.79	2.40e-4	65	28	36	0.8
55	1.13	5.53e-4	65	28	39	0.9
60	1.61	1.27e-3	65	28	43	1.0
65	2.30	2.93e-3	65	28	46	1.2
70	3.28	6.74e-3	65	28	48	1.4
75	4.69	1.55e-2	65	28	51	1.7
80	6.71	3.57e-2	65	28	54	2.1

tion 6.2 for disturbed rock masses, and a Poisson's ratio of 0.3 :

$$E_m = 10^{\frac{(RMR-10)}{40}}, \tag{6.2}$$

where E_m is the Young's Modulus, and RMR is the Rock Mass Rating (Bieniawski (1976)). Table 6.2 shows the elastic properties used in the present simulation.

Table 6.2: Rock mass elastic properties, modified from Tosney et al. (2000)

RMR 76	E (GPa)	K (GPa)	G (GPa)
40	5.6	4.7	2.2
45	7.5	6.2	2.9
50	10.0	8.3	3.8
55	13.3	11.1	5.1
60	17.8	14.8	6.8
65	23.7	19.8	9.1
70	31.6	26.4	12.2
75	42.2	35.1	16.2
80	56.2	46.9	21.6

Two sets of joints were modeled explicitly. The steeply inclined faults in the slope contained infilling, these fillings were tested in the laboratory, while the shear strength properties of the secondary set of discontinuities was estimated. Table 6.3 shows the discontinuities' properties, The normal and shear stiffness and the residual values of the fault gouge material of the two joint sets were adapted

Table 6.3: The discontinuities properties used in the model, modified from Tosney et al. (2000)

Parameter	In-Dipping faults	Secondary discontinuities
Orientation from horizontal (°)	70	125
Spacing (m)	30	15
Normal Stiffness (GPa/m)	4	4
Shear Stiffness (GPa/m)	1	1
Cohesion (kPa)	6.0	0
Friction (°)	12	25
Tensile Strength (kPa)	0	0

from Tosney's analysis in order to compare the results with the results from the UDEC-DM approach.

6.5 Displacement monitoring and movement rate

The Lornex Pit is mined in a deformable and poor-quality rock mass that experiences a high magnitude of deformation and instability. To monitor the slope and the mining operations' safety, many slope-monitoring prisms have been installed in the slope to determine the magnitude and location of any instability that might occur there. Figure 6.7 shows the location of the slope-monitoring prisms (SMP's) and the locations of problematic areas at the Lornex Pit.

Newcomen et al. (2003b) developed an automatic monitoring system to continuously monitor and record the pit wall displacement 24 hours a day. This system was utilized to establish movement rate thresholds under which mining operations could continue safely. Based on the use of this system, the movement rate thresholds at the slope were divided into three categories: Watch, Caution, and Alert. Whenever the movement rate is in the ”Alert” region, either the equipment and personnel should be moved, or the mining should be stopped. Figure 6.8 presents an example of the selected displacement thresholds for the Lornex southeast wall. According to Newcomen et al. (2003b) and Tosney et al. (2004), the background movement at

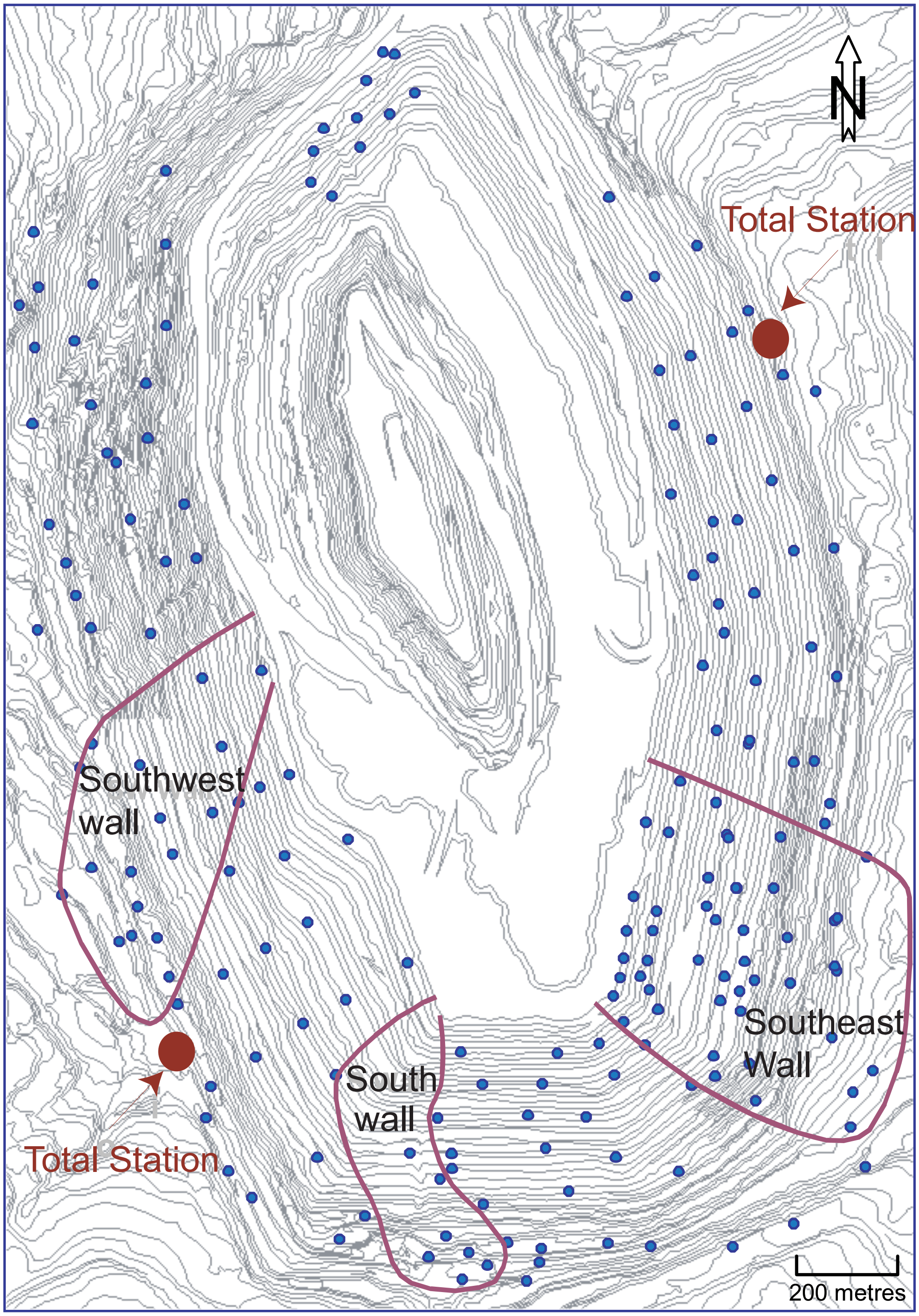

Figure 6.7: The location of the slope-monitoring prisms and regions of instablities in the Lornex Pit (modified from Newcomen et al., 2003b)

the Lornex southeast wall is between 150mm/month to 200mm/month.

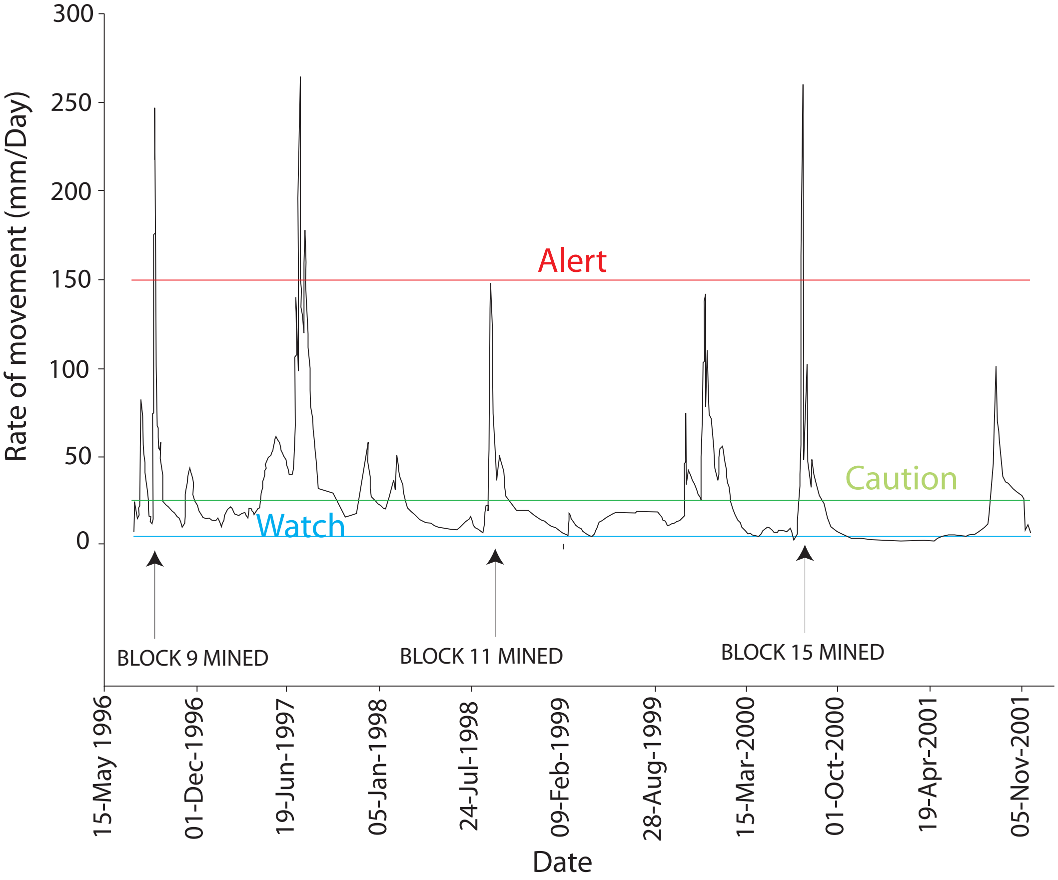

Figure 6.8: Typical movement rate pattern recorded at Lornex southeast wall (SMP#458), (modified from Newcomen et al., 2003b)

As shown in Figure 6.8, the movement rate peaks coincide with block excavation at the toe of the slope. Tosney (2001) stated that the majority of the recorded displacement is mining-induced displacement. By simulating the sequence of the excavations at the Lornex southeast wall, the numerical model can be calibrated and verified.

6.6 The Numerical model

One of the biggest advantages of numerical methods over other methods of rock-slopes analysis, such as Limit Equilibrium, is the numerical model's ability to model the displacement magnitudes. In addition, the UDEC-DM is also capable of handling fracturing throughout the intact material. The southeast wall of the Lornex Pit was used to verify the proposed UDEC-DM approach by comparing the movement mode and magnitudes observed in the field, with those predicted by the numerical simulation. This case history was chosen due to the availability of the displacement records associated with the physical processes of mining pushback. The geometry of the model was based on the actual mining history adapted by Tosney (2001). The mining steps are illustrated in Figure 6.9. The numbers inside the boxes show the sequence of the blocks excavation. During the mining of blocks 1 to 15, four slope-monitoring prisms (560, 468, 413, 454) were used to track the mining-induced deformation, Figure 6.10 shows the location of these SMP's along the slope face. Table 6.4 presents the mining-induced displacement associated with each block excavation which was calculated by subtracting the background movement from the total displacement. Tosney et al. (2004) suggested that during the mining of block number 5 (see Figure 6.9), a runoff event had increased the displacement, and that this displacement was not due to mining. This justification seems simplistic and need to further examined in future research. These researchers estimated that 1 m of displacement was associated with this runoff period. This displacement was subtracted from the displacement shown in Table 6.4 so that the displacements included in the analysis were due solely to the excavation process.

The major discontinuities dipped into the model at an angle of 70° with joint spacing of 30 m, while the secondary discontinuities dipped in the same direction as the slope face at angle of 55° from the horizontal with joint spacing of 15 m. The two joints intersected each other to form blocks. Inside each block, flaws with a 1.4 m edge length were implemented inside the area susceptible to toppling. The flaw implementation resulted in generating randomly polygonal blocks as shown in Figure 6.11, whose insert shows the details of the flaws inside the model. The

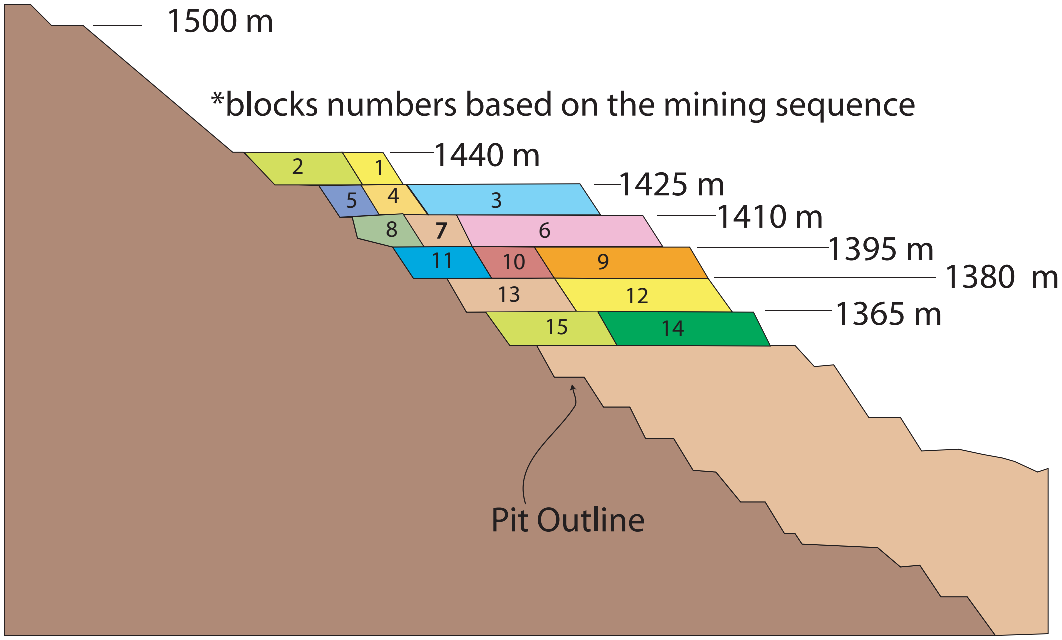

Figure 6.9: Blocks excavation sequence at Lornex southeast wall

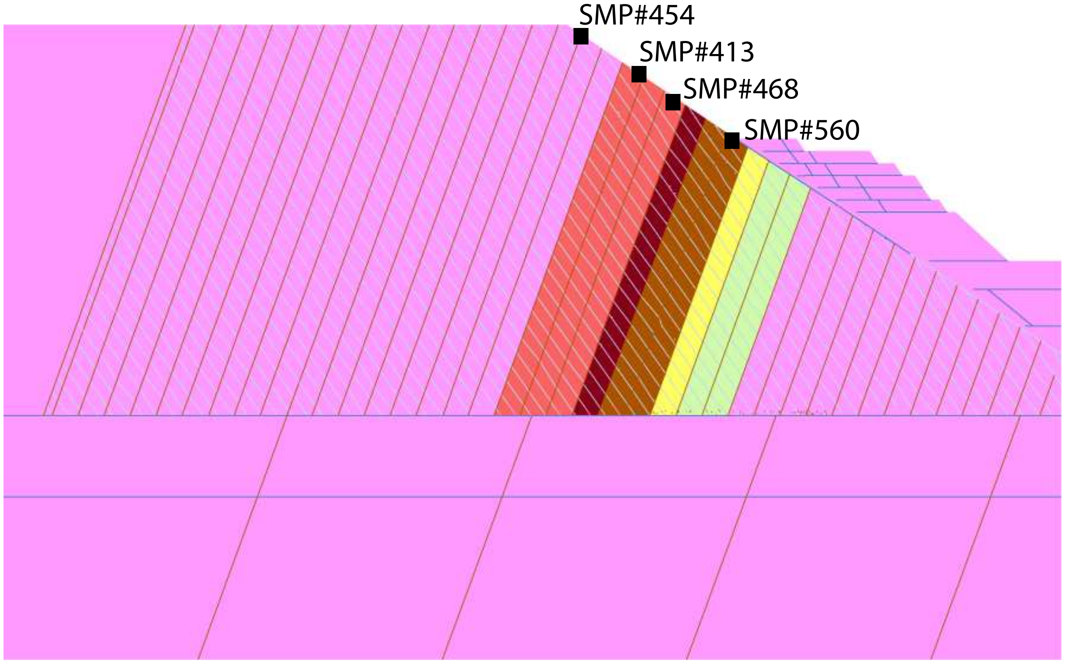

Figure 6.10: Locations of the slope-monitoring prisms at the UDEC-DM

flaws were generated in the region susceptible to toppling. This region was determined by using preliminary conventional UDEC similar to Tosney (2001) analysis.

Table 6.4: Cumulative mining-induced displacement, after Tosney et al. (2000)

Mining Block Number and Mining Location	Date of Mining m-m/yyyy	Displacemnet due to Mining (m)			
		SMP 560	SMP 468	SMP 413	SMP 454
1- Bench Pass	07-08-1996	0	0.1	0.0	0.1
2- Toe Pass	08-09-1996	0	0.20	0.0	0.50
3- Bench Pass	09-10-1996	0	0.90	0.4	1.50
4- Bench Pass	11-12-1996	0	1.10	0.50	1.80
5- Toe Pass	06-08-1997	2.5	1.70	0.80	3.20
6- Bench Pass	10-11-1997	2.95	2.10	1.10	3.60
7- Bench Pass	11-12-1997	3.55	2.50	1.50	4.10
8- Toe Pass	12-01-1997/98	4.15	2.85	2.00	4.45
9- Bench Pass	01-03-1998	6.05	3.75	2.90	5.45
10- Bench Pass	05-08-1998	6.55	4.10	3.35	5.75
11- Toe Pass	09-10-1998	8.95	6.10	5.55	7.65
12- Bench Pass	11-01-1998/99	9.40	6.50	5.95	8.00
13- Toe Pass	12-01-1999/00	12.90	9.20	9.15	10.50
14- Bench Pass	03-04-2000	14.1	10.40	10.35	11.70
15- Toe Pass	07-08-2000	16.3	12.40	13.05	13.30

Figure 6.12 shows the conventional UDEC model and the displacement vectors.

The strength and deformation properties were assigned to the model based on the RMR rating shown in Figure 6.13. Tables 6.1, 6.3, and 6.2 show the strength properties, the main discontinuities' properties, and the elastic properties used in the model, respectively. To include the effect of the groundwater pressure, the water table was applied to the model according to the water profile shown in Figure 6.5. A horizontal-to-vertical stress ratio of 1.5 was applied to the model. This value was adopted from Tosney (2001). The modeling process was started by bringing the model to equilibrium under high strength properties, bringing the model to equilibrium under realistic properties, and then the model was calibrated as described in the following section.

6.7 Calibration of the model

To build a reliable numerical model, the model needed to be calibrated against the field deformation attributed to the mining process. As mentioned earlier, the rock

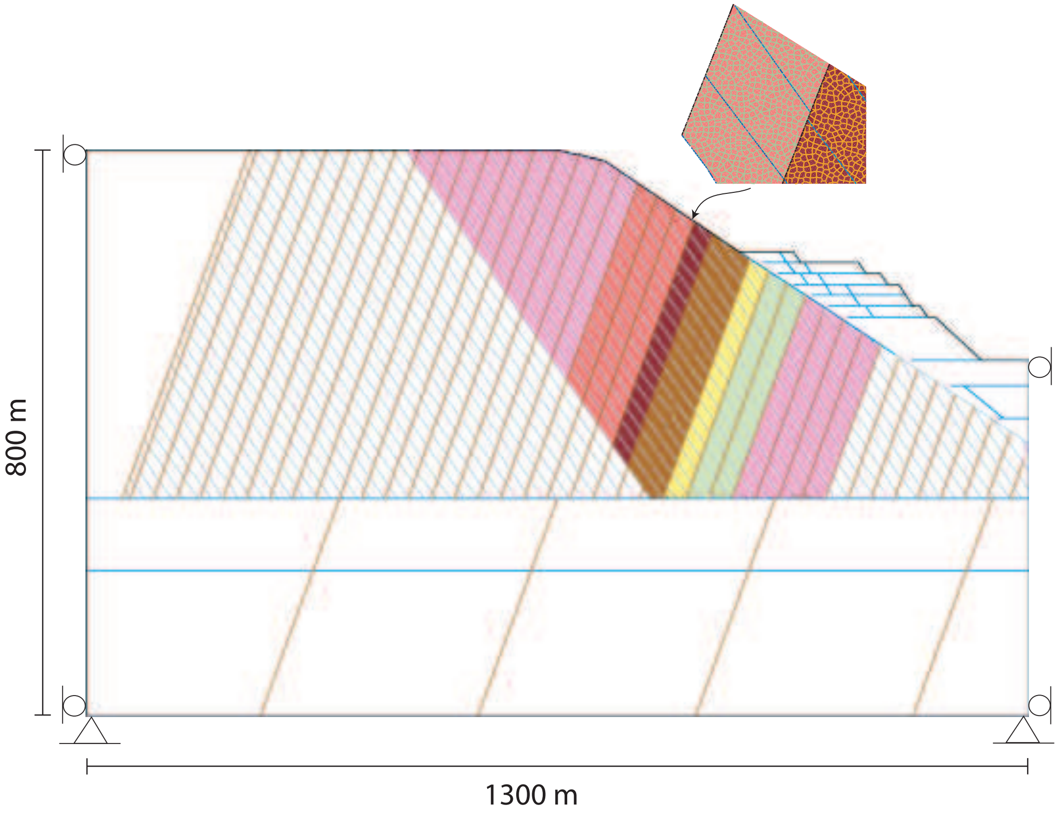

Figure 6.11: The Lornex southeast wall UDEC-DM; the insert shows the details of the flaws

slope is monitored by using SMP's, four of which are positioned in Figure 6.10. The mining-induced deformation captured by SMP number 413 was used to calibrate the model at two arbitrary stages of the mining excavation as follows:

1. The normal stiffness was calculated using equation 4.9.
2. The shear stiffness was assumed to be equal to the normal stiffness, which was calculated in step 1.
3. Blocks number 1 to 8 (see Figure 6.9) were excavated, and the total mining-induced displacement after equilibrium was calculated.
4. Blocks number 9 to 13 (see Figure 6.9) were excavated, and the total mining-induced displacement after equilibrium was calculated.

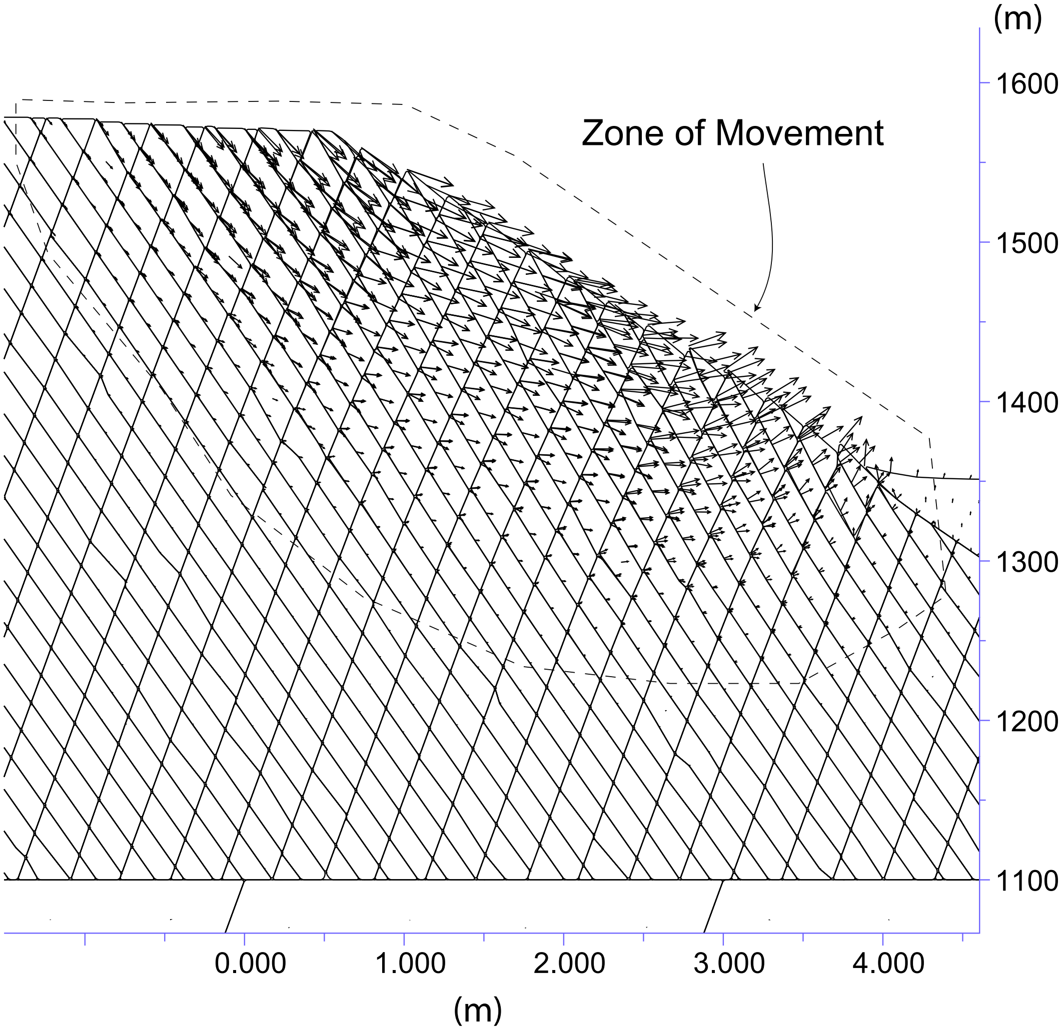

Figure 6.12: The conventional UDEC model used to determine the area susceptible to toppling

5. The total mining-induced displacement at the numerical model was compared to the total displacement observed at the field.
6. The shear stiffness was adjusted until the gap between the calculated and observed displacement became smaller.

After removing blocks 1-8 and 9-13, the model was re-run until equilibrium was achieved. For each run, the displacement, velocity, and unbalanced forces at the model were monitored. A good agreement between the calculated and observed

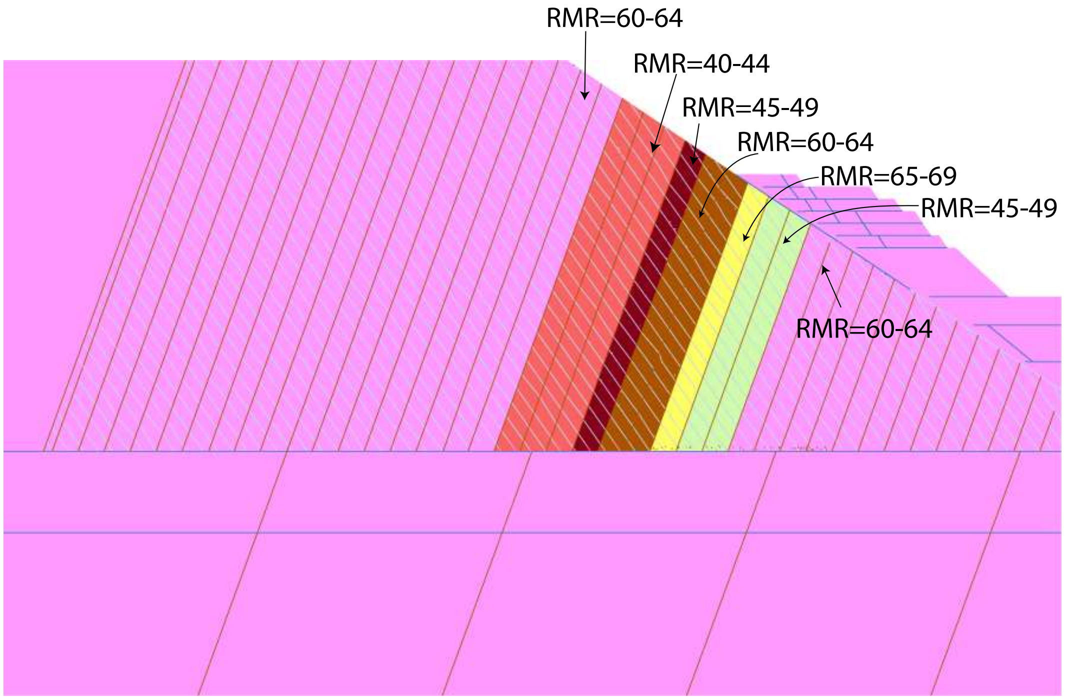

Figure 6.13: The RMR values and locations assigned to the UDEC-DM (modified from Tosney, 2001)

Table 6.5: Normal and shear stiffness resulting from the calibration process

RMR 76	Normal Stiffness (GPa/m)	Shear Stiffness (GPa/m)
40-44	11	3.5
45-49	14	4.5
60-64	34	11
65-69	46	15

displacement was achieved at the normal and the shear stiffness shown in Table 6.5. Figure 6.14 presents a comparison between the simulation results and the actual deformations.

6.8 The UDEC-DM results

An extensive numerical modeling program was carried out to investigate the Lornex southeast wall and to verify the UDEC-DM approach. After the model had been brought to equilibrium under high-strength property values, the actual strength

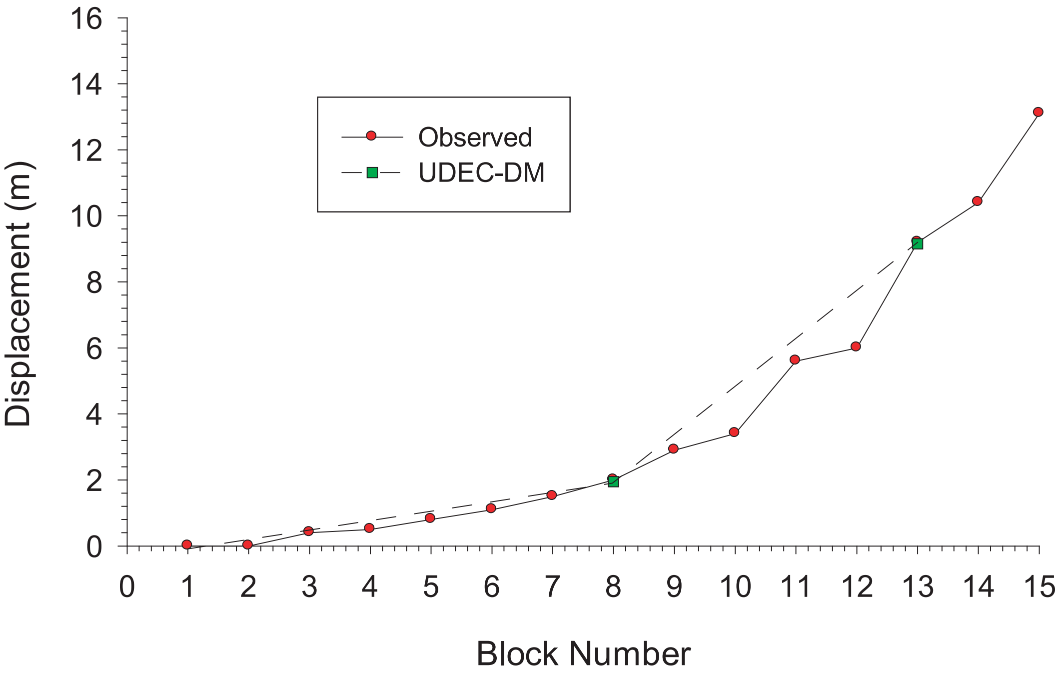

Figure 6.14: Cumulative displacement comparison for the calibrated model

properties presented in the above sections were assigned to the model. Blocks 1 to 15 (see Figure 6.9) were removed. After removing each block, the model was re-run until equilibrium was achieved. For each run, the displacement, velocity, and unbalanced forces at the model were monitored. In addition, the fracturing throughout the model was tracked to insure the validity of the model in terms of the field observations. The mining-induced displacement after each excavation step was calculated in order to compare this displacement to the field displacement. The following sections discuss the movement mode, the displacement at the field and the numerical model, and the differences between the UDEC-DM and the conventional UDEC.

6.8.1 Movement mode in the numerical model

The rock movement at the Highland Valley Copper Mine involved a sliding at the crest of the slope, toppling over most of the slope, and bulging and distortion at the toe of the slope. The mechanism of the movement was successfully simulated by using the UDEC-DM approach. Figure 6.15 shows the numerical model after excavation of block number 15. The simulation was able to reproduce the surface expressions observed at the Lornex southeast wall. The inserts in Figure 6.15 provide a closer look at the movement mode at the crest. Notice the formation of normal scarps.

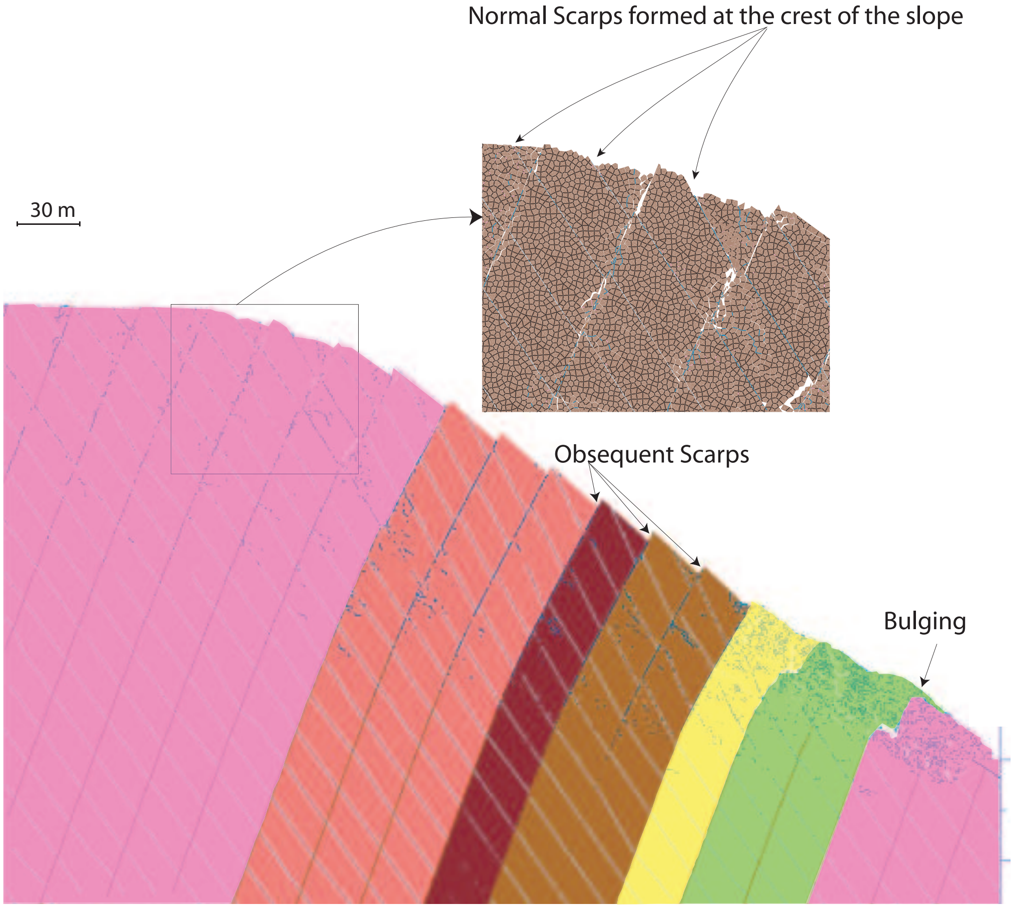

Figure 6.15: The movement mode at the Lornex southeast wall simulated by the UDEC-DM; the insert provides a closer look at the crest

The majority of the model suffered from toppling. The sliding along the in-dipping faults allowed the toppling of the rock blocks shown in Figure 6.15. This toppling movement formed obsequent scarps facing up the slope. This aspect of the movement has been observed at the Lornex southeast and the southwest walls (Newcomen et al., 2003a). Although toppling movement has occurred, no rupture surface has formed at the site (Tosney, 2001). The UDEC-DM model showed that no continuous rupture surface was formed in the model, as shown in Figure 6.16.

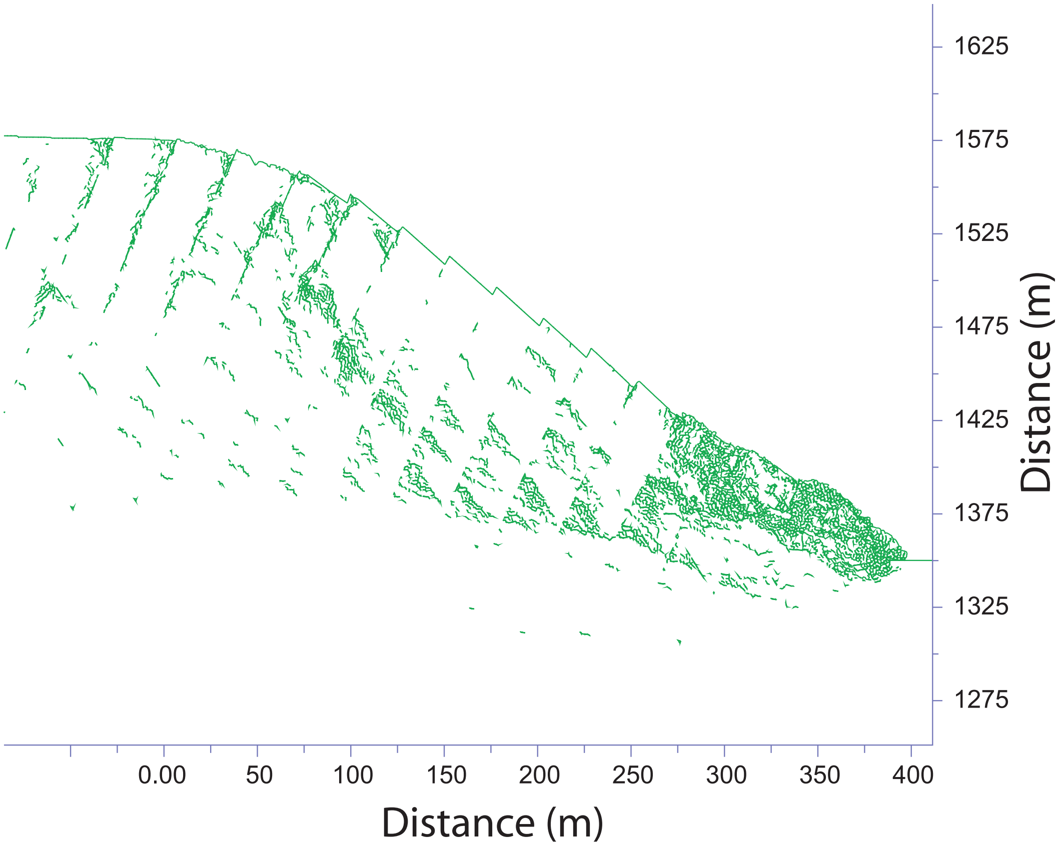

Figure 6.16: Plot of the numerical model, showing the rupturing in the slope

At the toe of the slope, bulging formed, Tosney (2001) reported that on several occasions during the mining, loose material at the toe delayed the operation. Bulging occurred at the toe of the slope as a result of mining excavations which removed the confinement provided by the mined blocks. As the confinement was decreased by the excavation, the stress concentration at the toe increased which caused extensive fracturing, fragmentation, and formed loose material, as shown in Figure 6.17. Cruden and Varnes (1996) characterized this type of movement at the toe as “flow”.

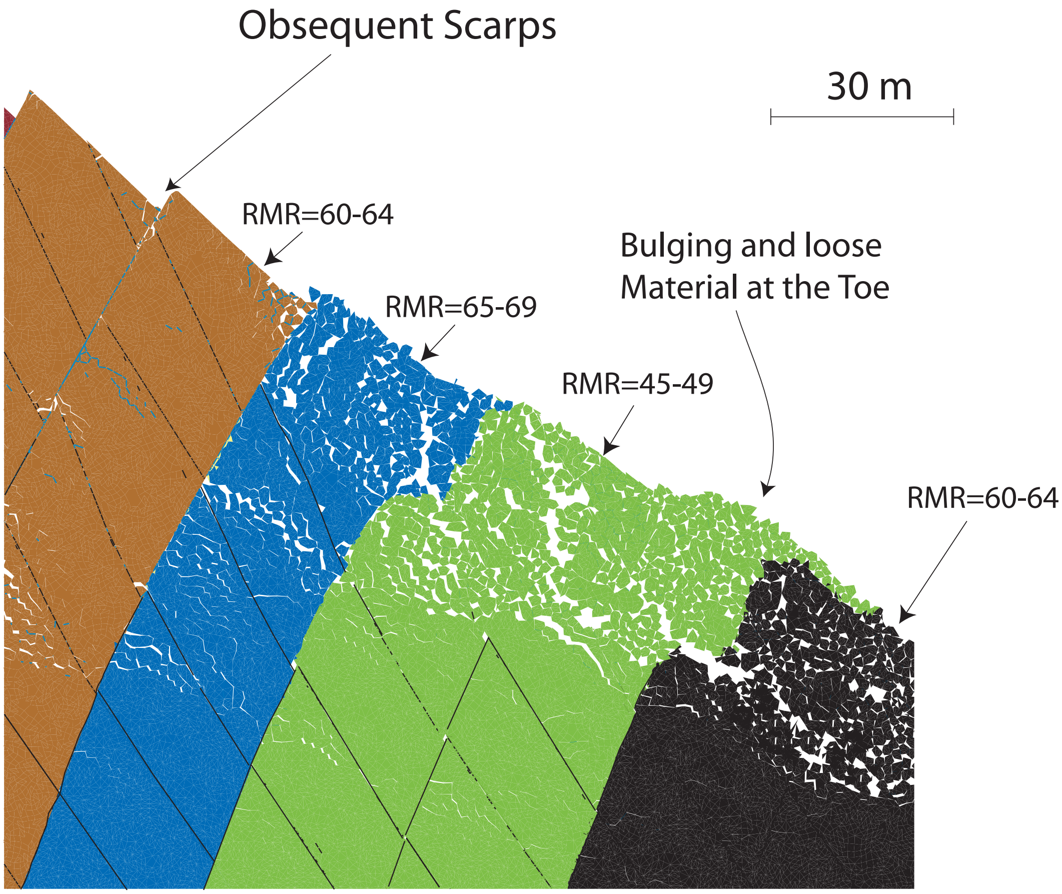

Figure 6.17: Bulging and crushed rock at the toe of the UDEC-DM model

6.8.2 Deformation comparison between the field and the numerical model

Comparison of the field displacement results with those from the numerical simulation is essential to verify a numerical model. As mentioned earlier, the Lornex southeast wall was monitored by using an automatic total station and slope-monitoring prisms (see Figure 6.7). The history function in the UDEC-DM was used to monitor the displacement as blocks 1 to 15 were excavated. The cumulative displacement was then plotted against the block number. Figure 6.18 presents a comparison between the measured displacement and the simulation results for SMP#468.

The simulated mining-induced deformations are in good agreement with the field records. The deformation in the numerical model was associated mainly with the removal of the toe blocks which were immediately adjacent to the slope. Excavating the bench blocks resulted in a smaller amount of deformation than excavating the blocks adjacent to the toe.

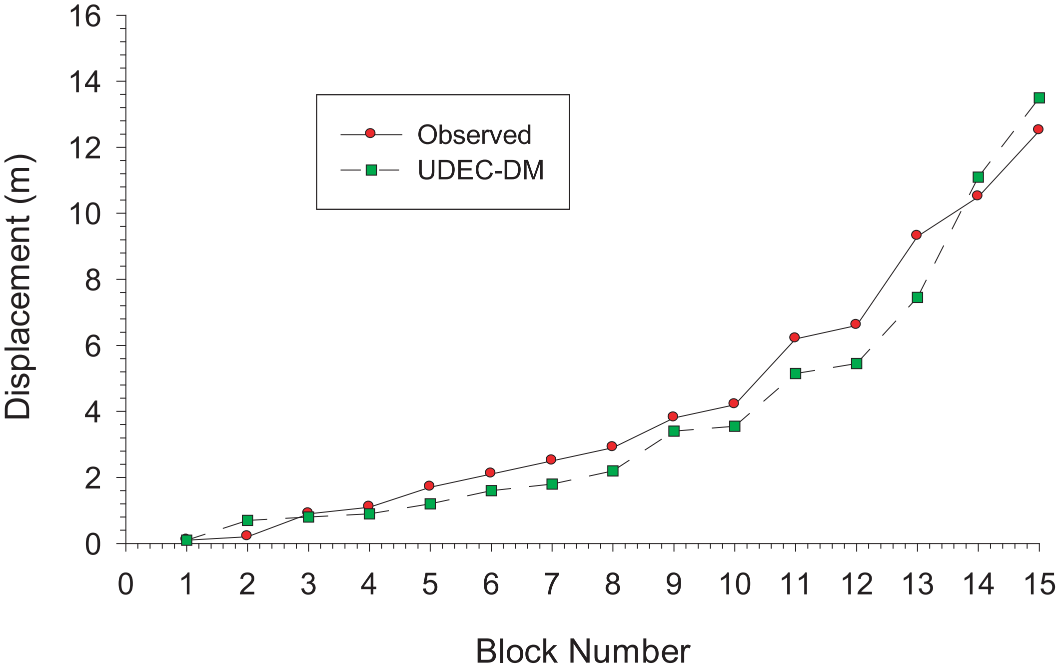

Figure 6.18: Comparison between mining-induced deformation at the field and the UDEC-DM at SMP#468

The mining-induced deformations at SMP#454 (Figure 6.19), also shows a good agreement between the damage model and the field records.

The deformation pattern observed in this toppling example is different from the one observed in the block-flexural toppling discussed in section 5.2.2. In this block toppling, the deformation at the toe is greater than the deformation the top of the slope (Figure 6.20), while in the block-flexural toppling, the deformation at the toe is much less than the deformation at the top of the slope (compare Figure 6.20 with Figure 5.9). This might be attributed to the difference in the orientation of the

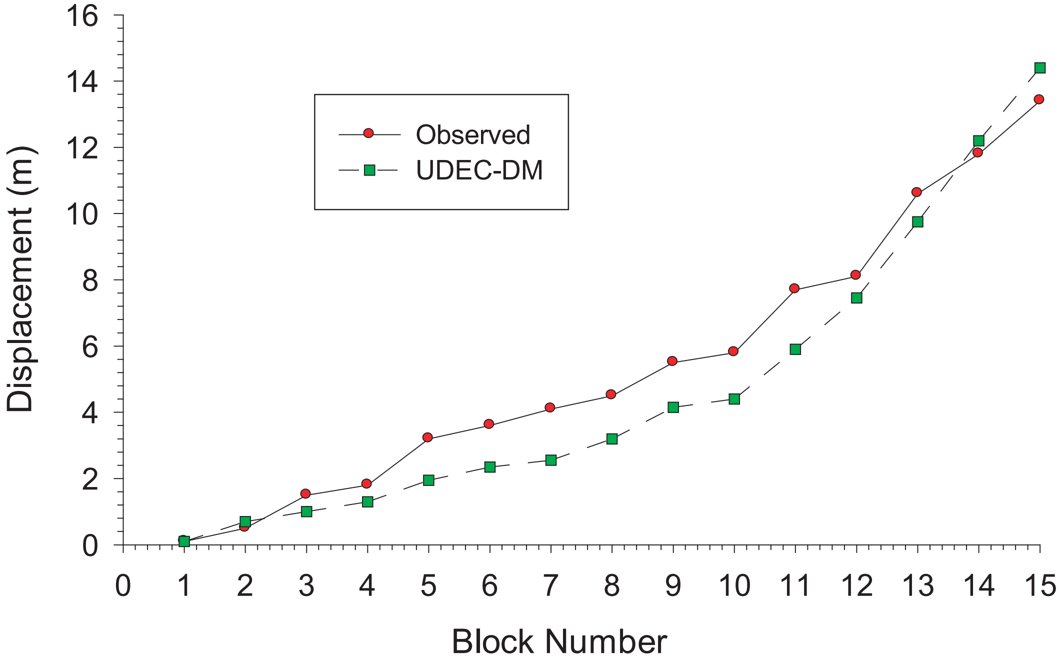

Figure 6.19: Comparison between mining-induced deformation at the field and the UDEC-DM at SMP#454

discontinuities and the dip of the slope face.

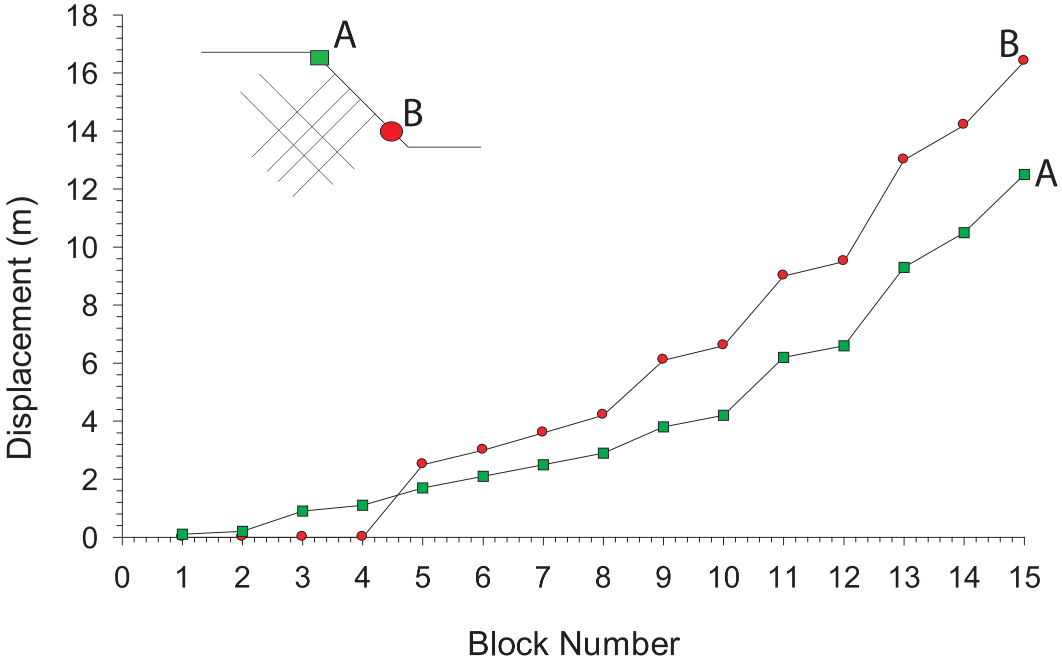

Figure 6.20: Deformation pattern observed in block toppling

6.8.3 Deformation comparison between conventional UDEC and the UDEC-DM approaches

Tosney et al. (2004) used the conventional UDEC to model the Lornex southeast wall. Their results were compared to the results from the UDEC-DM simulation. Figures 6.21 and 6.22 present the results at SMP#413 and SMP#560, respectively. A slight improvement was achieved by using the UDEC-DM at the location of SMP#413. At SMP#560, which is located at the bottom of the slope (see Figure 6.7), UDEC-DM shows a better agreement with the field readings than the conventional UDEC. This result can be attributed to the fracturing capabilities of the UDEC-DM approach. Fracturing through the intact material allow deformation to occur at the toe of the slope. This fracturing is not possible in conventional UDEC.

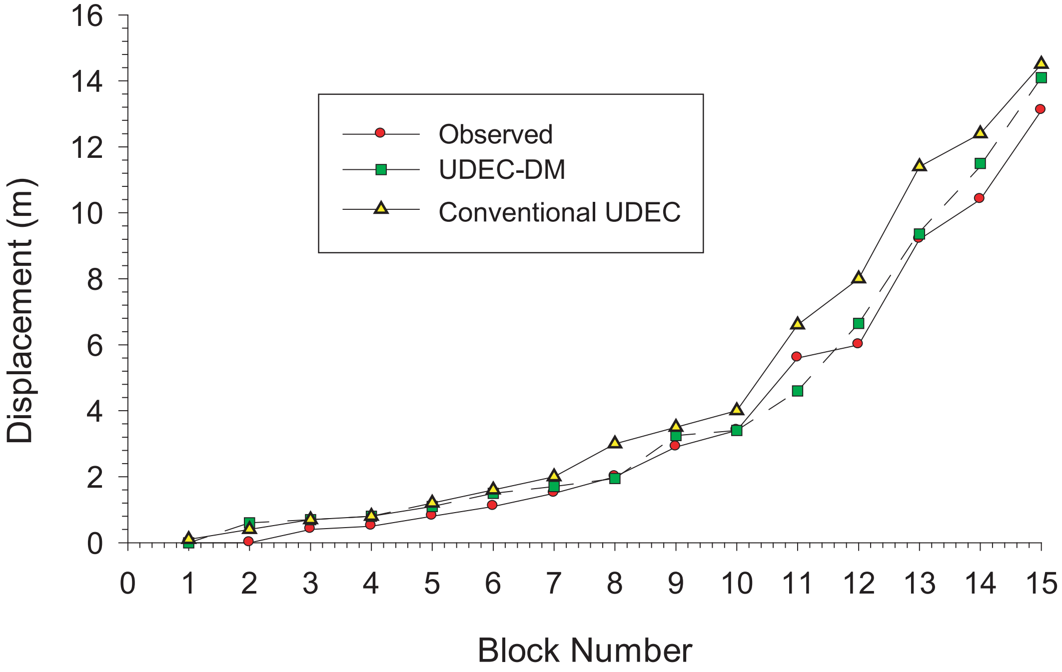

Figure 6.21: Comparison between measured mining-induced displacements and the simulated UDEC-DM displacements at SMP#413

Tosney et al. (2004) noted that the secondary joints was not detected in the fractured material at the toe of the slope. This finding means that fracturing occurred

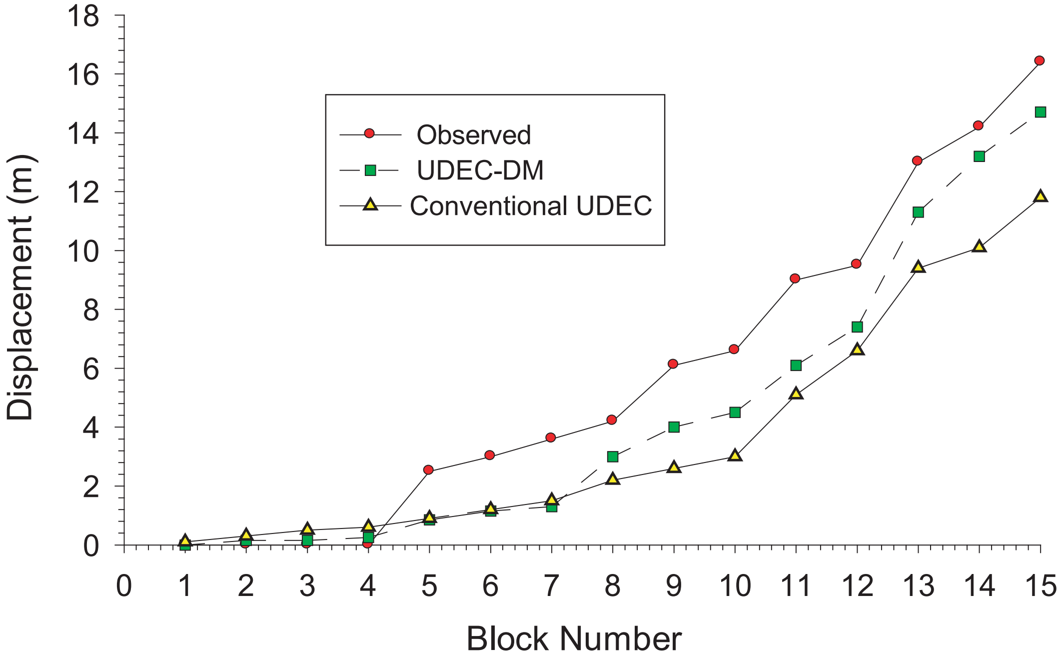

Figure 6.22: Comparison between measured mining-induced displacements and the simulated UDEC-DM displacements at SMP#560

throughout the intact material. In mining environments, risk management of slopes by moving the personnel and the equipment required knowledge of areas susceptible to fracturing and material moving, which might impose some risk on the mining operations. UDEC-DM successfully modeled the bulging and fracturing at the toe of the Lornex southeast wall and captured the deformations associated with this fracturing and the formation of loose material at the open-pit mine toe.

6.8.4 Effect of tensile strength

In the above analysis of the Lornex pit, the tensile strength was assumed to be 0.1 MPa for all the rock units in the slope, and the model was calibrated based on that value. To examine the tensile strength effect of the intact material, the tensile strength was increased to 1.0 MPa, while all the other parameters were kept constant. The mining-induced deformation, as well as the fracturing patterns was monitored to examine if the new tensile strength could alter the behaviour of the slope.

The analysis showed that the tensile strength played a major role in controlling the model. Fracturing inside the model was reduced compared to the fracturing in the low tensile strength model, Figure 6.23 shows the model after excavating block number 15 at the toe of the slope. In both models, the $\sigma_t = 0.1$ MPa and $\sigma_t = 1.0$ MPa, no continuous rupture surface was formed throughout the model as noticed in the field. The decrease of confinement caused intensive fracturing at the toe of the slope, local rupturing at the toe was observed in the numerical simulation as shown at the toe of the slope in Figure 6.23.

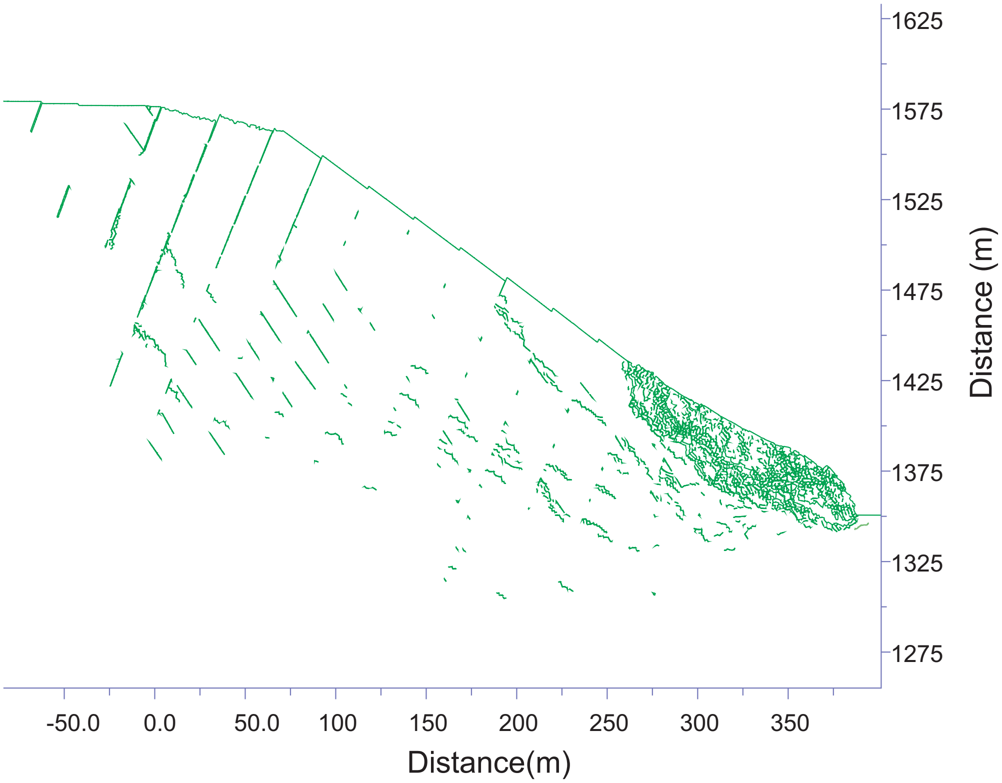

Figure 6.23: Rupturing of the Lornex pit at $\sigma_t = 1.0$ MPa, (compare this figure with Figure 6.16)

The mining-induced deformation in this model was also less than the measured deformation in the $\sigma_t = 0.1$ MPa model. Figure 6.24 shows a comparison between the simulated mining-induced deformation of the two models at SMP#413 along with the measured deformation. The increased tensile strength value reduced yielding and fracturing inside the model and restricted the deformation.

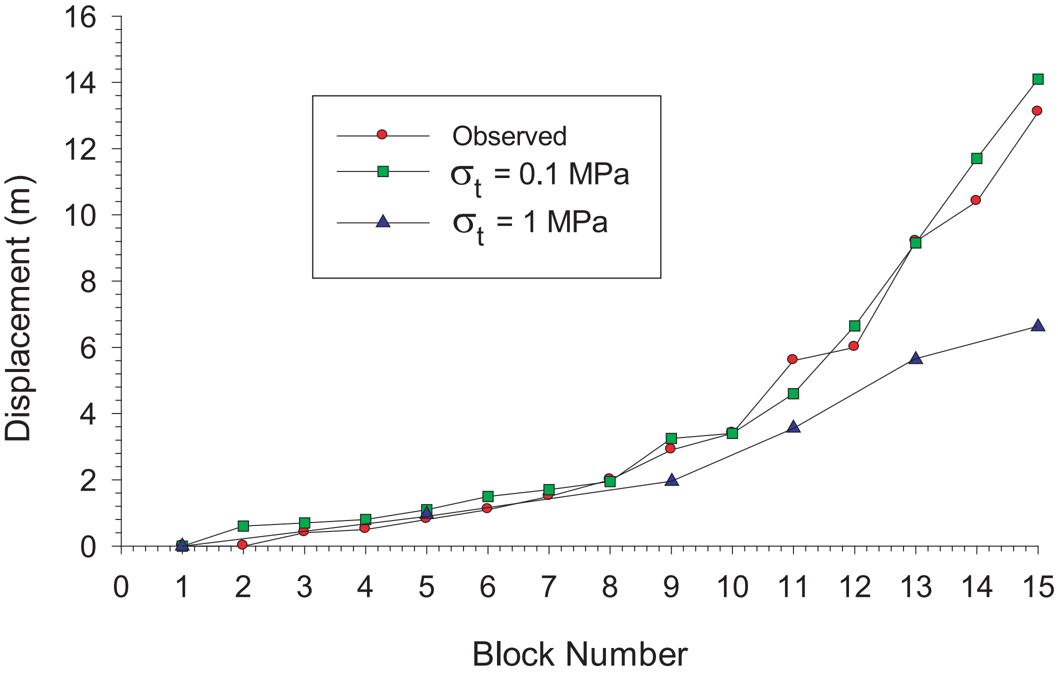

Figure 6.24: Deformation comparison at $\sigma_t = 1.0$ MPa, $\sigma_t = 1.0$ MPa at SMP#413

6.9 Conclusions

The UDEC-DM approach was applied successfully to model a composite rock slide-rock topple. Three main movement modes were observed and modeled using the UDEC-DM. The sliding of the top of the slope exposed normal scarps; the toppling at the middle part of the slope exposed obsequent scarps facing opposite to the slope face, and bulging at the toe formed loose material. The development of the rupture surface at the toe of the slope was traced and did not evolve into a continuous rupture surface throughout the slope. This method was able to capture the composite rock mass movement.

The deformations recorded in the field were compared to the simulation results, and a good agreement was achieved. The UDEC-DM results were also compared to the conventional UDEC results. UDEC-DM showed better agreement with the field observations than the conventional UDEC as a result of the fracturing characteristics implied in the discrete element damage model approach.

The increasing of the tensile strength of the intact material at the Lornex pit decreased damage throughout the slope, and reduced and suspended the mining-induced deformation.

Chapter 7

Progressive Failure in Rock Slopes, Checkerboard Rock Slope

7.1 Introduction

The Checkerboard Creek slope is located upstream of the Revelstoke hydroelectric dam, British Columbia, Canada (Figure 7.1). Upon the completion of the construction of the Revelstoke dam in 1984, a series of active and old tension cracks were discovered up to 150 m above the highway rock cut. This discovery triggered an intensive geotechnical and geological program carried out by British Colombia Hydro to investigate the moving slope, determine the moving volume, and monitor the slope to ensure the safety of the Revelstoke Dam. Figure 7.2 shows the dam and the slide.

After the discovery of the moving slope in 1984, BC Hydro started a detailed investigation of it. The intensive investigation (15 cored holes, shallow trenching, and extensive surface mapping) was to establish the geological stratification and geological structure and discontinuities , and to determine the moving volume, displacement rate, and the possibility of any instability in the Checkerboard Creek slope, (Watson et al., 2004). The slope was found to be moving toward the reservoir at a rate of 10-13 mm/year. This moving is cyclic, beginning as the ground surface cools in October and stopping when the ground begins to warm in April-May. The

Figure 7.1: The general location of the dam

investigation determined that the moving volume is between 2 to 3 million m^3 concentrated in a weathered rock mass near the ground surface.

The monitoring of the slope from 1984 until now has determined that the down slope movement is caused by the thermal cycle experienced by the slope. This thermal cycle, along with different environmental effects, weathered the rock mass and resulted in a weathered region along the slope face. Aydin and Basu (2006) conducted a series of Brazilian tension tests to evaluate the tensile strength of weathered igneous rocks and found that the process of weathering accompanying the microstructural weakening highly affected the tensile strength of the rock; different degrees of weathering resulted in different values in tensile strength. Aydin and Basu (2006) also found that as the tensile strength of the material decreased, the rupture strain increased as a function of the weathering.

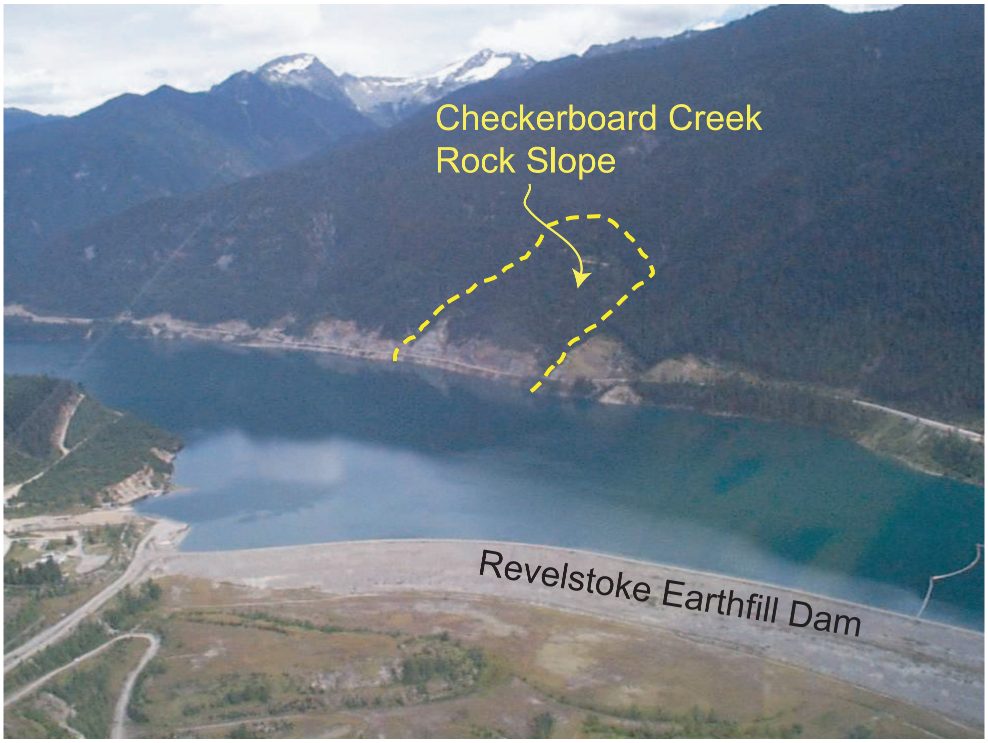

Figure 7.2: The dam and the the outline of the slide (modified from Watson et al., 2006)

This present study investigated the Checkerboard Creek case history to understand the effect of weathering on the slope by using the discrete element method (UDEC-DM). This method allows for the initiation and propagation of cracks in the rock mass and also for the formation of a rupture surface accompanying both the intact rock and the pre-existing discontinuities. The analysis revealed that although total collapse of the slope is highly unlikely, the rock mass adjacent to the highway is susceptible to failure under the weathering process. Two methods were used to simulate the weathering process in the rock mass: degradation of the tensile strength and the constant velocity boundary condition. This study also investigated the possibility of using a supporting system to stabilize the slope. The supporting system consisted of a shotcrete layer and a cable system.

7.2 Geology

The geotechnical and geological aspects of the Revelstoke Dam site have been presented and discussed by Lane (1984), Moore et al. (1997) and Moore and Lewis (1982). In the following, the geology of the site is discussed. The rock mass is composed of igneous rocks, mainly foliated granodiorite overlying the easterly dipping Columbia River Fault. Steeply dipping joints and shears were identified and traced. These joints and shears dip in and out of the slope at 60°-90° from the horizontal. The investigation revealed a variation in the rock mass quality of the slope. A weathered layer is present within the first 60 m from the surface into the slope. This layer composes poor-quality rock: highly weathered, weak, altered and disturbed rock with crushed zones and frequent shears. The movement of the slope is concentrated in this weathered region. Underneath this weathered layer a more competent rock was identified of fair-to-good-quality rock. Localized zones of poor-quality rock were found along the shear zones and joints. Figure 7.3 shows a cross-section through the slope, and Figure 7.4 shows the location of the cross-section. The cross-section shows the weathered region, the complex geological structures in the area subjected to movement, the instrumentation, and the location of the water table used in the numerical model developed in this study.

7.3 Instrumentation and monitoring of the slope

Between 1984 and 2000, extensive slope instrumentation was installed in the slope area to monitor the displacement, pore water pressure, and the temperature change. These instruments included inclinometers, borehole and surface extensometers, electronic distance measurement, time domain reflectmetry cables, surface strain metres, piezometeers and borehole and surface thermistors. For the details of the instrumentations and their distribution in the boreholes, see Watson et al. (2006).

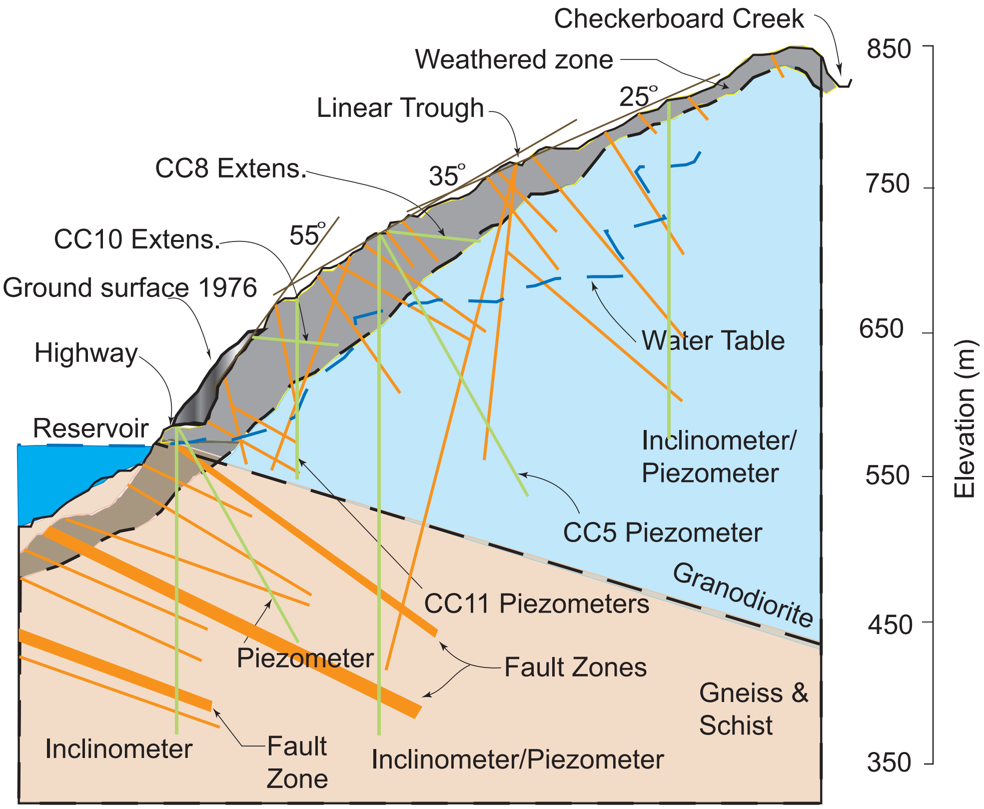

Figure 7.3: Detailed cross-section along the Checkerboard Creek slope (modified from Watson et al., 2006)

Readings from the instruments were recorded by an automatic data acquisition system and later processed.

The monitoring revealed that the slope is moving in a cyclic mode at a displacement rate between 0.5 to 13 mm/year depending on the location of the monitoring point at the slope. The cyclic nature of the displacement was found to be associated with the seasonal temperature. Figure 7.5 shows the displacement pattern along with the temperature and water level variation in the slope. The slope movement resumes during the cold weather between early autumn to late winter. During the rest of the year, limited to no displacement was recorded.

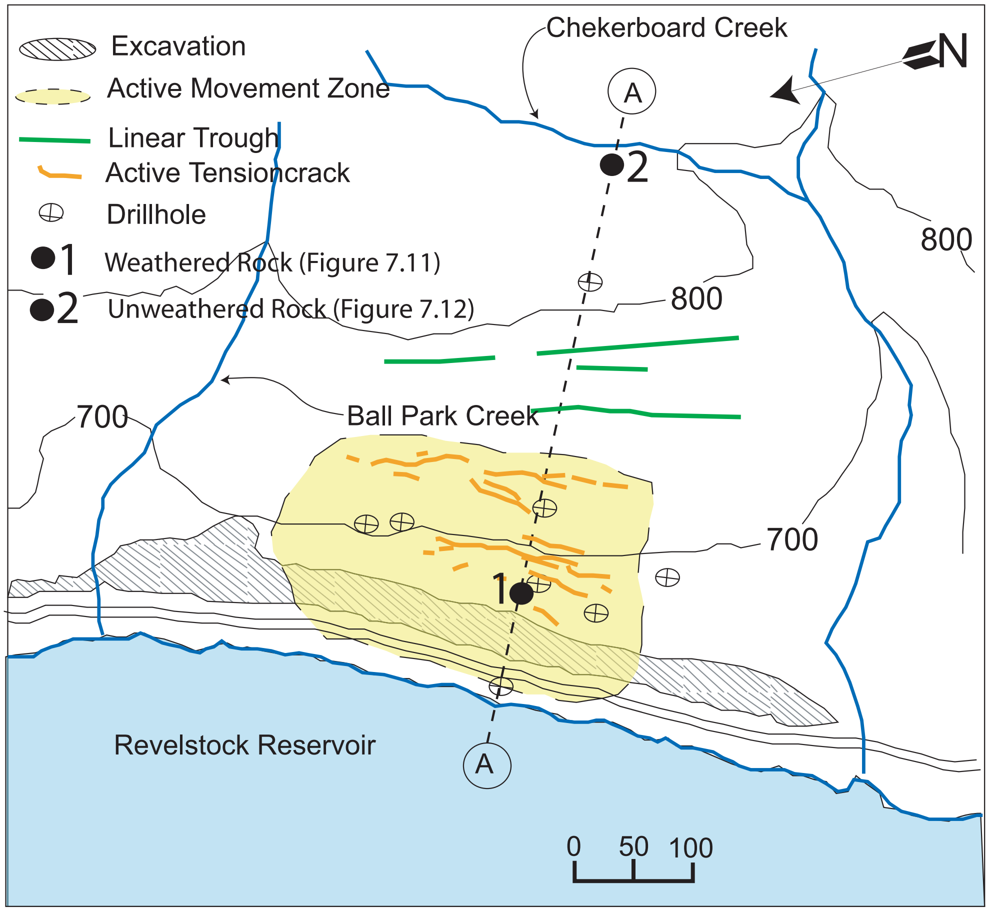

Figure 7.4: Location of the cross-section AA, 1 and 2 are locations of weathered and unweathered rock photographs, Figure 7.11 and Figure 7.12, respectively, (modified from Watson et al., 2006)

7.4 Groundwater and climate

The average annual precipitation at Checkerboard Creek is between 1500 mm to 2000 mm. The highest total monthly precipitation occurs in December. The average air temperature ranges from -25 °C to 35 °C. Freezing occurs between November to March. In 1993, packer tests were conducted to establish the ground water condition (Moore et al., 1997). In addition, continuous readings were taken from the piezometers installed in the slope. The piezometric data indicated that the saturated conditions exist 50m to 80m below the ground surface. See Figure 7.3 for the interpreted water table location. A downward pressure gradient exists, and the

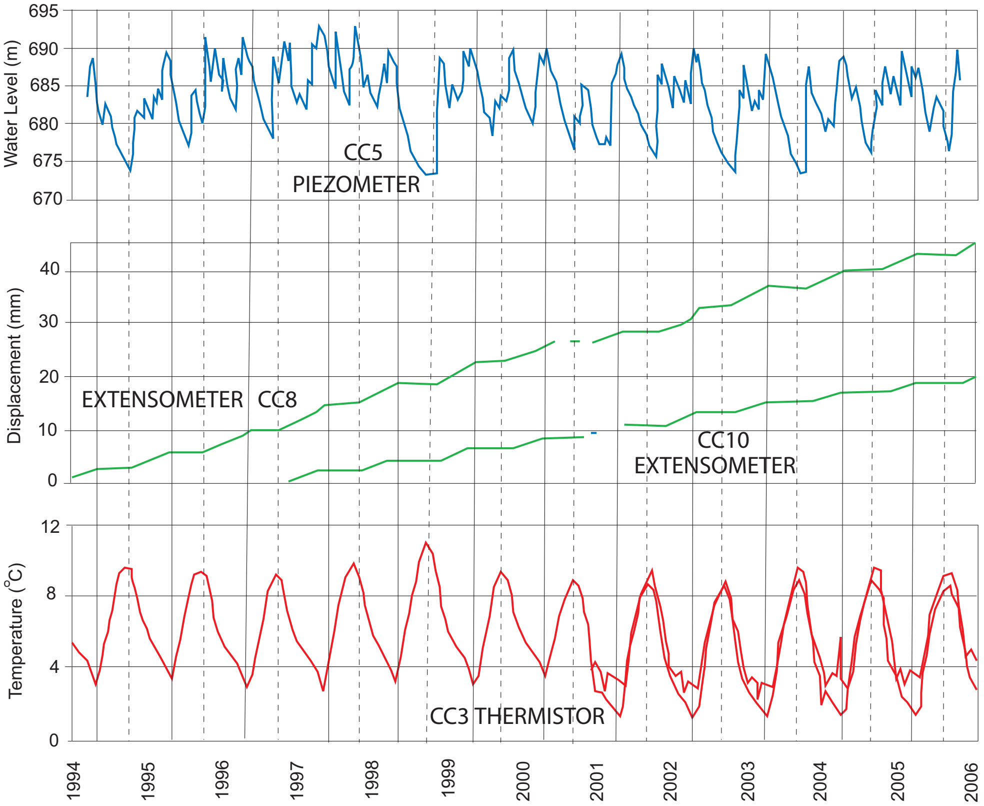

Figure 7.5: Deformation pattern along with the temperature and the variation of water level (modified from Watson et al., 2004)

main recharge source is from the infiltration of the surface water. The water table was incorporated into the numerical model presented in this study.

7.5 Previous work

Due to the risk associated with any potential failure of the Checkerboard Creek slide, Watson et al. (2006) conducted extensive numerical and physical modeling. In their numerical modeling program, these researchers used the conventional discrete element code UDEC to study the stability of the slope and the effect of the temperature variation on the slope. The aim of the physical modeling was to determine the risk associated with a small toe failure.

The numerical model confirmed that the down-slope movement observed by the monitoring system is associated with the seasonal temperature variation. According to Watson et al. (2006) the slope would be stable even during a large magnitude earthquake. The geometry and the joint distribution along with the joint's properties from Watson's analysis were used in this current study. In the physical modeling, the possibility of toe failure was studied; this failure would have a limited effect on the dam body and would not generate a wave that would overtop the dam.

The weathering of the rock slope was extensive within the first 60 m from the ground surface of the slope (Figure 7.6). This weathering process was not studied and might have a dramatic effect on the tensile strength of the rock mass. The degradation of the tensile strength over long period of time might compromise the safety of the rock slope, especially at its steepest angle near the highway shoulder (Figure 7.3). This process of weathering is discussed further in the following sections.

Figure 7.6: Weathering at the surface of the slope adjacent to the highway

Table 7.1: Elastic properties for the rock formations

Property	Hornblend Gneiss and Mica Schist		Granodiorite		Columbia River
	Fresh	Weathered	Fresh	Weathered	Fault and Shears
E (GPa)	6.5	3.6	17.7	3.6	0.5
υ	0.25	0.27	0.23	0.27	0.3

7.6 The numerical model

The discrete element method has been long recognized for its ability to model rock mass behaviour in underground and near- surface rock applications. This method can simulate explicitly discontinuities inside the rock mass. In this study, the proposed discrete element damage method is used to simulate the Checkerboard Creek rock slope and to examine the effect of the weathering process on the slope instability. The UDEC-DM is able to simulate fracturing through intact material, as the stresses in the rock mass exceed the strength of the intact material and allow these fractures to propagate and possibly coalesce to form a rupture surface. This method inherited the conventional UDEC's ability to simulate persistent discontinuities. Figure 7.7 shows the blocky nature of the rock mass that form the rock slope. As shown in the figure, the rock slope is highly heterogenous with randomly-shaped blocks. This justifies the use of the mosaic block tessellation to generate polygonal blocks in two dimensions that can simulate the rock slope behaviour realistically.

The numerical model geometry and discontinuities distribution were adapted from Watson et al. (2006) analysis. A network of flaws was generated inside the rock mass. These flaws, had an average length of 1.3 m, formed random polygonal blocks. All the discontinuities and the geological units were included in the simulation along with the weathered region. Figure 7.8 shows the general UDEC-DM used in this study. Figure 7.9 shows the details of the UDEC-DM in the area of interest. Table 7.1 shows the elastic properties of the rock units used in the current numerical model.

Figure 7.7: Rock mass surface exposure showing the blocky nature of the rock mass

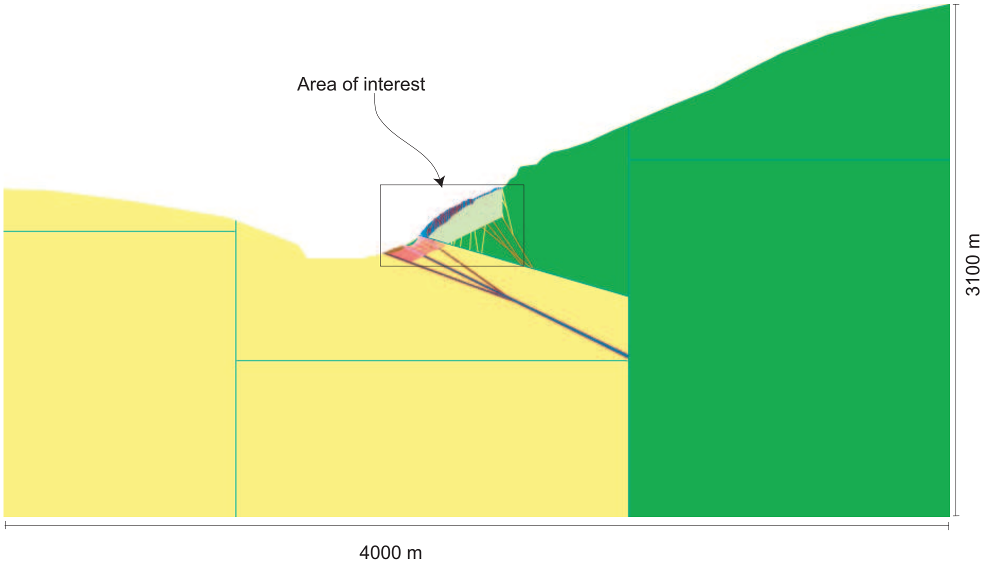

Figure 7.8: The numerical model used in the study

In order to determine the strength properties of the different rock units in the model, the Hoek-Brown failure criterion was used (Hoek et al. (2002)). The dis-

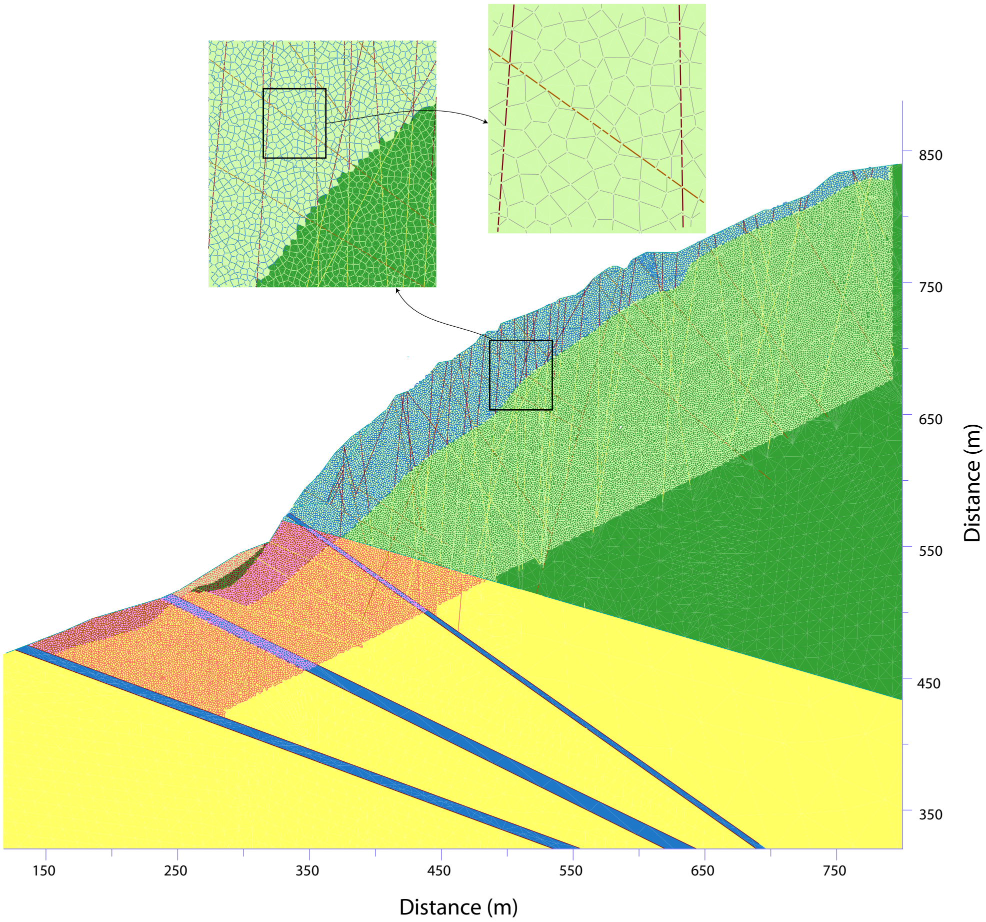

Figure 7.9: The details of the joints and flaws

continuities' properties (friction, cohesion and shear and normal stiffness) were adapted from Watson et al. (2006). Table 7.2 and Table 7.3 show the intact material and joints properties, respectively.

To establish the flaws' normal and shear stiffness, Equation 4.9 was used to estimate the the Normal and shea stiffness of the flaws in this current study. The failure criterion used in this numerical model was the Mohr-Coulomb failure criterion with tension cut-off.

7.7 Effect of weathering and stability analysis

Aydin and Basu (2006) thoroughly discussed the relation between the degree of

Table 7.2: Strength properties for the flaws

Property	Hornblende Gneiss and Mica Schist		Granodiorite		Columbia River
	Fresh	Weathered	Fresh	Weathered	Fault and Shears
σ_{ci} (MPa)	133	76	100	75	
GSI	60	35	35	35	
mi	26	20	29	26	
ϕ °	48	34	41	36	18
C (MPa)	5.0	2.4	3.2	2.5	0.1
σ_t	0.33	0.022	.026	0.016	0.0
kn (GPa/m)	18e9	5e9	22e9	6e9	1.5e9
ks (GPa/m)	18e8	5e8	22e8	6e8	1.5e8

Table 7.3: Joints properties used in the UDEC-DM

Property	Cross-Cutting Shears	Near-Vertical Joints		Major Faults	Shears in Hornblende Gneiss and Mica Schist
		Fresh	Weathered		
kn (GPa/m)	5	50	2	0.5	2
ks (GPa/m)	1	5	0.4	0.1	0.4
ϕ°	25	35	25	18	18
C (MPa)	0.0	0.005	0.0	0.0	0

weathering and the tensile strength and stated that as the degree of weathering increases, the tensile strength decreases dramatically. Aydin and Basu (2006) also argued that the strain at failure greatly increases as the degree of weathering increases. Figure 7.10 shows the effect of weathering on the tensile strength.

In the Checkerboard Creek slope, the weathering of the rock mass is extensive in the moving area (Figure 7.11), while up the slope the rock mass is unweathered as shown in Figure 7.12. Notice the amount of fracturing and discolouration in Figure 7.11 compared to Figure 7.12.

7.7.1 Tensile strength degradation

To study the effect of weathering on the Checkerboard Creek slope, the cohesion, and friction of each geological unit was estimated using the Hoek-Brown criterion and the GSI index for each rock formation. The GSI index used in this study was adapted from Watson et al. (2006) (see Table 7.2). Two methods to simulate the

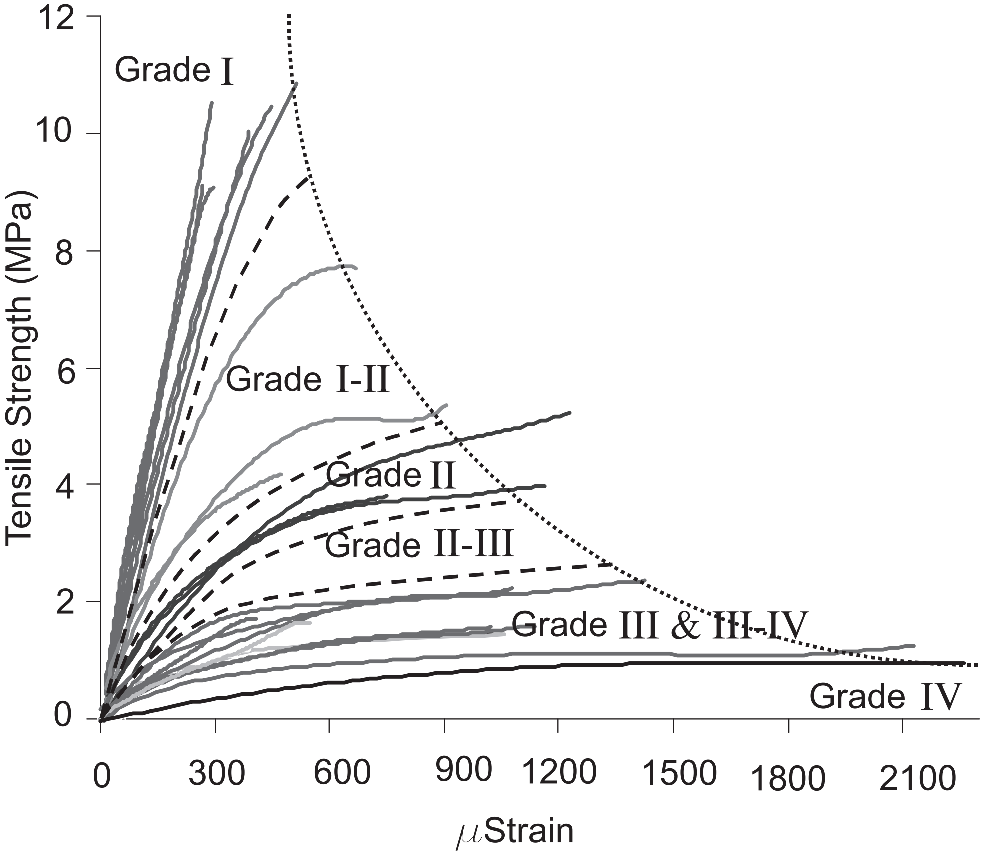

Figure 7.10: Effect of weathering on tensile strength and strain at failure (modified from Aydin and Basu, 2006)

weathering effect were used in this study. The first one included the degradation of tensile strength until failure, a method which simulates an increased degree of weathering. The second approach to modeling the weathering process was adapted from Aydin and Basu (2006) experimental results by applying a constant displacement rate at the weathered region.

The Unconfined Compressive Strength (UCS) of the geological units was varied to determine the back calculated tensile strength at failure. The UCS's used are 75, 60, 50, 40, and 30 MPa. Figure 7.13 shows the Hoek-Brown failure envelopes used to calculate the instantaneous friction angle and cohesion in this analysis. At each Unconfined Compressive Strength the tensile strength was assumed to be equal to the cohesion derived from the Hoek-Brown failure criterion. The tensile strength

Figure 7.11: Weathered rock mass along cross-section A-A, the photograph has been taken at location 1, as shown in Figure 7.3 (1)

was then decreased gradually until failure,if any, occurred. The displacement, velocity, fracturing and unbalanced forced was monitored to determine if the failure state had been achieved. Table 7.4 shows the back-calculated tensile strength at limit-equilibrium corresponding to the different values of the UCS. Table 7.4 shows that tensile strength degradation might result in failure.

Although failure occurred, it was limited to the area adjacent to the highway cut (Figure 7.14). The region adjacent to the highway cut shows initiation of fractures and formation of a rupture surface. The failure mechanism involved was sliding and, along the near-vertical joints, toppling of rock columns. The rock mass moved down the slope toward the reservoir. Figure 7.15 shows the propagation of failure at the slope toe. This failure was concentrated at the steepest part of the slope, the ground surface slope at the highway cut around 55° (see Figure 7.3). Watson et al.

Figure 7.12: Unweathered rock mass along cross-section A-A, the photograph has been taken at location 2, as shown in Figure 7.3 (2)

(2006) noticed that this portion of the slope might be at risk and used a physical model to study the effect of such slope failure on developing a wave that might overtop the Revelstoke Dam body. They concluded that such a failure would have a minor effect on the dam's safety.

As shown in Table 7.4 the back calculated tensile strength required for limit equilibrium increased as the unconfined compressive strength decreased, i.e., for

Table 7.4: Unconfined compressive strength versus the back calculated tensile strength at Failure

Unconfined Compressive Strength (MPa)	σ_t at failure
76	0.025
60	0.2
50	0.35
40	0.45
30	0.65

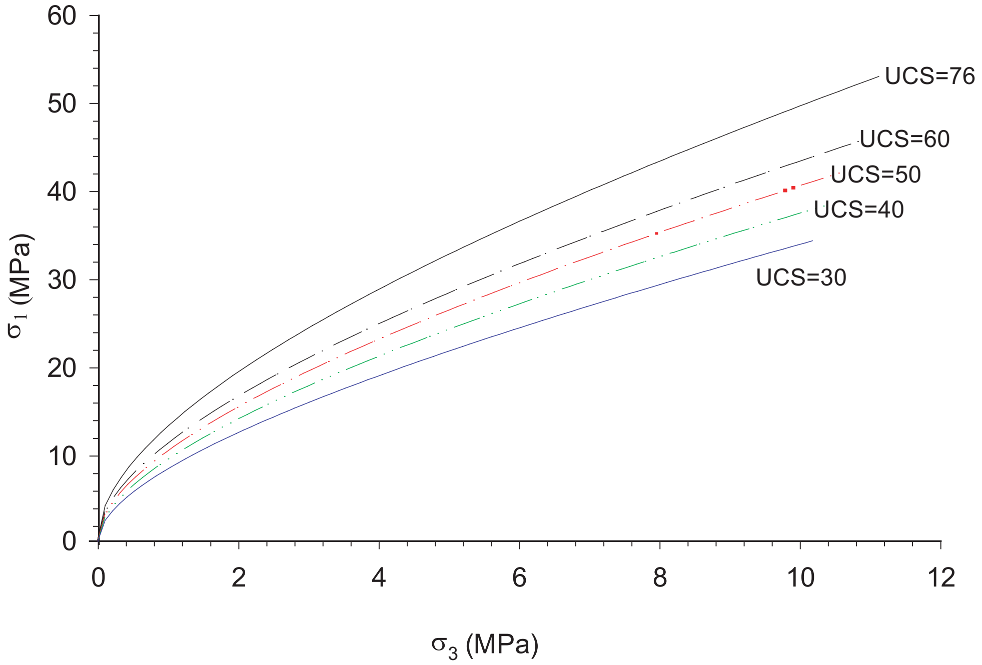

Figure 7.13: Hoek-Brown strength envelope used to obtain the friction angle and cohesion used in this study

lower UCS we need higher tensile strength to stabilize the slope. That implies that cohesion and friction angle affect the slope instability. However, in many rocks, the cohesive forces are dominated by ionic and covalent bonds which are not readily susceptible to environmental factors. These bonds are weaker in tension than in shear and may break at relatively low tensile stresses. Aydin and Basu (2006) showed using Brazilian tensile tests that the tensile strength of a rock is extremely sensitive to the degree of weathering. They found that the tensile strength could decrease by an order of magnitude depending on the extent of weathering and the stiffness of the rock decreased as the tensile strength decreased. By assuming that the weathering only affected the tensile strength while the friction and cohesion remained constant or varied at a very small rate, the tensile strength is destroyed long before the frictional strength and that compromises rock slope stability. In other words, weathering may be a significant factor in controlling the behaviour of rock slopes, if the stability of the slope is controlled by the tensile strength. The tensile strength effect on low stress-highly weathered slopes is usually ignored.

The tensile strength predicted by Hoek et al. (2002) ranged between 9 kPa to 20 kPa, while the back-calculated tensile strengths in this analysis as shown in Table 7.4 range between 25 kPa to 650 kPa. According to this present study, Hoek-Brown criterion tends to underestimate the tensile strength of rock masses.

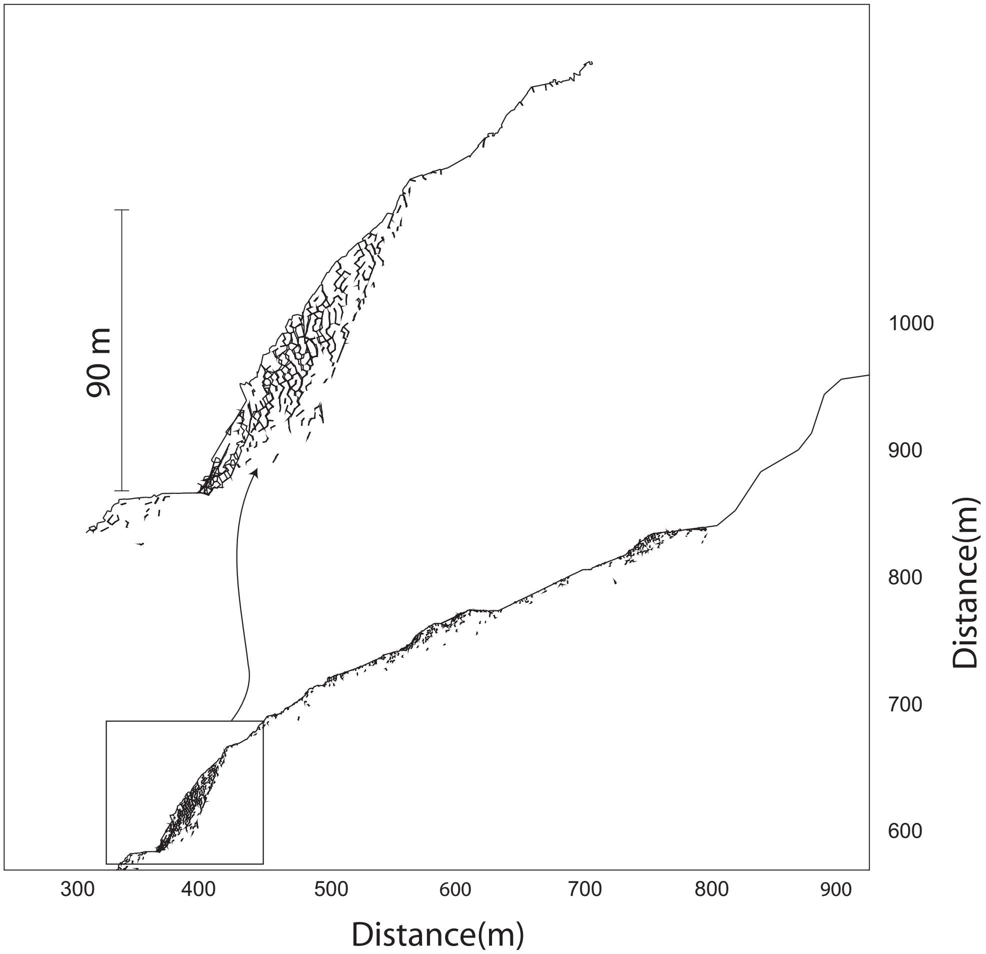

Figure 7.14: Initiation of failure at the side of the highway

Figure 7.16 shows the progressive movement of the failed material toward the reservoir as a result of tensile strength degradation. Another attempt was made to simulate the rock slope and to predict the failure mechanism and extent, if any, by assuming the same properties for the entire slope. The flaws in the weathered and unweathered geological units were assumed to have an unconfined compres-

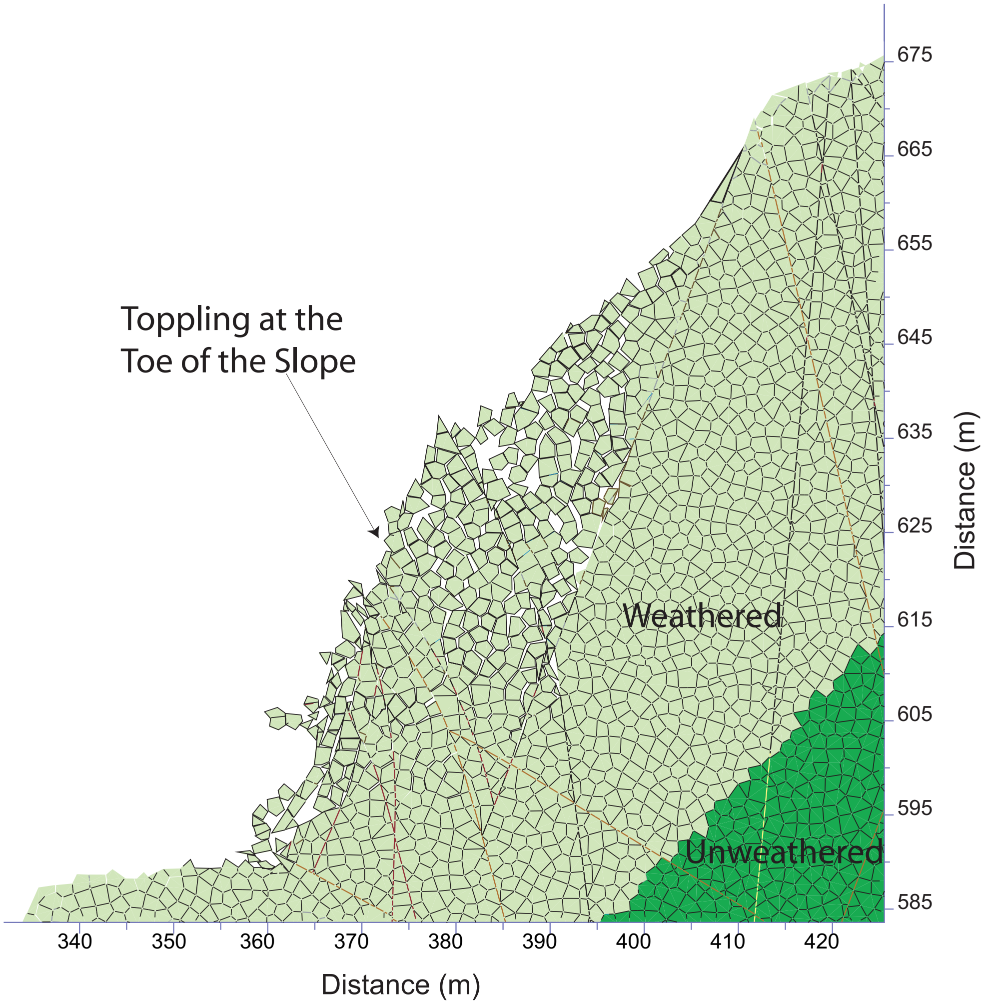

Figure 7.15: Failure development at the toe of the slope

sive strength of 60 MPa, and the tensile strength was back-calculated. Failure was initiated at a tensile strength of 0.2 MPa. The mechanism of failure involved sliding and toppling and was restricted to the steepest slope portion near the highway cut.

7.7.2 Displacement rate boundary condition

Aydin and Basu (2006) showed that the decay in tensile strength as a function of weathering is associated with an increase in the rupture strain. Figure 7.10 shows that as the tensile strength of the sample decreased, the strain at failure increased. In this present study, the simulation of this process involved the application of a

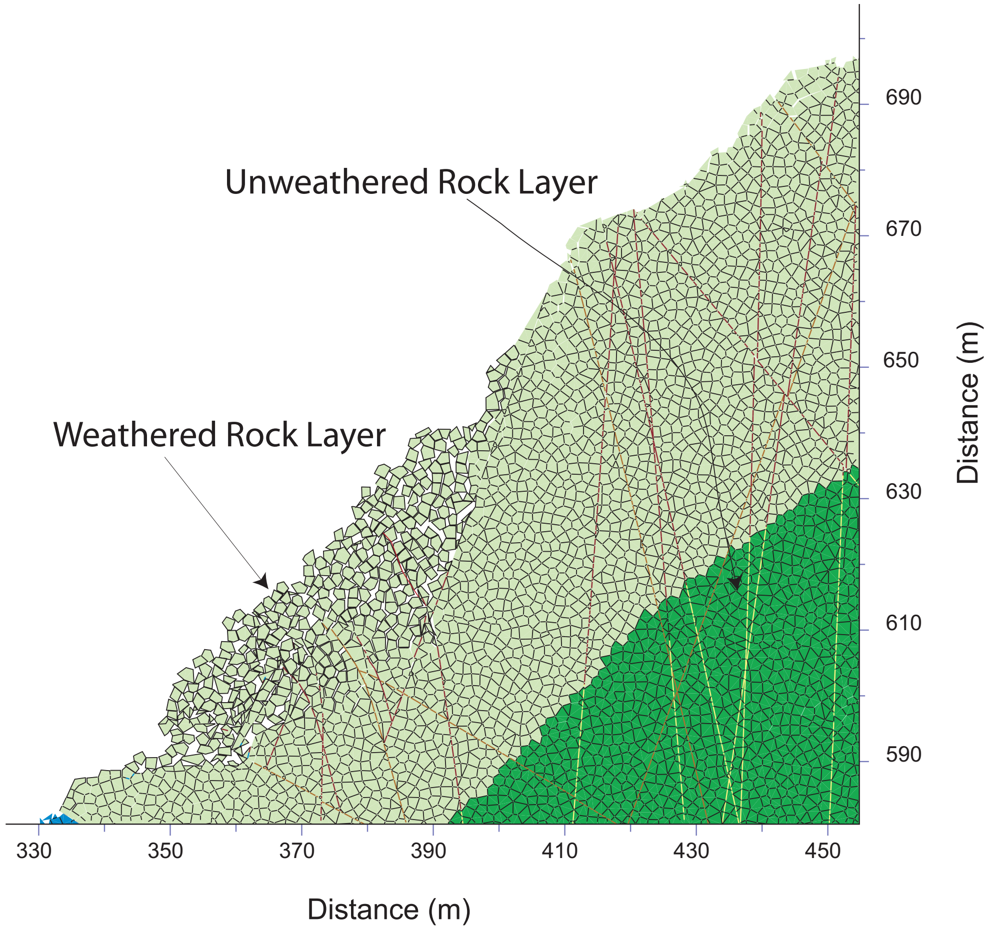

Figure 7.16: Progressive movement of the failed material toward the reservoir

constant velocity rate boundary condition at the weathered region of the rock slope. The boundary condition was applied to the weathered region and allowed a total displacement of 1.8-1.9 m at the surface to occur. The fracturing inside the weathered rock was more intense than the fracturing due to the direct tensile strength degradation. Figure 7.17 shows the fracturing in the weathered region as a result of the displacement applied to the surface. Compare Figure 7.14 with Figure 7.17. The insert in figure 7.17 shows the displacement profile in the weathered region. After subjecting the slope to the displacement rate boundary condition on the surface of the slope, it was set to the free condition to allow deformation to occur untill equilibrium or failure was achieved. This method allowed the slope to deform freely and resulted in extensive fracturing at the toe of the slope. Although the fracturing and joints opening were more extensive with this second method, only the part of the slope at the highway cut failed, and the failed material started to move toward the reservoir. The rest of the slope came to a stable condition. The results were very similar to the one shown in Figure 7.15. According to the monitoring program, the slope was moving at an average of 10 mm/year. Although, the weathered material moved around 1.8 m, no total failure occurred. The 1.8 m of displacement occurring in the simulation is equivalent to the displacement during 180 years at the current rate of displacement.

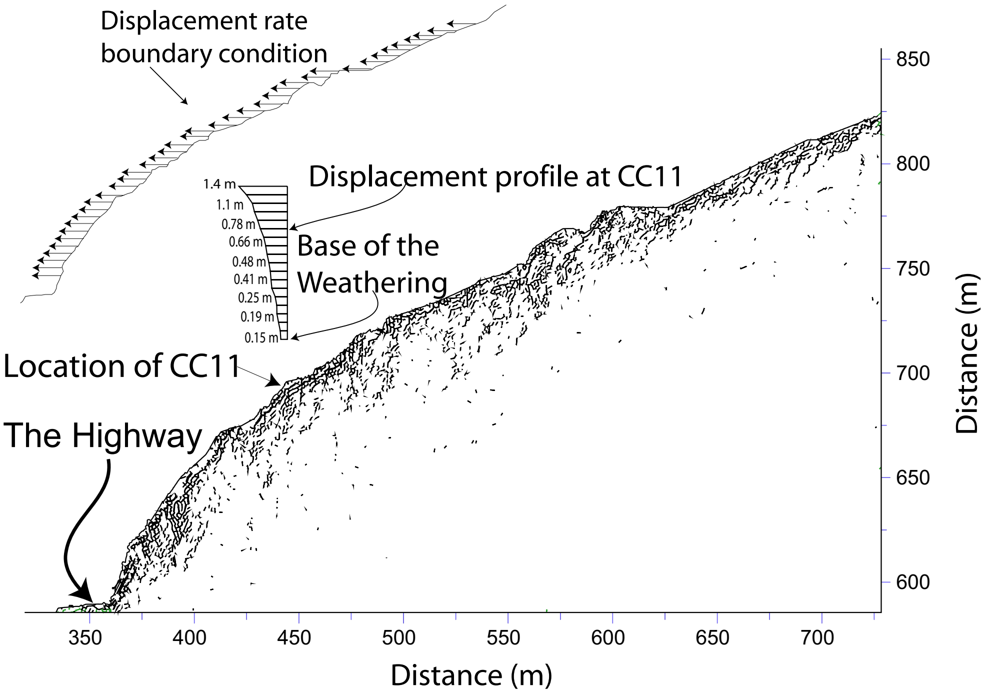

Figure 7.17: Fracturing in the weathered rock mass after 1.8 m of displacement under constant velocity

7.8 Suggested supporting system

The results of the analysis presented in this study showed that the weathering process might result in failure of the slope near the highway cut. This result might lead to retrogressive failure up the slope as a result of steepening the slope as the failed material moves toward the reservoir. To further investigate this possibility, the moved material at the toe of the slope was excavated. As expected, the numerical modeling showed that the previously stable part of the slope started to move toward the reservoir. The newly formed surface resulting from the excavation was a 60° slope. Figure 7.18 shows the failed material moving down the slope. To avoid the consequences of any retrogressive failure, a support system composed of a shotcrete layer and a cable system was designed and tested numerically. This simulation was not intended to optimize the support system but, rather, to facilitate using a support system at the site. Passive anchors were used to stabilize the Marble shear block, which is another slide at the Revelstoke project (Martin and Kaiser, 1984).

A cable system was installed inside the weathered rock region and back into the stable rock mass, as shown in Figure 7.19. The cables were spaced at an average of 8 m in apart. At the surface, 20 cm of shotcrete layer was applied (see Figure 7.19). The weathered rock mass was assumed to have weak properties: UCS of 30 MPa and tensile strength of 0.8 MPa. The tensile strength was then decreased gradually to 0.5 MPa. The velocity, displacement and unbalanced forces in the numerical model was monitored. The system was able to limit the displacement and stabilized the system, Figure 7.20 shows the effect of a support system on the displacement pattern at the model. To further test the model, the tensile strength was reduced to 0.2 and 0.1, respectively. The results were similar to those obtained from the 0.5 MPa of tensile strength model. The slope was stabilized with no failure propagation, and the fracturing was very minimal. Table 7.5 shows the properties of the shotcrete layer and the cables.

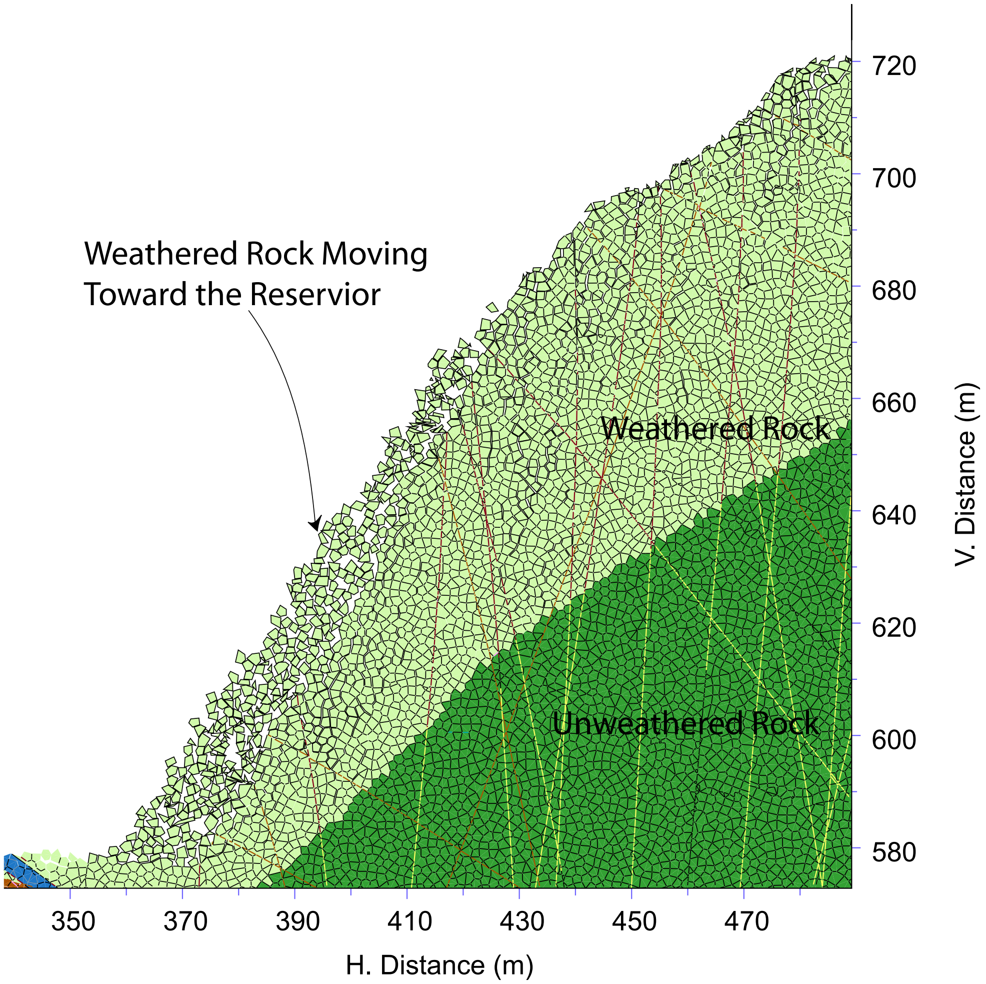

Figure 7.18: Continuous failure after the removal of the first failed material

Table 7.5: Support system properties

Property	Shotcrete	Cable
Area (mm^2)		625
Thickness (mm)	100	
E (GPa)	20	98
Tensile strength at yield	3.0 (MPa)	0.548 (MN)
Compressive Strength (MPa)	30	10000
Cohesion bond (MPa)	2.0	
Tensile bond (MPa)	1.0	
Grount shear stiffness (GN/m/m)		6
Grout Shear strength (MN/m)		0.32

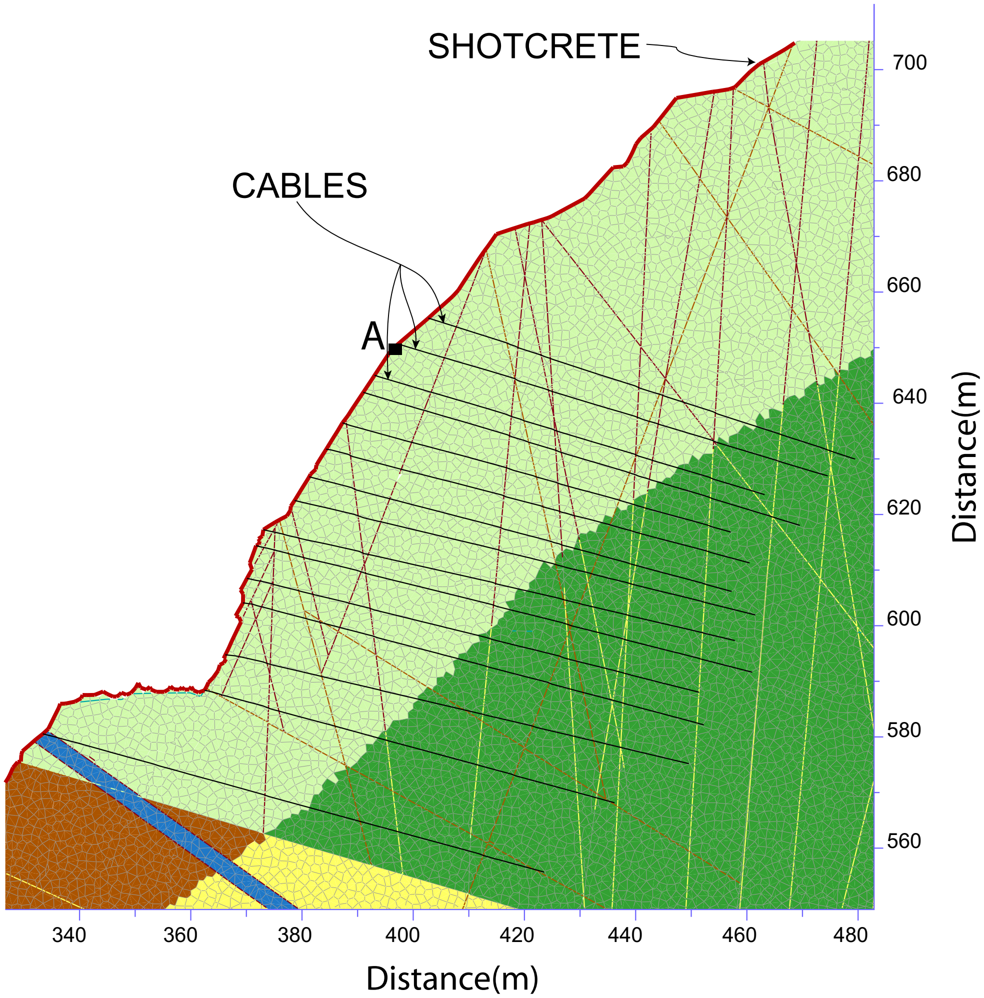

Figure 7.19: Proposed support system contains of 20 cm shotcrete and cables at an average distance of 8.0 m

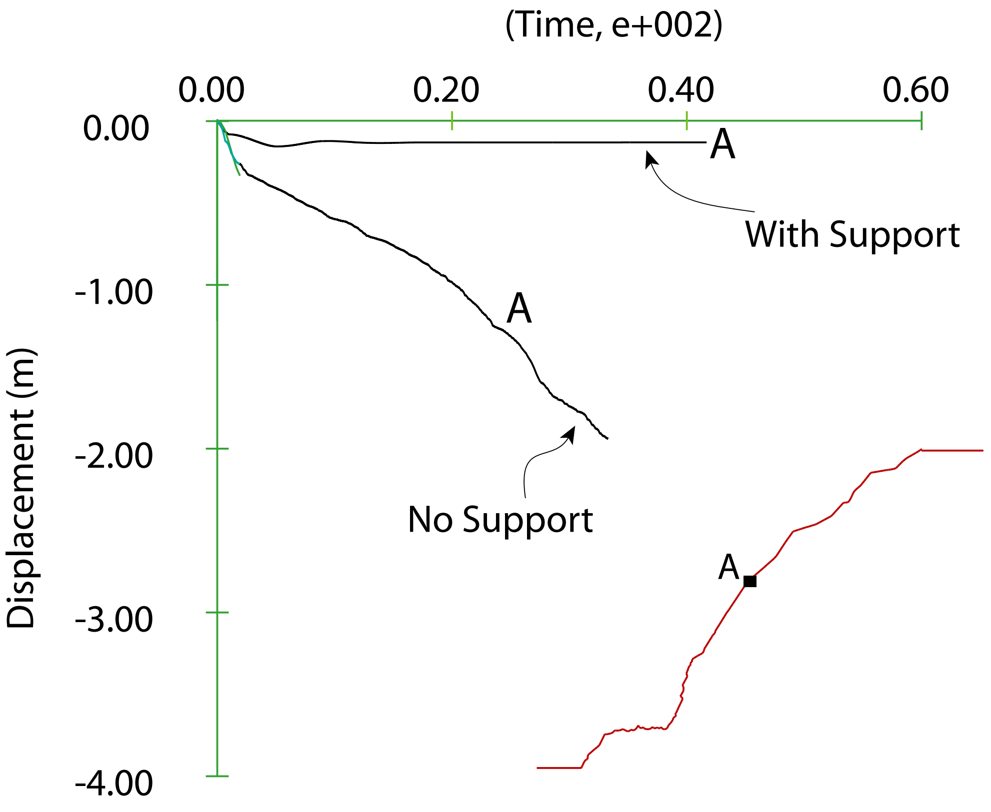

Figure 7.20: Effect of a support system at the displacements at point A (see Figure 7.19 for location of A)

7.9 Conclusion

The discrete element damage approach was applied to simulate the weathering process at the Checkerboard Creek rock slope. The weathering process was simulated using two methods: degradation of the tensile strength and a velocity boundary condition at the weathered region. Both methods predicted that the failure is concentrated at the slope toe near the highway cut at the steepest part of the slope. The tensile strength destruction for both the weathered and unweathered regions resulted in failure concentrated at the steepest part of the slope near the highway cut. To avoid the possibility of progressive failure, a support system consisting of shotcrete and cables was used successfully to stabilize the moving rock slope near the highway cut at a reduced tensile strength value. The UDEC-DM is capable of handling complex rock slopes and might be used to design and predict rock slopes' susceptibility to failure or movement. This hybrid numerical modeling approach was applied successfully to the Checkerboard Creek rock slope and might be incorporated in future studies to assess the risk associated with this case history.

Chapter 8

Summary and Conclusion

8.1 Summary

Rock slopes can be classified into many categories based on the material involved in the slope and the movement rate. The most common rock-slope movements are simple sliding, wedge failure, and toppling failure. Rock-slope movements involve many factors such as the discontinuities' distribution, in situ stress regime, coupled processes and complex geometries. To increase the reliability of an analysis, these factors and others should be considered. Many methods can be used to analyze rock slopes, such as limit equilibrium, physical modeling and numerical methods. This thesis discussed the most common methods used to analyze rock slopes.

Due to the great advances in computer' processing time, many numerical methods have been developed to handle complex and coupled processes in rock slopes. The most commonly used are the continuum modeling, discontinuum modeling, and, more recently, the hybrid methods. This thesis presented a modeling approach by implementing a degree of freedom inside the conventional discrete element code UDEC. This degree of freedom allowed non-directional rupturing to initiate and propagate throughout intact rock material. In UDEC-DM, the intact material is modeled as a network of connected flaws, which form interlocked randomly sized blocks. The boundaries between the blocks mimic the grain boundaries or any bigger flaws in any rock formation, and fracture will follow the polygonal boundaries of these blocks. As the stresses inside a rock mass exceed its strength, failure is initiated and might propagate to form a physical rupture surface in the rock formation. The UDEC-DM can be calibrated to model the evolution of a rupture surface and to track the effect of tensile strength degradation on rock slopes.

Lajtai (1969c) discussed the compatibly of the direct shear tests with the natural loading conditions in rock slopes. He argued that tensile stresses can be responsible for rock bridges fracturing and that the tensile strength contributes to the non-linearity of the failure envelope. Lajtai (1969b) presented direct shear tests results demonstrating the effect of the tensile strength on the failure envelope. The UDEC-DM was used to model Lajtai's experiment and showed good agreement with the non-linear experimental failure envelope. The results showed the effect of non-persistent joints and the progressive failure effect on the failure envelope. As the normal stress increased, the yielding point became closer to the frictional strength of the rock. Lajtai (1969a) also noticed this effect.

Simple rock slopes such as simple toppling, buckling were used to examine the ability of the UDEC-DM. The results showed good agreement with the field observations and that the tensile strength can affect the behaviour of rock slopes. Aydin and Basu (2006) examined the effect of the weathering process on the tensile strength on rock samples in the laboratory. They found that as the degree of weathering increased the tensile strength decreased dramatically. This conclusion showed the importance of considering the tensile strength effect on rock slopes. According to the numerical modeling tests on examples of simple rock slopes, the tensile strength degradation can trigger the movement of rock slopes. In the case of buckling failure, the tensile strength had a greater role in controlling the rock slopes than the frictional strength. A simple parametric study on a buckling movement in the Rocky Mountains showed that in situ stresses can affect the tensile strength required to stabilize the buckle.

To verify the UDEC-DM, two case studies from the laboratory were used. The first case was from Adhikary and Dyskin (2006), who used rock-like material to model flexural toppling through laboratory centrifugel modeling. Their model provided high-quality of data in terms of the strength properties and the deformation during loading. Two modeling approaches were used to model their experiment: the conventional UDEC, and the UDEC-DM. The deformations, rupture surface formation, and the load at failure were compared. The UDEC-DM simulation results showed a better agreement with the laboratory results than the conventional UDEC. The tensile strength of the intact material controls the flexural toppling while the frictional strength has only a minor role. The second case study was from Zhang et al. (2006). The UDEC-DM results showed a better agreement with the laboratory results than the conventional UDEC. In both simulations, UDEC tended to predict a deeper rupture than the experimental results while the UDEC-DM predicted a more accurate rupture surface. Also, the UDEC-DM was able to predict accurately the failure load.

In large-scale rock slopes susceptible to toppling movement, two cases were examined. The first was a hypothetical example used to examine flexural toppling and the effect of tensile strength on the slope height prior to failure, and the effect of the layer thickness on the tensile strength at failure. The results showed that as the tensile strength increased, the stable slope height increased. Also, as the layer thickness decreased, the tensile strength required to stabilize the slope increased. In the second example, a block toppling case study from the Highland Valley Copper Mine was examined to study the ability of the UDEC-DM approach in modeling large rock slopes. The field observations were compared to the ones predicted by the numerical simulation. The UDEC-DM approach was applied successfully to model a complex block toppling slope. Calibration of the model is essential to increase the reliability of the model. The southeast wall was calibrated and then compared to the field observations. Three main movement modes were observed and modeled using the UDEC-DM. Sliding at the top of the slope exposed normal scarps; toppling in the middle part of the slope exposed obsequent scarp facing opposite to the slope face, and bulging at the toe formed loose material. The deformations recorded in the field were compared to the simulation results, and a good agreement was achieved. The UDEC-DM results were also compared to the conventional UDEC results. UDEC-DM showed better agreement with the field observations than the conventional UDEC as a result of the fracturing characteristics inherent in the damage model approach. The deformation pattern in the block toppling example was different from that observed in flexural toppling.

A case study from the Revelstoke Dam project was modeled to examine the effect of weathering processes on rock slope behaviour. The Checkerboard Creek rock slope is moving at a range of 10 to 13 mm/year. This slope is located at the bank of a dam reservoir. If this rock slope fails, the failed mass might move toward the reservoir and cause a wave that might overtop the dam body. The rock slope is weathered from the surface down to 60 m. Aydin and Basu (2006) showed that as the degree of weathering increases, the rupture strain increases. Two methods were used to model the weathering process: degrading the tensile strength and applying a boundary condition to the surface of the slope. The simulation showed that the slope is not in imminent danger, and that if failure occurs, it will be limited to the steepest area of the slope near the toe. The results showed that even 180 years worth of deformation, at the current rate, will not cause a total failure of the slope. To avoid a retrogressive failure, a support system was used to stabilize the slope. The results are encouraging and showed the slope could be stabilized to limit the slope deformation and eventually stop it. The actual water table was included in the analysis.

8.2 Conclusion

The following summarizes the conclusions of this thesis:

- The UDEC-DM was successfully used to model direct shear tests. The resulting failure envelope was non-linear and was found to be in general agreement with the experimental results. At low normal stresses, the tensile strength of the intact rock affected the non-linearity of the failure envelope and as the normal stress increased, the failure envelope moved toward the frictional strength envelope.

- The role of the tensile strength in slope instability was investigated and found to be important when confining stress conditions were low in rock slopes. The degradation of the tensile strength caused fracture initiation, propagation, and coalescence between pre-existing non-persistent rock joints.

- Buckling movements occur in both open-pit and natural slopes and the tensile strength has an important role in controlling the movement initiation. The in situ stresses affect the tensile strength required to stabilize the slope and to limit the damage inside such layered rock slopes.

- The UDEC-DM predicted accurately the behaviour of the centrifugel experimental results of slopes susceptible to flexural toppling. The tensile strength controlled their stability and the load at failure, while the frictional strength was not found to be significant in such rock slopes. The deformation pattern predicted by the UDEC-DM was close to the experimental one and much closer than the the conventional UDEC.

- The proposed numerical modeling approach provides an excellent tool to simulate the fracturing of intact rock and the forming of an admissible rupture surface into the rock mass. The rupture surface predicted by the damage model was relatively accurate and coincided with the actual rupture surfaces observed in the real world. On the other hand, the conventional UDEC predicted a failure surface deeper than the actual one.

- With this modeling approach, complex continuous or discontinuous rock structures can be included in the simulation to mimic the rock mass structures in nature. This feature allow us to model the actual structure distribution in rock masses and to include both small and large rock discontinuities. Non-persistent rock joints can be incorporated in the modeling process.
- If enough data are available, calibration of the numerical model is relatively simple and can be conducted by using the normal stiffness and the shear stiffness of the flaws. This calibration can be done by using a trail-and-error procedure and tracking the deformation. The deformation predicted by the numerical model was found to be in good agreement with the actual deformation.
- The persistence of rock joints affects the mobilized strength in rock masses. This effect was clear in the direct shear simulation and the rock slopes instabilities. In the direct shear tests, as the joint length increased, the mobilized strength decreased. In rock slopes, as the degree of persistency increased, the tensile strength required to stabilize the slope increased.
- The numerical modeling approach proposed in this study is very effective for modeling stratified and foliated rock masses such as slopes susceptible to flexural toppling, buckling, and block toppling. The modeling of damage through intact material is important to accurately simulate such rock slopes.
- The weathering process can be modeled using the UDEC-DM. The tensile strength degradation can affect large and small rock slopes. Weathered rocks

are susceptible to instabilities triggered by the destruction of the tensile strength. Supporting rock slopes can be effective in limiting the damage and deformation inside them.

8.3 Recommendations

- To represent the actual rock fabric, ultimately the polygonal blocks inside the UDEC-DM must be of the same size as the grain size in the real rock fabric. In the case of large rock slopes, satisfying this condition would require huge computational power and would have to be conducted by using parallel processing to reduce the computational time and to handle a large number of blocks. One of the current limitations of this approach is the time required to generate a model.

- In this thesis, the damage model concept was applied to two-dimensions problems. In the real world, problems are in three dimensions. Extending the modeling methodology into three dimensions would be of great benefit to the geotechnical analysis of underground and surface rock mechanics applications.

- The relation between the the cohesion and the tensile strength is not clear. Studying the effect of weathering on both the cohesion and tensile strength simultaneously would help in understanding their variation as a function of weathering. Laboratory programs could be conducted to study this problem and to compare the results with known failure criteria.

- The effect of the grain shape on the failure characteristics should be considered. With UDEC-DM, the user has control over the shape of the blocks. Considering the effect of the grain shape would require comparing numerical modeling simulation results such as those from direct shear tests, unconfined compressive strength tests, and tensile strength tests with laboratory results.

Bibliography

Adhikary, D. and Dyskin, A. V., 2006. Modelling of progressive and instantaneous failures of foliated rock slopes. *Rock Mechanics and Rock Engineering*, **40(4)**: 349–362. online.

Adhikary, D. P., Dyskin, A. V., and Jewell, R. J., 1996. Numerical modelling of the flexural deformation of foliated rock slopes. *International Journal of Rock Mechanics and Mining Science and Geomechanics Abstract*, **33(6)**: 595–606.

Adhikary, D. P., Dyskin, A. V., Jewell, R. J., and Stewart, D. P., 1997a. A study of the mechanism of flexural toppling failure of rock slopes. *Rock Mechanics and Rock Enguneering*, **30**: 75–93.

Ahlgren, S., 2001. The nucleation and evolution of Riedel shear zones as deformation bands in porous sandstone. *Journal of Structural Geology*, **23**: 1203–1214.

Alzo'ubi, A., Martin, C., and Cruden, D., 2007. A distcrete element damage model for rock slopes. In *Rock Mechanics, Meeting Society's Challenges and demands*, edited by E. Eberhardt, D. Stead, and T. Morrison, vol. 1, pp. 503–510. Vancouver, B.C.

Ambarcumjan, R. V., 1974. Convex polygons and random tessellations. In *Stochastic Geometry*, edited by E. Harding and D. Kendall, pp. 176–191. Wiley, New York.

Arjang, B., 2006. Canadian crustal stresses and their application in mine design. Division Report MMSL 05-032(TR), Mining and Mineral Sciences Laboratories, Natural Resources Canada, Ottawa.

Aydin, A. and Basu, A., 2006. The use of Brazilian test as a quantitative measure of rock weathering. *Rock Mechanics and Rock Engineering*, **39(1)**: 77–85.

Barton, N., 1971. Progressive failure of excavated rock slopes. In *In: Stability of Rock Slopes, Proceedings of the 13th US Symposium of Rock Mechanics*, pp. 139–170. Urbana, IL.

Benko, B. and Stead, D., 1998. The Frank Slide: a reexamination of the failure mechanism. *Canadian Geotechnical Journal*, **35**: 299–311.

Bieniawski, Z., 1976. Rock mass classification in rock engineering. In *Exploration for Rock Engineering*, edited by A. Balkema, vol. 1, pp. 97–106. Cape Town, Johannesburg.

Brawner, C., Pentz, D., and Sharp, J., 1971. Stability studies of a footwall slope in layered coal deposits. In *13th US Symposium on Rock Mechanics*, pp. 329–365.

Brown, E., 2008. Estimating the mechanical properties of rock masses. In *1st Southern Hemisphere International Rock Mechanics Symposium*, edited by Y. Potvin, J. Carter, A. Dyskin, and R. Jeffrey, vol. 1, pp. 3–22. Australian Centre for Geomechanics.

Carvalho, J., Carter, T., and Diederichs, M., 2007. An approach for prediction of strength and post-yield behaviour for rock masses of low intact strength. In *Rock Mechanics, Meeting Society's Challenges and demands*, edited by E. Eberhardt, D. Stead, and T. Morrison, vol. 1, pp. 249–257. Vancouver, B.C.

Cavers, D., 1981. Simple methods to analyze buckling of rock slopes. *Rock Mechanics*, **14**: 87–104.

Cho, N., Martin, C., and Sego, D., 2008. Development of a shear zone in brittle rock subjected to direct shear. *International Journal of Rock Mechanics & Mining Sciences*, **doi:10.1016/j.ijrmms.2008.01.019**.

Cloos, E., 1955. Experimental analysis of fracture patterns. *Bulletin of The Geological Society of America*, **66**: 241–256.

Cresswell, A. and Barton, M., 2003. Direct shear tests on an uncemented, and a very slightly cemented, locked sand. *Quarterly Journal of Engineering Geology and Hydrogeology*, **36**: 119–132.

Cruden, D., 2003. The shapes of cold, high mountains in sedimentary rocks. *Geomorphology*, **55**: 249–261.

Cruden, D. and Hu, X.-Q., 1994. Topples on underdip slopes in the Highwood Pass, Alberta, Canada. *Quarterly Journal of Engineering Geology*, **27**: 57–68.

Cruden, D. and Martin, C., 2007. Before the Frank Slide. *Canadian Geotechnical Journal*, **44**: 765–780.

Cruden, D. and Varnes, D., 1996. Landslide types and processes. In *Landslides: Investigation and Mitigation, Special Report*, edited by A. Turner and R. Schuster, no. 247, pp. 36–75. Transportation Research Board (National Research Council), National Academy Press, Washington, D.C.

Cruden, D. M., 1989. Limits to common toppling. *Canadian Geotechnical Journal*, **26**: 737–742.

Cruden, D. M. and Hu, X. Q., 1988. Basic friction anglees of carbonate rocks from Kananaskis Country. *Bulletin International Association of Engineering Society*, **38**: 55–59.

Cundall, P., 2001. A discontinuous future for numerical modelling in geomechanics. *Geotechnical Engineering Journal*, **49**: 41–47.

Cundall, P. A., 1971. A computer model for simulating progressive large scale movements in blocky rock systems. In *Proceedings of the Symposium of the International Society of Rock Mechanics, ISRM*, pp. 129–136. ISRM, Nancy, France.

Dawson, R., 1990. Design Guidlines for Bedded Footwal Slopes. Master's thesis, University of Alberta, Edmonton, Alberta, Canada.

De Freitas, M. and Watters, R., 1973. Some field examples of toppling failure. *Geotechnique*, **23**: 485–514.

Dearman, W. R., 1991. Engineering Geological Mapping. Butterworth-Heinemann Ltd., Oxford.

Deere, D., 1963. Technical description of rock cores for engineering purposes. *Rock Mechanics and Engineering Geology*, **1**(1): 16–22.

Dershowitz, W. and Einstein, H., 1988. Characterizing rock joint geometry with joint system models. *Rock Mechanics and Rock Engineering*, **21**: 21–51.

Diederichs, M., Carvalho, J., and Carter, T., 2007. A modified approach for prediction of strength and post-yield behaviour for high GSI rock masses in strong, brittle rock. In *Rock Mechanics, Meeting Society's Challenges and demands*, edited by E. Eberhardt, D. Stead, and T. Morrison, vol. 1, p. 277285. Vancouver, B.C.

Eberhardt, E., Stead, D., and Coggan, J., 2004. Numerical analysis of initiation and progressive failure in natural rock slopes-the 1991 Randa rockslide. *International Journal of Rock Mechanics and Mining Science and Geomechanics Abstract*, **41(1)**: 69–87.

Eberhardt, E., Stead, D., Coggan, J., and Willenberg, H., 2002. An integrated numerical analysis approach applied to the Randa rock slide. In *1st European Conference on Landslides*, pp. 355–362. Prague, Czech Republic.

Einstein, H., Venezaino, D., Baecher, G., and O'reilly, K., 1983. The effect of discontinuity persistence on rock slope stability. *International journal of rock mechanics and mining science and geomechanics abstract*, **20(5)**: 227–236.

Fredlund, D. and Krahn, J., 1977. Comparison of slope stability methods of analysis. *Canadian Geotechnical Journal*, **14**: 429–439.

Goodman, R. and Bray, J., 1976. Toppling of rock slopes. In *Specialty Conference on Rock Engineering for Foundations and Slopes*, pp. 201–234. ASCE, Boulder, CO.

Goodman, R., Taylor, R., and Brekke, T., 1968. A model for the mechanics of jointed rock. *Journal of Soil Mechanics Division, Society of Civil Engineering*, **94**: 637–658.

Griffith, A. A., 1920. The phenomena of rupture and flow in solids. *Philosophical Transaction of the Royal Society of London*, **A221**: 163–198.

Hajiabdolmajid, V., 2001. Mobilization of strength in Brittle failure of rock. Ph.D. thesis, Queen's University, Kingston, Canada.

Hajiabdolmajid, V. and Kaiser, P., 2002a. Modelling slopes in brittle rock. In *5th North American Rock Mechanics Symposium*, pp. 331–338. NARMS-TAC, Toronto.

Hajiabdolmajid, V. and Kaiser, P., 2002b. Slope stability assesment in strain-sensitive rocks. In *EUROCK 2002, Proceedings of the ISRM International Symposium on Rock Engineeringfor Mountainous Regions*. Fuchal, Madeira.

Hajiabdolmajid, V., Kaiser, P., and Martin, C., 2002c. Modelling brittle failure of rock. *International Journal of Rock Mechanics and Mining Sciences and Geomechanics Abstract*, **39**: 731–741.

Hajiabdolmajid, V., Kaiser, P., and Martin, C., 2003. Mobilised strength components in brittle failure of rock. *Geotechnique*, **53**: 327–336.

Harrison, J. and Falcon, N., 1936. Gravity collapse structures and mountain ranges as exemplified in south-western Iran. *Quarterly Journal of the Geological Society of London*, **92**: 91–102.

Hoek, E. and Brown, E., 1980. Empirical strength criterion for rock masses. *Journal of Geotechnical Engineering Division, ASCE,*, **106(GT9)**: 1013–1035.

Hoek, E. and Brown, E., 1988. The Hoek-Brown failure criterion- a 1988 update. In *Proceedings of the 15th Canadian Rock Mechanics Symposium*, pp. 31–38. Department of Civil Engineering, University of Toronto, Toronto, Canada.

Hoek, E., Carranza-Torres, C., and Corkum, B., 2002. Hoek-Brown failure criterion-2002 edition. In *Proceedings of the 5th North American Rock Mechanics Symp*, vol. 1, pp. 267–273. Toronto, Canada.

Hu, X. and Cruden, D., 1993. Buckling deformation in the Highwood Pass, Alberta. *Canadian Geotechnical Journal*, **30**: 276–286.

Ingraffea, A. and Heuze, F., 1980. Finite element model for rock fracture mechanics. *International Journal for Numerical and Analytical Method in Geomechanics*, **4**: 24–43.

Itasca, 2000. FLAC -Fast Lagrangian Analysis of Continua, Version 4.0. Itasca consulting group, Minneapolis, U.S.A.

Itasca, 2004a. PFC2D-Particle Flow Code in 2 Dimensions, Version 3.1. Itasca Cons Group, Minneapolis, U.S.A.

Itasca, 2004b. Udec-Universal Distinct Element Code, Version 4.0. Itasca Consulting Group,Inc., Minneapolis:.

Jaeger, J., 1971. The 11th Rankine Lecture: friction of rocks and stability of rock slopes. *Geotechnique*, **21**: 97–134.

Jennings, J., 1970. A mathematical theory for calculation of the stability of slopes in open cast mines. In *In: Planning of Open Pit Mines*, pp. 87–102. Johannesburg.

Kaneko, K., Otani, J., Noguchi, Y., and Togashiki, N., 1997. Rock fracture mechanics analysis of slope failure. In *In: Deformation and Progressive Failure Geomechanics*, pp. 671–676. Nagoya, Japan.

Kemeny, J. M., 1991. A model for non-linear rock deformation under compression due to sub-critical crack growth. *International Journal of Rock Mechanics and Mining Sciences and Geomechanics Abstract*, **28(6)**: 459–467.

Krahn, J., 2003. The 2001 R.M. Hardy lecture: The limits of limit equilibrium analyses. *Canadian Geotechnical Journal*, **40(3)**: 643–660.

Ladanyi, B. and Archambault, G., 1980. Direct and indirect determination of shear strength of rock mass. In *Preprint Number 80-25, AIME Annual Meeting*. Littleton: Society of Mining Engineering of A.I.M.E., Las Vegas, Nevada.

Lajtai, E., 1969a. Mechanics of second order faults and tension gashes. *Geological society of American Bulletin*, **80**: 2253–2272.

Lajtai, E., 1969b. Shear strength of weakness planes in rock. *International Journal of Rock Mechanics and Mining Science*, **6**: 499–515.

Lajtai, E., 1969c. Strength of discontinuous rocks in direct shear. *Geotechnique*, **6**: 499–515.

Lajtai, E., 1974. Brittle fracture in compression. *International Journal of Fracture*, **10**(4): 525–536.

Lane, L., 1984. Brittle deformation in the columbia river fault zone near Revelstoke, southeastern British Columbia, Canada. *Canadaian Journal of Earth Sciences*, **21**: 584–598.

Lockner, D., 1995. Rock physics and phase relations, A handbook of physical constants. American Geophysical Union. 127-147.

Lorig, L. J. and Cundall, P. A., 1987. Modeling of reinforced concrete using the Distinct Element Method. In *Fracture of Concrete and Rock*, edited by S. B. Shah and S. E. Swartz, pp. 276–287. SEM-RILEM international Conference, Springer-Verlag New York Inc., Houston, Texas, USA.

Martin, C., 1993. The Strength of Massive Lac du Bonnet Granite around Underground Openings. Ph.D. thesis, University of Manitoba.

Martin, C. D., 1997. Seventeenth Canadian Geotechnical Colloquium:the effect of cohesion loss and stress path on brittle rock strength. *Canadian Geotechnical Journal*, **34(5)**: 698–725.

Martin, C. D. and Kaiser, P. K., 1984. Analysis of rock slopes with internal dilatioin. *Canadian Geotechnical Journal*, **21(4)**: 605–624.

McAffee, R. and Cruden, D., 1996. Landslides at Rock Glacier site, Highwood Pass, Alberta. *Canadian Geotechnical Journal*, **33**: 685–695.

Moore, D., Imrie, A., and Enegren, E., 1997. Evaluation and management of Revelstoke dam reservoir slopes. In *Proceedings of the 19th ICOLD Congress*, vol. 3, pp. 1–22. Florence, Italy.

Moore, D. P. and Lewis, M. R., 1982. Rock slope reinforcement with passive anchors. In *23rd United States Symposium on Rock Mechanics*, pp. 945–952. University of California, Berkeley, CA.

Morgenstern, N. and Price, V., 1965. The analysis of the stability of general slip surfaces. *Geotechnique*, **15**: 79–93.

Morgenstern, N. R. and Tchalenko, J. S., 1967a. Microscopic structures in Kaolin subjected to direct shear. *Geotechnique*, **17**: 309–328.

Morgenstern, N. R. and Tchalenko, J. S., 1967b. Microstructural observations on shear zones from slips in natural clays. In *Proceedings of the Geotech conference on shear strength of natural soils and rocks*, vol. 1, pp. 147–152. Norwegian Geotechnical Institute, Oslo.

Mughieda, O. and Alzo'ubi, A., 2004. Fracture mechanisms of offset rock joints-a laboratory investigation. *Geotechnical and Geological Engineering*, **22**: 545–562.

Nemcok, A., Pasek, J., and Rybar, J., 1972. Classification of landslides and other mass movements. *Rock mechanics*, **4**: 71–78.

Newcomen, H., Maggs, C., and Shwydiuk, L., 2003a. Managing pit slope displacments: Highland Valley Copper's Lornex pit southwest wall. In *Canadian Institute of Mining, Metallurgy and Petroleum (CIM) Bulletin*, vol. 96.

Newcomen, W., Murray, C., and Shwydiuk, L., 2003b. Monitoring pit wall deformation in real time at Highland Valley Copper. In *CAMI Conference,*.

Nichol, S., Hungr, O., and Evans, S., 2002. Large-scale brittle and ductile toppling of rock slopes. *Canadian Geotechnical Journal*, **39**: 773–788.

Ortlepp, W., 2000. Observation of mining-induced faults in an intact rock mass at depth. *International Journal of Rock Mechanics & Mining Sciences*, **37**: 423–436.

Petit, J. P. and Barquins, M., 1988. Can natural faults propagate under mode II conditions? *Tectonics*, **7**(6): 1243–1256.

Pierce, M., Cundall, P., Potyondy, D., and Mas Ivars, D., 2007. A synthetic rock mass model for jointed rock. In *Rock Mechanics, Meeting Society's Challenges and demands*, edited by E. Eberhardt, D. Stead, and T. Morrison, vol. 1, pp. 341–349. Vancouver, B.C.

Pine, R., Coggan, J. S., Flynn, Z., and Elmo, D., 2006. The development of a new numerical modelling approach for naturally fractured rock masses. *Rock Mechanics and Rock Engineering*, **39**(5): 395–419.

Pine, R. J., Owen, D. R. J., Coggan, J. S., and Rance, J. M., 2007. A new discrete fracture modelling approach for rock masses. *Geotechnique*, **57**(9): 757766.

Potyondy, D. and Cundall, P., 2004. A bonded-particle model for rock. *International Journal of Rock Mechanics and Mining Sciences and Geomechanics Abstract*, **41**: 1329–1364.

Rocscience, 2006. Rocscience Software products, DIPS, SWEDGE, SLIDE and PHASE2. Rocsience Inc., Toronton.

Sarma, S. K., 1979. Stability analysis of embankments and slopes. *Journal of the Geotechnical Engineering Division, ASCE*, **105(GT12)**: 1511–1524.

Scavia, C., 1995. A method to study the crack propagation in rock structures. *Geotechnique*, **45(3)**: 447–463.

Schlangen, E., 1995. Fracture simulation of brittle heterogeneous materials. In *Engineering mechanics, Proceedings of the 10th Conference*, vol. 1, pp. 130–133. New York: American Society of Civil Engineers (ASCE), Boulder.

Shen, B., Stephanson, O., Einstein, H. H., and Ghahreman, B., 1995. Coalescence of fractures under shear stresses in experiments. *Journal of Geophysical Research*, **100**: 5975–5990.

Sjoberg, J., 1996. Large scale slope stability in open pit mining- a review. Tech. rep., Lulea University of Technology, Sweden.

Sjoberg, J., 1999. Analysis of large scale rock slopes. Ph.D. thesis, Lulea University of Technology, Lulea, Sweden.

Skempton, A., 1964. Long-term stability of clay slopes. *Geotechnique*, **14**: 75–101.

Skempton, A. W., 1967. Some observations on tectonic shear zones. In *Proceedings of the 1st international congress on rock mechanics*, vol. 1, pp. 329–335. Lisbon.

Stacey, T. R., Xianbin, Y., Armstrong, R., and J., K. G., 2003. New slope stability considerations for deep open pit mines. *Journal of the South African Institute of Mining and Metallurgy*, **103**: 373–389.

Stead, D. and Coggan, J., 2006. Numerical modelling of rock slopes using a total slope failure approach. In *Landslides from Massive Rock Slope Failures*, edited by S. Evans, G. Mugnozza, A. Strom, and R. Hermanns, vol. 49, pp. 129–138.

Stead, D., Coggan, J., and Eberhardt, E., 2004a. Modelling of complex rock slope failure mechanisms using a hybrid finite-/discrete-element code. In *9th International Symposium on Landslides*, pp. 1067–1072. Rio de Janeiro.

Stead, D., Coggan, J., and Eberhardt, E., 2004b. Realistic simulation of rock slope failure mechanisms: the need to incorporate principles of fracture mechanics. In *SINOROCK 2004 symposium.*, pp. 1–6. International Journal of Rock of Rock Mechanics and Mining Science.

Stead, D. and Eberhardt, E., 1997. Development in the analysis of footwall slopes in surface coal mines,. *Engineering geology*, **46**: 41–61.

Stead, D., Eberhardt, E., Coggan, J., and Benko, B., 2001. Advanced numerical techniques in rock slope stability analysis-application and limitations. In *In: Landslide-Causes, Impacts and Countermeasures*, pp. 615–624. Davos, Switzerland.

Tchalenko, J. S., 1970. Similarities between shear zones of different magnitudes. *Geological Society of America Bulletin*, **81**: 1625–1640.

Terzaghi, K., 1962. Stability of steep slopes on hard unweathered rock. *Geotechnique*, **12**: 251–270.

Tosney, J., 2001. A design Approach for Large Scale Rock Slopes. Master's thesis, University of Saskatchewan, Saskatoon.

Tosney, J., Chance, A., Milne, D., and Amon, F., 2000. A modelling approach for large scale slope instability at Highland Valley Copper. In *Mining Millennium 2000: International Convention and Trade Exhibition*. Content Management Corp. Richmond Hill, ON., Toronto, Canada.

Tosney, J., Milne, D., and Chance, A.V.and Amon, F., 2004. Verification of a large scale slope instability mechanism at Highland Valley Copper. *International Journal of Surface Mining, Reclamation and Environment*, **18(4)**: 273–288.

Vallejo, L., 1982. Development of a shear zone structure in stiff clays. In *Proceedings of the 4th international conference on numerical methods of geomechanics*, edited by Z. Eisenstein, pp. 255–262. Edmonton.

Vekinis, G., Ashby, M. F., and Beaumont, P. W. R., 1993. Plaster of Paris as a model material for brittle porous solids. *Journal of Material Science*, **28**: 3221–7.

Vyazmensky, A., Elmo, D., Stead, D., and Rance, J., 2007. Combined finite-discrete element modelling of surface subsidence associated with block caving mining. In *Rock Mechanics, Meeting Society's Challenges and demands*, edited by E. Eberhardt, D. Stead, and T. Morrison, vol. 1, pp. 467–475. Vancouver, B.C.

Waldner, M., Smith, G., and Willis, R., 1976. Lornex. In *Prophyry Deposits of The Canadian Cordillera*, edited by A. Brown, vol. 15. CIM.

Wang, C., Tannant, D., and Lilly, P., 2003. Numerical analysis of the stability of heavily jointed rock slopes using PFC2D. *International Journal of Rock Mechanics and Mining Science*, **40**: 415–424.

Watson, A., Martin, C., Moore, D., Thomas, W., and Loren, J., 2006. Integration of geology, monitoring and modelling to assess rockslide risk. *Rock and Soil Engineering, Felsbau*, **3**: 50–58.

Watson, A., Moore, D., and Stewart, T., 2004. Temperature influence on rock slope movements at Checkerboard Creek. In *International Symposium on Landslides, Evaluation and Stabilization*, edited by Lacerda, Ehrlich, Fotoura, and Sayao, vol. 2, pp. 1293–1304. Rotterdam, Balkema, Rio de Janeiro.

Yan, M., Elmo, D., and Stead, D., 2007. Characterization of step-path failure mechanisms: A combined field based-numerical modeling study. In *Rock Mechanics, Meeting Society's Challenges and Demands*, edited by E. Eberhardt, D. Stead, and T. Morrison, vol. 1, pp. 493–501. Vancouver, B.C.

Zhang, J. H., Chen, Z. Y., and Wang, X., 2006. Centrifugal modeling of rock slopes susceptible to block toppling. *Rock Mechanics and Rock Engineering*, **40**: 363–382.